

UC San Diego

UC San Diego Electronic Theses and Dissertations

Title

Advanced Characterization Methods for Reaction Mechanism Investigation in Next Generation Energy Storage Systems

Permalink

<https://escholarship.org/uc/item/9fm0b9mn>

Author

Sayahpour, Baharak

Publication Date

2023

Peer reviewed|Thesis/dissertation

UNIVERSITY OF CALIFORNIA SAN DIEGO

Advanced Characterization Methods for Reaction Mechanism Investigation
in Next Generation Energy Storage Systems

A Dissertation submitted in partial satisfaction of the requirements
for the degree Doctor of Philosophy

in

Materials Science and Engineering

by

Baharak Sayahpour

Committee in charge:

Professor Ying Shirley Meng, Chair
Professor Andrea Tao, Co-Chair
Professor Zheng Chen
Professor Alex Frano
Professor Michael Sailor

2023

Copyright

Baharak Sayahpour, 2023

All rights reserved.

The Dissertation of Baharak Sayahpour is approved, and it is acceptable in quality and form for publication on microfilm and electronically.

University of California San Diego

2023

DEDICATION

To “Women, Life, Freedom”

In memory of PS752; 176+1 innocent victims

In quest of justice for all loved ones we lost unjustly

TABLE OF CONTENTS

DISSERTATION APPROVAL PAGE	iii
DEDICATION	iv
TABLE OF CONTENTS	v
LIST OF FIGURES	vii
LIST OF TABLES	xiv
LIST OF ABBREVIATIONS	xv
ACKNOWLEDGEMENTS	xix
VITA	xxii
ABSTRACT OF THE DISSERTATION	xxv
1. CHAPTER 1 - INTRODUCTION	1
1.1. ROLE OF PRIMARY BATTERIES IN THE FUTURE ENERGY STORAGE: CASE OF FLUORINATED CARBON	2
1.2. SODIUM-ION BATTERIES; ALTERNATIVE AND/OR COMPLEMENTARY TECHNOLOGY	6
1.2.1. <i>Positive Cathode Electrode</i>	8
1.2.2. <i>Negative Anode Electrode</i>	10
2. CHAPTER 2 – DISCHARGE MECHANISM STUDY OF LI-CF _x	13
2.1. INTRODUCTION	13
2.2. MATERIAL AND METHODS	17
2.3. RESULTS AND DISCUSSION	20
2.3.1. <i>Evaluating possible metallic/intercalated Lithium after discharge</i>	22
2.3.2. <i>Investigating the type and crystalline structure of carbon</i>	24
2.3.3. <i>Inspecting the size and distribution of LiF</i>	28
2.4. THREE-REGION DISCHARGE MECHANISM IN LI-CF _x SYSTEMS.....	37
2.5. CONCLUSIONS	39
2.6. ACKNOWLEDGEMENTS	40
3. CHAPTER 3 – RECHARGEABLE LITHIUM BATTERY BASED ON CF _x CATHODE MATERIAL	
41	
3.1. INTRODUCTION	41
3.2. MATERIALS AND METHODS	42
3.3. RESULTS AND DISCUSSIONS	44
3.3.1. <i>Modification of Fluorinated Carbon Material using Liquid-Exfoliation Method</i>	44
3.3.2. <i>Interaction between CF_x and FeF₃</i>	48
3.4. CONCLUSION	57
3.5. ACKNOWLEDGMENT	58

4.	CHAPTER 4 – HIGH ENERGY-DENSITY LOW-TEMPERATURE LI-CF _x BATTERY	59
4.1.	INTRODUCTION	59
4.2.	MATERIALS AND METHODS	64
4.3.	RESULTS AND DISCUSSIONS	66
4.3.1.	<i>Development of A Sustainable and Recyclable Liquid-Exfoliation Method.....</i>	<i>66</i>
4.3.2.	<i>Rate Capability and Ultra-Low Temperature Performance of the Exfoliated CF_x</i>	<i>70</i>
4.4.	CONCLUSION	80
4.5.	ACKNOWLEDGMENT.....	80
5.	CHAPTER 5 – SUSTAINABLE DESIGN OF SODIUM CATHODE MATERIALS	81
5.1.	INTRODUCTION.....	81
5.2.	ELEMENTS APPLIED IN CATHODE MATERIALS FOR NIBS.....	88
5.3.	GLOBAL RESERVES AND SUPPLY RISK FOR CRITICAL ELEMENTS	91
5.4.	MAIN SODIUM CATHODE CATEGORIES – OXIDES, POLYANIONS, AND PBAS	92
5.5.	DATA REPORTING STANDARD FOR NIBS	101
5.6.	CONCLUSIONS	103
5.7.	ACKNOWLEDGEMENTS	104
6.	CHAPTER 6 – QUANTITATIVE ANALYSIS OF SODIUM METAL DEPOSITION AND INTERPHASE	105
6.1.	INTRODUCTION	105
6.2.	MATERIALS AND METHODS	108
6.3.	RESULTS AND DISCUSSION.....	110
6.3.1.	<i>Impact of electrolyte compositions on ICE of Na metal anode</i>	<i>110</i>
6.3.2.	<i>Pressure effect on the morphology and capacity usage of plated Na metal anode</i>	<i>114</i>
6.3.3.	<i>Chemical composition of the SEI layer</i>	<i>125</i>
6.3.4.	<i>Electrochemical evaluation</i>	<i>133</i>
6.4.	CONCLUSIONS.....	136
6.5.	ACKNOWLEDGMENT.....	137
	REFERENCES	138

LIST OF FIGURES

- Figure 1-1.** A comparison of the key parameters for (a) Li-CF_x, (b) Li-SO₂, (c) Li-SOCl₂, and (d) Li-MnO₂ primary lithium batteries. The figure is adapted from this reference.⁴ 3
- Figure 1-2.** Global distribution of current lithium resources (2019).^{9,15} 7
- Figure 1-3.** The three main types of cathode materials for SIBs; oxide, PBA, and polyanion. A representative crystal structure of oxide, PBA, and polyanion as the three main types of cathode materials for sodium-ion batteries. The general formula for each type of material is listed below the schematic. M is the representative of the transition metal (TM). 9
- Figure 1-4.** (a) A brief timeline of the development of anodes for NIBs. (b) A schematic of main anode categories. (c) Research progress on anodes in NIBs. The figures are adapted from the references.^{58,60} 11
- Figure 2-1.** The evolution of the proposed reaction mechanism for Li-CF_x batteries through the years. 16
- Figure 2-2.** Representative electrochemical performance of the modified cathode structure. Li chip as the anode and 50 μL PC : DME (1:4, v:v) with 0.5 M LiTFSI as the electrolyte was used under 10 mA/g applied current density. The cathode loadings are 2.93-3.12 mg/cm²..... 20
- Figure 2-3.** Titration Gas Chromatography (TGC) Study on Li-CF_x system. (a) The electrochemical performance of the Li-CF_x cells using PC: DME (1:4, v:v) with 0.5 M LiTFSI as the electrolyte under 10 mA/g applied current density.; (b) Detected H₂ gas for pristine and fully discharged cathodes using water and ethanol solvents..... 22
- Figure 2-4.** The electrochemical performance of the Li-CF_x battery discharged to 0.001 V. The first discharge and the following charge profiles are presented. 23
- Figure 2-5.** (a) The electrochemical performance of Li-CF_x system; (b) Ex-situ XRD results on CF_x cathode at different DoD; The zoomed-in range showing (c) the disappearance of CF_x phase after 40% DoD.; (d) the graphitic peak remains without change; (e) the presence of LiF as the only discharge product and the disappearance of CF_x phase after 40% DoD. 25
- Figure 2-6.** Raman spectra on the cathodes [CF_x: CMC (98:2 wt.%)] through depths of discharge. 26
- Figure 2-7.** Raman spectroscopy on CF_x cathodes [CF_x:CMC (98:2 wt.%)]. (a) The electrochemical performance of the Li-CF_x system through different depths of discharge. (b) The ratio of D-band over G-band (I_D/I_G), (c) The G-peak position (cm⁻¹), and (d) The G-peak bandwidth (cm⁻¹) are shown through depths of discharge. 27
- Figure 2-8.** X-ray photoelectron spectroscopy (XPS) spectra on CF_x cathodes at different depths of discharge (data presented in Figure 2.9) in the binding energy range of 1200-5 eV. .. 29

Figure 2-9. X-ray photoelectron spectroscopy (XPS) on CF _x cathodes [CF _x :CMC (98:2 wt.%)] at different depths of discharge (DoD). The data is shown in different regions of (a) Li 1s; (b) F 1s; (c) C 1s; and (d) O 1s.	30
Figure 2-10. The XPS on the fully discharged CF _x cathodes for washed and unwashed cases are shown in different regions of (a) Li 1s; (b) F 1s; (c) C 1s; and (d) O 1s. The results demonstrate a minimal change in the amount of LiF on washed and un-washed electrodes as well as a limited amount of LiF on the surface.	31
Figure 2-11. The SEM and EELS elemental mapping on the pristine cathode sample. (a) The SEM image of the pristine CF _x powder, and (b) The cross-sectional FIB-SEM image of the pristine CF _x powder. (c) The EELS elemental mapping in (d) Carbon (C) and (e) Fluorine (F) regions.	32
Figure 2-12. The cross-sectional focused ion beam SEM (FIB-SEM) and energy dispersive x-ray spectroscopy (EDS) mapping on the discharged cathode [CF _{1.05} :CMC (98:2 wt%)] sample. The cross-sectional FIB-SEM images in (a), (b), and (c). The cross-sectional SEM and EDS mapping in (e) Carbon (C), (f) Fluorine (F), and (g) Oxygen (O) regions.	32
Figure 2-13. The cross-sectional scanning electron microscopy (SEM) images of the three cathode electrodes for (a) The pristine cathode; and (b) The fully discharged cathode [CF _x : C65: PVDF (80:10:10 wt.%)]. The scale bars are 100 μm. (c) The average of electrode thickness for pristine and fully discharged cathodes in three different sample.	33
Figure 2-14. (a) The operando dilatometry measurement results of a cathode [CF _x : C65: PVDF (80:10:10) wt.%]. (b) The voltage profile and the first derivation of height change through depth of discharge. (c) The voltage profile and the second derivation of height change through depths of discharge.	34
Figure 2-15. The EELS data on pristine and discharged cathode samples in (a) C K-edge region; (b) F K-edge region; and (c) Li K-edge region; (d) Cryo-HRTEM on the discharged sample (e) The FFT showing LiF. EELS elemental mapping on (f) the surface; and (g) the bulk of the sample in Li and C regions.	35
Figure 2-16. STEM sample preparation using FIB TEM lift-out method. (a) The cross-sectional thinning on the fully discharged sample. (b) The cross-sectional FIB-SEM image of the sample; The EDS data after thinning the sample are shown for (c) oxygen element; (d) carbon element; and (e) fluorine element. The scale bars are 600 nm.	36
Figure 2-17. The electron energy loss spectroscopy (EELS) elemental mapping on the discharged cathode [CF _{1.05} :CMC (98:2 wt%)] sample on (a) the surface of the sample, (b) the bulk of the sample in F region.	37
Figure 3-1. A schematic of the liquid exfoliation method in four main steps.	44
Figure 3-2. The morphology and size of exfoliated CF _x powder compared to pristine CF _x powder. SEM images of (a) pristine, and (b) exfoliated CF _x powders. (c-d) AFM measurement of the exfoliated CF _x powder.	45

Figure 3-3. The surface and bulk characterizations of the pristine and exfoliated CF _x powders show chemical stability of the material after the liquid exfoliation. (a) XPS results of pristine and exfoliated CF _x powders in two main core levels of C 1s and F 1s. (b) Raman spectroscopy analysis of pristine and exfoliated CF _x powders.....	47
Figure 3-4. The electrochemical performance of the hybrid cathode structure based on 50 wt% CF _x and 50 wt% FeF ₃ in comparison with the pure CF _x and pure FeF ₃ in (a) the 1 st and (b) the 2 nd cycles.....	50
Figure 3-5. The second cycle discharge capacities of the hybrid structure of CF _x and FeF ₃ based on different weight percentage of FeF ₃ in cathode active material (CF _x +FeF ₃).....	51
Figure 3-6. The ex-situ XRD results through the depths of discharge in hybrid structure of CF _x and FeF ₃ with 1:1 weight ratio.....	52
Figure 3-7. The modified cathode design to the conventional cathode structure by substituting PVDF binder with fluorine-free PAN binder.....	53
Figure 3-8. The XPS results of the charged cathodes compared with pristine FeF ₃ cathode in C core level. The samples are charged FeF ₃ , 5 wt% FeF ₃ , and 50 wt% FeF ₃ with CF _x	55
Figure 3-9. The relative resistance of coin-cells using CF _x with FeF ₃ in comparison with C65 with FeF ₃ using EIS measurement. The data is shown for “as assembled” and “after the 1 st charge”.....	56
Figure 3-10. (a) The discharge capacities of hybrid structures over 10 cycles in comparison with pure CF _x and pure FeF ₃ . (b) The comparison of the discharge capacity of exfoliated CF _x with pristine CF _x in hybrid structure of CF _x :FeF ₃ over 10 cycles.	56
Figure 3-11. A summary figure of the interaction between CF _x and FeF ₃ through the first cycle.	58
Figure 4-1. The possible structural models and calculated heat of formation in CF ₁ for the infinite array of trans-linked cyclohexane chairs in layer stacking of (a) AB, (b) AA', and for the cis-trans-linked cyclohexane boats in layer stacking of (c) AB, and (d) AA'. The figure is adopted from the reference ⁶⁶	60
Figure 4-2. A schematic of challenges that hindered the performance of a battery at low temperatures.....	62
Figure 4-3. A comparison of yield and size distribution of exfoliated CF _x powders using IPA and Cyrene solvents with varied sonication times. Table shows liquid exfoliation yield for 1g pristine powder. The DLS data show the size distribution of exfoliated powders under (a) IPA-12hr, (b) Cyrene-8hr, (c) Cyrene-12hr, and (d) Cyrene-12hr-recycled.....	68
Figure 4-4. The electrochemical performance of the exfoliated CF _x powders using recycled and fresh Cyrene solvent.	69

Figure 4-5. The electrochemical performance of Li-CF_x battery using the exfoliated powder in comparison with the pristine powder at (a) room-temperature (25°C) and (b) ultra-low temperature (-60°C). The applied current density is 10 mA/g in all tests. 71

Figure 4-6. The EIS measurement through the depth of discharge on the cells using (a,c) the pristine-based cathode and (b,d) exfoliated-based cathode, at room temperature. The impedance spectra are shown through the depths of discharge to 1.5 V. 72

Figure 4-7. A comparison of the (a) bulk resistance and (b) charge transfer resistance in the pristine-based and the exfoliated-based cathode. The EIS analysis performed using the equivalent circuit shown in the inset of the figure. 73

Figure 4-8. The GITT discharge curves of Li-CF_x cells using the exfoliated-based cathode in comparison with the pristine-based cathode at (a) room-temperature (25°C) and (b) ultra-low temperature (-60°C). 74

Figure 4-9. A schematic of the GITT discharge curve in a single step, labeling the required parameters for the Fick's second law of diffusion. 75

Figure 4-10. The linear behavior of the potential (E) as a function of $\tau^{1/2}$ for pristine-based cathode at (a) room-temperature (25°C) and (b) ultra-low temperature (-60°C) and for exfoliated-based cathode at (c) room-temperature (25°C) and (d) ultra-low temperature (-60°C). .. 76

Figure 4-11. The ionic diffusion of lithium-ion (D_{Li^+}) during the first discharge for (a) pristine-based and (b) exfoliated-based cathodes, at room-temperature (25°C) and ultra-low temperature (-60°C). The D_{Li^+} is calculated based on the Fick's second law applied on the GITT measurement. 77

Figure 4-12. A summary of the Li-CF_x batteries using the exfoliated-based cathode in comparison with the pristine-based cathode (a) at varied operating temperatures of 25°C, 0°C, -20°C, and -60°C, and (b) under varied applied current densities of 10, 100, 500, 1000, and 1500 mA/g. 78

Figure 4-13. The standing of the Li-CF_x battery using the exfoliated-based cathode in comparison with the literature under varied low temperatures. 79

Figure 5-1. The schematic roadmap of sodium-ion batteries over years, highlighting the discovery of key materials and the relevant prototypes. 87

Figure 5-2. (a) The abundance of elements in the earth's crust and the main methods of their mining. (b) Spider plot comparing various desirable parameters for the main mining methods. (c) Share of global reserves for the main metal elements presented on the world's map. (d) Supply risk for the main metal elements from 2015 to 2030. 89

Figure 5-3. The three main types of cathode materials for SIBs. (a) A representative crystal structure of oxide, polyanion (NASICON), and PBA. The performance of the 295 NIB system is presented as (b) Upper cut off voltage versus capacity, and (c) Capacity retention versus energy density. 93

- Figure 5-4.** Energy density ($\text{Wh}\cdot\text{kg}^{-1}$) and capacity retention (%) for the three main types of cathode materials for the most common phases used in NIBs. The size of the dot represents number of cycles while the color indicates the type of metal. 95
- Figure 5-5.** Statistical summary of reported data from 295 sodium-ion half-cells reported in the literature. 102
- Figure 6-1.** The controlled TGC experiment on standard commercial powders showed no hydrogen generation. This test was performed using ethanol as the solvent. 112
- Figure 6-2.** Quantification of capacity usage and capacity loss using TGC method. Analysis of capacity usage and capacity loss are shown in **(a-b)** using 1 M NaPF_6 in different solvents; carbonate-based and ether-based, and **(c-d)** using 1 M of the different salts in EC:DMC and in DME. 113
- Figure 6-3.** The schematic of the pressure setup and the cell components used in this study. The axial pressure was controlled using the load cell. 114
- Figure 6-4.** The first cycle columbic efficiency of sodium on Al foil under different applied axial pressure **(a)** in DME and **(b)** in EC:DMC electrolytes. Analysis of the capacity usage for applied axial pressures using TGC method are also shown. Cross-sectional cryo-FIB-SEM images of the plated Na at opt. pressures **(c)** in DME and **(d)** in EC:DMC. 115
- Figure 6-5.** The surface of sodium is unstable at room temperature. The images at room temperature are shown for **(a-b)** top-view before milling, **(c)** top-view after milling, and **(d)** cross-sectional view after milling. The sample is freshly cut commercial sodium metal. 116
- Figure 6-6.** The surface of sodium is stable at cryogenic temperature. The images at cryogenic temperature are shown for **(a-b)** top-view before milling, **(c)** top-view after milling, and **(d)** cross-sectional view after milling. The sample is freshly cut commercial sodium metal. 117
- Figure 6-7.** The cross-sectional cryogenic **(a)** FIB-SEM image of the deposited sodium in DME under 180 kPa and **(b)** the EDS elemental mapping in **(c)** Na, **(d)** Al, **(e)** C, **(f)** O regions. The cross-sectional cryogenic **(g)** FIB-SEM image of the deposited sodium in EC:DMC under 250 kPa and **(h)** the EDS mapping in **(i)** Na, **(j)** Al, **(k)** C, **(l)** O regions. 118
- Figure 6-8.** Top-view cryogenic FIB-SEM images of plated sodium surface **(a)** in 1M NaPF_6 in DME electrolyte under 180 kPa uniaxial pressure and **(b)** in 1M NaPF_6 in EC:DMC (1:1) electrolyte under 250 kPa uniaxial pressure. 118
- Figure 6-9.** Cross-sectional cryogenic FIB-SEM images of the plated sodium at 10 kPa uniaxial pressures **(a)** in 1M NaPF_6 in DME electrolyte and **(b)** in 1M NaPF_6 in EC:DMC (1:1) electrolyte. The sodium was plated at $0.5 \text{ mA}/\text{cm}^2$ for $0.1 \text{ mAh}/\text{cm}^2$ on Al foil. 119
- Figure 6-10.** Top-view and cross-sectional cryogenic FIB-SEM images of stripped sodium in 1M NaPF_6 in EC:DMC (1:1) electrolyte at **(a-b)** 10 kPa and **(c-d)** 250 kPa. The sodium was

- platted at 0.5 mA/cm^2 for 1 mAh/cm^2 on Al foil at 250 kPa uniaxial pressure and stripped to 1V at 0.5 mA/cm^2 120
- Figure 6-11.** The cross-sectional cryogenic FIB-SEM images of the stripped sodium in 1M NaPF₆ in DME electrolyte under 180 kPa. The sodium was platted at 0.5 mA/cm^2 for 1 mAh/cm^2 on Al foil at 180 kPa uniaxial pressure and stripped to 1V at 0.5 mA/cm^2 120
- Figure 6-12.** Top-view cryogenic FIB-SEM images of platted sodium in 1M NaPF₆ in DME electrolyte under 10 kPa. The sodium was platted at 0.5 mA/cm^2 for 1 mAh/cm^2 on Al foil at 10 kPa uniaxial pressure. 121
- Figure 6-13.** Cross-sectional cryogenic FIB-SEM images of the platted sodium in 1M NaPF₆ in DME electrolyte under the uniaxial pressures of (a) 10 kPa, (b) 70 kPa, (c) 120 kPa, (d) 180 kPa, and (e) 250 kPa. The sodium was platted on Al foil at 0.5 mA/cm^2 for 0.1 mAh/cm² in (a) and for 1 mAh/cm^2 in (b-e). The scale bars are 5 μm. 121
- Figure 6-14.** Cross-sectional cryogenic FIB-SEM images of the platted sodium in 1M NaPF₆ in EC:DMC electrolyte under the uniaxial pressures of (a) 10 kPa, (b) 70 kPa, (c) 120 kPa, (d) 180 kPa, (e) 250 kPa, and (f) 320 kPa. The sodium was platted on Al foil at 0.5 mA/cm^2 for 0.1 mAh/cm² in (a-b) and for 1 mAh/cm^2 in (c-f). The scale bars are 5 μm. 122
- Figure 6-15.** EIS measurement of Na||Al cells using both electrolytes at min. and opt. pressures at three stages. The data for DME is shown for (a) 10 kPa and (b) 180 kPa, and (c) compared in overall. The data for EC:DMC is shown for (d) 10 kPa and (e) 250 kPa, and (f) compared in overall. 123
- Figure 6-16.** Change of ion diffusion under applied axial pressure. The results are shown for (a) 1 M NaPF₆ in DME and (b) 1 M NaPF₆ in EC:DMC (1:1) at the minimum and optimum pressures after the first plating and after the first stripping. 124
- Figure 6-17.** The surface characterization of SEI layer using the depth profiling XPS on the stripped sodium sample in C 1s, Na 1s, O 1s, F 1s, and P 2p regions. The atomic ratio of each element through the depth of etching is presented for the case of (a) 1M NaPF₆ in DME, and (b) 1M NaPF₆ in EC:DMC. 126
- Figure 6-18.** XPS spectra at different depth of etching on the stripped sodium in the binding energy range of 1200-10 eV. The spectra show the presence of Na, C, F, O, and P bonding and there is no impurity from any other elements. The data is shown for (a) 1M NaPF₆ in DME electrolyte and (b) 1M NaPF₆ in EC:DMC electrolyte. 128
- Figure 6-19.** The surface characterization of SEI layer on the stripped sodium sample. The cryo-TEM of the stripped sodium (a) in 1M NaPF₆ in DME, and (b) in 1M NaPF₆ in EC:DMC (1:1). The SAED patterns show the crystalline structure of SEI components are shown in (c) 1M NaPF₆ in DME, and (d) 1M NaPF₆ in EC:DMC (1:1). 129
- Figure 6-20.** The EDS elemental mapping on the stripped sodium in 1M NaPF₆ in DME. (a) HAADF image, and elemental composition scans in (b) Na, (c) C, (d) overlaid of Na and

C, (e) O, (f) overlaid of Na and O, (g) F, and (h) P regions. The sodium was plated at 0.5 mA/cm² for 1 mAh/cm² on TEM grid at 180 kPa and stripped to 1V at 0.5 mA/cm².... 130

Figure 6-21. The EDS elemental mapping on the stripped sodium in 1M NaPF₆ in EC:DMC (1:1). (a) HAADF image, and elemental composition scans in (b) Na, (c) C, (d) overlaid of Na and C, (e) O, (f) F, and (g) P regions. The sodium was plated at 0.5 mA/cm² for 1 mAh/cm² on TEM grid at 250 kPa uniaxial pressure and stripped to 1V at 0.5 mA/cm²..... 131

Figure 6-22. The XRD pattern shows the pure O3 phase of NaCrO₂ cathode material. 133

Figure 6-23. The electrochemical performance of the cell. The cells have controlled 100% excess sodium anode. (a) Discharge capacity (mAh/g) and columbic efficiency (%) versus numbers of cycles at the rate of C/3. (b) The representative voltage profiles. 134

Figure 6-24. The electrochemical performance of the cell. (a) Discharge capacity (mAh/g) and columbic efficiency (%) versus numbers of cycles at 40°C temperature at the rate of C/3. (b) The representative voltage profiles. 135

Figure 6-25. The electrochemical performance of the cell. The cells have controlled 100% excess sodium anode. (a) The first cycle voltage profiles of cell at different C rates of C/10, C/5, C/3, C/2, 1C, and 2C. (b) Rate capability evaluation at room-temperature. 135

Figure 6-26. The electrochemical performance of the cell consisting of controlled electroplated sodium as the anode, NaCrO₂ as the cathode, and 1M NaPF₆ in DME as the electrolyte. The cells have controlled 100% excess sodium anode. (a) The self-discharge protocol. (b) The Self-discharge recovery of the cell at room-temperature. 136

LIST OF TABLES

Table 1-1. A summary of chemistry, theoretical capacity and energy density, and nominal voltages of the well-known lithium primary batteries.	3
Table 1-2. The physical, mechanical, and electrochemical properties of sodium in comparison with lithium. The data are acquired from the references. ^{16,17}	8
Table 2-1. Coin cell testing specifications used in sample preparation for the characterizations.	21
Table 3-1. The physical properties of the exfoliated CF _x powder compared with pristine CF _x powder.....	46
Table 3-2. The summary of the discharge capacities and columbic efficiencies. The discharge capacities in the 2 nd cycles are calculated based on the mass of the FeF ₃ in the cathode structure.....	50
Table 4-1. The physical properties of Cyrene, NMP, and IPA solvents.	67
Table 4-2. The coin-cell testing specifications used in low-temperature study.	70
Table 4-3. A summary of the protocols and approaches used in the literature in the Figure 4.13.	79
Table 6-1. The physical properties of the common carbonate- and ether- based solvents. Abbreviations: PC, EC, EMC, DMC, DEC, DME, DEGDME, TEGDME.	111
Table 6-2. Coin-cell testing specifications – Sodium-ion battery using sodium metal anode. ...	132

LIST OF ABBREVIATIONS

AFM	Atomic Force Microscopy
Al	Aluminum
As	Arsenic
BET	Brunauer-Emmett-Teller
Bi	Bismuth
C	Carbon
CATL	Contemporary Ampere Technology Co., Ltd.
CEI	Cathode Electrolyte Interphase
CF _x	Fluorinated graphite
CMC	Carboxymethyl cellulose
Co	Cobalt
Cryo-FIB	Cryogenic Focused Ion Beam
Cryo-STEM	Cryogenic scanning transmission electron microscopy
Cu	Copper
Cyrene	Dihydrolevoglucosenone
DFT	Density Functional Theory
Diglyme	Bis(2- methoxyethyl) ether
DLS	Dynamic Light Scattering
DMC	Dimethyl Carbonate
DME	Dimethoxyethane
DMF	Dimethylformamide
DoD	Depths of Discharge (DoD)

EC	Ethylene Carbonate
EDS	Energy Dispersive X-ray Spectroscopy
EELS	Electron Energy Loss Spectroscopy (EELS)
EIS	Electrochemical Impedance Spectroscopy
EOL	End of Life
EVs	Electric Vehicles
F	Fluorine
Fe	Iron
FEC	Fluoroethylene Carbonate
FeF ₃	Iron Fluoride
FFT	Fast Fourier Transform
GIC	Graphite Intercalation Compounds
GITT	Galvanostatic Intermittent Titration Technique
HRTEM	High Resolution Transmission Electron Microscopy
ICE	Initial Columbic Efficiency
Li	Lithium
Li/Ag ₂ CrO ₄	Lithium Silver Chromate
Li/CuS	Lithium Cupric Sulfide
Li/MnO ₂	Lithium Manganese Dioxide
Li/SOCl ₂	Lithium Thionyl Chloride
Li ₂ CO ₃	Lithium Carbonate
Li ₂ O	Lithium Oxide
LiBF ₄	Lithium Tetrafluoroborate

LIBs	Lithium Ion Batteries
Li-CF _x	Lithium Fluorinated Carbon
LiF	Lithium Fluoride
LiI	Lithium Iodide
Li-I ₂	Lithium Iodine
LiTFSI	Lithium bis(trifluoromethanesulfonyl)imide
Mn	Manganese
Na	Sodium
Na ₂ O	Sodium Oxide
Na ₂ CO ₃	Sodium Carbonate
NCO	Sodium Chromite
NaF	Sodium Fluoride
NaPF ₆	Sodium hexafluorophosphate
Ni	Nickel
NIBs	Na Ion Batteries
NMP	N-methyl-2-pyrrolidone
O ₃	Octahedral
O ₂	Oxygen
OCV	Open Circuit Voltage
P	Phosphor/Phosphorus
P2	Prismatic
PAN	Polyacrylonitrile
PBA	Prussian blue analogs

PC	Propylene Carbonate
PFIB	Plasma Focused Ion Beam
PVDF	Polyvinylidene Fluoride
S	Sulfur
SAED	Selected Area Diffraction
Sb	Antimony
SEI	Solid Electrolyte Interphase
SEM	Scanning Electron Microscopy
SHE	Standard Hydrogen Electrode
Si	Silicon
SIB	Sodium Ion Battery
Sn	Tin
STEM	Scanning Transmission Electron Microscopy
SVHC	Substances of Very High Concern
TEGDME	Tetraethylene Glycol Dimethyl Ether
TGC	Titration Gas Chromatography (TGC)
Ti	Titanium
TiS ₂	Titanium Sulfides
TMDC	Transition Metal Dichalcogenides
UK	United Kingdom
V	Vanadium
XPS	X-ray Photoelectron Spectroscopy
XRD	X-ray Diffraction

ACKNOWLEDGEMENTS

This effort would not have been possible without the support of many, whose contributions are commendable.

First of all, I would like to express my sincere gratitude to my Ph.D. advisor, Prof. Ying Shirley Meng, for her guidance, support, and supervision throughout my Ph.D. journey. She has always been full of insights and vision, not only in my scientific career but also in my personal life. Her mentorship helped me become a better scientist, and I am grateful for the opportunity to work in her research group at UC San Diego.

I would like to express my deep gratitude to my committee members, Prof. Andrea Tao, Prof. Michael Sailor, Prof. Alex Frano, and Prof. Zheng Chen, for their thoughtful feedback and valuable advisement on my thesis.

I would like to thank my collaborators at Sandia National Laboratories, Dr. Katharine Harrison, Dr. Timothy Lambert, Dr. Noah Schorr, and Dr. Kevin Leung, for their support and fruitful discussions.

I would like to sincerely thank Dr. Mohammad Yousef Bahadori at MAE department at UC San Diego. I had the opportunity to serve as a teaching assistant in multiple quarters under his supervision. This opportunity provided me with the chance of close interaction with undergraduate students and to develop my teaching and class management skills. I would like to also acknowledge Dr. Milan Gembicky at Crystallography Facility at UC San Diego, Dr. Ich Tran at XPS Facility at UC Irvine IMRI Research Facility, Dr. Ryan Nicholl and Dr. Jeff Wu at UC San Diego Nano 3 SDNI Facility, Ricardo De-luna at UC San Diego MRSEC Facility, and Xuemei Huang at UC San Diego NMR/EPR Facility, for their generous assistance for different materials characterizations.

I would like to acknowledge my funding source, UC San Diego Materials Research Science and Engineering Center (UCSD MRSEC), supported by the National Science Foundation (Grant DMR-2011924).

I would like to also thank my colleagues at Laboratory of Energy Storage and Conversion (LESC). The awesome project scientists and post-docs, Dr. Minghao Zhang, Dr. Weikang Li, Dr. Long H.B. Nguyen, Dr. Jean-Marie Doux, Dr. Abhik Banerjee, Dr. Wurigumula Bao, Dr. Bing Han, Dr. Jihyun Jang, Dr. Guomin Zhu, Dr. Xiaowei Wang, Dr. Sam Oh, Dr. Xuefeng Wang, and Dr. Dijo Damien, for their helpful discussions and guidance through my PhD. The previous and current PhD students at LESC, Dr. Hyeseung (Haelie) Chung, Dr. Han Nguyen, Dr. Darren Tan, Dr. Hayley Hirsh, Dr. Pritesh Parikh, Dr. Jonathan Scharf, Dr. Yixuan Li, Ryosuke Shimizu, Bingyu Lu, Matthew Mayer, Weiliang Yao, Phillip Ridley, Grayson Deysher, Yijie (Jackie) Yin, Saurabh Parab, Ganesh Raghavendran, Shuang Bai, So-Yeon Ham, Ashley Cronk, Bhagath Sreenarayanan, and Na-Ri Park, for their friendship. I truly enjoyed working with you and learning from you. A lot of my work could never be completed without their intellectual contributions.

My wonderful friend, Dr. Mandana Norouzi, who defines the meaning of friendship.

And a special thank you to my family: My mother, Mahrang, and my father, Darioush, for being such wonderful role models for me since I was a child, who embedded in me the values of curiosity and compassion while also inspiring me throughout my life. And my only brother, Bardia, with his zest for life and unique sense of humor, was always an inspiration to me. I would like to express my heartfelt gratitude for your unconditional love and support throughout my life.

Last but not least, my beloved, Pedram. Who believed in me even when I did not believe in myself. None of this would have been possible without his endless encouragement and support.

Chapter 2, in full, is a reprint of the material as it appears in *Advanced Energy Materials Journal* and in partial in *The Electrochemical Society Meeting Abstract*. Baharak Sayahpour, Hayley Hirsh, Shuang Bai, Noah Schorr, Timothy Lambert, Matthew Mayer, Wurigumula Bao, Diyi Cheng, Minghao Zhang, Kevin Leung, Katharine Harrison, Weikang Li, Ying Shirley Meng “Revisiting Discharge Mechanism of CF_x as a High Energy Density Cathode Material for Lithium Primary Battery” 12.5 (2022) 2103196. Baharak Sayahpour, Shuang Bai, Diyi Cheng, Minghao Zhang, Weikang Li, Ying Shirley Meng “Elucidation of Discharge Mechanism in CF_x as a High Energy Density Cathode Material for Lithium Primary Battery” 241. No. 2. *The Electrochemical Society, Inc.*, 2022. The dissertation author was the primary investigator and author of this paper.

Chapter 3, contains unpublished material coauthored with Yin, Yijie, Li, Weikang and Meng, Ying Shirley. The dissertation author was the primary author of this chapter.

Chapter 4, contains unpublished material coauthored with Yin, Yijie, Li, Weikang and Meng, Ying Shirley. The dissertation author was the primary author of this chapter.

Chapter 5, in full, is a reprint of the material as it appears in the *MRS Energy & Sustainability Journal*. “Perspective: Design of Cathode Materials for Sustainable Sodium-ion Batteries” by Baharak Sayahpour, Hayley Hirsh, Saurabh Parab, Long Hoang Bao Nguyen, Minghao Zhang, Ying Shirley Meng 9.2 (2022): 183-197. The dissertation author was the primary investigator and author of this paper.

Chapter 6, in part, is currently being prepared for submission for publication of the material. Sayahpour, Baharak; Lu, Bingyu; Bai, Shuang; Han, Bing; Chen, Yu-Ting; Li, Weikang; Deysheer, Grayson; Chouchane; Mehdi, Parab, Saurabh; Ridley, Phillip; Raghavendran, Ganesh; Nguyen, Long H. B.; Zhang, Minghao; Meng, Ying Shirley. The dissertation author was the primary researcher and author of this material.

VITA

- 2014 Bachelor of Science in Chemical Engineering, University of Tehran
- 2017 Master of Science in Mechanical Engineering, University of Illinois at Chicago
- 2023 Doctor of Philosophy in Materials Science, University of California San Diego

PUBLICATIONS

Peer-reviewed Journals:

14. A. Cronk, Y. Chen, G. Deysher, S. Ham, H. Yang, P. Ridley, **B. Sayahpour**, L. Nguyen, J. Oh, J. Jang, D. Tan, Y.S. Meng "Overcoming the Interfacial Challenges of LiFePO₄ in Inorganic All-Solid-State Batteries" *ACS Energy Letters* 8.1 (2023): 827-835.
13. W. Yao, M. Chouchane, W. Li, S. Bai, Z. Liu, L. Li, A. Chen, D. Lipomi, **B. Sayahpour**, R. Shimizu, G. Raghavendran, M. Schroeder, Y. Chen, D. Tan, B. Sreenarayanan, C. Waters, A. Sichler, B. Gould, D. Kountz, M. Zhang, Y.S. Meng "A 5V-Class Cobalt-free Battery Cathode with abled by Dry Coating" *Energy and Environmental Science* (2023).
12. Y. Yin, J. Holoubek, A. Liu, **B. Sayahpour**, G. Raghavendran, G. Cai, B. Han, M. Mayer, N. Schorr, T. Lambert, K. Harrison, W. Li, Z. Chen, Y. S. Meng "Ultra-Low Temperature Li/CF_x Batteries Enabled by Fast-transport and Anion-pairing Liquefied Gas Electrolytes" *Advanced Materials* 35.3 (2023): 2207932.
11. P. Ridley, L. Nguyen, E. Sebti, G. Duong, Y. Chen, **B. Sayahpour**, A. Cronk, G. Deysher, S. Ham, J. Oh, E. Wu, D. Tan, J.M. Doux, R. Clement, J. Jang, Y.S. Meng "Glass-Ceramic Sodium-Deficient Chlorides with High Sodium-ion Conductivity" 10.26434/chemrxiv-2022-x7llq.
10. G. Deysher, Y. Chen, **B. Sayahpour**, S. Lin, S. Ham, P. Ridley, A. Cronk, E. Wu, D. Tan, J.M. Doux, J. Oh, J. Jang, L. Nguyen, Y.S. Meng "Evaluating Electrolyte–Anode Interface Stability in Sodium All-Solid-State Batteries" *ACS Applied Materials & Interfaces* 14.42 (2022): 47706-47715.
9. **B. Sayahpour**, H. Hirsh, S. Parab, L. Nguyen, M. Zhang, Y.S. Meng "Perspective: Design of Cathode Materials for Sustainable Sodium-ion Batteries" *MRS Energy & Sustainability* 9.2 (2022) 183-197.
8. H. Chung, Y. Li, M. Zhang, A. Grenier, C. Mejia, D. Cheng, **B. Sayahpour**, C. Song, M. Shen, R. Huang, E. Wu, K. Chapman, S. Kim, Y. S. Meng, "Mitigating Anisotropic Changes in Classical Layered Oxide Materials by Controlled Twin Boundary Defects for Long Cycle Life Li-ion Batteries" *Chemistry of Materials* 34.16 (2022) 7302-7312.

7. J. Jang, Y. Chen, G. Deysher, D. Cheng, S. Ham, A. Cronk, P. Ridley, H. Yang, **B. Sayahpour**, B. Han, W. Li, W. Yao, E. Wu, J.M. Doux, L. Nguyen, J. Oh, D. Tan, Y.S. Meng “Enabling a Co-Free, High-Voltage $\text{LiNi}_{0.5}\text{Mn}_{1.5}\text{O}_4$ Cathode in All-Solid-State Batteries with a Halide Electrolyte” *ACS Energy Letter* 7.8 (2022) 2531-2539.
6. **B. Sayahpour**, H. Hirsh, S. Bai, N. Schorr, T. Lambert, M. Mayer, W. Bao, D. Cheng, M. Zhang, K. Leung, K. Harrison, W. Li, Y.S. Meng “Revisiting Discharge Mechanism of CF_x as a High Energy Density Cathode Material for Lithium Primary Battery” *Advanced Energy Materials* 12.5 (2022) 2103196.
5. U. Pal, D. Rakov, B. Lu, **B. Sayahpour**, F. Chen, B. Roy, D. MacFarlane, M. Armand, P. Howlett, Y.S. Meng, M. Forsyth, D. Rakov “Interphase Control in Lithium Metal Batteries Through Electrolyte Design” *Energy and Environmental Science* 15 (2022) 1907-1919.
4. D. Tan, Y. Chen, H. Yang, W. Bao, B. Sreenarayanan, J.M. Doux, W. Li, B. Lu, S. Ham, **B. Sayahpour**, J. Scharf, E. Wu, G. Deysher, H. Han, H. Hah, H. Jeong, J. Lee, Z. Chen, Y.S. Meng “Carbon-Free High-Loading Silicon Anodes Enabled by Sulfide Solid Electrolytes” *Science* (2022) 373 (6562), 1494-1499.
3. Y. Chen, M. Marple, D. Tan, S. Ham, **B. Sayahpour**, W. Li, H. Yang, E. Wu, J.M. Doux, J. Jang, P. Ridley, A. Cronk, G. Deysher, Z. Chen, Y.S. Meng “Investigating Dry Room Compatibility of Sulfide Solid-State Electrolytes for Scalable Manufacturing” *Journal of Materials Chemistry A* (2022) A 10 (13), 7155-7164.
2. H. Hirsh, **B. Sayahpour**, A. Shen, W. Li, E. Zhao, M. Zhang, Y.S. Meng “Role of Electrolyte in Stabilizing Hard Carbon as an Anode for Rechargeable Sodium-ion Batteries with Long Cycle Life” *Energy Storage Materials*, 2021, 42, 78-87.
1. H. Chung, Z. Lebens-Higgins, **B. Sayahpour**, C. Mejia, A. Grenier, G. Kamm, Y. Li, R. Huang, L. Piper, K. Chapman, J.M. Doux, Y.S. Meng. “Experimental Considerations to Study Li-excess Disordered Rock Salt Cathode Materials” *Journal of Materials Chemistry A*, 2021, 9, 1720-1732.

Conferences:

3. **B. Sayahpour**, S. Bai, D. Cheng, M. Zhang, W. Li, Y.S. Meng “Elucidation of Discharge Mechanism in CF_x As a High Energy Density Cathode Material for Lithium Primary Battery” The Electrochemical Society (ECS) Meeting 241 (2022) 335.
2. H.S. Hirsh, **B. Sayahpour**, A. Shen, W. Li, E. Zhao, Y.S. Meng “Role of Electrolyte in Stabilizing the Solid Electrolyte Interface of Hard Carbon as an Anode for Sodium-Ion Batteries” The Electrochemical Society (ECS) meeting 239 (2021), 236.
1. H. Chung, J.M. Doux, A. Grenier, C. Mejia, **B. Sayahpour**, Y.S. Meng "Morphology Control to Enable High Capacity Li-Rich Disordered Rock Salt Cathodes" The Electrochemical Society (ECS) Meeting 237 (2020) 537.

ABSTRACT OF THE DISSERTATION

Advanced Characterization Methods for Reaction Mechanism Investigation
in Next Generation Energy Storage Systems

by

Baharak Sayahpour

Doctor of Philosophy in Materials Science and Engineering

University of California San Diego, 2023

Professor Ying Shirley Meng, Chair
Professor Andrea Tao, Co-Chair

Continuous increase in global energy demand along with supply chain risks associated with Li metal has underscored the need for advanced energy storage technologies in the past decade. Generally modern energy storage systems are divided into primary (non-rechargeable) and secondary (rechargeable) types of batteries, both of which currently suffer from the lack of high energy density for emerging technologies and compatibility with the harsh and extreme

environments. This thesis is an effort to design, fabricate, and characterize two energy storage systems that hold a great promise as an alternative for the future of primary and secondary energy storage systems.

Lithium/fluorinated graphite (Li/CF_x) batteries are one of the most well-known primary batteries due to their high energy density (>2100 Wh kg⁻¹) and low self-discharge rate (< 0.5% per year at 25 °C). While the electrochemical performance of the CF_x cathode is indeed promising, the discharge reaction mechanism is not thoroughly understood. Here, we use a combination of titration gas chromatography, X-ray diffraction, focused ion beam scanning electron microscopy, and cryogenic scanning transmission electron microscopy with electron energy loss spectroscopy methods to propose a more comprehensive discharge mechanism in CF_x cathodes. We further investigate the possible rechargeability of the CF_x-based cathode using a hybrid structure with FeF₃.

Next, we focus on Sodium-ion batteries as one of the most promising alternatives to rechargeable lithium-based battery technologies. Implementation of this technology has been practically hindered due to a lack of high energy density cathode materials and stable anode materials with a desired cycle-life. To address these points, we implement uniaxial pressure as a knob to control sodium metal deposition with dense morphology to enable high initial coulombic efficiencies. Moreover, we use titration gas chromatography to precisely quantify the sodium capacity loss in ether- and carbonate-based electrolytes. With that, we enabled a long cycling battery using a controlled electroplated sodium metal as the anode with high-rate performance.

Implementation of advanced characterization for fundamental understanding of reaction mechanisms and interface properties in conjunction with synthesis and performance evaluation as demonstrated in this thesis is critical for designing next generation of energy storage.

1. CHAPTER 1 - INTRODUCTION

During the past few decades, lithium-ion batteries (LIBs) have been the gold standard technology for mobile and grid level energy storage. It is expected that global demand for LIBs will increase by almost 10 times by 2030. This has triggered extensive research on development of advanced materials for Lithium-ion batteries with higher energy density and life cycle to meet the increasing demand as well as modern applications such as electric vehicles (EVs) and portable electronics. Besides that, a major challenge in current li-ion technologies is high cost of lithium and its supply chain risks. These facts highlight the importance of developing alternatives or complementary options that can sustain this growing energy demand.

Another emerging area where current Li-ion technology fall behind is powering electronic devices in non-conventional and harsh conditions where recharging the battery is not possible including implantable medical devices, NASA's lunar and Mars' surface exploration, or military applications requiring human and robotic operation in harsh environments (i.e., ultra-low temperature, radiation, complex terrain).

Conventional Li-ion technologies paired with complex thermal management systems, which provide less than 200 Wh/kg at temperatures between -40°C and -80°C , cannot satisfy these requirements. Given the added complexity, weight, and cost of external heating or internal self-heating systems, advancing the battery chemistry to operate at these extreme temperatures is a more efficient approach. This has led to a growing research effort on primary batteries in which the electrochemical reaction occurring in the cell is not reversible. This is mainly due to a strong covalent bond between lithium and cation sites in the cathode structure after first discharge cycle.

In this thesis, we attempt to use advanced characterization methods in conjunction with synthesis and in-depth electrochemical performance evaluation to tackle two main research questions: (i) understanding the reaction mechanism in primary CF_x batteries and finding possible avenues for reachability of this conventionally non-rechargeable system, and (ii) developing Na-ion batteries based on sodium metal anode and highlighting the important factors in sustainable design of the cathode materials as an alternative for rechargeable Li-ion technology.

1.1. Role of Primary Batteries in the Future Energy Storage: Case of Fluorinated Carbon

Among the well-known lithium primary batteries¹⁻³, lithium fluorinated carbon (Li- CF_x) presents the highest theoretical specific capacity and energy density, while e.g. lithium iodine (Li/I₂), Lithium Manganese Dioxide (Li/MnO₂), lithium silver chromate (Li/Ag₂CrO₄), and lithium cupric sulfide (Li/CuS) suffer from reduced theoretical energy density. For example, the continuous growth of lithium iodide (LiI) interface will significantly decrease its low-temperature performance. Moreover, Li/CuS suffers from its low nominal voltage (1.2 V) and Li/MnO₂ battery suffers from a cathode swelling (gassing) at the rest stage.² Although lithium thionyl chloride (Li/SOCl₂) has high energy density (1470 Wh/kg) and nominal voltage (3.65 V), its remaining safety concerns make it unsuitable for space applications. A comparison of the key parameters and a summary of chemistry, theoretical capacity and energy density, and nominal voltages of the well-known lithium primary batteries are presented in Figure 1.1 and in Table 1.1, respectively. The figure and the values in the table are adapted from the reference.²⁻⁵

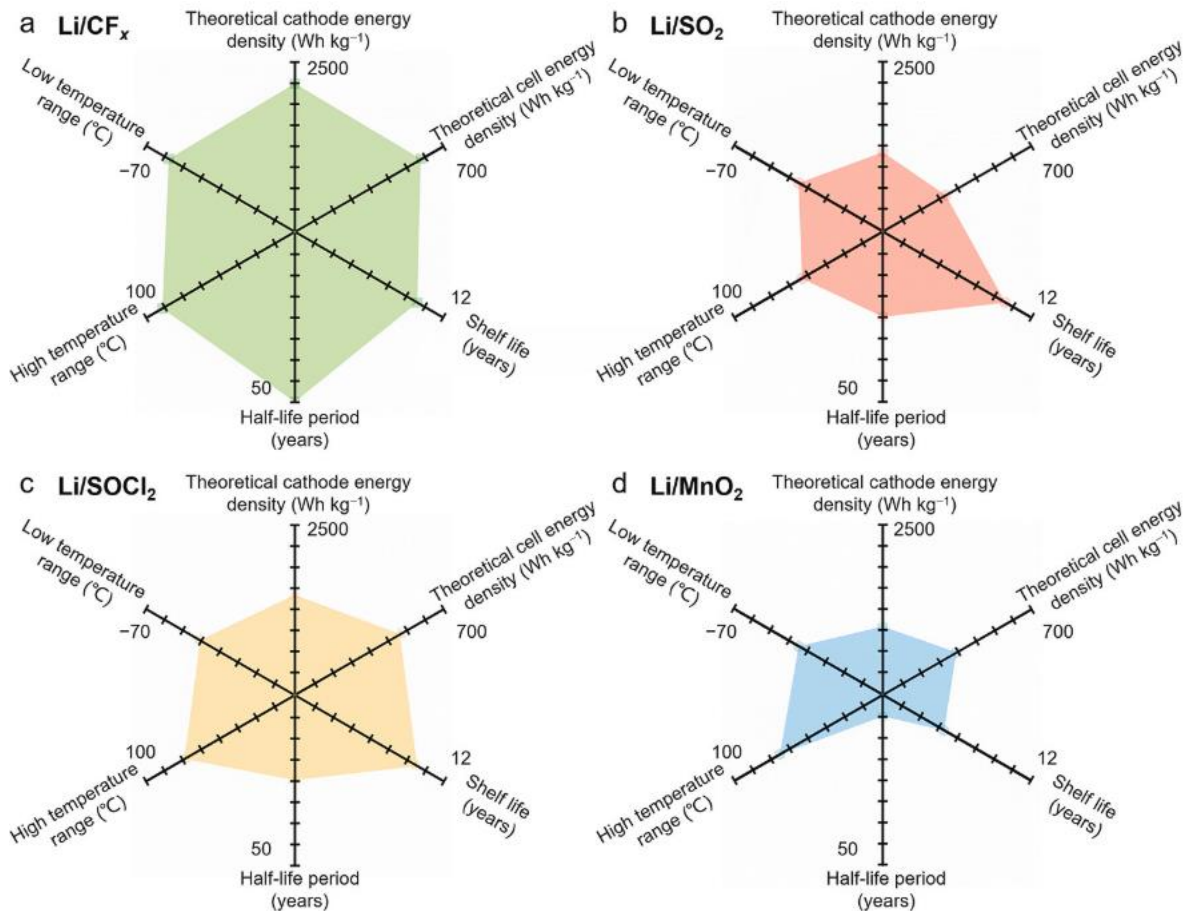


Figure 1-1. A comparison of the key parameters for (a) Li-CF_x, (b) Li-SO₂, (c) Li-SOCl₂, and (d) Li-MnO₂ primary lithium batteries. The figure is adapted from this reference.⁴

Table 1-1. A summary of chemistry, theoretical capacity and energy density, and nominal voltages of the well-known lithium primary batteries.

Battery Type	Anode	Cathode	Known Reaction	Theoretical Capacity (mAh/g)	Theoretical Energy Density (Wh/kg)	Nominal Voltage (V)
Li-CF _x	Li	CF _x	$x\text{Li} + (\text{CF})_x \rightarrow x\text{LiF} + x\text{C}$	865	2189	2.8
Li-SOCl ₂	Li	SOCl ₂	$4\text{Li} + 2\text{SOCl}_2 \rightarrow 4\text{LiCl} + \text{S} + \text{SO}_2$	450	1470	3.6
Li-CuS	Li	CuS	$2\text{Li} + \text{CuS} \rightarrow \text{Li}_2\text{S} + \text{Cu}$	560	1050	2.2
Li-MnO ₂	Li	MnO ₂	$\text{Li} + \text{Mn}^{\text{IV}}\text{O}_2 \rightarrow \text{Mn}^{\text{IV}}\text{O}_2(\text{Li}^+)$	310	1005	3.0
Li-I ₂	Li	I ₂	$\text{Li} + \frac{1}{2}\text{I}_2 \rightarrow \text{LiI}$	211	591	2.8
Li-Ag ₂ CrO ₄	Li	Ag ₂ CrO ₄	$\text{Li} + \text{Ag}_2\text{CrO}_4 \rightarrow \text{Li}_2\text{CrO}_4 + \text{Ag}$	160	515	3.1

As it can be seen, lithium fluorinated carbon (Li-CF_x) batteries are very promising to overcome this limitation mainly due to their high theoretical capacity (865 mAh/g), operating voltage (~2.6-2.7V at 25°C), and the low self-discharge rate (<0.5% per year at 20°C).¹ The following reaction is known to be the governing reaction in this class of materials: CF_x + Li → LiF + C. Fluorinated carbon is a non-stoichiometric compound with 0.5<x<1.3, exhibiting a low electrical conductivity due to the nature of covalent C-F bonds.^{6,7}

Although the lithium fluorinated graphite system has been under investigation for a few decades, there is still a lack of fundamental understanding of the reaction mechanism in this system. There is no clear and concise perspective about the discharge products and the possibility of lithium metal deposition in the cathode. Moreover, the kinetic limitations that hinder the Li⁺ diffusion and further rate capability of the system.

Despite these challenges, high theoretical energy density of Li-CF_x chemistry encourages further investigations in order to (i) tackle kinetic limitations at both ionic and electronic conductivity as the governing parameters for enabling high energy density low-temperature primary battery and (ii) evaluate the possibility of the rechargeability in this high energy density system with earth abundant and light weight elements. At ultra-low temperatures, the decrease of electronic conductivity and sluggish solid-state diffusion of Li⁺ between the fluorinated graphite layers will rapidly exacerbate, which restricts the kinetics property at the cathode side.⁸ Moreover, it is known that the fluorination of CF_x further hampers the electronic conductivity at all temperature ranges due to the covalent C-F bond.

In chapter two, a multiscale investigation on the CF_x discharge mechanism was performed using a novel cathode structure to minimize the carbon and fluorine additives for precise cathode characterizations. Titration gas chromatography (TGC), X-ray diffraction (XRD), Raman

spectroscopy, X-ray photoelectron spectroscopy (XPS), scanning electron microscopy (SEM), dilatometry measurement, cross-sectional focused ion beam (FIB), high-resolution transmission electron microscopy (HRTEM), and scanning transmission electron microscopy with electron energy loss spectroscopy (STEM-EELS) were utilized to investigate this system. This multiscale discharge mechanism study plays an important role in future experimental and computational works toward designing a higher power density cathode and help pave the path for developing a rechargeable Li-CF_x battery.

In chapter three, the possible rechargeability of the CF_x as a high energy density cathode material was investigated due to the low-cost abundant elements carbon and fluorine with the high energy density of active material CF_x. The rechargeability of this system depends on reversibility of the discharge reaction. Thus, there are two main parts in this study: (i) decomposition or limited formation of LiF as the main discharge product; (ii) re-fluorination of carbon for the subsequent cycles. The findings from discharge mechanism investigation encourage us to take a closer look into the rechargeable Li-FeF₃ system with similar nano-size LiF as the main discharge product. The possible interaction of FeF₃ with CF_x is investigated to evaluate the possible rechargeability of the Li-CF_x primary battery with the high energy density.

Despite all the advantages of the Li-CF_x battery system, there are kinetic limitations associated with the poor electrical conductivity and strong covalent C-F bonds results in slow cell reaction kinetics which further inhibits the utilization of lithium CF_x system in low temperature applications and high-power devices. To address this, in chapter four, a sustainable and recyclable liquid-phase exfoliation method was developed to convert pristine CF_x powder to nanoparticles with higher active surface area and lower thickness. The uniformity and size distribution of particles were measured using SEM, AFM and DLS. The chemical and structural stability of the

obtained powder was also evaluated by XPS, Raman spectroscopy, and XRD. The exfoliated powder has shown enhanced physical properties that boost the electrochemical performance of Li-CF_x battery at ultra-low temperature (-60°C) and higher rate capability due to the improved lithium-ion diffusion.

These works deepen the understanding of CF_x as a high energy density cathode material and highlight the need for future investigations on primary battery materials to advance performance and further consider their rechargeability.

1.2. Sodium-ion Batteries; Alternative and/or Complementary Technology

Lithium-containing resources, key components in most of the current energy storage systems, are centered in three main countries: Bolivia, Chile, and Argentina.⁹⁻¹¹ Such localized distribution of Li (Figure 1.2) accounts for more than 80% of the global reserves¹² and creates an imbalance in supply and demand for growing large-scale applications. Prior to 2010, the cost of lithium metal accounted only for a very small fraction (< 2%) of total cost of LIBs. Emerging new technologies, such as electric vehicles and exponential production rise in small electronics, has disrupted the lithium metal market and led to a continuous increase on the market price of lithium metal.

For instance, the price of Li₂CO₃, a well-known extraction resource for lithium metal, has tripled over the past 10 years.¹³ The high demand of Li resources and its increasing cost have triggered the exploration of alternatives or complementarities to Li-based technologies.¹⁴

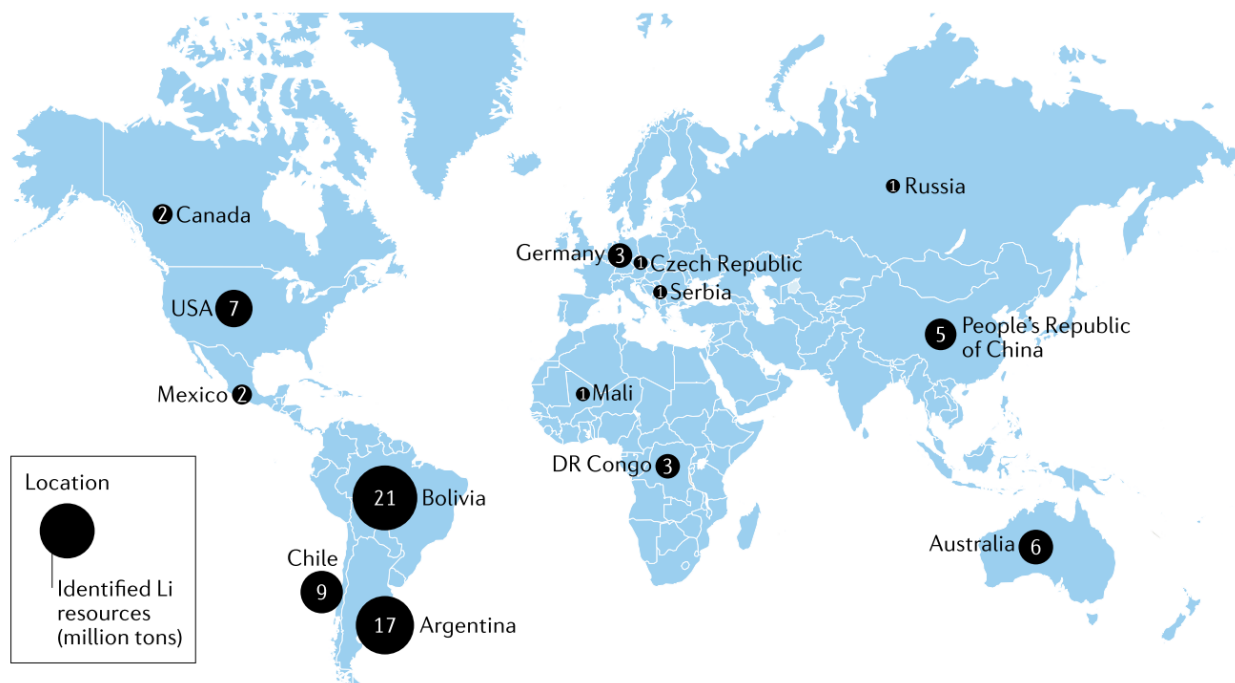


Figure 1-2. Global distribution of current lithium resources (2019).^{9,15}

Among different candidates, sodium-ion batteries (NIBs) metal is a great candidate for future energy grid storage due to high earth abundance of sodium (sixth most abundant element in the Earth's crust, ~2.6%), low cost per energy density, and sustainability. This alkali metal possesses a high theoretical specific capacity (1166 mAh/g), low reduction potential (-2.73 V vs. standard hydrogen electrode (SHE) compared to -3.02V vs. SHE for Li⁺/Li), and small ionic radius (1.02 Å).¹⁶ These features further highlight this metal as a promising alternative/complementary candidate to lithium metal. However, the differences in the chemical and electrochemical properties of sodium compared to lithium, as listed in Table 1.2, open up new challenges to explore this system.

Table 1-2. The physical, mechanical, and electrochemical properties of sodium in comparison with lithium. The data are acquired from the references.^{16,17}

Physical Properties						Mechanical Properties		Electrochemical Properties		
	Atomic Weight (g/mol)	Atomic Radius (Å)	Ionic Radius (Å)	Molar Volume (cm ³ /mol)	Melting Point (K)	Heat of Vaporization (kJ/mol)	Bulk Modulus (GPa)	Brinell Hardness (MPa)	Voltage vs. SHE (V)	1 st ionization energy (kJ/mol)
Na	23	1.86	1.02	23.75	371	97	6.3	0.69	-2.7	495.8
Li	6.9	1.52	0.76	12.97	454	136	11	5	-3.0	520.2

Despite the growing research in this field, the implementation of this technology has been practically hindered due to a lack of high energy density cathode materials and stable anode materials with a long cycle-life. It is also vital to consider that liquid electrolyte as the unique component with direct physical contact to all cell components requires to be particularly taken into account in the investigation of anode or cathode, separately.¹⁸ The high chemical and electrochemical reactivity of sodium leads to occurrence of side reaction with a fast electrolyte decomposition and further the formation of the irreversible solid electrolyte interphase (SEI) layer.

1.2.1. Positive Cathode Electrode

The perspective sodium cathode electrodes for NIBs are investigated in main categories of layered oxides, Prussian blue analogs (PBAs), polyanions, and organic compounds. Between these, the first three types of cathode materials are leading candidates for cathode materials in NIB technology. Theoretical specific and volumetric capacities, operational voltage, ionic diffusivity, chemical and structural stability, cost-efficiency, and easy processibility are among the key parameters to evaluate a suitable cathode material. A schematic of three main types of sodium cathode structures is shown in Figure 1.3.

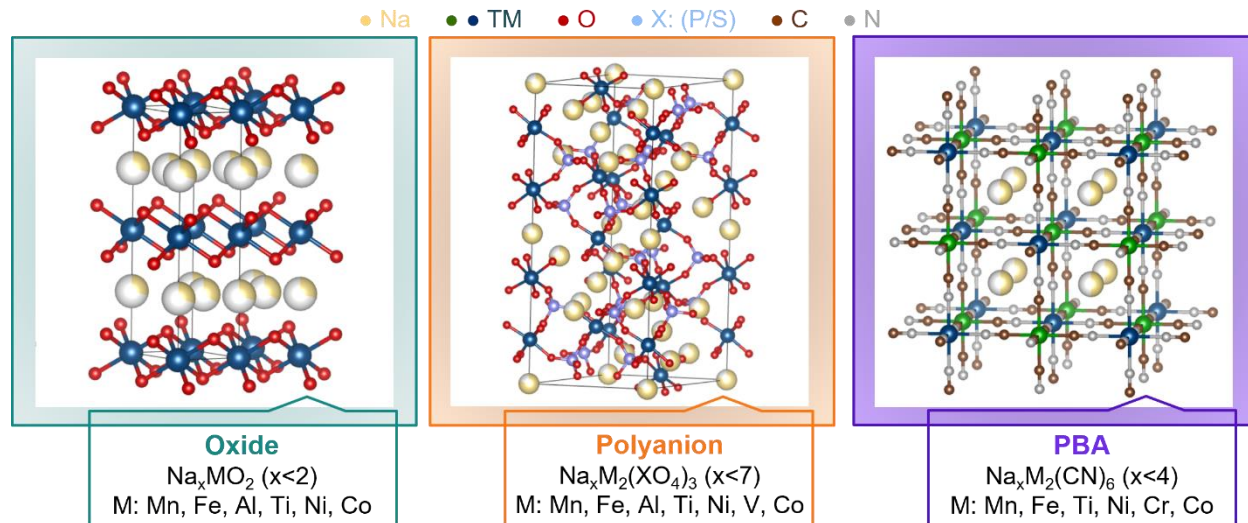


Figure 1-3. The three main types of cathode materials for SIBs; oxide, PBA, and polyanion. A representative crystal structure of oxide, PBA, and polyanion as the three main types of cathode materials for sodium-ion batteries. The general formula for each type of material is listed below the schematic. M is the representative of the transition metal (TM).

In chapter five, an overview of the milestones in the development of NIB systems over time is provided. Next, critical metrics in extraction of key elements used in NIB cathode materials which may impact the supply chain in near future has been discussed. Finally, in the quest of most promising cathode materials for the next generation of NIBs, an extensive perspective on the main findings in design and test of more than 295 reports in the past 10 years is overlaid, exhibiting that layered oxides, PBAs, and polyanions are leading candidates for cathode materials.

Based on this, an in-depth comparison of energy density and capacity retention of all the currently available cathode materials is provided.

1.2.2. Negative Anode Electrode

Despite advances in cathode materials for sodium-ion systems^{19–21}, development of a stable anode and electrolyte is still the key limiting factor in large-scale utilization of this battery technology.^{17,22,23} Unlike LIBs, graphite cannot be used as anode material for SIBs due to its incapability to intercalate Na⁺ into the structure.^{24,25} Only Na⁺ in the solvated state with diglyme (bis(2- methoxyethyl) ether) can be co-intercalated into graphite; however, the capacity of the reaction is too low that it can hardly find any practical applications.^{26,27}

Hard carbon was introduced as a carbon-based negative electrode alternative to graphite; however, hard carbon is not an impeccable anode for SIBs due to several drawbacks: (i) relatively low specific capacity ($\sim 300 \text{ mAh}\cdot\text{g}^{-1}$), (ii) high irreversible capacity loss due to Na trapping in the first sodiation, and (iii) poor understanding of the sodiation mechanism.^{28,29}

Besides hard carbon, non-carbonaceous anodes for NIBs were also developed in the last few years.³⁰ Depending on the reaction mechanism with Na⁺, they can be classified as conversion (metal oxides^{31,32}, sulfides^{33,34}, and selenides^{35,36}), alloying (tin (Sn)^{37–39}, bismuth (Bi)⁴⁰, phosphorus (P)^{41,42}, and antimony (Sb)^{43,44}), or insertion materials (titanium-based oxides^{45–47}, transition metal chalcogenides^{48,49}, and MXenes⁵⁰). Among them, Sn and Sb have shown the greatest promises^{51–55} due to their high theoretical capacities (with a theoretical gravimetric capacity of $847 \text{ mAh}\cdot\text{g}^{-1}$ for Sn and $660 \text{ mAh}\cdot\text{g}^{-1}$ for Sb)^{56,57}, good electrical conductivity ($8.7\times 10^6 \text{ S}\cdot\text{m}^{-1}$ for Sn and $2.55\times 10^6 \text{ S}\cdot\text{m}^{-1}$ for Sb at 20°C), low reaction potentials vs. Na⁺/Na (0.2–0.4V for Sn and 0.4–0.8V for Sb)⁵⁷, and less safety concerns associated with them.

However, both Sn and Sb suffer significant volume expansions during sodiation process ($\sim 420\%$ for Sn and $\sim 390\%$ for Sb)^{40,58}, which might lead to contact loss and substantial irreversible capacities upon long-term cycling. Furthermore, the high price and the low abundance in the

earth's crust of these two elements (0.00023% for Sn and 0.00002% for Sb)⁵⁹ have prevented their wide implementation in NIBs. A summary of main anode categories, timeline and materials development is presented in Figure 1.4.^{58,60}

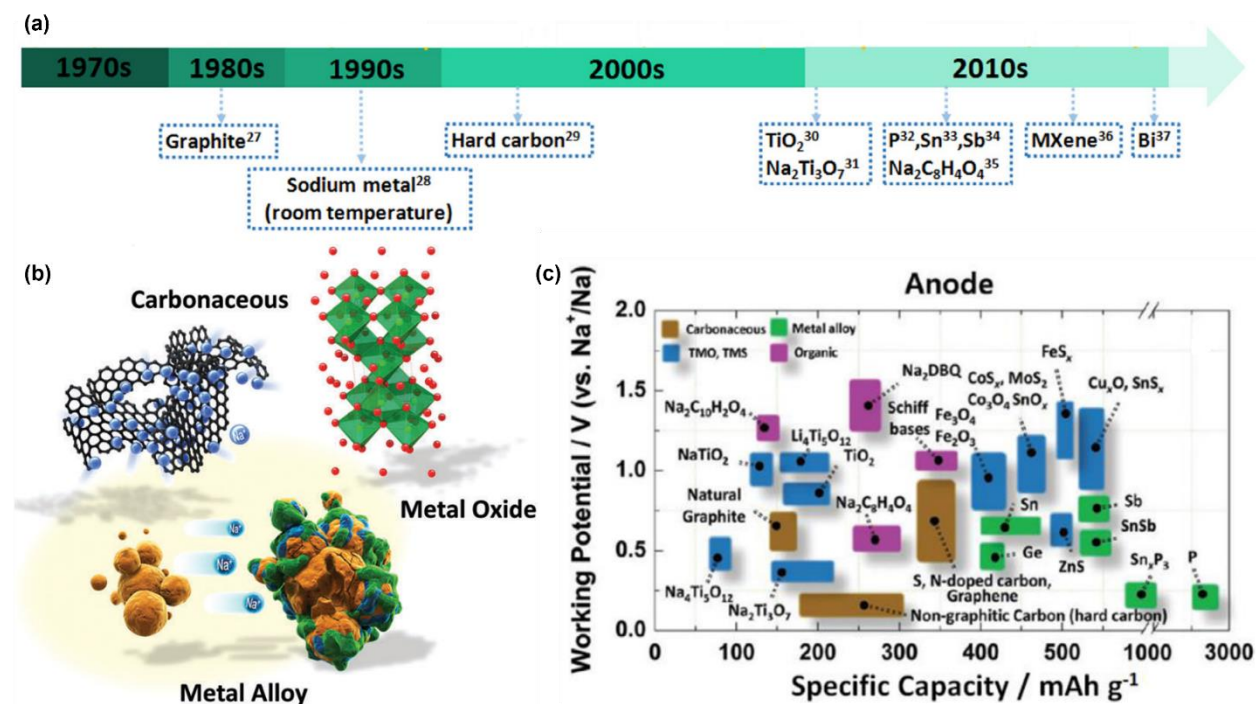


Figure 1-4. (a) A brief timeline of the development of anodes for NIBs. (b) A schematic of main anode categories. (c) Research progress on anodes in NIBs. The figures are adapted from the references.^{58,60}

Among a wide range of possible anode materials for NIBs, sodium metal is the ultimate one thanks to its high theoretical specific capacity (1166 mAh·g⁻¹) and low reduction potential (-2.73 V vs. SHE) (Table 1.2).¹⁶ Nonetheless, there exist several challenges hindering the large-scale utilization of sodium metal as a practical anode, mainly associated to its low melting point and high reactivity. Consequently, a considerable amount of electrolyte is consumed in the first cycle, leading to a significant SEI formation process as well as low initial columbic efficiency (ICE) and poor cyclability.⁶¹⁻⁶³

In chapter six, the effect of pressure on morphology, electrochemical performance, as well as the mechanism of capacity loss of Na metal anode in ether- and carbonate-based electrolytes is comprehensively investigated. For the first time, the sodium capacity usage and loss in the first cycle at different applied pressures was evaluated by titration gas chromatography. Interestingly, the obtained results indicate that SEI formation is main cause of capacity loss for Na metal anode; nonetheless, this phenomenon can be mitigated by applying a suitable pressure on the cell. Through XPS, cryogenic TEM, and EELS, a dense and uniform SEI layer with a dominant presence of organic species on the surface and inorganic species underneath is detected in ether-based electrolyte. On the other hand, the SEI layer in carbonate-based electrolytes is rather thick with a fluffy structure consisting of organic carbonyl and carboxyl species.

Finally, a long-term cycling of Na||NaCrO₂ cell possessing a controlled amount Na metal is demonstrated with ether-based electrolytes. The cells exhibit fast charging at 20C rate and excellent performance even at elevated temperatures (40°C). The findings in this study may pave the way in the development of high energy NIBs using Na metal anode and trigger further investigations in this field.

2. CHAPTER 2 – DISCHARGE MECHANISM STUDY OF LI-CF_x

2.1. Introduction

Fluorinated graphite (CF_x) is a class of cathode materials with the highest theoretical specific energy (>2100 Wh kg⁻¹ with theoretical specific capacity of 865 mAh g⁻¹ in case of x=1) for lithium primary (non-rechargeable) batteries.^{1,2} When using Li metal as the anode material, the primary battery exhibits a low self-discharge rate (<0.5% per year at 25°C) compared to current alternative chemistries.^{1-3,64} This system, with the proposed governing reaction of CF_x + Li → LiF + C, is one of the leading candidates for a variety of applications where high energy density is required and recharging of the battery is not feasible, e.g. implantable medical devices, military and space applications or other extreme environments.⁵ CF_x is a non-stoichiometric compound with 0.5 < x < 1.3, exhibiting a low electrical conductivity due to the nature of covalent C-F bonds.^{1,65} The F/C ratio (x) is shown to be dependent on the synthesis process and structural properties of precursor carbon material (such as coke, graphite, fiber).⁶⁵ Ideally, CF_x has a layered structure in which each carbon atom is bonded to three other carbon atoms and one fluorine atom, minimizing the total energy of the structure.^{66,67}

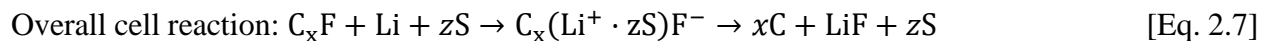
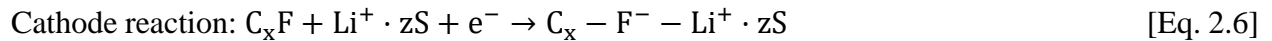
The study on possible cathode materials based on fluorides, chlorides, sulfides, etc., initiated in the 1960s, led to the introduction of CF_x as one of the most promising cathode materials in systems based on a lithium anode.^{68,69} The first CF_x reaction mechanism was proposed by Watanabe et al.⁶⁹⁻⁷¹ with the following steps:



In these studies, it has been suggested that poly-carbon monofluoride was converted into amorphous carbon while crystalline lithium fluoride (LiF) was formed in the cathode structure during the discharge process. Soon after these studies, in 1975, Whittingham⁷² suggested an alternative hypothesis for the overall reaction mechanism as shown below:



The presence of a non-stoichiometric graphite intercalation compound (GIC) intermediate was proposed to explain the discrepancy between the practical open-circuit voltage (~2.8 V) from its theoretical value (4.0 V). Through this reaction, an intermediate ternary non-stoichiometric phase as a compound of CLi_xF with $x < 1$ was initially suggested, which then disproportionated to form lithium fluoride and graphite. Later, Watanabe et al. investigated the thermodynamic characteristics of CF_x by experimental measurements of entropy and enthalpy, and further confirmed the different values with theoretical calculations.⁷³⁻⁷⁵ They also studied the Gibbs free energies of lithium-ion (Li^+) solvation in different solvents,⁷⁶ demonstrating that the open-circuit voltage and the voltage plateau increase with higher solvation energies of Li^+ . Based on these electrochemical results, it has been suggested that the solvent molecules affect the cell reaction and performance of the Li- CF_x cell. Later in the early 1980s, Watanabe et al.^{74,76} proposed the following reaction pathway with “S” representative of solvent:



The above mechanism is based on the insertion of the solvated Li^+ into CF_x layers to form $\text{C}_x(\text{Li}^+ \cdot z\text{S})\text{F}^-$ (GIC formation), and later, this compound decomposed to carbon, LiF , and solvent, with the solvated discharge product controlling the cathode potential.

This mechanism was generally accepted until 2009 when Read et al.⁷⁷ proposed a complementary idea to address the voltage delay in the initial discharge process named as a core-shell model. The authors suggested that the discharge reaction occurs between the CF_x and GIC intermediate phases through a shrinking core model with CF_x as core and a product shell consisting of GIC intermediate, carbon, and lithium fluoride. Most recently, Leung et al.⁶⁷ suggested that such solvent-coordinated Li^+ complex undergoes an edge-propagation mechanism rather than a bulk-phase reaction pathway. Using density functional theory (DFT) calculations, they demonstrated this discharge mechanism based on lithium insertion at the zigzag edge boundary of the CF_x structure and showed an operating voltage range of 2.5-2.9 V that varied based on electrolyte solvent. This theoretical voltage range was further confirmed by experimental investigations using both solid and liquid state electrolytes in Li-CF_x systems.^{78,79} Figure 2.1 shows the evolution of the proposed reaction mechanism for Li-CF_x batteries over the years.

Most published studies have mainly relied on the discharge voltage profile and OCV recovery of the Li-CF_x system as the performance criteria with minimal surface and bulk characterizations on the cathode structure or determination of the discharge mechanism due to the sample preparation and air sensitivity of discharge products. Therefore, despite the progress made on this class of cathode material, there is still a lack of understanding of discharge mechanisms and product types.

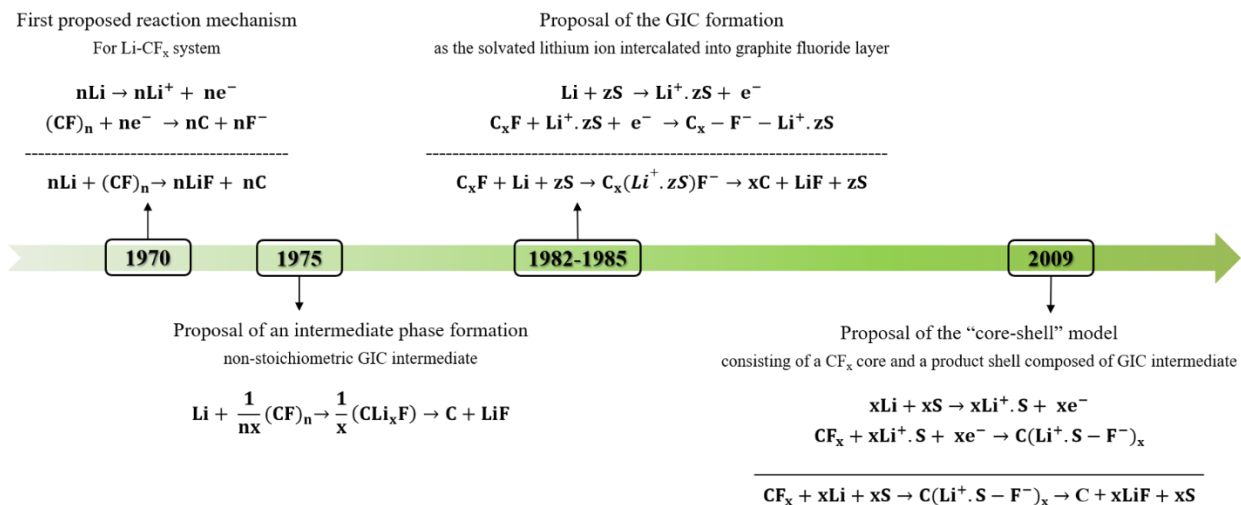


Figure 2-1. The evolution of the proposed reaction mechanism for Li-CF_x batteries through the years.

To fully understand the discharge mechanisms in Li-CF_x batteries, the following points need to be thoroughly investigated: (i) the possibility of metallic lithium deposition or intercalation during the discharge reaction, (ii) the type and crystalline structure of the carbon species formed during discharge reaction, and (iii) the size and distribution of formed LiF particles. To provide insights on these main points, we took the following steps to investigate reaction mechanisms in primary lithium systems based on CF_x cathodes in this study. First, a controlled sample preparation method was developed to minimize air exposure given the high reactivity of lithium, lithium compounds, and electrolytes with oxygen and moisture. Second, a cryogenic FIB and STEM setup was utilized to study the size and distribution of discharge products. Using cryogenic electron microscopy enabled us to carefully study the discharge products and avoid possible beam damage to the beam sensitive products as shown by previous studies.⁸⁰ Additionally, we designed a novel CF_x cathode electrode with the no extra conductive agent and a non-fluorine-containing binder to investigate the Li-CF_x reaction mechanism precisely. This novel cathode structure, in addition to our custom characterization setups, enabled us to perform a wide range of bulk [Titration gas

chromatography (TGC), X-ray diffraction (XRD), Raman spectroscopy, and cryogenic focused ion beam scanning electron microscopy (FIB-SEM) imaging] and surface-sensitive characterizations [X-ray photoelectron spectroscopy (XPS), cryogenic scanning transmission electron microscopy with electron energy loss spectroscopy (Cryo-(S)TEM-EELS)] at different depths of discharge to gain a fuller picture of the Li-CF_x discharge mechanism.

2.2. Material and Methods

Electrochemical Tests: All the electrochemical performances were tested using CR2032 coin cells. The cathode electrodes consisted of pristine CF_x powder (ACS Materials, F/C ratio-1.05) as the active material and carboxymethyl cellulose (CMC) (Sigma-Aldrich) as the F-free binder with the ratio of 98:2 wt.% coated on aluminum mesh (MTI). 50 μ L of 0.5 M Lithium bis(trifluoromethanesulfonyl)imide (LiTFSI) in propylene carbonate (PC): dimethoxyethane (DME) (1:4, v:v) electrolyte was used with pure Li chip (1 mm thickness) as the anode. This modified cathode structure is used for all characterization techniques unless otherwise noted. The current rate was 10 mA/g with cathode loading of $\sim 3.5 \pm 0.5$ mg cm⁻². 1.5 V was used as the cut-off voltage with an 8 hr rest at the beginning of the program. Detailed summary information of the coin-cell testing specifications is presented in Table S1, Section 1 in the Supplementary Information (SI) file.

X-ray Diffraction (XRD): The XRD measurements were done by a Bruker APEX II Ultra diffractometer with Mo K α ($\lambda = 0.71073$ Å) radiations to check the crystal structures. The diffraction images gathered by the 2D detector within an angular range of 4° to 40° were merged and integrated with DIFFRAC.EVA (Bruker, 2018) to produce 2d-plots. The samples were prepared by scratching the cathode electrode and filling the capillary tubes inside an Ar-filled

glovebox with < 0.1 ppm H_2O level. The cathode samples were not washed before these measurements.

Scanning Electron Microscopy (SEM): A FEI Apreo scanning electron microscope was used for cross-sectional imaging on the cathode electrodes. The standard mode with ETD detector using 0.1 nA and 2 kV was utilized in these imaging tests. The samples were not washed before these tests and were prepared inside an Ar-filled glovebox with < 0.1 ppm H_2O level.

Raman Spectroscopy: Raman spectroscopy was performed using Renishaw inVia Raman Microscope. The samples were sealed between two thin transparent glass slides inside an Ar-filled glovebox with < 0.1 ppm H_2O level. The measurements were run using a 532 nm laser source, 1800 l/mm grating, and x20 magnification.

X-ray Photoelectron Spectroscopy (XPS): XPS was performed using an AXIS Supra by Kratos Analytica. XPS electrode samples were disassembled and prepared inside an Ar-filled glovebox with < 0.1 ppm H_2O level. Unwashed samples were directly dried under vacuum before measurements. The washed samples were rinsed with PC solvent before this procedure. The XPS was operated using an Al anode source at 15 kV, scanning with a step size of 0.1 eV and 200 ms dwell time. Fits of the XPS spectra were performed with CasaXPS software to identify the chemical composition on the surface of the electrodes.

Dilatometry Measurement: An EL-CELL electrochemical dilatometer ECD-3-nano was used for measuring height changes during the discharge of a CF_x cathode. The instrument has a < 5 nm resolution with a total range of 250 μm , within the maximum cathode thickness and height changes. Measurements were made with a three-electrode configuration. The CF_x cathode [CF_x: Carbon C65: PVDF (80:10:10) wt.%] was punched into a 10 mm diameter disk and assembled into the dilatometer. A 12 mm diameter Lithium metal disk (750 μm thick) was used as an anode

and a separate piece of lithium was connected to serve as the reference. Approximately 500 μl of 0.5 M LiTFSI in PC: DME (1:4, v:v) was used to fill the dilatometer. Assembly and filling of the dilatometer were undertaken within an Ar filled mBraun glovebox with < 0.1 ppm O_2 and H_2O . After a 20 h rest the cathode was discharged at 10 mA/g until the 1.5 V cut-off was reached with height displacements measured every 30 s throughout this period.

Titration Gas Chromatography (TGC): TGC was performed using a Shimadzu GC instrument equipped with a BID detector and using an ultra-high purity Helium (99.999%) as the carrier gas. The samples were prepared in an Ar-filled glovebox with less than 0.1 ppm moisture level. Each sample was immediately transferred to a glass flask after disassembling and sealed using a septum under Ar. A 0.5 mL of ethanol was injected into the container to fully react with metallic lithium. After reaction completion, a 30 μL gas sample was taken from the container using a gastight Hamilton syringe and immediately injected into the GC. The amount of metallic lithium was quantified based on the amount of detected H_2 gas by the GC.

Cryogenic Focused Ion Beam (Cryo-FIB): The FIB-SEM was conducted on the FEI Scios Dual-beam microscopy; the discharged cells were disassembled in the Ar-filled glovebox after cycling. The samples were transferred to the FIB chamber via quick loader without any exposure to air. The electron beam operating voltage was 5 kV, and the stage was cooled with liquid nitrogen to -180 $^\circ\text{C}$ or below. Sample cross-sections were exposed using a 1 nA ion beam current and cleaned at 0.1 nA.

Scanning Transmission Electron Microscopy – Electron Energy Loss Spectroscopy (STEM-EELS): The lift-out sample from the FIB chamber was transferred to an Ar-filled glovebox using an air-free quick loader (FEI). The lamella was mounted to a vacuum cooling holder (Mel-build) to eliminate air exposure and transferred to the TEM column directly.

HRTEM/STEM/EELS results for discharged samples were obtained on ThermoFisher Talos X200 equipped with a Gatan Oneview camera operated at 200 kV and UltraFast DualEELS Spectrum Imaging detector. The image was acquired with minimum beam damage at spot size 6 with a dose rate of 200 electrons/Å²*s. The EELS spectrum and mapping were collected with an exposure time of 0.02 s, and the dispersion energy was 0.25 eV/channel.

2.3. Results and Discussion

One of the principal challenges in studying the discharge mechanism in Li-CF_x systems is the presence of carbon and fluorine as dominant elements in various cathode components, e.g., active material, conductive agent, and binder, given the similar and lightweight nature of these elements. To address this, we developed a novel cathode structure with 98 wt.% CF_x active material and 2 wt.% CMC binder coated on an aluminum mesh. The removal of the carbon conductive additive and fluorine from common binders, such as PVDF or PTFE, minimizes the interference in characterizing the existing fluorine and carbon elements in the CF_x structure and discharge products.

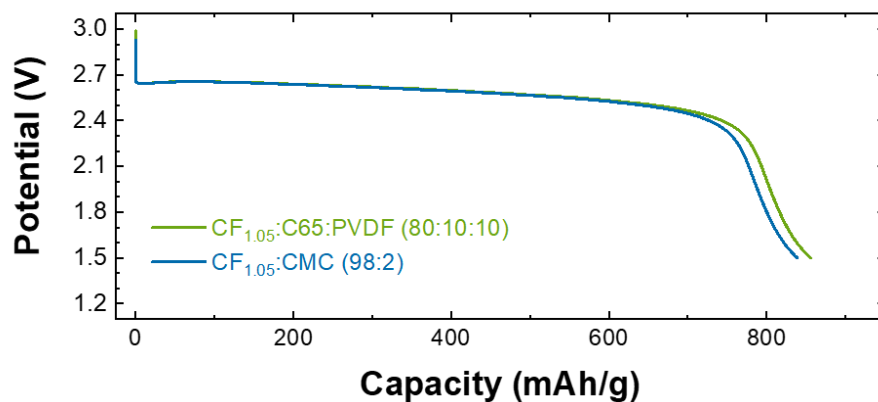


Figure 2-2. Representative electrochemical performance of the modified cathode structure. Li chip as the anode and 50 μ L PC : DME (1:4, v:v) with 0.5 M LiTFSI as the electrolyte was used under 10 mA/g applied current density. The cathode loadings are 2.93-3.12 mg/cm².

The aluminum mesh acts as a conductive network and current collector in the cathode electrode. The electrochemical performance of modified cathode structure compared to a more conventional cathode structure is presented in Figure 2.2. More details on this cathode and the coin-cell specifications used in sample preparations are provided in Table 2.1.

Table 2-1. Coin cell testing specifications used in sample preparation for the characterizations.

Coin Cell Specifications	
Cell type	CR2032
Cathode active material	CF _x (x=1.05) – 98 wt.%
Binder	CMC – 2 wt.%
Cathode Current Collector	Aluminum mesh (MTI)
Counter electrode	Li metal chip (thickness: 1mm, diameter: 15.4 mm)
Separator	Celgard 2325
Electrolyte	0.5 M LiTFSI in PC:DME (1:4, v:v)
Electrolyte amount	50 μ L
Coin cell setup	0.5 mm thick spacer and one spring at the anode side
Voltage cut-off	1.5 V
Active material loading	2.84-3.92 mg/cm ²
Applied current density	10 mA/g

2.3.1. Evaluating possible metallic/intercalated Lithium after discharge

Our group has recently demonstrated the TGC technique as an effective method to quantify metallic/intercalated lithium.⁸¹ Given that the reaction of Li^0 (metallic) or Li_xC_6 (intercalated) with ethanol solvent (eq. 2.8-2.9) leads to H_2 gas evolution, we can apply the TGC technique to evaluate possible metallic or intercalated lithium in a discharged CF_x cathode.

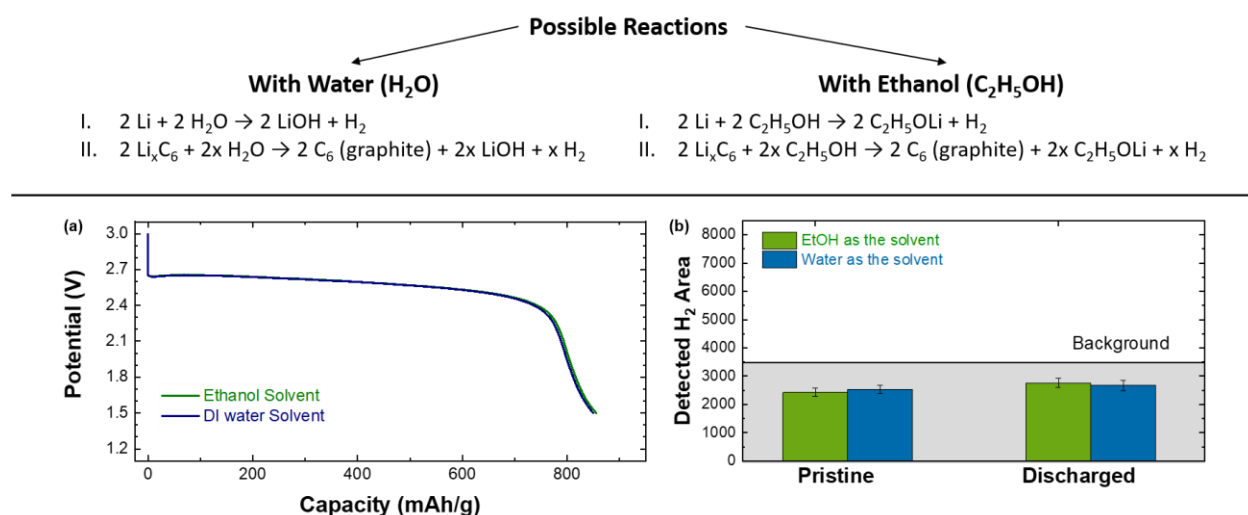


Figure 2-3. Titration Gas Chromatography (TGC) Study on Li-CF_x system. **(a)** The electrochemical performance of the Li-CF_x cells using PC: DME (1:4, v:v) with 0.5 M LiTFSI as the electrolyte under 10 mA/g applied current density.; **(b)** Detected H_2 gas for pristine and fully discharged cathodes using water and ethanol solvents.

TGC was performed on the pristine and fully discharged cathodes to reveal the possible presence of the trapped unreacted metallic lithium or intercalated lithium (LiC_6) in the cathode structure. It should be noted that a copper foil current collector was used to replace aluminum in the case of using water to avoid the possible H_2 formation by presence of the aluminum in the system. It is shown that the LiF in the system can react with water to produce H^+ and F^- ions which

further can react with the aluminum to generate hydrogen gas.⁸² We also used ethanol as the solvent to further check the lithium deposition or intercalation using an aluminum current collector. TGC results for both water and ethanol solvents are shown in Figure 2.3. The absence of detected H₂ above the background levels indicates no metallic or intercalated lithium in the system.

We further evaluated this observation using galvanostatic cycling of Li-CF_x at a lower discharge voltage range (down to 0.001V) and attempted recharge to understand the possible voltage plateaus for lithium (de)intercalation into graphitic layers.^{83,84} The cell was assembled using Li chip as the anode and 50 μ L 0.5 M LiTFSI in PC: DME (1:4, v:v) as the electrolyte. The current rate was 10 mA/g with cathode loading of 3.65 mg/cm². The electrochemical performance of the Li-CF_x cell is presented in Figure 2.4.

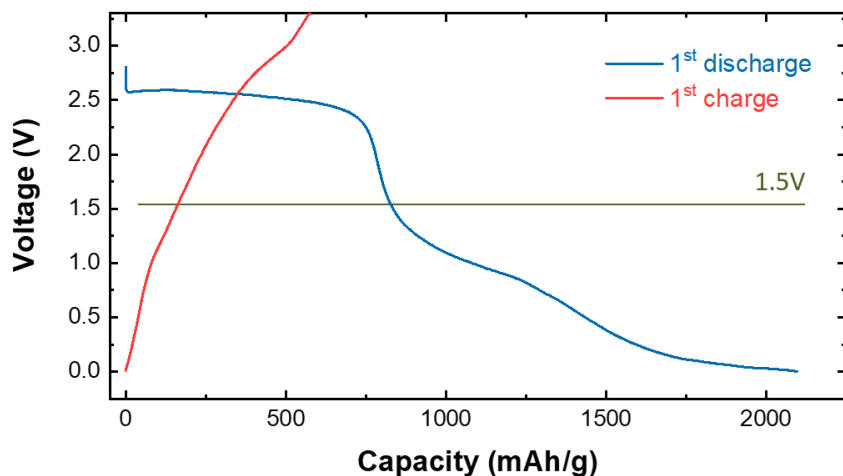


Figure 2-4. The electrochemical performance of the Li-CF_x battery discharged to 0.001 V. The first discharge and the following charge profiles are presented.

The voltage profile of the system during the charging process started at and continued with a steep curve, with no plateau observed at low voltages. This confirms the absence of any lithium

deposition or intercalation, and the resulting charging is likely purely capacitive in nature. Interestingly, the electrochemical performance of the Li-CF_x during discharge and consequently charge show that the CF_x structure acts similar to the hard carbon structure reported in the literature.⁸⁵ This suggests the transformation of CF_x structure to hard-carbon type structure at discharge state to 1.5 V.

2.3.2. Investigating the type and crystalline structure of carbon

To investigate the type and crystalline structure of the formed carbon species, we evaluated the formation of the products through various depths of discharge (DoD) using XRD and Raman spectroscopy. Figure 2.5 presents XRD results from pristine to discharged (to 1.5 V) samples.

Our results confirm crystalline LiF (Fm-3m) as the main product at the beginning of the discharge, in line with the previous reports.^{86,87} An important point that was not considered in previous reports⁸⁷⁻⁹⁰ is the overlap of the crystalline LiF (Fm-3m) peak with the dominant form of Al (Fm-3m). To address this here, the XRD measurement was directly performed on the cathode powder without aluminum mesh. CF_x peaks at 7° and 18° were observed in the pristine sample with no evident change up to 10% DoD. The presence of CF_x in the early stages of discharge when LiF begins to form can imply the possibility of starting the reaction from the edges and surface of the CF_x particles, preserving the overall bulk CF_x structure.

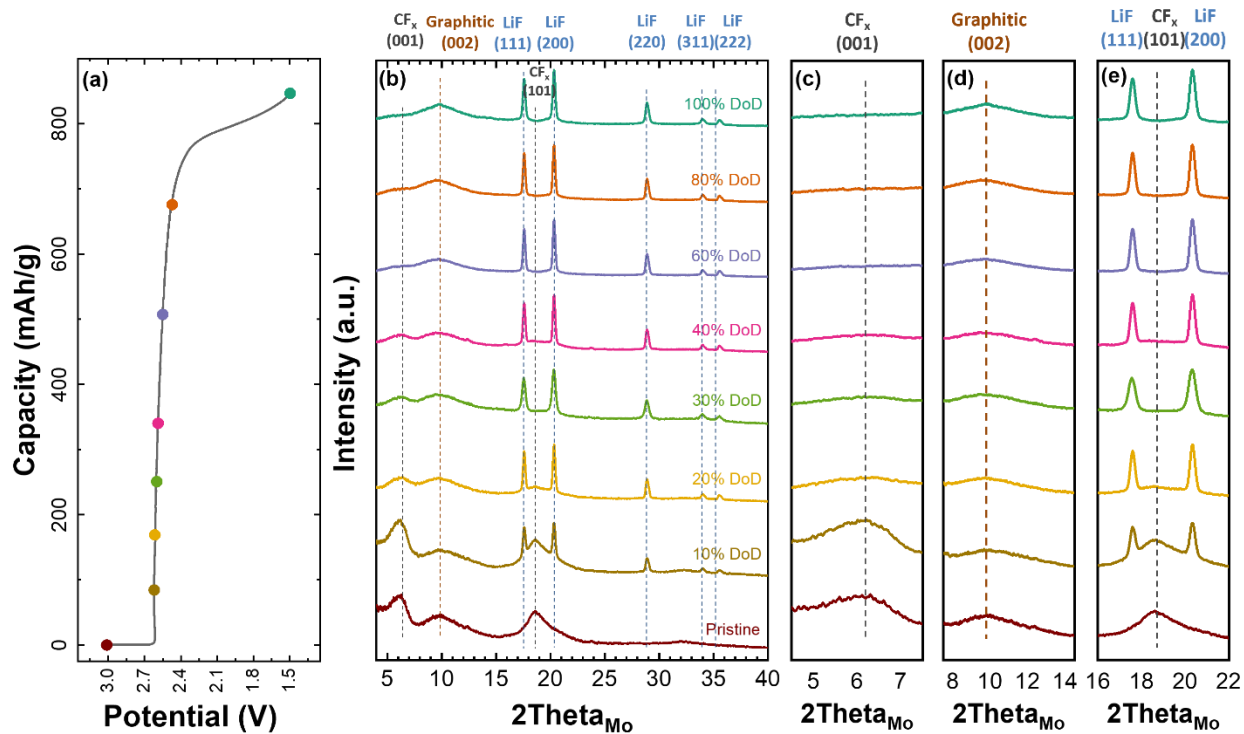


Figure 2-5. (a) The electrochemical performance of Li-CF_x system; (b) Ex-situ XRD results on CF_x cathode at different DoD; The zoomed-in range showing (c) the disappearance of CF_x phase after 40% DoD.; (d) the graphitic peak remains without change; (e) the presence of LiF as the only discharge product and the disappearance of CF_x phase after 40% DoD.

This observation is consistent with previous computational work by Leung et al. proposing the edge-propagation mechanism in Li-CF_x system.⁶⁷ CF_x peaks started to disappear after 40% DoD, while the presence of a graphitic peak at around 9° remained through discharged to 1.5 V state. This result confirmed the presence of both the graphitic and amorphous characteristics of CF_x materials and is in good agreement with previous computational work by Goddard et al.⁶⁶ It should also be noted that no intermediate phases were detected in our ex-situ XRD measurement, which is consistent with the previous reports.^{87,89}

Raman spectroscopy was also performed using the modified cathode structure at different depths of discharge to better understand the nature of carbon species in the system. The data for

Raman spectroscopy on the cathodes [CF_x: CMC (98:2 wt.%)] through depths of discharge is presented in Figure 2.6.

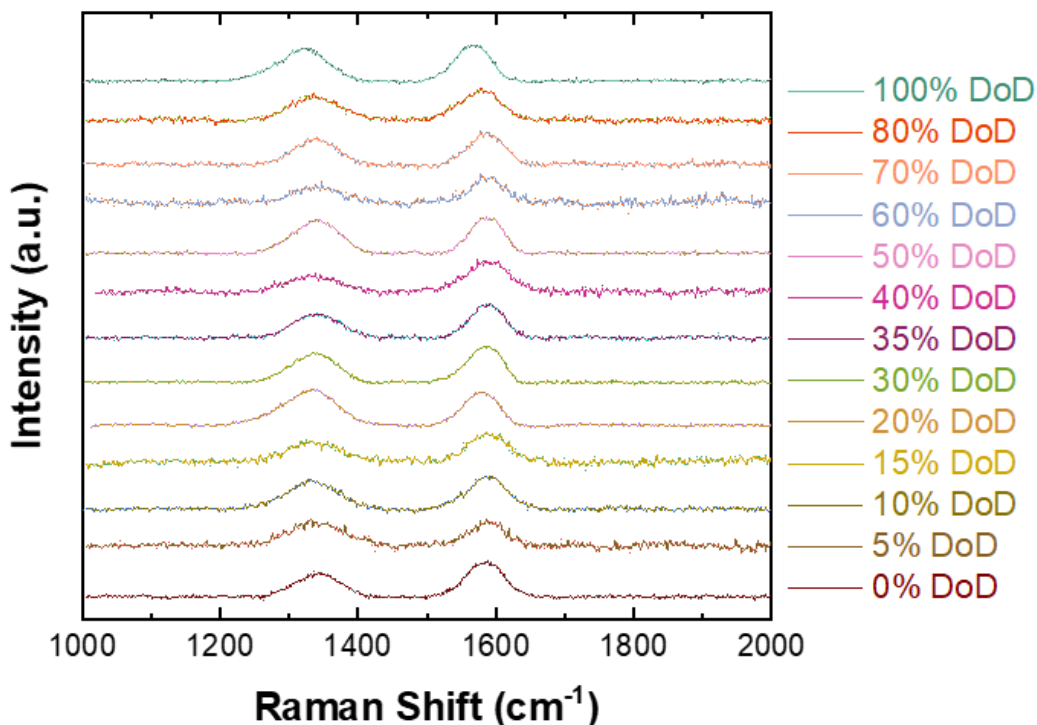


Figure 2-6. Raman spectra on the cathodes [CF_x: CMC (98:2 wt.%)] through depths of discharge.

The G-band ($\sim 1580\text{ cm}^{-1}$) is the characteristic peak of graphitic carbon representative of the stretching mode of C-C sp^2 species^{91,92}, while the D-band ($\sim 1350\text{ cm}^{-1}$) is linked to breathing modes of carbon rings and requires defects in the carbon structure to materialize.^{91,92} The ratio of the D-band to G-band peaks (I_D/I_G) has been previously used to quantify the extent of disordering as well as sp^2 content in CF_x structures.^{91,93} A smaller I_D/I_G ratio is attributed to a higher degree of sp^2 in the structure^{91,93} and also lower disordering and defects in graphitic layers.^{92,94}

In our measurements, the I_D/I_G began around 0.55 and increased to 1.1 through 20% DoD, and then decreased through 20-40% DoD back to about 0.6. Again, after 40% DoD, this ratio increased with a lower ratio to around 0.9. The overall increasing trend is not severe.⁹²

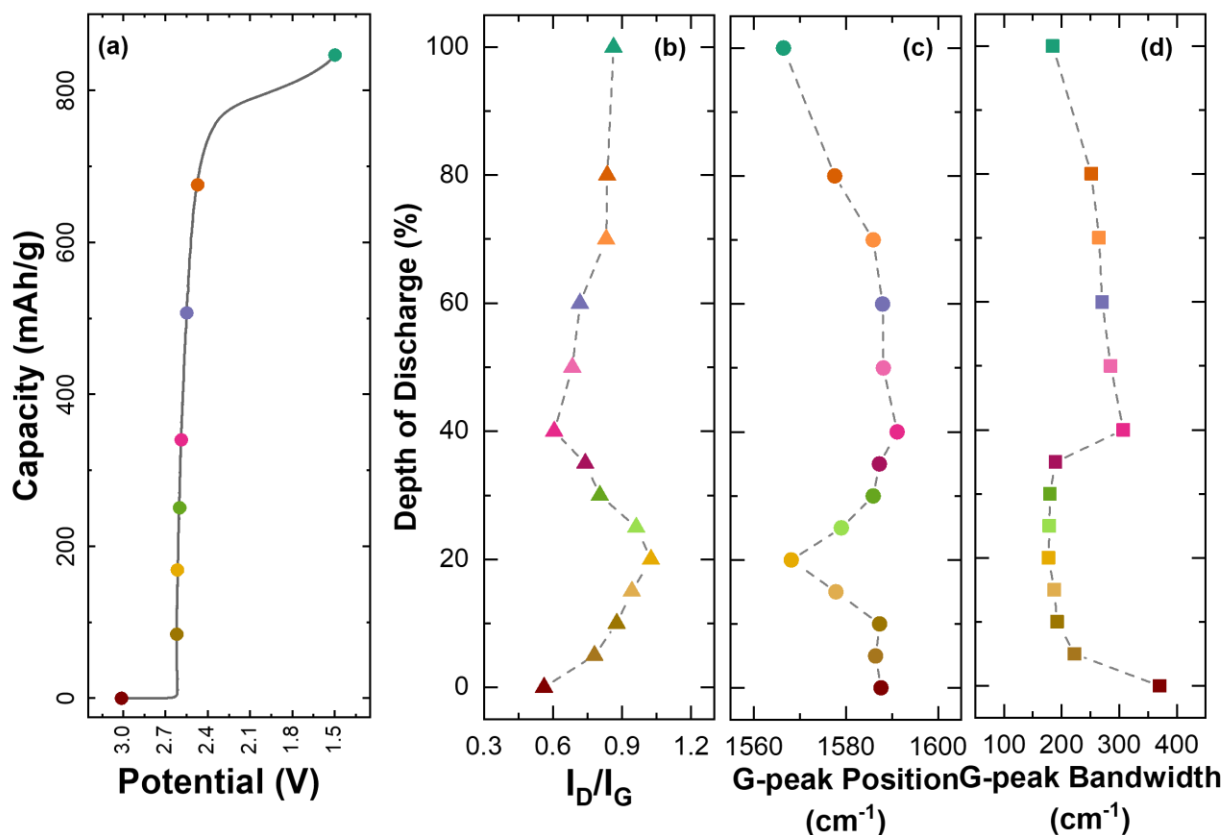


Figure 2-7. Raman spectroscopy on CF_x cathodes [CF_x:CMC (98:2 wt.%)]. (a) The electrochemical performance of the Li-CF_x system through different depths of discharge. (b) The ratio of D-band over G-band (I_D/I_G), (c) The G-peak position (cm⁻¹), and (d) The G-peak bandwidth (cm⁻¹) are shown through depths of discharge.

Furthermore, the absence of doublets on G peaks suggests no staging process of lithium intercalation into the carbon structure.⁹⁵⁻⁹⁷ This observation complements our results from TGC and the electrochemical performance measurements. Previously, Ferrari et al. observed a reversed correlation between I_D/I_G ratio and G-peak position based on experimental results.^{91,98} G-peak

position is susceptible to lattice parameter changes, possibly caused by chemical structure transformation during discharge.^{96,97}

We observed that the I_D/I_G initially increased through 20% DoD due to the lithium-ion insertion into the CF_x layers and the consequent expansion. Together, the G-peak position initially shifted to lower wavenumbers through 20% DoD due to the CF_x reacting with lithium to form the C-C bonds with lower energy. This phenomenon can also be further observed in the narrowing of G-peak in this region, as shown in Figure 2.7d. The G-peak position then blue-shifted up to 40% DoD. This shift can be attributed to the increase of the force constants of the in-plane C-C bonds by solvent insertion into CF_x structure and the continued formation of LiF, which can also be seen in the widening of G-peak in this region.⁹⁷ Later, this shift moved to lower wavenumbers through the discharge to 1.5 V, indicating continuation of Li-ion reaction with CF_x throughout the layers leading to the accumulation of LiF and lower energy C-C bonds.

A combination of XRD, Raman spectroscopy, and electrochemical performance provides a comprehensive understanding of the carbon species formed during discharge reactions. Overall, the increasing trend in I_D/I_G and the decreasing trend in the G-peak position show a lower sp^2 content of carbon in the discharged cathode than the pristine cathode.

2.3.3. Inspecting the size and distribution of LiF

To understand the surface chemistry of the CF_x cathode throughout the discharge reaction, we performed XPS on carbon (C), fluorine (F), lithium (Li), and oxygen (O) core levels. The survey spectra presented in Figure 2.8 show no other elements in the system, indicating no contamination or impurities in the samples. It should be noted that the sodium (Na) bonds observed

in the spectra are from the carboxymethyl cellulose (CMC) binder [cathode CF_x : CMC (98:2 wt.%)].

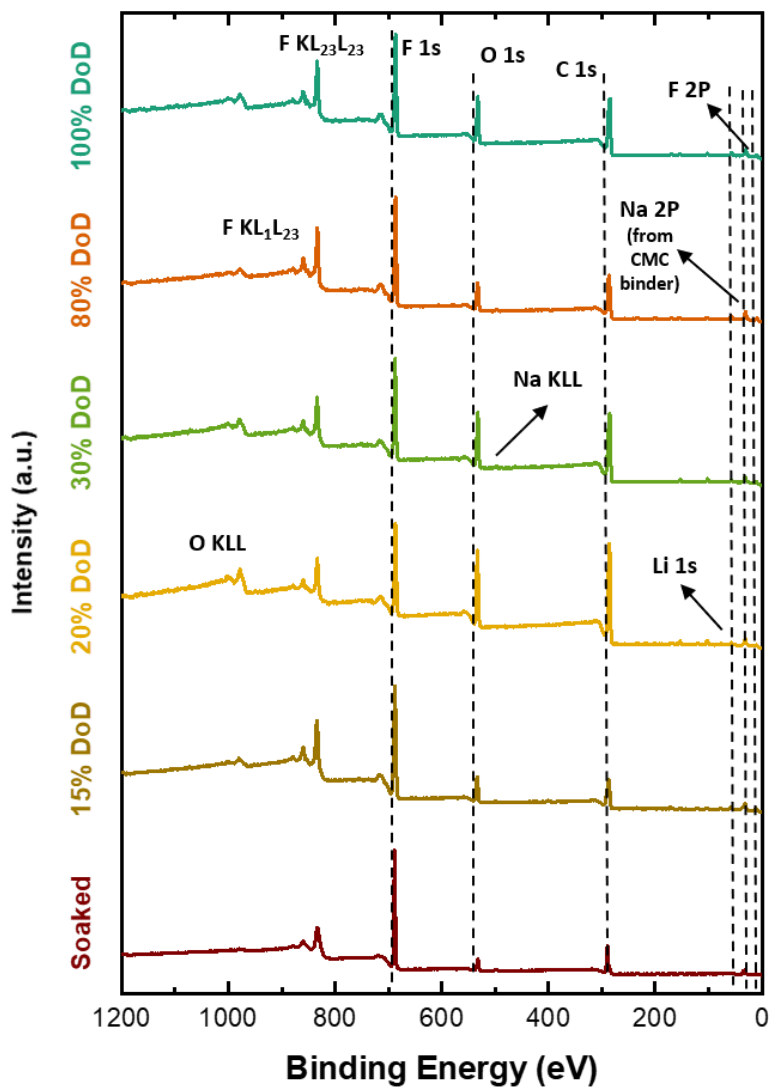


Figure 2-8. X-ray photoelectron spectroscopy (XPS) spectra on CF_x cathodes at different depths of discharge (data presented in Figure 2.9) in the binding energy range of 1200-5 eV.

The XPS results at different depths of discharge for the main four regions are shown in Figure 2.9. The pristine sample shows C-F bonding in both C and F regions with no signal in the Li region. We observed a decrease in C-F and an increase in C-C/C-H components as CF_x decomposed through depths of discharge. The ratio of C-F/C-C components decreased as the cell

progressed to deeper discharge stages. Consistent with XRD data, the intensity of C-F spectra from XPS significantly decreased after 30% DoD and C-C remained through discharge to the 1.5 V state that corresponds with the formation of carbon products. Meanwhile, we observed the formation of LiF and cathode electrolyte interphase (CEI) components. XPS results show that CEI consists of C-O, C=O, R-CO-Li, and R-COO species that mainly form in the range of 20% to 40% DoD.^{99,100}

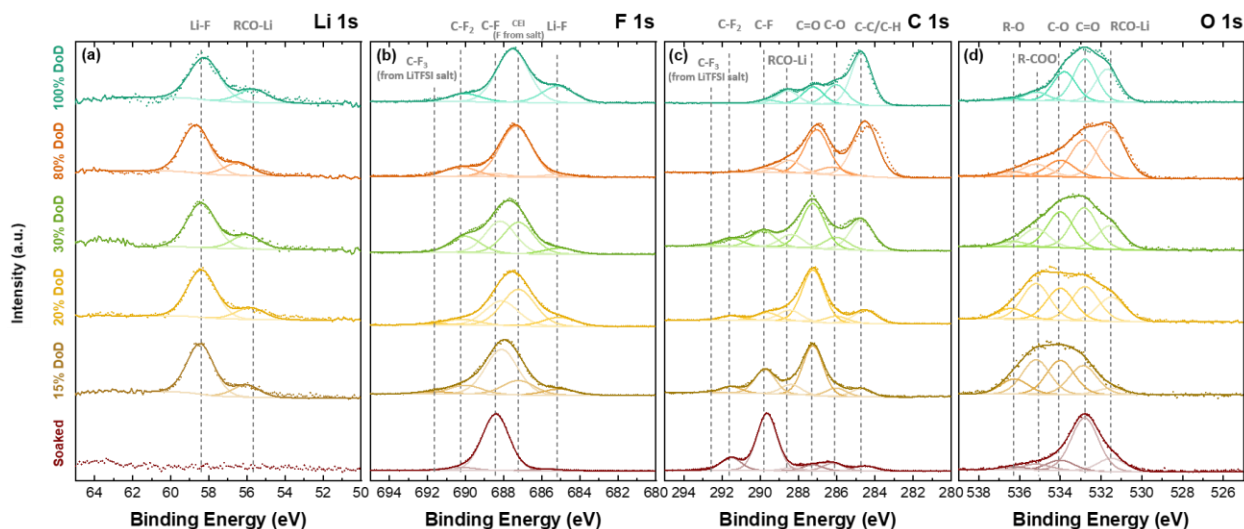


Figure 2-9. X-ray photoelectron spectroscopy (XPS) on CF_x cathodes [CF_x :CMC (98:2 wt.%)] at different depths of discharge (DoD). The data is shown in different regions of (a) Li 1s; (b) F 1s; (c) C 1s; and (d) O 1s.

LiF formation shows a low intensity and a minimal growth through depths of discharge, suggesting a limited formation of LiF on the surface and the possibility of LiF formation between the CF_x layers. We also performed a control experiment on the discharged to 1.5 V sample with two types of washed and unwashed samples. Unwashed samples were directly dried under vacuum before measurements. The washed samples were rinsed with PC solvent before vacuum drying.

The results presented in Figure 2.10 demonstrated a minimal change in the amount of LiF on the surface of the washed and unwashed electrodes, further confirming the hypothesis that the LiF particles are limited on the electrode surface.

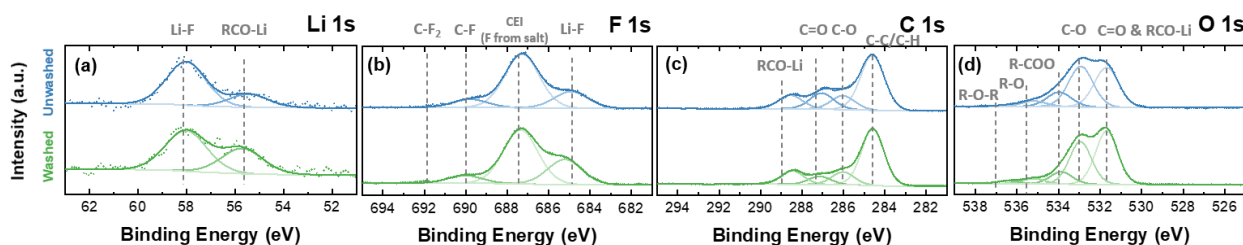


Figure 2-10. The XPS on the fully discharged CF_x cathodes for washed and unwashed cases are shown in different regions of (a) Li 1s; (b) F 1s; (c) C 1s; and (d) O 1s. The results demonstrate a minimal change in the amount of LiF on washed and un-washed electrodes as well as a limited amount of LiF on the surface.

Previous studies reported LiF products of spherical, cubic, or random morphology with the sizes of 100-600 nm on the surface of the CF_x particles demonstrated by SEM.^{87,89,101–103} A critical point to consider here is the possibility of air exposure and formation of other products such as lithium oxide (Li_2O) and lithium carbonate (Li_2CO_3) with similar spherical or cubic shapes.^{104,105}

While overlooked in most previous studies, it is vital to implement chemical mapping on the cathode surface to distinguish the products formed during discharge reactions from those formed by air contamination.

Here, we performed cross-sectional FIB and SEM to check the size and morphology of LiF particles formed during the discharge reaction. SEM and cross-sectional FIB-SEM images along with elemental mappings for the pristine and discharged CF_x cathodes without air exposure are presented in Figure 2.11 and 2.12, respectively.

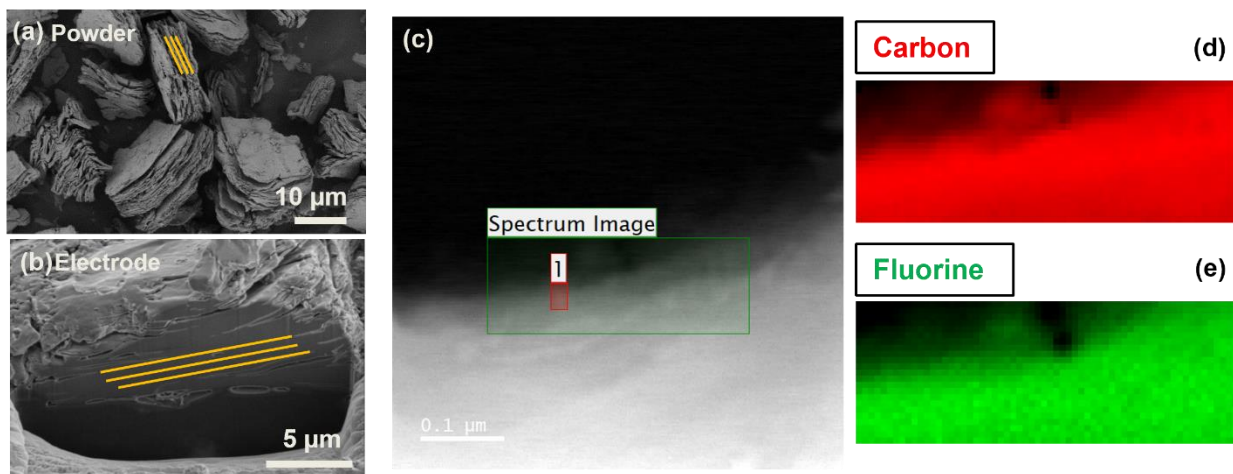


Figure 2-11. The SEM and EELS elemental mapping on the pristine cathode sample. (a) The SEM image of the pristine CF_x powder, and (b) The cross-sectional FIB-SEM image of the pristine CF_x powder. (c) The EELS elemental mapping in (d) Carbon (C) and (e) Fluorine (F) regions.

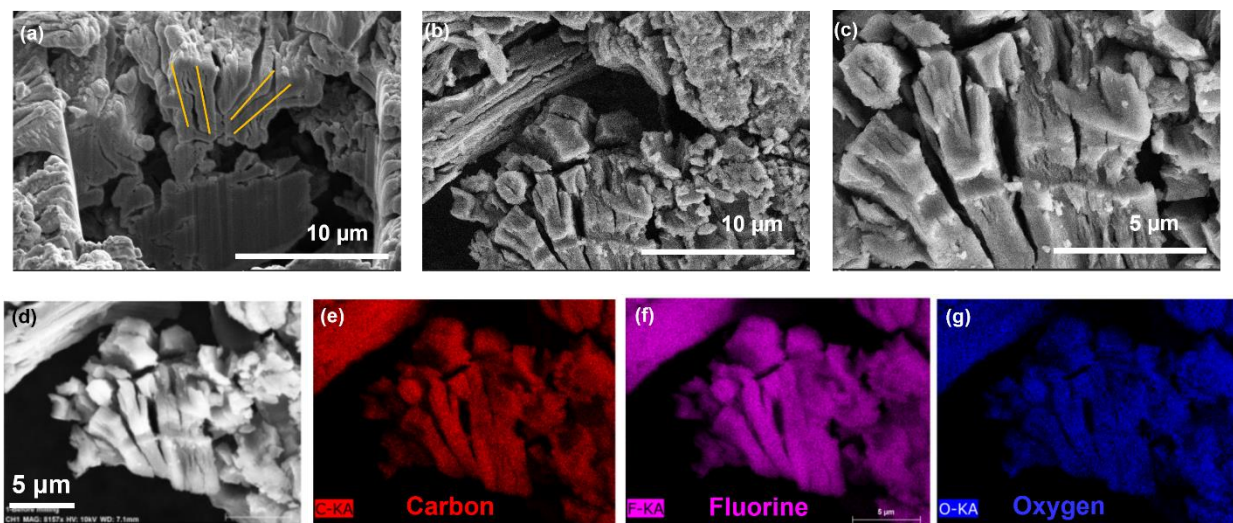


Figure 2-12. The cross-sectional focused ion beam SEM (FIB-SEM) and energy dispersive x-ray spectroscopy (EDS) mapping on the discharged cathode [$\text{CF}_{1.05}$:CMC (98:2 wt%)] sample. The cross-sectional FIB-SEM images in (a), (b), and (c). The cross-sectional SEM and EDS mapping in (e) Carbon (C), (f) Fluorine (F), and (g) Oxygen (O) regions.

The pristine CF_x powder shows a dense layered structure with nearly parallel layers. After discharge, no spherical or cubic LiF particles were observed in the cross-sectional images. However, the layered CF_x structure clearly changed to a more disordered structure. This change is

likely due to the $-F$ removal from the surface and possibly the accumulation of LiF between the layers. Earlier studies suggested a possible volume expansion after discharge in other primary batteries.^{80,101}

To better understand this, we further evaluated the thickness change of the cathode electrode through various depths of discharge using cross-sectional imaging and operando dilatometry. The cross-sectional SEM images showed a volume expansion of the cathode electrode after discharge. The cross-sectional SEM images of the cathode electrode for the pristine and discharged cathodes are shown in Figure 2.13. About two times volume expansion was observed due to the LiF and CEI formations.

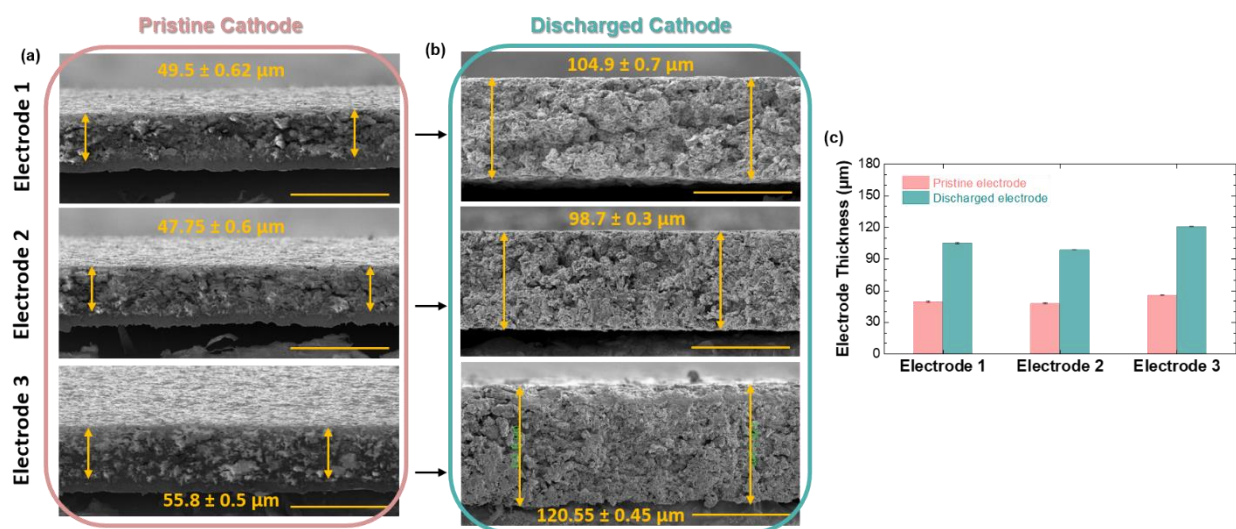


Figure 2-13. The cross-sectional scanning electron microscopy (SEM) images of the three cathode electrodes for (a) The pristine cathode; and (b) The fully discharged cathode [CF_x: C65: PVDF (80:10:10 wt.)]. The scale bars are 100 μm. (c) The average of electrode thickness for pristine and fully discharged cathodes in three different sample.

Operando electrochemical dilatometry technique was utilized to evaluate the vertical dimensional changes in the CF_x cathode electrode during the discharge without cell disassembly.

The result is presented in Figure 2.14. This operando measurement demonstrates a change of CF_x electrode thickness from 33 μm to about 67 μm after discharge, corresponding to a $\sim 203\%$ increase in height during discharge.

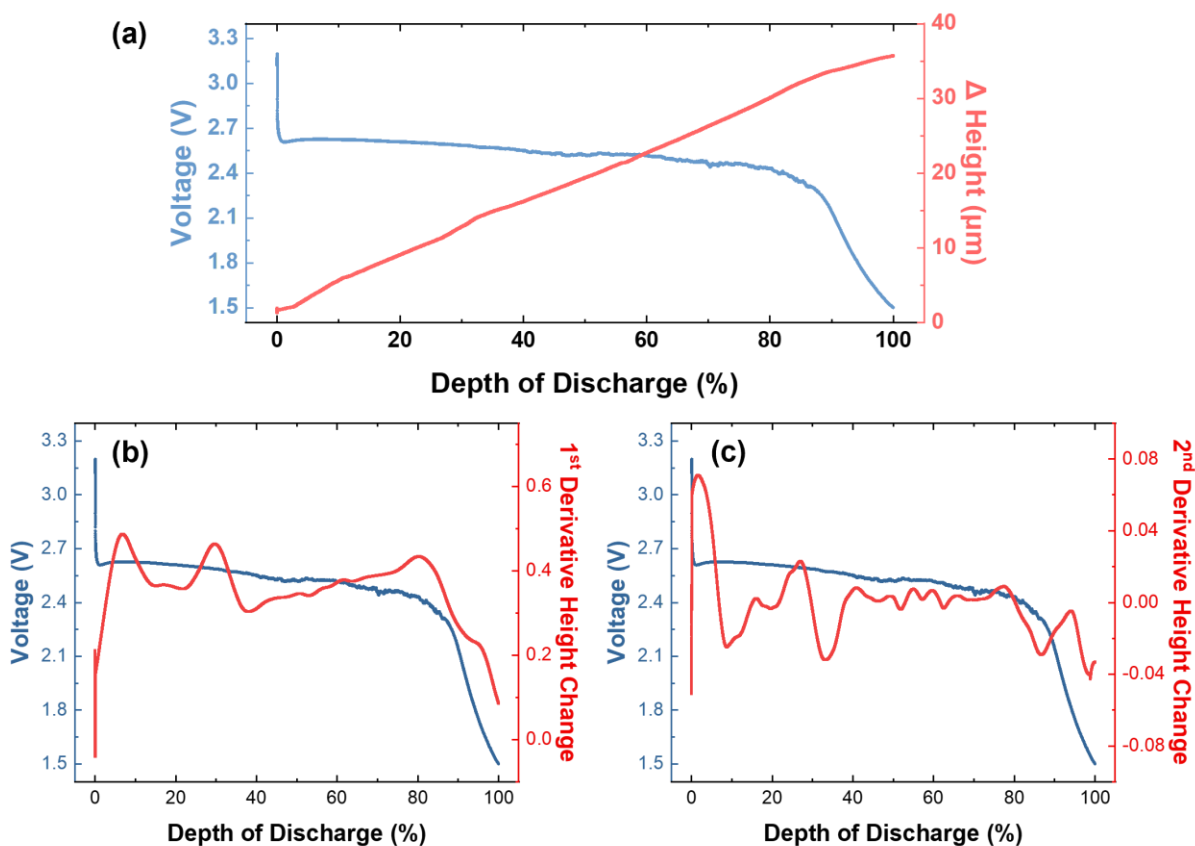


Figure 2-14. (a) The operando dilatometry measurement results of a cathode [CF_x : C65: PVDF (80:10:10) wt.%]. (b) The voltage profile and the first derivation of height change through depth of discharge. (c) The voltage profile and the second derivation of height change through depths of discharge.

Evaluating the 1st derivation of the thickness change shows two minima around 20% and 40% depths of discharge which indicate major changes of the reaction mechanism in these points.

While cross-sectional SEM and operando dilatometry provide useful insights on the cathode volume expansion due to products and CEI formation, it provides limited information on

the nature of the species responsible for this expansion. To thoroughly investigate this, we utilized the Cryo-(S)TEM-EELS on the discharged CF_x cathode. Cryogenic techniques minimize the possible impact on the morphology and chemical structure of the particles from the beam.¹⁰⁶ STEM-EELS was performed on pristine and discharged (1.5 V) electrodes. The EELS spectra of C K-edge, F K-edge, and Li K-edge are compared with reference samples in Figure 2.15a-c.

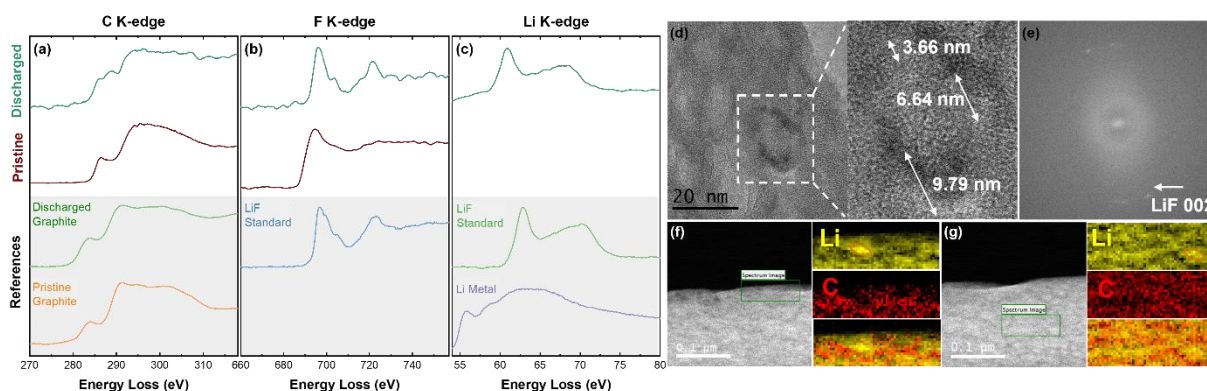


Figure 2-15. The EELS data on pristine and discharged cathode samples in (a) C K-edge region; (b) F K-edge region; and (c) Li K-edge region; (d) Cryo-HRTEM on the discharged sample (e) The FFT showing LiF. EELS elemental mapping on (f) the surface; and (g) the bulk of the sample in Li and C regions.

The C K-edge of the pristine electrode exhibits an amorphous carbon structure similar to the previously reported data in the literature.¹⁰⁷ Upon discharge to 1.5 V, the signal in C K-edge shows a combination of amorphous and graphitic structures. This observation for carbon is well aligned with our XRD data, where a broad graphitic peak (002) at 9° was observed through different depths of discharge. No lithium signal was detected in pristine cathode electrodes, while in the discharged samples, the newly formed LiF was identified in both F K-edge and Li K-edge regions in line with the characteristic peaks of the LiF reference sample. The EELS data also show

no metallic lithium on cathode electrodes, confirming our previous TGC, Raman spectroscopy, and electrochemical performance tests.

We performed EELS mapping to further elucidate the distribution and size of LiF particles on lamella samples prepared by the Cryo-FIB lift-out method previously developed in our group.¹⁰⁸ The EDS images are presented in Figure 2.16. The EDS data shows the full coverage of carbon and fluorine elements on the sample as well as no accumulation of fluorine in any specific location. It should be noted that there is no oxygen observed in high intensity on the sample. The lift-out sample from the FIB chamber was transferred to an Ar-filled glovebox using an air-free quick loader for cryo-STEM-EELS measurement.

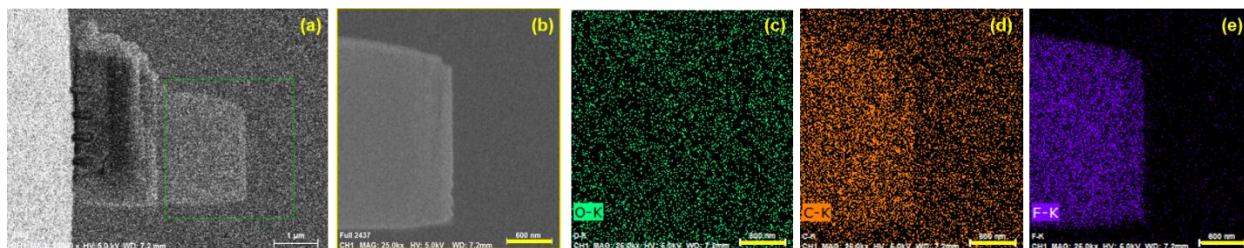


Figure 2-16. STEM sample preparation using FIB TEM lift-out method. (a) The cross-sectional thinning on the fully discharged sample. (b) The cross-sectional FIB-SEM image of the sample; The EDS data after thinning the sample are shown for (c) oxygen element; (d) carbon element; and (e) fluorine element. The scale bars are 600 nm.

The fast Fourier transform (FFT) further confirms crystalline LiF as the reaction product. The distribution of LiF particles was investigated using inverse FFT analysis, which shows a particle size of less than 10 nm. This observation was also verified by the EELS mapping conducted on the surface and bulk of the electrode. The EELS elemental mapping on the surface and the bulk of the sample in Li and C regions are presented in Figure 2.15, while F region is shown in Figure 2.17 in a well alignment with Li. In this study, we focused on the detection of the lithium as the representative of the LiF particles. The cryo-STEM EELS elemental mapping of fluorine (F) from

the same region of the surface and the bulk is shown in Figure S14. Note that the spatial resolution of fluorine is lower than that of lithium and carbon. It is because the fluorine K-edge is at a high energy loss region so that requires long time for the signal collection. It is shown in the literature that the discharge products are not stable under the electron beam.⁸⁰ To better protect the sample during the EELS mapping process, we increased the step size to reduce the electron per area, which will result to a ‘blurry’ image.

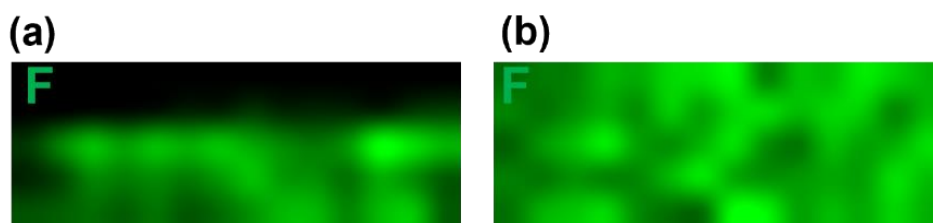


Figure 2-17. The electron energy loss spectroscopy (EELS) elemental mapping on the discharged cathode [CF_{1.05}:CMC (98:2 wt%)] sample on (a) the surface of the sample, (b) the bulk of the sample in F region.

The EELS mappings show the enhanced signal for Li in random locations as a representative of LiF particles with sizes smaller than 10 nm. It is important to note that this is the first direct observation of LiF particle size and distribution on a CF_x electrode ever reported in the literature. The LiF particles were observed on the layers of formed carbon. We found no evidence of aggregation of LiF particles on the surface or outside of the carbon layers. This observation implies a limited movement of fluorine ions during the discharge while the Li ions were traveling through the layers.

2.4. Three-region discharge mechanism in Li-CF_x systems

Based on the findings presented here, we propose a three-region discharge mechanism in Li-CF_x systems: (I) beginning the discharge process up to 20% depth of discharge, the lithium ions start to react with CF_x and form LiF. The formation of LiF and the presence of the CF_x structure were observed in XRD and XPS results in this initial stage. XPS results also showed that the CEI starts to form in this region. The lithium-ion insertion and defluorination of the CF_x particles due to the LiF formation can be the main reason for the increase in I_D/I_G ratio and decrease in G-peak position in Raman spectroscopy results. (II) In the range of 20-40% depth of discharge, lithium ions continue to react with CF_x resulting in the transformation of CF_x structure to more carbon formation. These points were clearly shown by considerable reduction of CF_x peaks in XRD as well as reduction of C-F bond and increasing of C-C bond in XPS results in this region. Solvent insertion into CF_x structure is also observed in this region, with a decrease in I_D/I_G ratio and an increase in G-peak position and FWHM bandwidth in the Raman spectroscopy results. XPS results also showed that the CEI mainly grows in this region. (III) Above 40% depth of discharge to the discharged to 1.5 V state, LiF particles continue to form, but no change in the graphitic carbon was observed. There is about two times volume expansion in the cathode electrode through the discharge process shown by cross-sectional SEM images and operando dilatometry measurement. No metallic or intercalated lithium was observed at discharge to 1.5 V. Figure 6 summarizes the three-step model mentioned above.

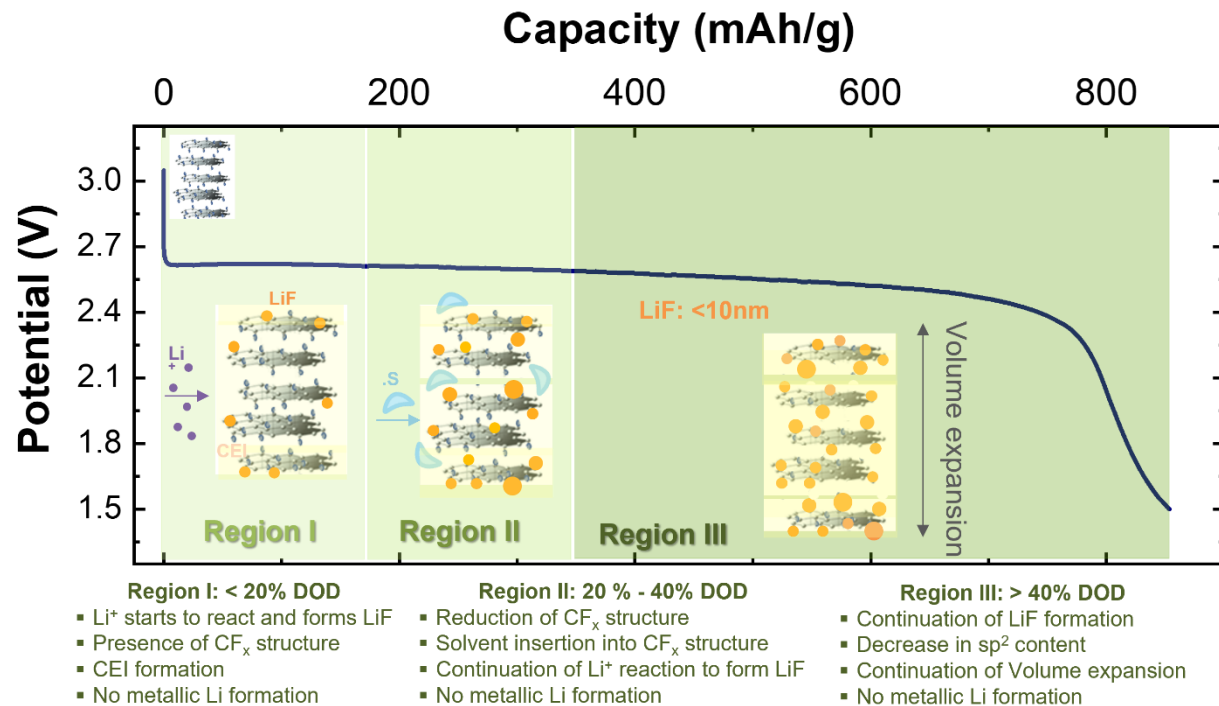


Figure 6. The schematic of the Li-CF_x system mechanism through the depth of discharge.

2.5. Conclusions

In this work, a CF_x cathode electrode with minimal carbon and fluorine additives was developed for a precise study of the Li-CF_x discharge mechanism. We demonstrated that: (i) There is no lithium deposition or intercalation through the entire discharge. This was shown with TGC, Raman spectroscopy, STEM-EELS, and electrochemical performance tests. (ii) The CF_x structure transforms to a hard-carbon like structure with less sp² content by increasing depth of discharge, as shown by XRD, Raman spectroscopy, STEM-EELS, and the electrochemical performance tests. (iii) The crystalline LiF particles, detected by XRD and XPS, uniformly covered the layers of CF_x structure as shown by Cryo-(S)TEM-EELS, and the LiF has a size range of < 10 nm throughout the CF_x layers. A three-step discharge reaction mechanism is proposed in agreement with our electrochemical performances. This multiscale discharge mechanism study will play an important

role in future experimental and computational works toward designing a higher power density cathode and help pave the path for developing a rechargeable Li-CF_x battery.

2.6. Acknowledgements

Chapter 2, in full, is a reprint of the material as it appears in *Advanced Energy Materials Journal* and in partial in *The Electrochemical Society Meeting Abstract*. Baharak Sayahpour, Hayley Hirsh, Shuang Bai, Noah Schorr, Timothy Lambert, Matthew Mayer, Wurigumula Bao, Diyi Cheng, Minghao Zhang, Kevin Leung, Katharine Harrison, Weikang Li, Ying Shirley Meng “Revisiting Discharge Mechanism of CF_x as a High Energy Density Cathode Material for Lithium Primary Battery” 12.5 (2022) 2103196. Baharak Sayahpour, Shuang Bai, Diyi Cheng, Minghao Zhang, Weikang Li, Ying Shirley Meng “Elucidation of Discharge Mechanism in CF_x as a High Energy Density Cathode Material for Lithium Primary Battery” 241. No. 2. *The Electrochemical Society, Inc.*, 2022. The dissertation author was the primary investigator and author of this paper.

3. CHAPTER 3 – RECHARGEABLE LITHIUM BATTERY BASED ON CF_x CATHODE MATERIAL

3.1. Introduction

The advancement of high performance, safe, reliable, and long shelf-life battery systems are vital for applications in extreme conditions, such as military rescue devices, space research missions, and implantable medical devices. Among different types of primary batteries (e.g. Li/I₂, Li/MnO₂, Li/Ag₂CrO₄, and Li/CuS), lithium fluorinated carbon (Li/CF_x) batteries are very promising for harsh and limited accessible applications mainly due to their high theoretical capacity (865 mAh/g in case of x=1 in CF_x), high energy density (>2100 Wh/kg), reliability, and low self-discharge rate (<0.5% per year at 25°C).¹

The following reaction is known to be the governing reaction in lithium fluorinated carbon (Li/CF_x) primary battery: $CF_x + Li \rightarrow LiF + C$. The reactant, CF_x, exhibits a low electrical conductivity due to the nature of covalent C-F bonds while the product, LiF, presents as a stable chemical with a strong ionic bond.

The goal of this study is to investigate the possible rechargeability of a high energy density lithium battery based on the CF_x cathode material, because of the encouragement from the low-cost abundant elements carbon and fluorine with the high energy density of active material CF_x. The challenging rechargeability of this system depends on reversibility of LiF as the main discharge product with a very strong bond that theoretically requires the high voltage of 6.1V to be decomposed.

According to our previous study of the Li-CF_x discharge mechanism^{109,110} results (i) Crystalline lithium fluoride particles uniformly distributed with <10 nm sizes into the CF_x layers, and (ii) carbon with lower sp² content similar to the hard-carbon structure are the products during

discharge. (iii) There is also no metallic lithium deposition or intercalation during the discharge reaction.

These findings encourage us to consider the rechargeable Li-FeF₃ system with similar nano-size LiF as the main discharge product. The possible interaction of FeF₃ with CF_x is investigated to evaluate the possible rechargeability of the Li-CF_x primary battery with the high energy density.

3.2. Materials and Methods

Active materials: The commercial fluorinated carbon refer to CF_x (ACS Materials) was used through this study with x=1.05. The purity and F/C ratio of this powder were assessed using EDS, XPS and elemental analysis (CHN/S analysis). In these tests, the powder samples were dried under vacuum for 12-hr before each test. Nano-size iron fluoride (FeF₃) powder was received from Sandia National Laboratory.

Electrochemical Tests: All the electrochemical performances were tested using a CR2032 coin cell. The cathode electrodes consisted of the active material, carbon super C65 as the conductive agent, and polyvinylidene fluoride (PVDF) as the binder with the weight ratio of 75:15:10. In coin cells, 55μL of 0.5M LiTFSI in PC:DME (1:4) was used as the electrolyte with pure Li chip (1mm thickness) as the anode. The cathode loadings were in the range of 3.3-4.5 mg/cm². The cells were cycled in the voltage range of 1V to 4.2V with an 8-hr rest at the beginning of the program. The applied current density of 20 mA/g was used in electrochemical tests.

Scanning Electron Microscopy (SEM): A FEI Apreo microscope was used to characterize the particle size and morphology. The immersion mode with T1 detector using 0.1nA and 2kV was used to reduce the charge accumulation on the sample.

Raman Spectroscopy: Raman spectroscopy was performed using Renishaw inVia Raman Microscope. The measurements were run using a 532-nm laser source, 1800 l/mm grating, and x20 magnification.

X-ray Photoelectron Spectroscopy (XPS): XPS was performed using an AXIS Supra by Kratos Analytica. The XPS was operated using an Al anode source at 15 kV, scanning with a step size of 0.1 eV and 200 ms dwell time. Fits of the XPS spectra were performed with CasaXPS software to identify the chemical composition on the surface species.

X-ray Diffraction (XRD): The XRD measurements were done by a Bruker SMART Platinum diffractometer with Cu K α (1.54056Å) radiation to check the crystal structures. The diffraction images gathered by the 2D detector within an angular range of 4° to 80° were merged and integrated with DIFFRAC.EVA (Bruker, 2018) to produce 2d-plots. The samples were prepared by scratching the cathode electrode and filling the capillary tubes inside an Ar-filled glovebox with <0.1ppm H₂O level. The cathode samples were not washed before these measurements. The measurements were performed at Crystallography Facility at University of California, San Diego.

Brunauer-Emmett-Teller (BET): The BET tests were performed using Micromeritics ASAP2020 to measure the specific surface area. The samples were dried under vacuum at 90°C for 12-hr, and then degassed in the sample tubes for 4-hr at 95°C under high vacuum before sorption experiment. The results were processed using the software of ASAP 2020 V4.02.

3.3. Results and Discussions

3.3.1. Modification of Fluorinated Carbon Material using Liquid-Exfoliation Method

A scalable liquid-phase exfoliation method was developed to convert pristine CF_x powder to thin exfoliated CF_x powder. The liquid exfoliation technique is currently of growing interest for large scale synthesis of few-layer particles due to its flexibility, safety, and low-cost.¹¹¹ After the successful demonstration of this technique for graphene synthesis from graphite¹¹¹, various groups have attempted to produce a large quantity of different layered materials including transition metal dichalcogenides (TMDCs), MXenes, and other two dimensional materials, e.g. hBN and black phosphorous.^{112–114} Here, we utilized this technique to create few-layer CF_x with significantly higher surface area and fluorine active sites, smaller particle sizes, and better ionic diffusion.

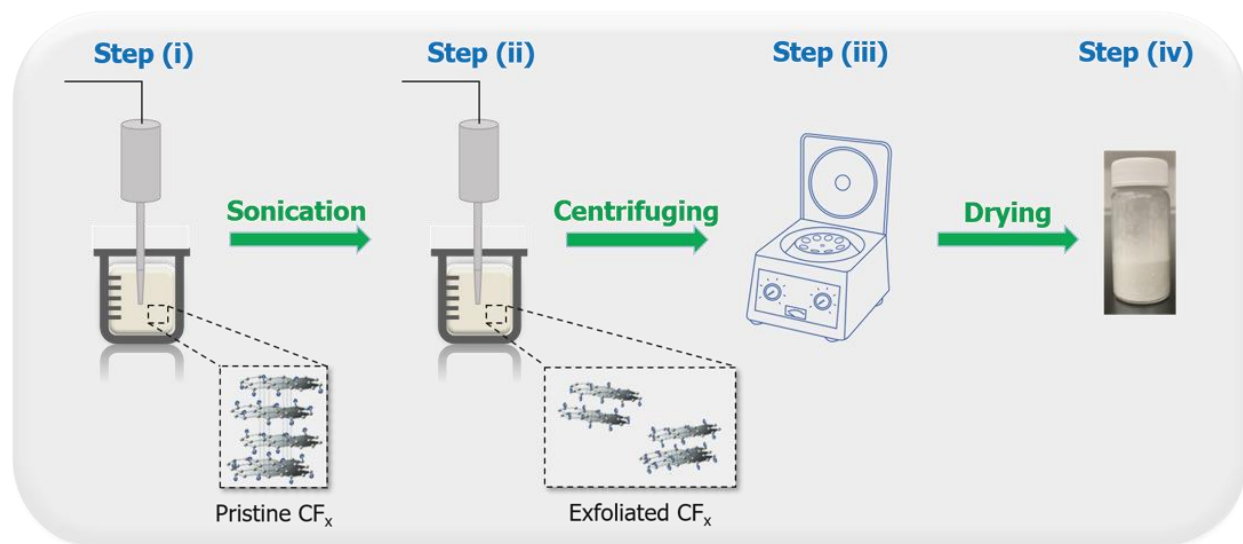


Figure 3-1. A schematic of the liquid exfoliation method in four main steps.

This liquid-phase exfoliation technique consists of (i) sonication of pristine CF_x powder in a solvent under ultra-sonic power to (ii) get dispersed exfoliated particles. This process results in

a uniform and stable dispersion of exfoliated particles in the solution. Then, the obtained solution is (iii) centrifuged to extract the supernatant containing exfoliated CF_x powders, and (iv) dry them out as the final product. A schematic of the procedure is shown in Figure 3.1.

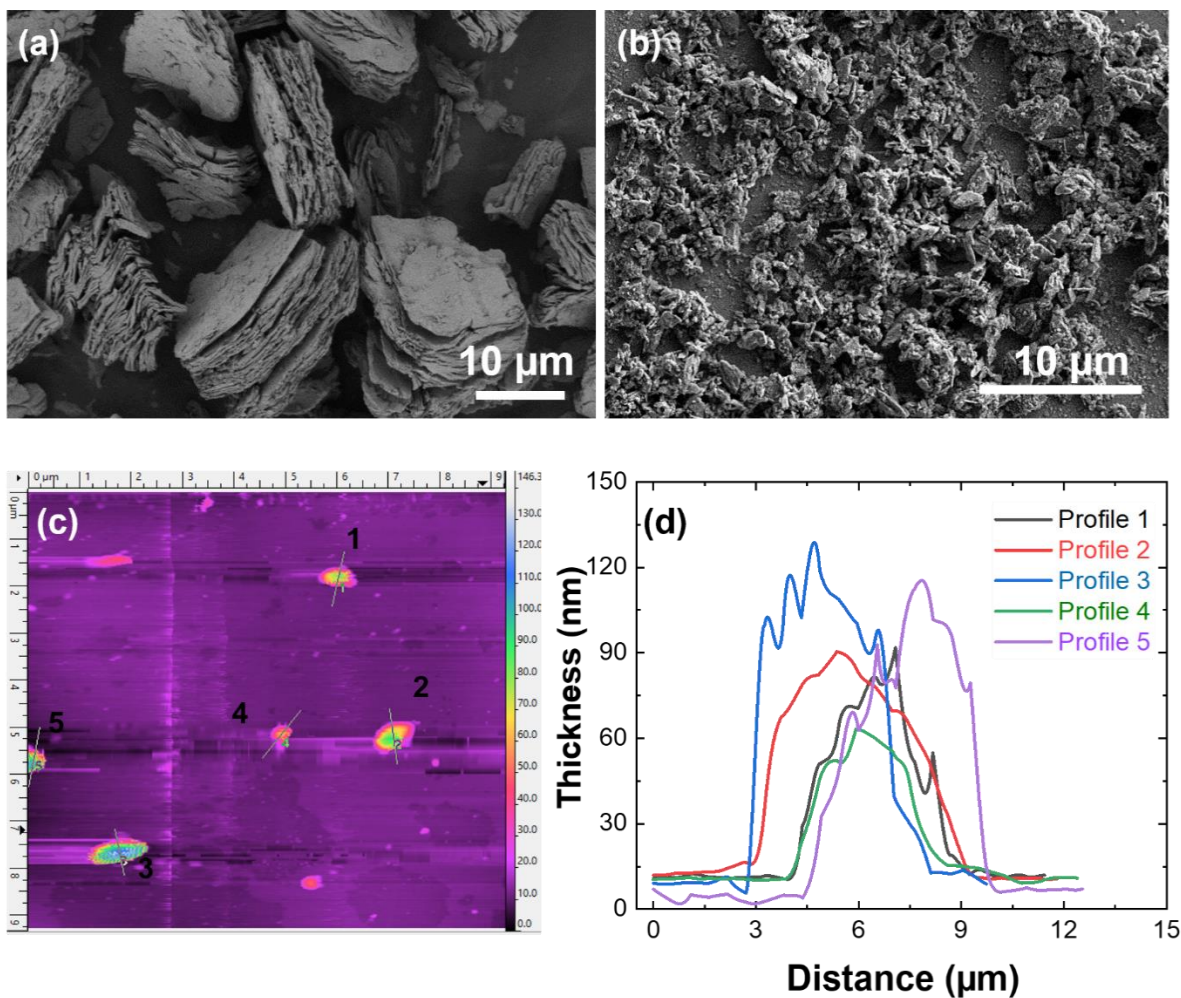


Figure 3-2. The morphology and size of exfoliated CF_x powder compared to pristine CF_x powder. SEM images of (a) pristine, and (b) exfoliated CF_x powders. (c-d) AFM measurement of the exfoliated CF_x powder.

The morphology and size distribution of particles were evaluated by scanning electron microscopy (SEM) for pristine and exfoliated CF_x powders (Figure 3.2(a-b)). The results show

that the particle thicknesses decreased significantly after exfoliation. Specifically, the pristine powder is the stack of the multilayers with $\sim 20\mu\text{m}$ length while the exfoliated powder shows less than $3\mu\text{m}$ length particles. The thickness of the produced exfoliated CF_x powder was also measured using atomic force microscopy (AFM), and the results are shown in Figure 3.2(c-d).

The particle sizes with the lengths of 1-2 μm and the thickness of 40-140 nm after exfoliation. The uniformity of the exfoliated CF_x particles were also confirmed by dynamic light scattering (DLS) method. Fluorine (F) to carbon (C) ratio were further measured using the elemental analysis in pristine and exfoliated CF_x powders and showed a consistent F/C ratio before and after the exfoliation. The surface area of powders was measured using Brunauer–Emmett–Teller (BET) technique. The surface area of the exfoliated CF_x powder shows $209.96\text{ m}^2/\text{g}$ compared to the surface area of $23.49\text{ m}^2/\text{g}$ for the pristine CF_x powder. These results show about 9 times higher surface area achieved after exfoliation. A summary of these results is shown in Table 3.1.

Table 3-1. The physical properties of the exfoliated CF_x powder compared with pristine CF_x powder.

	Pristine Powder	Exfoliated Powder
F/C ratio	1.05±0.01	1.04±0.01
BET (m^2/g)	23.49	209.96
Length	$\sim 20\ \mu\text{m}$	$< 3\ \mu\text{m}$
Thickness	$\sim 10\ \mu\text{m}$	40-140nm

Further surface and bulk characterizations on the pristine and exfoliated CF_x powders show a chemical stability of CF_x after liquid exfoliation. XPS and Raman spectroscopy were performed on both powders. The results are presented in Figure 3.3.

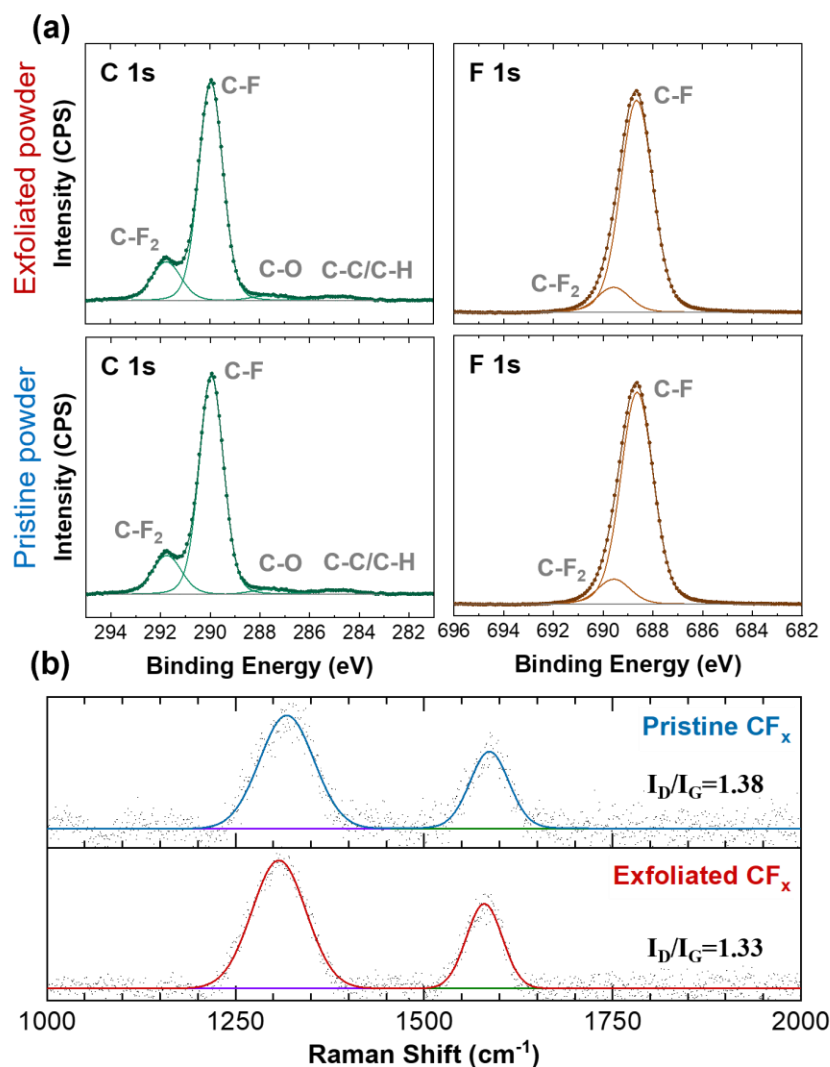


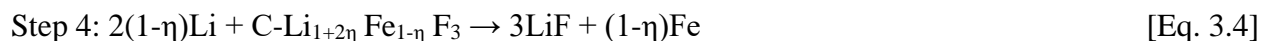
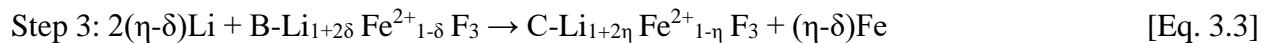
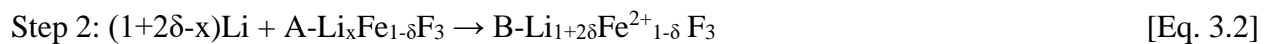
Figure 3-3. The surface and bulk characterizations of the pristine and exfoliated CF_x powders show chemical stability of the material after the liquid exfoliation. (a) XPS results of pristine and exfoliated CF_x powders in two main core levels of C 1s and F 1s. (b) Raman spectroscopy analysis of pristine and exfoliated CF_x powders.

The data show no C-F bond changes after liquid exfoliation that indicates the structural stability of CF_x powder. Besides, the C/F ratio was further confirmed by XPS semi-quantification, and values were consistent with the element analysis results for both samples. The above analyses results demonstrated that the exfoliation process mainly reduced the powder size of CF_x , while the chemical properties were well reserved.

3.3.2. Interaction between CF_x and FeF_3

As discussed before, LiF possesses the strongest ionic bonding that could barely break down, while it is the main product of CF_x discharge reactions. Meanwhile, iron fluoride (FeF_3), which is a promising rechargeable cathode material for lithium-ion batteries (LIBs), has LiF as the discharge product.^{115,116} The overall reaction mechanism for FeF_3 using Li anode is shown as follows: $FeF_3 + 3Li \rightleftharpoons 3LiF + Fe$, with discharge products of iron (Fe) and LiF. Noted that when utilizing the complete three-electron reaction, FeF_3 cathodes have poor rate performance and a short lifetime.¹¹⁶

The exact reaction mechanism for FeF_3 during electrochemical cycling was resolved recently that deepened the understanding on FeF_3 as a cathode material.¹¹⁵ It has been revealed that the simplified chemical equation, $FeF_3 + 3Li \rightleftharpoons 3LiF + Fe$, omits the complexity of the intermediate reactions and phases in four main steps describes below:



The intermediate phases and the size of the resulting Fe metal particles were first proposed by computation¹¹⁷ and further shown experimentally¹¹⁸.

It has been experimentally determined that FeF₃ reacts with Li ion to form multiple Li_xFe_yF₃ phases and FeF₂ during the first step of the discharge, while the original hcp F-sublattice is largely retained.¹¹⁹ The subsequent step of the discharge forms nanosized Fe metal and LiF, accompanied by the disappearance of hcp F-sublattice. The generated Fe metal nanoparticles (<5 nm in diameter) form a connective network throughout the discharge products¹²⁰ that plays an essential role in the reversibility of metal fluorides.¹²¹ During charge, the reverse reactions occur with the formation of Li_xFe_yF₃ phases and FeF₂ followed by the formation of FeF₃. However, residual Li_xFe_yF₃ and FeF₂ limit the reversibility.

The intrinsic low ionic and electronic conductivity of FeF₃ cathode must be considered, which are caused by the highly ionic Fe-F bonding in the material. Nanosized particles were employed¹²² to mitigate the poor ionic conductivity along with a conductive carbon coating to mitigate the poor electronic conductivity.

To recall, LiF is one of the discharge products in Li-CF_x, similar to Li-FeF₃.¹⁰⁹ This brings the idea to evaluate the possible interaction of CF_x with FeF₃ as a hybrid cathode. First, continuous carbon formation during discharge of CF_x can further help the connective network in the hybrid cathode structure, which may greatly help address the poor electronic conductivity of FeF₃; second, the intermediate Li-Fe-F phases may help restrict the LiF formation from CF_x, which can potentially improve the rechargeability.

To evaluate the possible interplay between CF_x and FeF₃, a hybrid cathode based on the physical mixing of these two powder materials was investigated. A 50 wt.% CF_x and 50 wt.% FeF₃ mixture as the active material used in the hybrid cathode was evaluated in half-cell using the 0.5M

LiTFSI in PC:DME (1:4) electrolyte. The voltage profile of this system is compared with the pure CF_x and pure FeF_3 and presented in Figure 3.4. Here, both pristine and exfoliated CF_x powders were evaluated since the exfoliated powder may offer abundant reaction sites. As a result, a higher capacity was achieved.

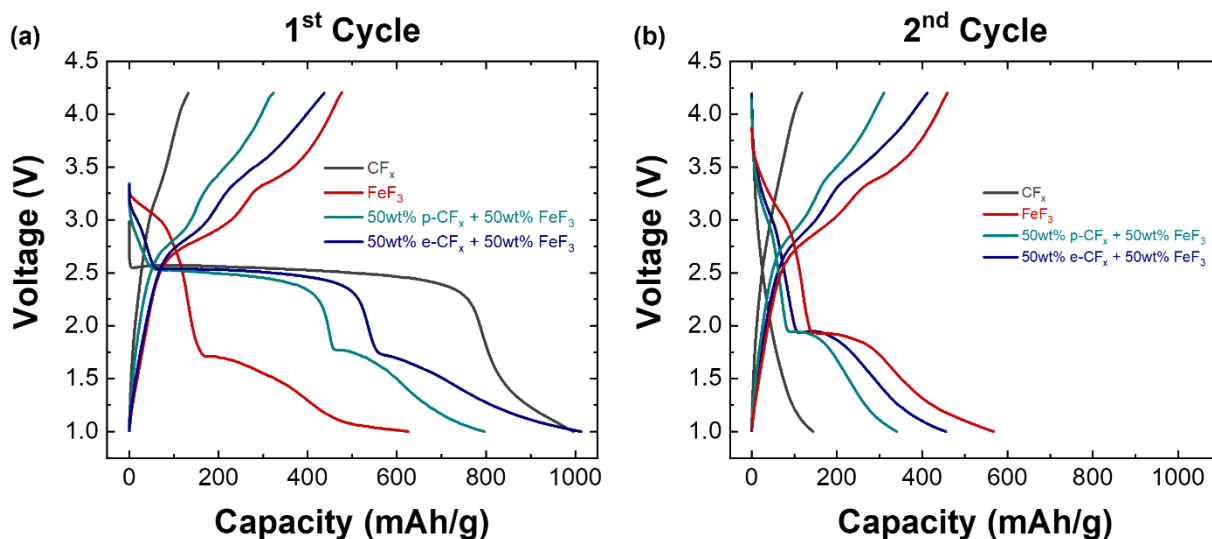


Figure 3-4. The electrochemical performance of the hybrid cathode structure based on 50 wt% CF_x and 50 wt% FeF_3 in comparison with the pure CF_x and pure FeF_3 in (a) the 1st and (b) the 2nd cycles.

Table 3-2. The summary of the discharge capacities and columbic efficiencies.

	1 st Cycle		2 nd Cycle	
	Discharge Capacity (mAh/g)	Columbic Efficiency (%)	Discharge Capacity (mAh/g)	Columbic Efficiency (%)
CF_x	996.03	13.26	143.73	81.84
FeF_3	625.48	76.18	567.49	80.00
50wt% pristine CF_x + 50wt% FeF_3	785.28	41.71	339.97	91.26
50wt% exfoliated CF_x + 50wt% FeF_3	1013.03	43.15	455.14	90.47

The summary of the discharge capacities and columbic efficiencies in the first and second cycles are shown in Table 3.2. The capacities in the second cycle are calculated based on the weight of combination of CF_x and FeF_3 as the active material. This voltage profiles show that there is an interaction between CF_x and FeF_3 .

An interesting observation achieved by looking into the electrochemical performance of the hybrid structure of CF_x and FeF_3 with different weight ratios. Different weight percentages of FeF_3 were mixed with CF_x to evaluate the discharge capacities. In particular, the investigation was focused on the second cycles to evaluate the possible contribution of re-fluorination of carbon after the first cycle. The second cycle discharge capacities were calculated based on total mass of active materials (CF_x and FeF_3). These results are shown in Figure 3.5. This observation requires further characterization to grasp a better idea. The trend of governed capacities further shows an interaction between these two active materials.

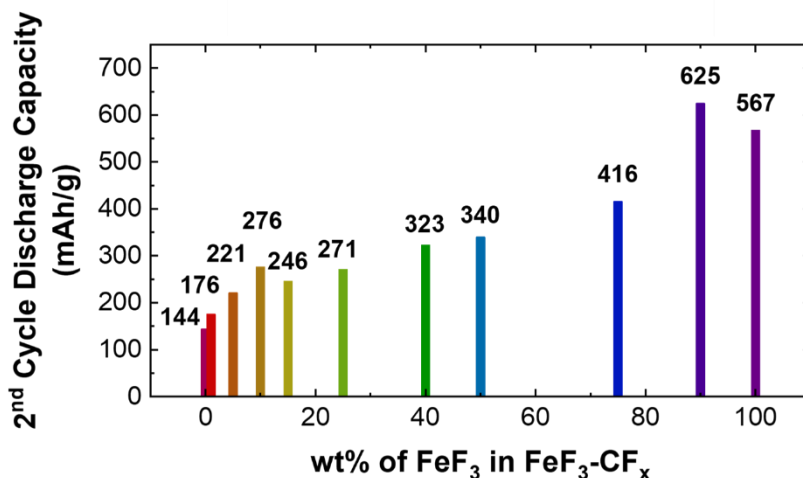


Figure 3-5. The second cycle discharge capacities of the hybrid structure of CF_x and FeF_3 based on different weight percentage of FeF_3 in cathode active material (CF_x+FeF_3).

The hybrid structure of CF_x and FeF_3 with 1:1 weight ratio was further characterized for its chemical composition and changes over the first discharge. Ex-situ XRD was performed at different depths of discharge and the presence of crystalline species was evaluated. The samples were not washed and not exposed to air. The results are shown in Figure 3.6. The XRD measurements show a limited formation of LiF after the 1st plateau of discharge at around 460 mAh/g. It was shown previously that the LiF is present and detected starting the lower depths of discharge in pure CF_x cathode.¹⁰⁹ However, LiF is not detected during and after the first plateau in the hybrid structure. This is a remarkable observation for limiting the formation of LiF in a system containing CF_x .

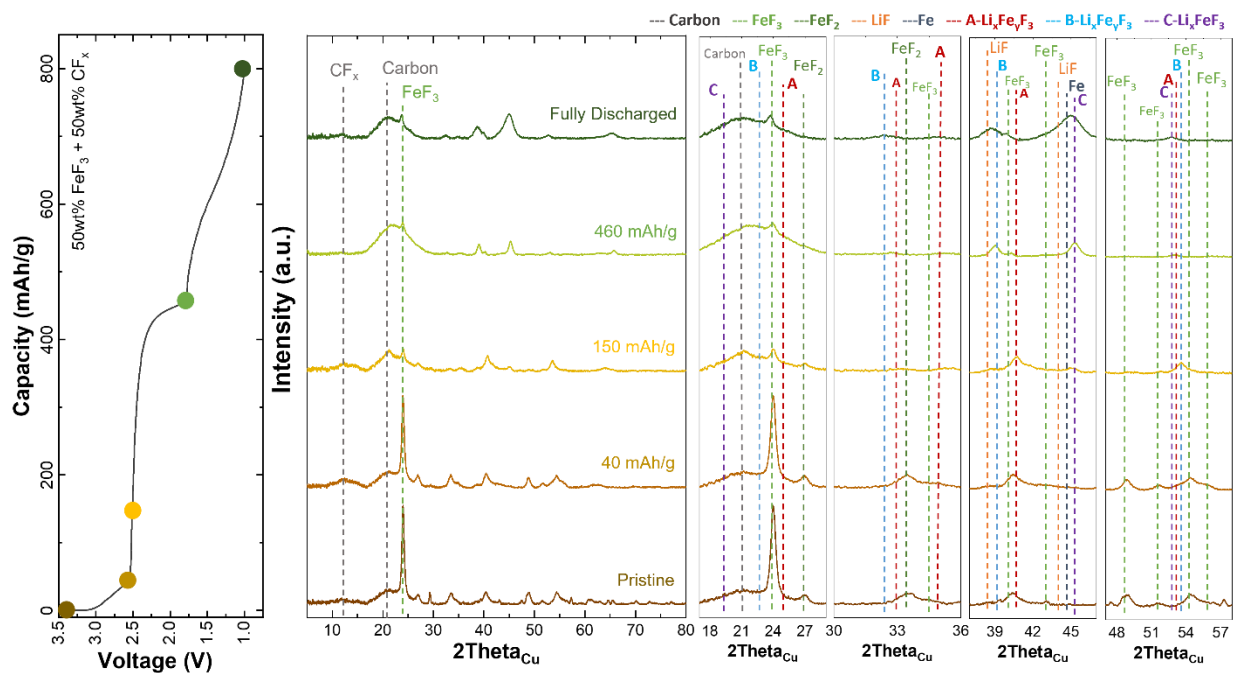


Figure 3-6. The ex-situ XRD results through the depths of discharge in hybrid structure of CF_x and FeF_3 with 1:1 weight ratio.

It is also observed that the CF_x and FeF_3 decreased, and carbon and intermediate species formed through the depths of discharge. The intermediate species are in a good agreement with the species reported recently by Hua et al.¹¹⁸ over the discharge of FeF_3 half-cell system. Detection of intermediate species is another notable observation in a system containing CF_x .

The interesting observation of the electrochemical performance of hybrid structure of CF_x and FeF_3 requires further investigation to evaluate the C-F bonding in this system.

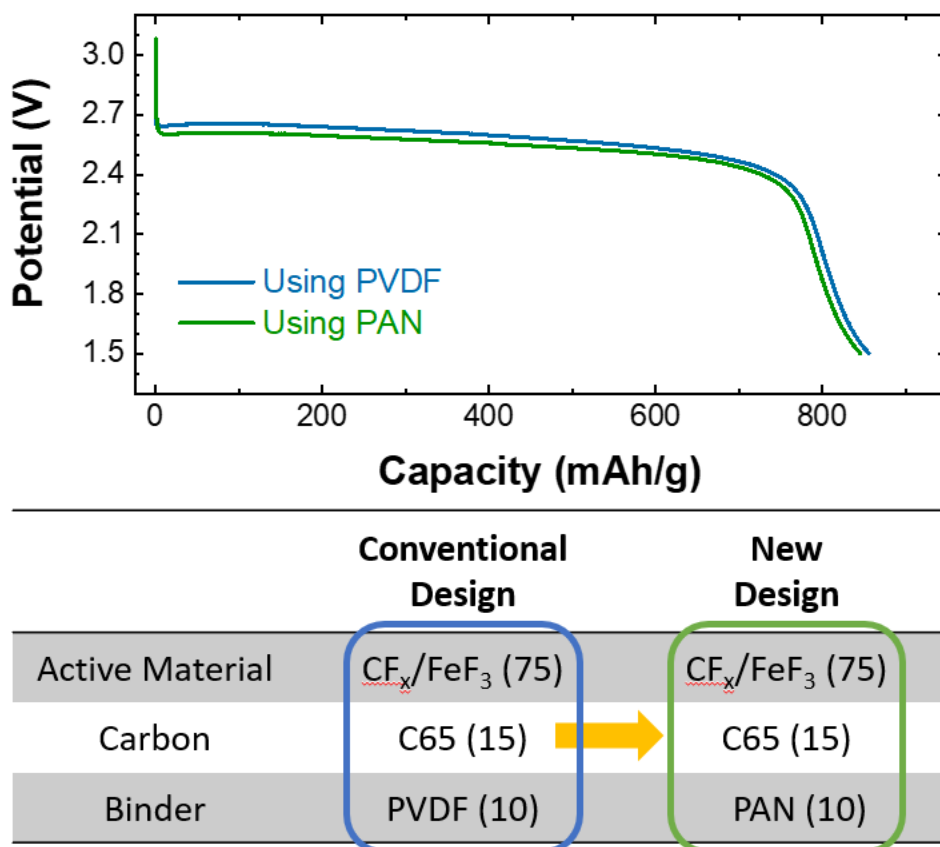


Figure 3-7. The modified cathode design to the conventional cathode structure by substituting PVDF binder with fluorine-free PAN binder.

First, to avoid the contribution of the fluorine from the PVDF binder, the conventional cathode structure was modified to substitute PVDF with fluorine-free polyacrylonitrile (PAN) binder in the similar cathode composition. The electrochemical performance of this novel cathode structure was evaluated and presented in Figure 3.7. A consistent electrochemical performance was observed using the modified cathode compared to the conventional one. This cathode electrode is used in the following XPS characterization test, to precisely evaluate the C-F bonding in hybrid structure.

XPS was performed on the hybrid cathode structures of CF_x and FeF_3 to evaluate the C-F bond. The cathode electrodes of the pure CF_x , pure FeF_3 , and hybrid structure of CF_x and FeF_3 ($\text{CF}_x:\text{FeF}_3$ 50:50 wt%) after the first charge to 4.2V with no air-exposure were compared with pure CF_x cathode at pristine state. The XPS results in C 1s and F 1s core levels are shown in Figure 3.8. No C-F bonds detected in carbon and fluorine regions.¹²³ However, large amount of carbon was detected, especially in samples containing CF_x active material.

Observing higher capacity and change of redox chemistry in hybrid structure while there is no reformed C-F bond indicates a better utilization of FeF_3 active material in the second cycle. This highlights the previous hypothesis on the notable effect of in-situ formation of conductive carbon from discharged CF_x .

A controlled experiment was performed using the carbon C65 in replacement of CF_x powder to evaluate the contribution of CF_x in comparison with carbon in better utilization of FeF_3 . First, higher capacity from FeF_3 governed in the 2nd discharge with CF_x compared to carbon C65.

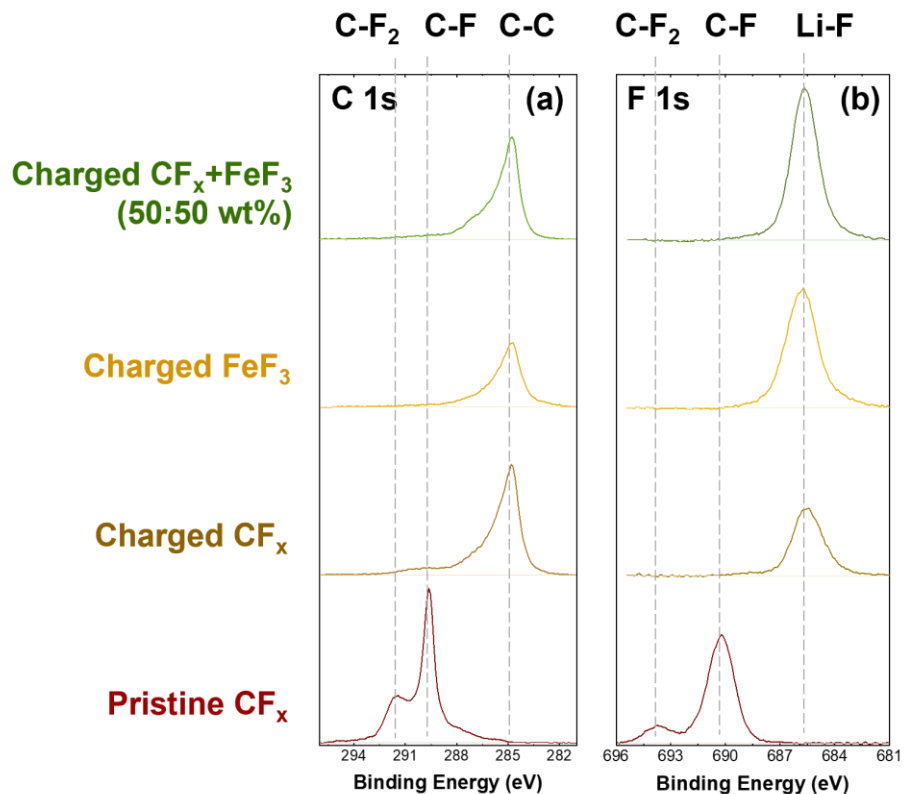


Figure 3-8. The XPS results of the charged cathodes compared with pristine FeF₃ cathode in C core level. The samples are charged FeF₃, 5 wt% FeF₃, and 50 wt% FeF₃ with CF_x.

Second, EIS measurement was performed on the coin-cell using these two cathode electrodes. The relative charge transfer resistances between “as assembled” compared to “after 1st charge” in these two samples is shown in Figure 3.9. The EIS data shows a decrease of resistance in case of CF_x while an increase of resistance in case of only added C65. This highlights the role of in-situ formation of carbon in the cathode from CF_x that boost the low electronic conductivity of FeF₃ ($1.3 \times 10^{-8} \text{ S/cm}^2$) and leads to better utilization of FeF₃ active material.

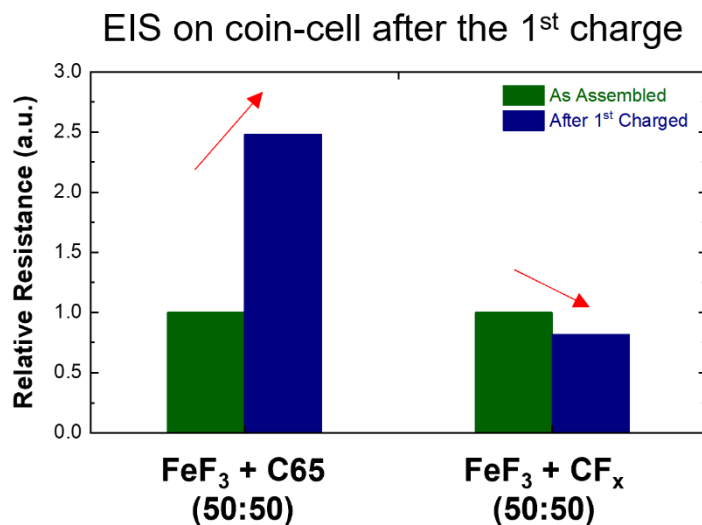


Figure 3-9. The relative resistance of coin-cells using CF_x with FeF₃ in comparison with C65 with FeF₃ using EIS measurement. The data is shown for “as assembled” and “after the 1st charge”.

Moreover, the comparison of the longer cycling performance of cathodes using the hybrid structure shows higher capacity in the consequent cycles than pure CF_x and pure FeF₃ cathodes. This phenomena was also confirmed in case of using exfoliated CF_x powder with smaller particle sizes than the pristine one. These data are shown in Figure 3.10.

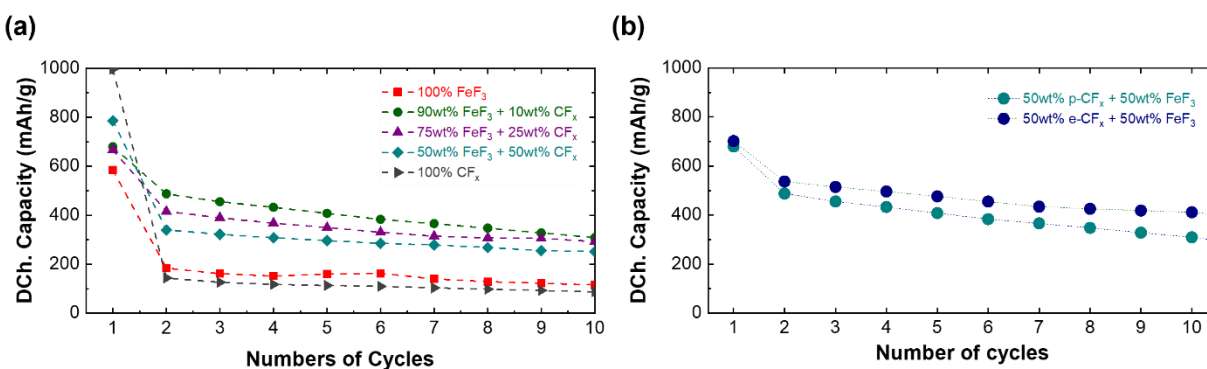


Figure 3-10. (a) The discharge capacities of hybrid structures over 10 cycles in comparison with pure CF_x and pure FeF₃. (b) The comparison of the discharge capacity of exfoliated CF_x with pristine CF_x in hybrid structure of CF_x:FeF₃ over 10 cycles.

3.4. Conclusion

The aim of this project was to probe the possible rechargeability of a high energy density lithium battery based on CF_x cathode material. The rechargeability of this system depends on reversibility of the discharge reaction. The interaction of FeF_3 with CF_x was selected to achieve the mentioned goals.

First, a liquid-exfoliation method was also developed to get smaller CF_x particles in order to achieve better volume contact with nano-sized FeF_3 particles. Second, it is shown that the interaction between CF_x and FeF_3 resulting in higher discharge capacity in the first and subsequent cycles. We confirmed that the addition of FeF_3 in CF_x can control the formation of LiF and instead lead the reaction to form reversible intermediate species. Moreover, it was observed that this interaction can lead to higher capacity utilization of FeF_3 due to the in-situ formation of carbon in the cathode structure from the discharged CF_x that boost the low electronic conductivity of FeF_3 . The electrochemical performance of the hybrid cathodes shows higher capacities than pure cathode structures. This observation highlights the contribution of CF_x in subsequent cycles from the in-situ formation of conductive carbon through the cathode structure after the first cycle that significantly facilitates the charge transfer in cathode.

After the 1st charge, fluorine content as the active source of capacity can be transformed in four possible forms after the charging process: (i) Li-F bonds, formed through the discharge process of CF_x and FeF_3 with lithium, (ii) Li-Fe-F bonds, originated from not reversible intermediate species, (iii) Fe-F bonds, combination of reversible and possible unreacted FeF_3 , and (iv) C-F bonds, possible unreacted pristine CF_x . A summary of active materials content through the first discharge and charge is shown in Figure 3.11.

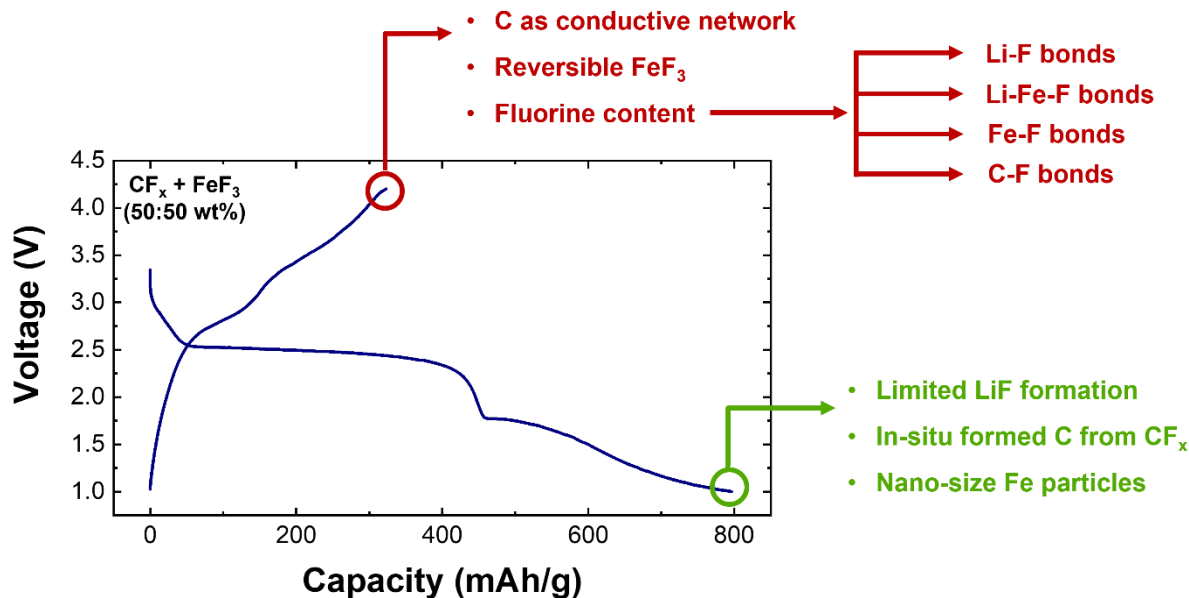


Figure 3-11. A summary figure of the interaction between CF_x and FeF_3 through the first cycle.

In this study, the possible decomposition or limiting the formation of LiF as the main discharge product was shown. However, the investigation on the rechargeability of CF_x -based cathodes should be focused on the possible re-fluorination of carbon to obtain the C-F bonding for the subsequent cycles.

The study of possible re-fluorination of carbon is of great interest in investigation of the possible rechargeability of the Li-CF_x primary battery with the high energy density, reliability, and low self-discharge. This study highlights the need for future investigations on primary battery materials to advance performance and extend the possibility of rechargeability in this system.

3.5. Acknowledgment

Chapter 3, contains unpublished material coauthored with Yin, Yijie, Li, Weikang and Meng, Ying Shirley. The dissertation author was the primary author of this chapter.

4. CHAPTER 4 – HIGH ENERGY-DENSITY LOW-TEMPERATURE LI-CF_x BATTERY

4.1. Introduction

Fluorinated carbon is a non-stoichiometric solid fluorocarbon with empirical formula of CF_x in which 0.5 < x < 1.3. The fluorine content (x) in CF_x depends on the synthesis process and structural properties of the pristine carbon material (such as coke, graphite, fiber). This compound is synthesized by direct fluorination of carbon with fluorine gas in temperatures higher than 350°C. It has been shown that the higher reaction temperature during synthesis will result in higher fluorination level and higher C-F covalent character (even compared to undesired CF₂ and CF₃).

Goddard et al. have previously investigated the possible structure of fluorinated graphite by density functional theory (DFT) for different compositions.⁶⁶ They have considered x in CF_x to be equal to 0.0625, 0.25, 0.33, 0.5, and 1, and for each composition, investigated the formation mechanism and calculated the formation heat based on pristine graphite and fluorine gas.

For the first time, they showed that the carbon in CF_{0.5} structure is the combination of sp³ hybridization owing to C-F covalent bonds and sp² hybridization similar to pristine graphite.⁶⁶ This finding was contrary to the previous belief that the whole structure is consisted of C-F and C-C covalent bonds with sp³ hybridization.

The structural models for CF₁ have been shown in Figure 4.1. The two possible structural model of the infinite array of trans-linked cyclohexane chairs and the cis-trans-linked cyclohexane boats have been shown and compared in two possible layer stackings of AB and AA'. The calculated formation heat in each case is also presented in kcal/mol in each case. The influence of layer stacking sequence was in the structure was also investigated previously and it was found that the effect of layer stacking (i.e. AB or AA') is insignificant.

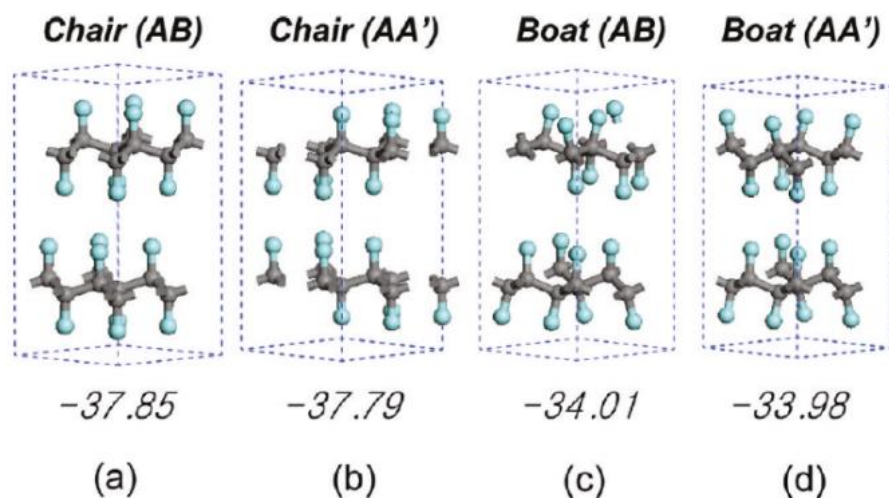


Figure 4-1. The possible structural models and calculated heat of formation in CF_1 for the infinite array of trans-linked cyclohexane chairs in layer stacking of (a) AB, (b) AA', and for the cis-trans-linked cyclohexane boats in layer stacking of (c) AB, and (d) AA'. The figure is adopted from the reference ⁶⁶.

Conventionally, fluorinated carbon material has been synthesized through direct fluorination of carbon at high temperatures ($>350^\circ\text{C}$). However, fluorinated carbon material obtained by this method possesses a high insulating character. Therefore, new methods were suggested to improve the properties of this material including electronic conductivity and ionic diffusion.¹²⁴

Notably, it was shown that the fluorination conditions strongly influence the electrochemical performance. Hamwi et al. have summarized the fluorination methods and their effects on the discharge potential, the energy density, the power density or the faradic yield as the main electrochemical parameters.¹²⁵ They have considered three advance fluorination methods including (a) catalytic fluorination followed by a post fluorination under pure fluorine gas, (b) sub-fluorination process, and (c) fluorination by solid fluorinating agent such as TbF_4 and XeF_2 ; and compared them with conventional method as the direct reaction of fluorine gas with carbonaceous materials.

Another important parameter is the carbon material as the basis of the synthesis. In case of using low crystalline structure or amorphous carbon, such as carbon black and petroleum coke, it may lead to a less active fluorinated carbon structure or to over fluorination means more fluorine atoms per carbon atom, such as formation of CF_2 or CF_3 .

Li-CF_x primary battery was one of the most promising systems due to its high theoretical specific capacity and energy density (865 mAh/g and 2180 Wh/kg), long shelf life (>10 years at 25°C), stable operation and wide operating temperatures (-60°C to +170° C), low self-discharge (annual capacity loss of <0.5% in 25°C and <4% at 70°C), and high reliability and safety.^{1,68,126,127} This system is considered as convenient, reliable, and cost-efficient energy storage system that can be sized and shaped easily in different configurations for varied applications. They are widely used in portable electric and electronic devices, communication equipment, hearing aids, military tools, and implantable medical devices due to their lightweight and good shelf-life with no maintenance requirements.

Despite all the advantages of the Li-CF_x battery system, there are kinetic limitations associated with the poor electrical conductivity and strong covalent C-F bonds results in slow cell reaction kinetics which further inhibits the utilization of lithium CF_x system in low temperature applications and high-power devices.

When the battery is exposed to sub-zero temperatures, several aspects begin to influence its low-temperature performance^{128,129} (Figure 4.2): (i) Li^+ diffusion through the solid electrolyte interface (SEI) and cathode electrolyte interface (CEI) layers; (ii) Li^+ solvation and de-solvation processes; (iii) Li^+ diffusion through bulk electrolytes; (iv) Solid-state diffusion in CF_x layers; (v) Redox reactions. Therefore, current research efforts to improve low-temperature performance encompasses electrolyte optimizations, electrode modifications, and interfacial engineering.

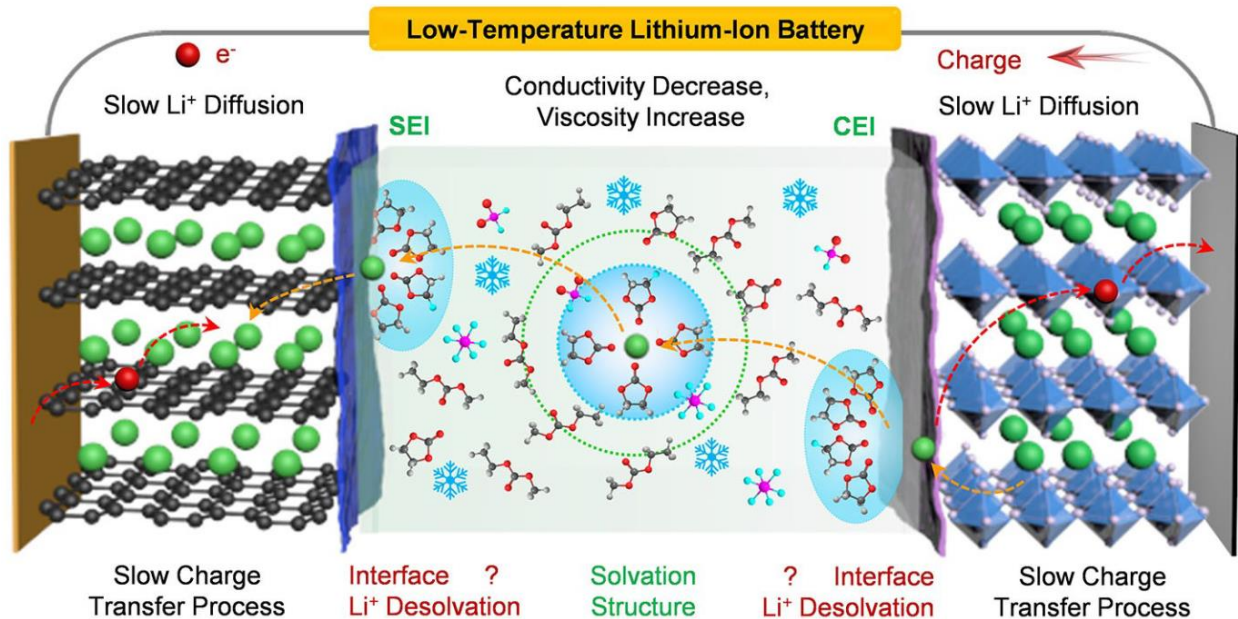


Figure 4-2. A schematic of challenges that hindered the performance of a battery at low temperatures.

Developing primary batteries with competitive performance at low temperatures requires a comprehensive picture of both ionic and electronic conductivity as the governing parameters. At ultra-low temperature, the decrease of electronic conductivity and sluggish solid-state diffusion of Li^+ between the fluorinated graphite layers will rapidly exacerbate, which restricts the kinetics property at the cathode side⁸. Moreover, it is known that the fluorination of CF_x further hampers the electronic conductivity at all temperature ranges due to the covalent C-F bond^{6,7}. There have been different approaches to improve electrical conductivity, such as different strategies of fluorination^{89,125}, coating or doping the fluorinated graphite with conductive additives, e.g. noble metals¹³⁰, metal oxides^{131–133}, or other cathode materials¹³⁴, and employing carbon nanostructures^{2,6,127,135–143}. Although they have been reported with an enhancement of the energy density, power density, or faradic yield, however, most of them can be considered unscalable,

difficult to engineer, and expensive which limits the implementation of them in practical applications.

To address this issue for low-temperature cathodes, there have been a few studies mainly focused on the following strategies: (i) using a thinner electrode to decrease the cell resistance¹⁴⁴⁻¹⁴⁶, (ii) utilizing a sub-fluorinated carbon which has been attributed to better electronic conductivity^{147,148}, (iii) considering a room-temperature pre-discharge step to make a fluorine-free carbon layer at the electrode/electrolyte interface (GIC layer engineering) to enhance electrolyte wettability and conductivity^{147,149}, and (iv) employing $\text{CF}_x\text{-MnO}_2$ hybrid structure as a co-catalytic cathode to improve the reaction kinetics.^{150,151}

Previously, utilization of sub-fluorinated graphitic carbon ($\text{CF}_{0.65}$) with a better electronic conductivity along with a room-temperature pre-discharge step was reported to deliver a higher energy density compared to fluorinated graphite ($\text{CF}_{1.08}$).¹⁴⁹ Using the same PC:DME (1:4) with 1M LiBF_4 as the electrolyte, it has been shown that commercial $\text{CF}_{1.08}$ with excess carbon conductive agent (30%) delivered about 200 mAh/g discharged capacity (C/40) at -40°C while this discharged capacity increased to about 600 mAh/g with the same condition using $\text{CF}_{0.65}$. Later, another group investigated four different commercial CF_x ($0.8 < x < 1.2$) along with two different electrolytes in the temperature range of -51°C to 72°C .¹⁵¹ These studies confirmed the importance of structural modification and their effect on ionic and electronic conductivity for improved electrochemical performance of CF_x cathodes.

Despite the limited studies to overcome the electronic conductivity barrier of the CF_x cathode, such as using the thinner electrodes or sub-fluorinated carbon, there are still many outstanding questions and challenges for low-temperature performance of this system. (i) it is not well-understood what the effect of the size and morphology of CF_x particles on the performance

of CF_x cathodes at low temperatures is. (ii) a systematic study on ionic and electronic conductivity of CF_x cathode materials at different temperatures, e.g., room temperature compared to low temperature (-40°C or lower). Addressing such questions can lead to a better understanding of the current limitations of low-temperature CF_x cathodes and improving their performance.

To overcome this, we have modified CF_x cathode structure to obtain smaller particle sizes, larger specific surface area, better ion diffusion and charge mobility while maintaining structural, chemical and thermal stability. We use a wide array of characterization methods to investigate how these changes affect the electrochemical performance of modified CF_x cathodes. The details of methods are discussed in detail in Section 4.2.

4.2. Materials and Methods

Electrochemical Tests: All the electrochemical performances were tested using a CR2032 coin cell. The cathode electrodes were consisted of pristine or exfoliated CF_x powder as the active material, carbon super C65 as the conductive agent, and PVDF as the binder with the weight ratio of 8:1:1. The commercial CF_x (ACS Materials) was used through this study as the pristine powder. In all coin cells, 55 μL of 0.5M LiBF_4 in PC:DME (1:4) as the electrolyte was used with Li chip (1mm thickness, >99.9%) as the anode. The cathode loading was kept in the range of 3-3.5 mg/cm^2 .

Galvanostatic Intermittent Titration Technique (GITT): The GITT tests were performed in the first discharge step under 10 mA/g pulse current for 100 minutes with 4-hr relaxation time in each step to reach the steady state.

Electrochemical Impedance Spectroscopy (EIS): EIS was performed with an applied AC potential of 10 mV in the frequency range of 1 MHz to 0.01 Hz, using a Solartron 1260 impedance

analyzer. The EIS measurements for each case were performed on the same coin cell in the three steps of: pristine, after the first discharge, and after the first charge.

Scanning Electron Microscopy (SEM) and Energy Dispersive X-ray Spectroscopy (EDS):

A FEI Apreo microscope was used to characterize the particle size and morphology. The immersion mode with T2 detector using 0.1 nA and 2 kV was used to reduce the charge accumulation on the sample. On the same instrument, the EDS chemical mapping was performed using 5 kV and 6.4 nA.

X-ray Photoelectron Spectroscopy (XPS): XPS was performed using an AXIS Supra by Kratos Analytica. The XPS was operated using an Al anode source at 15 kV, scanning with a step size of 0.1 eV and 200 ms dwell time. XPS spectra were analyzed using CasaXPS software.

Elemental Analysis (CHN/S Analysis): The elemental analysis was performed by NuMega Resonance Labs in San Diego, CA. The powder samples were dried under vacuum at 90 °C for 24-hr before the measurement. The tests were done using a Perkin Elmer PE2400 – Series II instrument.

Brunauer-Emmett-Teller (BET): The BET tests were performed using a Micromeritics ASAP2020 instrument to measure the specific surface area. The samples were initially dried under vacuum at 90 °C for 24-hr. Then, the powders were degassed in the sample tubes for 4-hr at 95 °C under high vacuum before sorption experiment. The results were processed using the software of ASAP 2020 V4.02.

Dynamic Light Scattering (DLS): The DLS tests were performed using Malvern Zetasizer nano range instrument to measure the particle size of samples at room temperature. The instrument was equipped with 670 nm laser and a thermoelectric temperature controller. The powder samples were dispersed in IPA solution using 15-min bath sonication.

4.3. Results and Discussions

4.3.1. Development of A Sustainable and Recyclable Liquid-Exfoliation Method

In this study, a scalable liquid-phase exfoliation method was developed to convert pristine CF_x powder to thinner exfoliated CF_x powder. The liquid exfoliation technique is breaking interlayer weak van der Waals bonds to create a few monolayers particles and is currently of growing interest for large scale synthesis of nanoparticles due to its high yield, safety, and low synthesis cost.¹¹¹ After the successful demonstration of this technique for graphene synthesis from graphite¹¹¹, various groups^{112–114,152–154} have attempted to produce a large quantity of different layered materials including transition metal dichalcogenides (TMDCs), MXene, and other two dimensional materials, e.g. hBN and black phosphorous. Here, we utilized this technique as this process can potentially create CF_x thin-sheets with significantly higher active surface area to improve ionic diffusion, which is proven to be vital for ultra-low-temperature battery operation.

A four-step liquid exfoliation method was used to prepare exfoliated CF_x powder as described in section 3.3.1. A schematic of the procedure was shown in Figure 3.1. The size and morphology of the pristine and exfoliated CF_x powders using SEM and AFM methods besides the chemical and structural stability of the material after exfoliation using XPS and Raman spectroscopy were shown in Figure 3.2 and figure 3.3, respectively. The Brunauer–Emmett–Teller (BET) technique showed about 9 times higher surface area after exfoliation (surface area of 209.96 m^2/g for the exfoliated CF_x powder compared to the surface area of 23.49 m^2/g for the pristine CF_x powder). Moreover, the conductivity measurement on the pressed pallet using the four-probe method shows a value of 2.85×10^{-7} S/cm for exfoliated CF_x compared to 3.47×10^{-9} S/cm for pristine CF_x powder. The increased electronic conductivity of the CF_x powder after exfoliation might be attributed to higher sheet conductivity of CF_x flakes compared to the bulk structure.

Liquid exfoliation is a versatile, scalable, and safe method that be applied to a wide range of materials; however, it raised environmental concerns due to the requirement of a relatively large amount of a solvent. The current common solvents are chloroform, n-methyl-2-pyrrolidone (NMP), or dimethylformamide (DMF) which all are toxic and carcinogenic liquids, and substances of very high concern (SVHC).

In 2014, Cyrene (dihydrolevoglucosenone) was for the first time introduced by Sherwood et al. as a bio-based alternative solvent to petrochemical-derived solvents.¹⁵⁵ Cyrene is a bio-based dipolar molecule which is a sustainable and green solvent and can be simply derived in two steps from cellulose.^{155,156} The physical properties of Cyrene with two most common aprotic solvents, NMP and IPA, are shown in Table 4.1. The data are obtained from the chemical safety data sheets.

Table 4-1. The physical properties of Cyrene, NMP, and IPA solvents.

Physical Properties	Cyrene	NMP	IPA
Empirical Formula	$C_6H_8O_3$	C_5H_9NO	$(CH_3)_2CHOH$
Molecular Weight (g/mol)	128.13	99.13	60.1
Density (g/mL)	1.25	1.028	0.785
Dipolarity	0.93	0.9	0.68
Viscosity (mPa.s)	14.5	1.67	2.37
Boiling Point (°C)	227	202	89
Melting Point (°C)	-18	-24	-89.5

Later in 2016, this solvent was tested for the dispersion of graphene from graphite and has shown an order of magnitude higher concentration system.¹⁵⁷ In this work, Cyrene was used as the solvent for liquid exfoliation of pristine CF_x powders, following the similar procedure with IPA. Different sonication time has been tried to evaluate the effect of the duration of the liquid exfoliation on yield and size distribution of the exfoliated powders. A summary of the liquid exfoliation yield and the size distribution of the exfoliated CF_x powders measured by dynamic light scattering (DLS) technique are shown in Figure 4.3. These tests were performed on total 1g of the pristine powders.

Liquid Exfoliation Yield (%) for 1g powder

	30min	4-hr	8-hr	12-hr
IPA	12%	27%	33-34%	34-35%
Cyrene	37%	42%	56%	58%

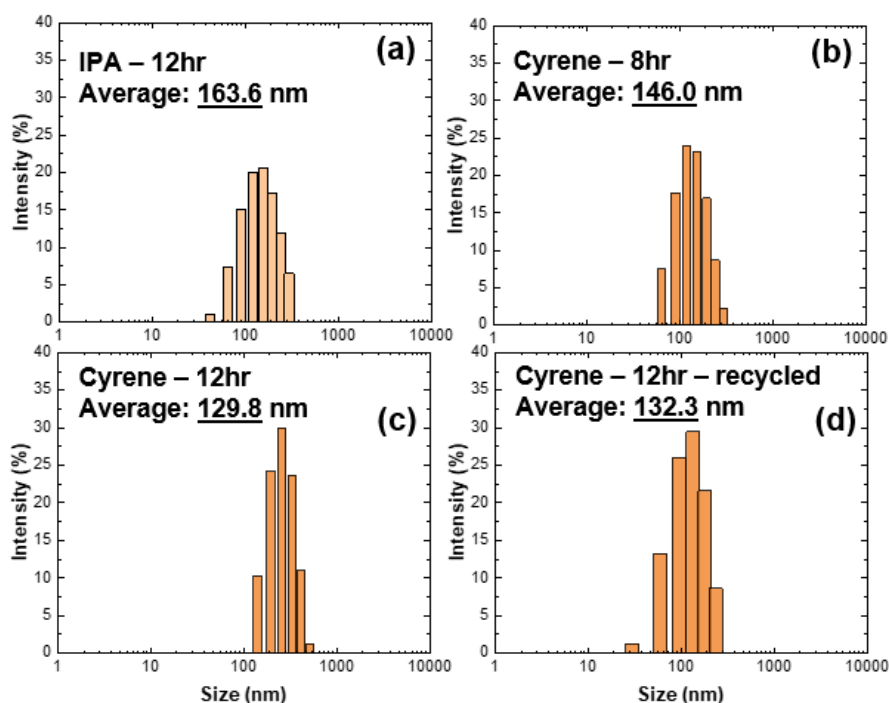


Figure 4-3. A comparison of yield and size distribution of exfoliated CF_x powders using IPA and Cyrene solvents with varied sonication times. Table shows liquid exfoliation yield for 1g pristine powder. The DLS data show the size distribution of exfoliated powders under (a) IPA-12hr, (b) Cyrene-8hr, (c) Cyrene-12hr, and (d) Cyrene-12hr-recycled.

It is shown that Cyrene, with higher di-polarity and surface tension, has a higher efficiency than IPA solvent with smaller particles sizes. It is interesting to observe that increasing the exfoliation time from 8-hr to 12-hr does not increase the yield significantly but results in smaller particle sizes. Therefore, 8-hr exfoliation time was fixed through the later experiments using Cyrene as the solvent for liquid exfoliation method to scale-up the synthesis and increase the overall yield. This solvent also helps to avoid other common intercalated molecules, such as NMP and chloroform molecules, or expensive ionic liquids.

The recyclability of the Cyrene is also considered as another important factor of sustainability. To evaluate the recyclability of the Cyrene solvent, the CF_x powders left in the used Cyrene were separated out using a membrane filtration and the cleaned Cyrene solvent was obtained. This recycled Cyrene was used again in liquid exfoliation procedure with a new batch of pristine CF_x powders. The size distribution of the exfoliated particles in recycled solvent shows similar range of size distribution (Figure 4.3-d). The electrochemical performance of the exfoliated CF_x powders using recycled Cyrene is also evaluated in comparison with fresh Cyrene (Figure 4.4). These results highlight the recyclability of the Cyrene as a sustainable solvent for liquid-exfoliation method.

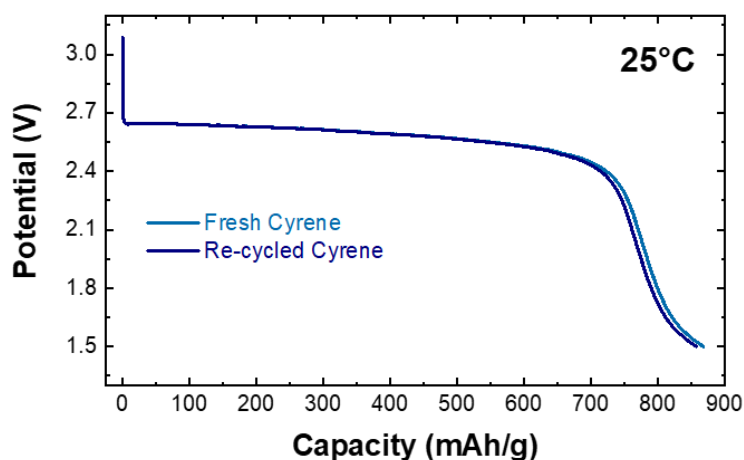


Figure 4-4. The electrochemical performance of the exfoliated CF_x powders using recycled and fresh Cyrene solvent.

4.3.2. Rate Capability and Ultra-Low Temperature Performance of the Exfoliated CF_x

First, the electrochemical performance of the obtained exfoliated powders in comparison with the pristine powders was tested at room-temperature (25°C) and low-temperature (-60°C). The cells were assembled using the CF_x cathodes, Li chip as the anode, and 0.5M LiBF₄ in PC:DME (1:4) as the electrolyte. The detailed testing configurations are presented in Table 4.2. The electrochemical performance results are presented in Figure 4.5.

Table 4-2. The coin-cell testing specifications used in low-temperature study.

Coin-Cell Specifications	
Cell type	CR2032
Cathode active material	CF _{1.05} – 80%
Conductive Agent	Carbon C65 – 10%
Binder	PVDF – 10%
Counter electrode	Li metal chip (thickness: 1mm, diameter: 15.4 mm)
Separator	Celgard 2325
Electrolyte	0.5M LiBF ₄ in PC:DME (1:4vol%)
Electrolyte amount	50 μL
Coin cell setup	0.5 mm thick spacer and one spring at the anode side
Voltage cut-off	1-1.5V
Active material loading	2.5-3.3 mg/cm ²
Applied current density	10 mA/g

The electrochemical voltage profiles show similar performance for both systems using pristine and exfoliated CF_x powders indicating a proper utilization of CF_x cathode in the first discharge (theoretical capacity of 881 mAh/g for CF_x with $x=1.05$). At -60°C , the system using the exfoliated CF_x shows a superior energy density by showing higher operating voltage plateau (1.96 V vs 1.78 V in pristine case) and higher governed specific capacity (748 mAh/g vs 415 mAh/g in pristine case) in the case of discharged to 1.5 V.

An about 0.2V higher voltage plateau and >400 mAh/g more specific capacity using the exfoliated-based cathode show a great promise of using exfoliated CF_x powder for the ultra-low temperature application.

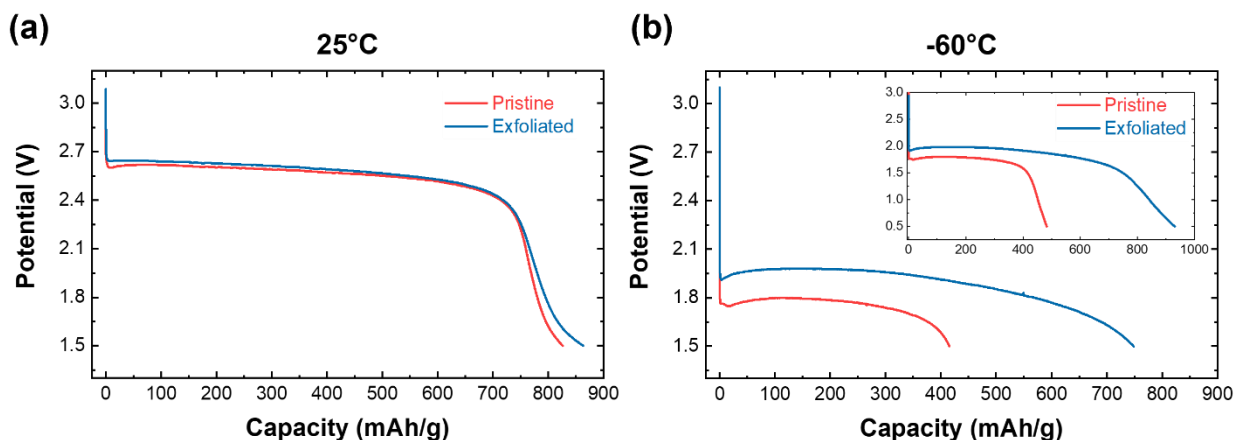


Figure 4-5. The electrochemical performance of Li- CF_x battery using the exfoliated powder in comparison with the pristine powder at (a) room-temperature (25°C) and (b) ultra-low temperature (-60°C). The applied current density is 10 mA/g in all tests.

The electrochemical impedance spectroscopy (EIS) measurement was also performed through the depth of discharge on the cells using the pristine-based cathode and exfoliated-based cathode, at room temperature (25°C). A semicircle at high frequencies and a followed tail at low frequencies are observed in impedance spectra. The results are shown in Figure 4.6. The

impedance spectra are shown through the depths of discharge to 1.5 V. A better charge mobility and lower charge transfer resistance from EIS analysis (Figure 4.7) was observed using the exfoliated-based cathode compared with the pristine-based cathode. The equivalent circuit used for EIS analysis is shown in the inset of the figure where the R_b reflects the bulk resistance, R_{ct} reflects the charge transfer resistance, CPE reflects the double layer capacitance, and W_0 reflects the Warburg impedance.

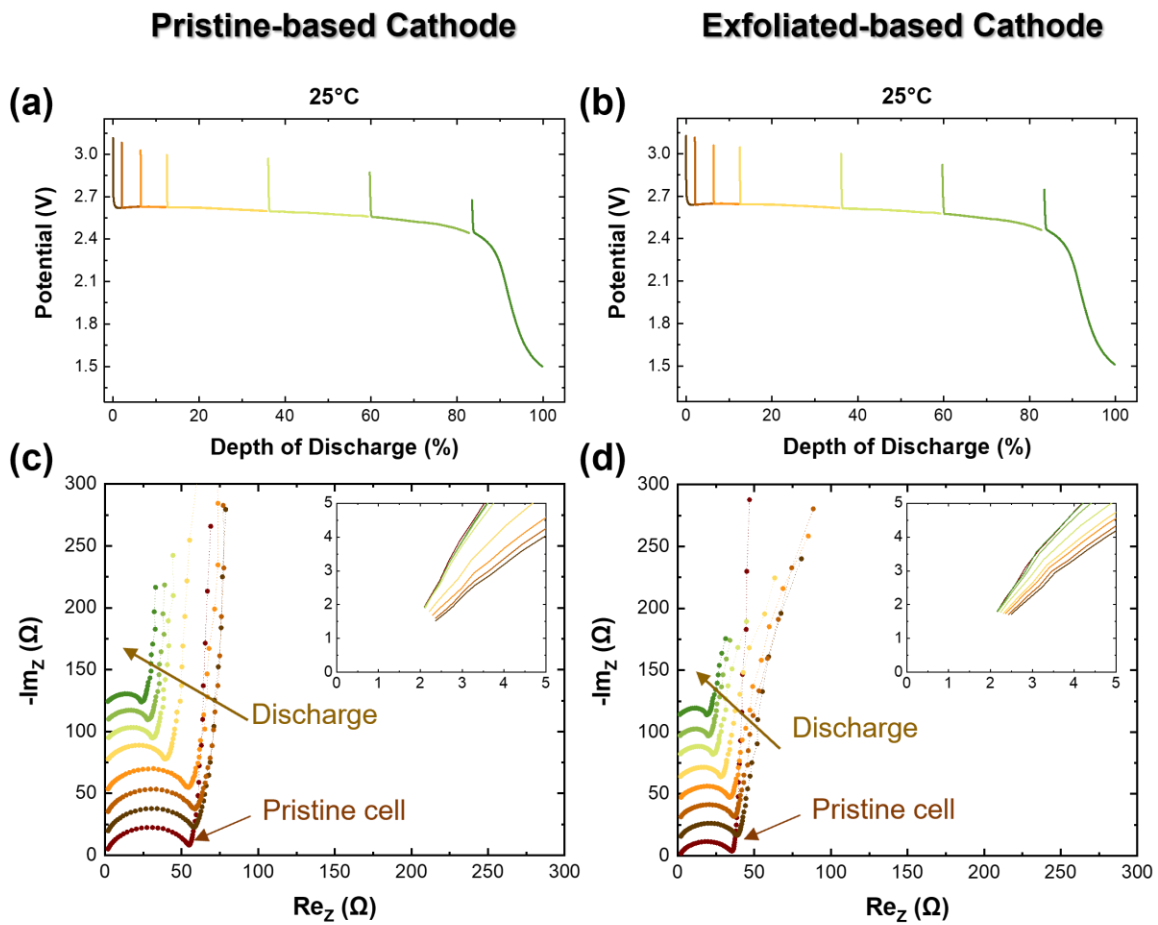


Figure 4-6. The EIS measurement through the depth of discharge on the cells using (a,c) the pristine-based cathode and (b,d) exfoliated-based cathode, at room temperature. The impedance spectra are shown through the depths of discharge to 1.5 V.

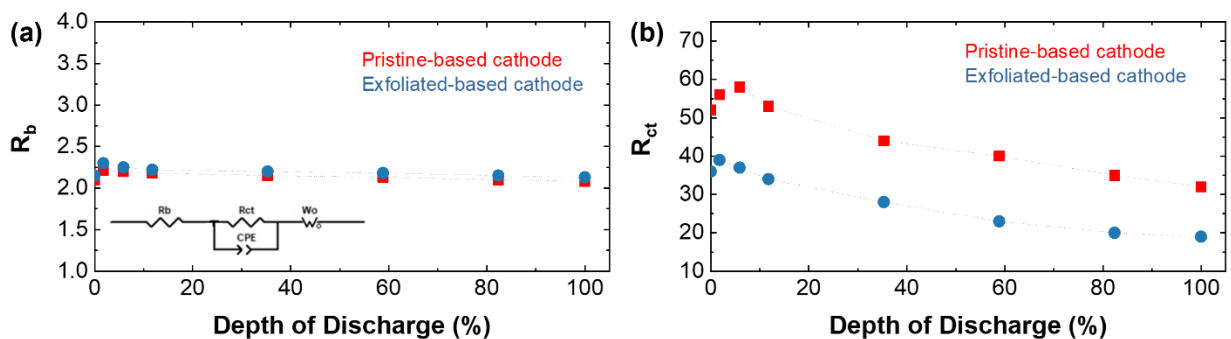


Figure 4-7. A comparison of the (a) bulk resistance and (b) charge transfer resistance in the pristine-based and the exfoliated-based cathode. The EIS analysis performed using the equivalent circuit shown in the inset of the figure.

Next, the galvanostatic intermittent titration technique (GITT) was performed to evaluate the lithium-ion diffusion in the pristine and exfoliated CF_x powders at room- and low-temperatures. This method has been used to measure the chemical diffusion coefficients of lithium ion in different cathode electrode materials.^{133,158}

The GITT discharge curves of Li- CF_x cells using the exfoliated-based cathode in comparison with the pristine-based cathode at room-temperature (25°C) and ultra-low temperature (-60°C) are shown in Figure 4.8. This measurement was performed with discharge step at 10 mA/g for 100 min and followed by an open circuit stand for 4hr to relax the cell to reach to its equilibrium. This procedure is repeated for the full discharge to 1.5 V. The systems using the exfoliated-based cathode show higher operating voltage plateaus with longer performance run than the pristine-based cathode.

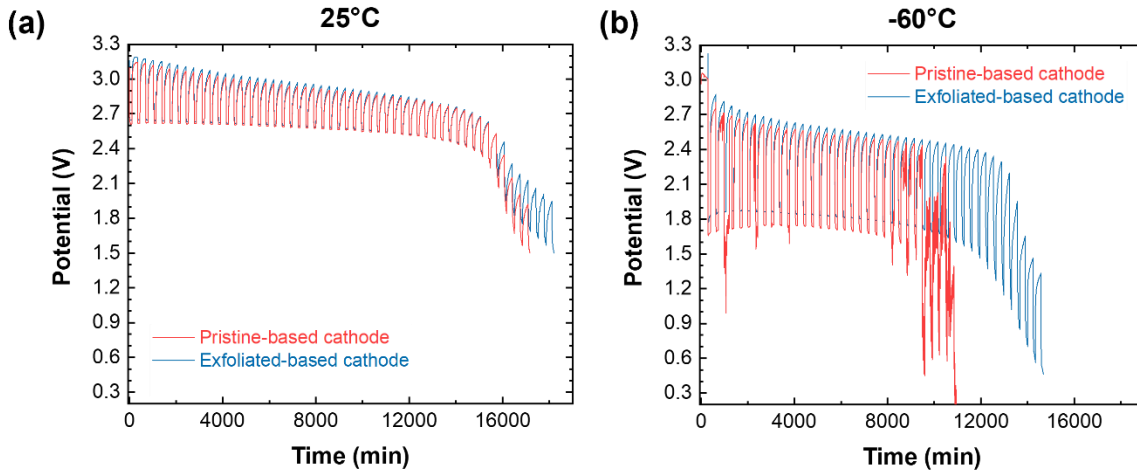


Figure 4-8. The GITT discharge curves of Li-CF_x cells using the exfoliated-based cathode in comparison with the pristine-based cathode at (a) room-temperature (25°C) and (b) ultra-low temperature (-60°C).

The lithium-ion diffusion was calculated based on the Fick's second law of diffusion. The simplified version of this theory for lithium ion diffusion calculation¹⁵⁹ can be written as the following equation:

$$D_{\text{Li}^+} = \frac{4\tau}{\pi} \left(I_0 \frac{V_m}{SFz_i} \right)^2 \left(\frac{\Delta E_s}{\Delta E_\tau} \right)^2 \quad (\text{Eq. 4.1})$$

Where I_0 is the applied current (A), V_m is the molar volume (cm³/mol), z_i is the number of charge transfer, F is the Faraday constant, and S is surface area (cm²). In this equation, ΔE_s is the potential decay between consequent relaxing times ($E_0 - E_s$) and ΔE_τ is the potential drop from the equilibrium potential state after the relaxation time to the consequent discharge potential ($E_0 - E_\tau$). For a better clarification, a schematic of GITT discharge curve with labels of these parameters is shown in Figure 4.9.

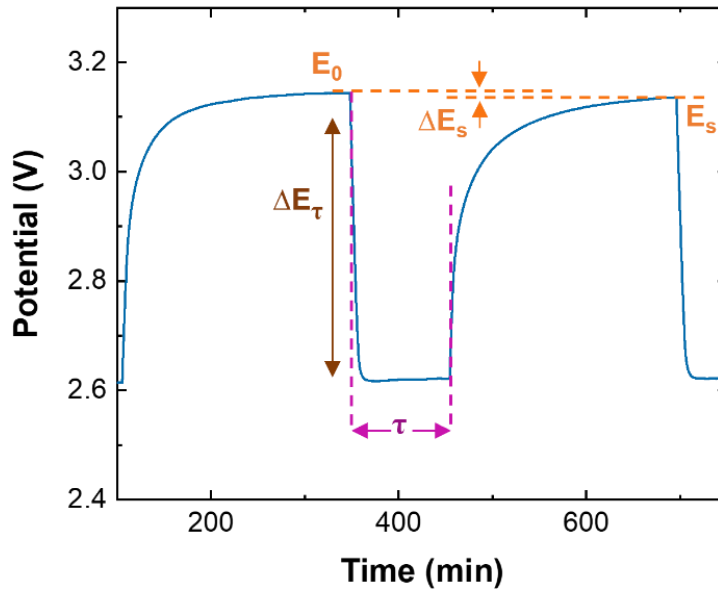


Figure 4-9. A schematic of the GITT discharge curve in a single step, labeling the required parameters for the Fick's second law of diffusion.

The last term of the equation is this term $\left(\frac{\Delta E_s}{\Delta E_\tau}\right)^2$ which is the simplified form of $\left(\frac{\frac{dE}{dx}}{dE_\tau}\right)^2$ that

requires a linearity between E and $\sqrt{\tau}$. To validate this factor in the measurements, the plots of potential E as a function of $\sqrt{\tau}$ for the both systems of pristine-based and exfoliated-based cathodes at room-temperature (25°C) and ultra-low temperature (-60°C) are shown in Figure 4.10. The roughly linear initial slopes in all cases to about 800 s^{1/2} are considered as the validity of using equation 4.1.

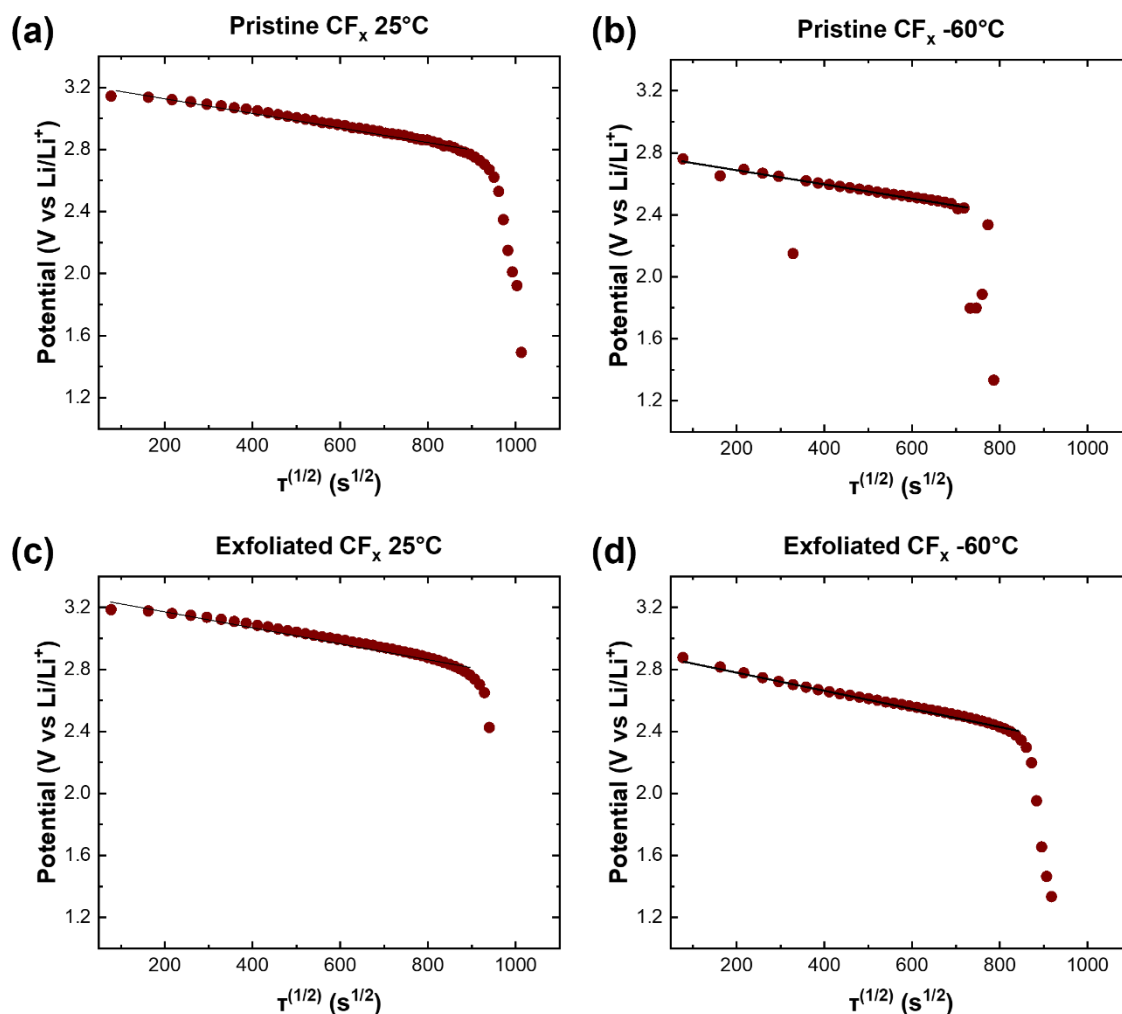


Figure 4-10. The linear behavior of the potential (E) as a function of $\tau^{1/2}$ for pristine-based cathode at (a) room-temperature (25°C) and (b) ultra-low temperature (-60°C) and for exfoliated-based cathode at (c) room-temperature (25°C) and (d) ultra-low temperature (-60°C).

The ionic diffusion of lithium-ion (D_{Li^+}) during the first discharge for pristine-based and exfoliated-based cathodes at room-temperature (25°C) and ultra-low temperature (-60°C) is calculated based on the equation 4.1 and the results are shown in Figure 4.11. It is observed that the D_{Li^+} in the exfoliated-based cathode is about two orders of magnitude higher than the pristine-based cathode at room temperature. It is interesting that this trend is more significant at ultra-low temperature.

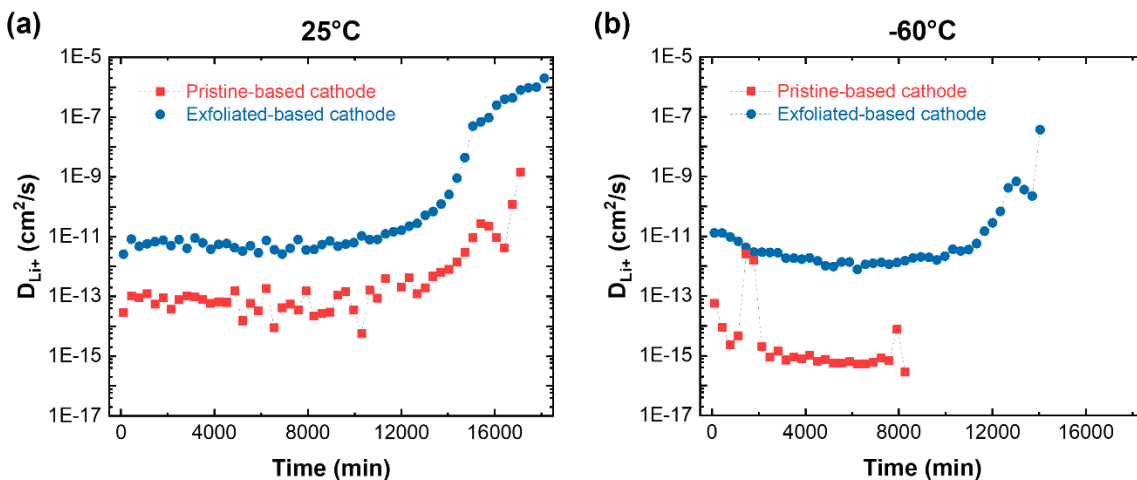


Figure 4-11. The ionic diffusion of lithium-ion (D_{Li^+}) during the first discharge for (a) pristine-based and (b) exfoliated-based cathodes, at room-temperature (25°C) and ultra-low temperature (-60°C). The D_{Li^+} is calculated based on the Fick's second law applied on the GITT measurement.

The improved ionic diffusion at room temperature indicates a better rate capability of the system using the exfoliated-based cathode. This phenomenon might be due to the larger surface area and more exposed CF_x sheets that facilitate the lithium-ion and electrolyte diffusion. Furthermore, the rate capability of the system using the exfoliated-based cathode under varied applied current densities have been explored and showed an improved performance.

A summary of the low-temperature performance at different operating temperatures of 25°C, 0°C, -20°C, and -60°C for the exfoliated-based cathode compared to the pristine-based cathode is shown in Figure 4.12(a). The improvement of performance is more highlighted at lower temperatures. The exfoliated-based cathode provides high capacity of 748 mAh/g and high energy density of 1095 Wh/kg at -60°C (discharged to 1.5V).

Similarly, a summary of the rate capability of the Li- CF_x battery at different applied current densities of 10, 100, 500, 1000, and 1500 mA/g using the exfoliated-based cathode compared to

the pristine-based cathode is shown in Figure 4.12(b). The exfoliated-based cathode show about 1500 Wh/kg energy density at 1500 mA/g applied current density (discharge to 1.5V).

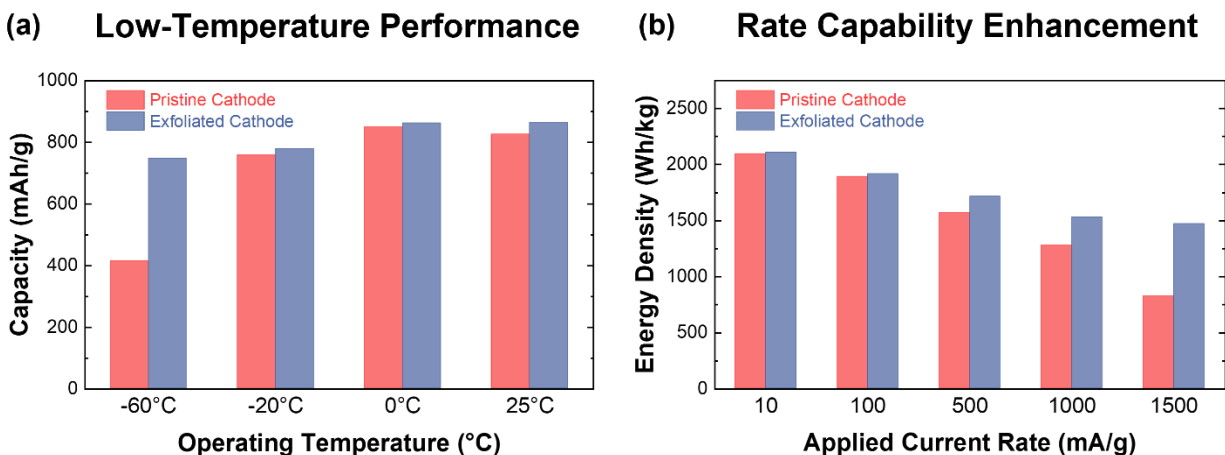


Figure 4-12. A summary of the Li-CF_x batteries using the exfoliated-based cathode in comparison with the pristine-based cathode **(a)** at varied operating temperatures of 25°C, 0°C, -20°C, and -60°C, and **(b)** under varied applied current densities of 10, 100, 500, 1000, and 1500 mA/g.

Furthermore, the performance of the Li-CF_x system using the exfoliated-based cathode is compared with the literature (Figure 4.13). Different approaches and protocols have been used in these works (Table 4.3) to modify the cathode or the operating condition to improve the performance of the Li-CF_x battery.

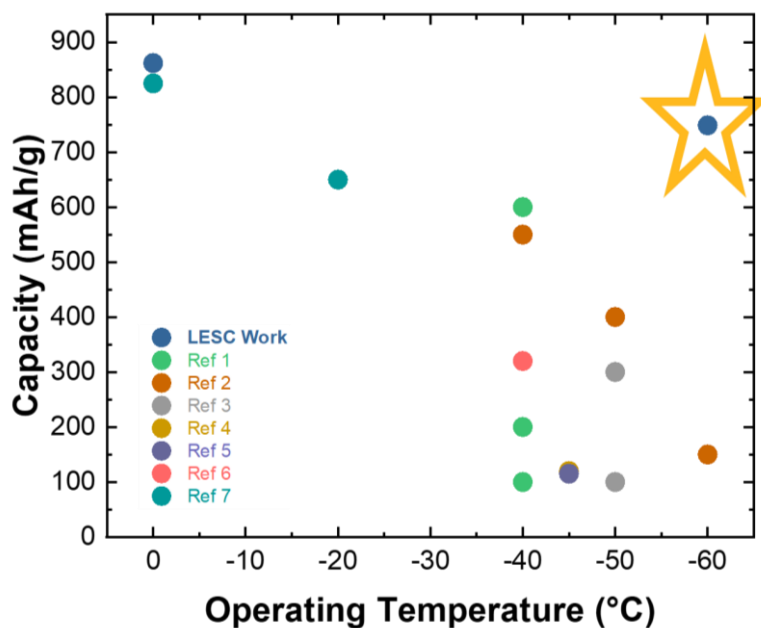


Figure 4-13. The standing of the Li-CF_x battery using the exfoliated-based cathode in comparison with the literature under varied low temperatures.

Table 4-3. A summary of the protocols and approaches used in the literature in the Figure 4.13.

	Cathode	Electrolyte	C rate	Capacity	Approach	Ref
1	CF _{0.65}	1M LiBF ₄ in PC:DME (1:4)	C/40	600	Sub-fluorinated CF _x and room temp. pre-discharge	149
2	CF _{0.647}	0.5M LiBF ₄ in PC:DME (1:4)	C/50	550	Sub-fluorinated CF _x and anion receptor	160
3	CF ₁	0.5M LiBF ₄ in 1:1 AN/γ-GBL	C/50	300	Room temp. pre-discharge	161
4	CF ₁	1M LiBF ₄ in γ-GBL +2% 15-crown-5	C/100	120	Sub-fluorinated CF _x and electrolyte additive	162
5	CF _x :MnO ₂ (35:65)	1M LiBF ₄ in GBL	C/120	115	CF _x mixing with other cathode material	150
6	CF ₁	0.5M LiBF ₄ in PC:DME (1:4)	10 mA/g	320	Room temp. pre-discharge	163
7	CF ₁	1M LiBF ₄ in EC:PC:EMC (1:1:3 wt.%)	C/100	650	Electrolyte modification	151

4.4. Conclusion

In summary, we investigated the effect of liquid exfoliation and low temperatures on the electrochemical performance of primary CF_x batteries. Our results show that at low temperatures electronic conductivity and sluggish solid-state diffusion of Li^+ between the fluorinated graphite layers will rapidly exacerbate, which restricts the performance of CF_x cathodes.

In order to improve the high-rate performance of Li- CF_x battery at low temperature, we attempted to modify the electrode materials with liquid exfoliation technique toward a higher electronic conductivity and ion diffusion. Notably, the liquid-exfoliation method was developed and optimized based on a sustainable and recyclable solvent. The uniformity and size distribution of particles were measured using SEM, AFM and DLS. The chemical and structural stability of the obtained powder was also measured by XPS, Raman spectroscopy, and XRD. The exfoliated powder exhibited about nine times higher surface area compared to pristine powder. This modified powder demonstrates a considerable higher energy density at low temperatures and better rate capability compared to pristine powder. The cell resistance and ion diffusion in these systems were also evaluated using the EIS and GITT measurements at room- and low- temperatures.

We believe further studies on this field can be focused on three main area: (i) scaling up the system toward a high-loading cathode,^{123,164} (ii) understanding and improving the electrode and electrolyte interface, and (iii) optimizing electrolyte, toward enabling high energy-density Li- CF_x at lower temperatures ($< -80^\circ\text{C}$).

4.5. Acknowledgment

Chapter 4, contains unpublished material coauthored with Yin, Yijie, Li, Weikang and Meng, Ying Shirley. The dissertation author was the primary author of this chapter.

5. CHAPTER 5 – SUSTAINABLE DESIGN OF SODIUM CATHODE MATERIALS

5.1. Introduction

The world's ever-growing energy demand has highlighted the role of energy storage systems more than ever. During the past few decades, lithium-ion batteries (LIBs) has been the gold standard technology both for mobile and grid level storage. Lithium-containing resources, e.g. mineral ore spodumene or mineral rich brine, are centered in three main countries: Australia, Chile, and Argentina.⁹⁻¹¹ Such localized distribution of lithium (Li) accounts for more than 80% of the global reserves¹² and creates an imbalance in supply and demand for growing large-scale applications. Prior to 2010, the cost of lithium metal accounted only for a very small fraction (< 2%) of total cost of LIBs. Emerging new technologies, such as electric vehicles and exponential production rise in small electronics, has disrupted the lithium metal market and led to a continuous increase on the market price of lithium metal. For instance, the price of Li_2CO_3 , a well-known extraction resource for lithium metal, has tripled over the past 10 years.¹³ The high demand of Li resources and its increasing cost have triggered the exploration of alternatives or complementarities to Li-based battery technologies.^{165,166}

Low cost per energy density, high safety, reliability, and sustainability are the key requirements for alternatives of lithium-ion batteries. Among different candidates, Na-ion batteries (NIBs) hold a great promise mainly due to the fact that, unlike Li, sodium (Na) is an earth abundant and cost-effective element. Moreover, Na^+/Na redox couple possesses a reduction potential of -2.73 V vs. standard hydrogen electrode (SHE) (compared to -3.02 V vs. SHE for Li^+/Li) making it a promising candidate by enabling a similar operating voltage in NIBs compared to LIBs.^{13,58} Sodium has a higher molar mass ($23 \text{ g}\cdot\text{mol}^{-1}$ vs. $6.9 \text{ g}\cdot\text{mol}^{-1}$ for Li^+) and larger ionic radius (1.02 \AA vs. 0.76 \AA for Li^+), leading to great differences in its chemical and electrochemical properties,

compared to lithium.¹⁶ Higher chemical reactivity of sodium can cause faster solid electrolyte interphase (SEI) formation and a rapid electrolyte consumption.^{167–169} On the other hand, since sodium does not form an alloy with aluminum, even at reduced potentials, aluminum (Al) instead of copper (Cu) can be used as the current collector in NIBs. Al is more favorable due to its higher earth's abundance and lower price compared to Cu (abundance in earth's crust: 8.23% for Al and 0.0068% for Cu)⁵⁹. Moreover, the charge density (q/r ratio) of Na^+ is lower than Li^+ in solid materials and in certain cases the diffusion of Na^+ in solid phases is much faster than Li^+ , thus allowing a fast-charging up to 500 C current rate ($58.5 \text{ A}\cdot\text{g}^{-1}$) as recorded by Yang et al.¹⁷⁰ Despite the higher molar mass of Na, Na-containing materials exhibit a great diversity in their structures, especially in polyanions, where Na^+ -extracting voltages can be tuned easily through the so-called “inductive effect”, which can be used to design high-voltage materials and compensate the energy density loss due to the weight penalty.^{171–173}

The attempt of employing the Na^+ as the intercalating guest ion was first introduced in 1980 by G. Newman and L. Klemann from Exxon Research and Engineering Company.¹⁷⁴ A reversible Na^+ insertion/extraction using titanium sulfides (TiS_2) as the host structure at ambient temperature was demonstrated with the cycling up to 16 cycles using sodium triethyl (N-pyrrolyl) borate in 1,3-dioxolane as the electrolyte. Nevertheless, the (de)-sodiation of TiS_2 occurred at rather low voltages (below 2.0 vs. Na^+/Na)¹⁷⁴ that it is not an ideal cathode for NIBs.

In the same year, Delmas et al.¹⁷⁵ published a summary study on the structural classification and properties of A_xMO_2 layered oxides (where A stands for alkali metal and M stands for transition metals). In this study, the authors carefully investigated the crystal structures of several A_xMO_2 compositions, including $\text{A} = \text{Na}$, and classified them as O3, P2, and P3 types, depending on the Na crystallographic site and stacking sequence of MO_2 slabs. This nomenclature is still

widely used up to the present time. The transport properties such as the ionic mobility of the alkali ions based on the crystal chemistry were studied in continuation of their previous works on sodium oxides.^{176,177} Soon, the same team reported the electrochemical performance of Na_xCoO_2 ($0.5 \leq x \leq 1$) layered oxide with a promising performance and this was also considered as the first layered oxide for the cathode in NIBs.^{178,179} Based on this pioneering work, several generations of layered oxides¹⁸⁰ were developed including those with anionic redox activity^{181–183}.

Besides layered oxides, polyanions are an important class of cathode materials for SIBs. Depending on the structure of the crystallized materials, polyanions can be classified as olivine¹⁸⁴, alluaudite^{185,186}, tavorite¹⁸⁷, $\text{Na}_3\text{V}_2(\text{PO}_4)_2\text{F}_3$,^{188–190} or NA-Super-Ionic-CONductors^{191,192} (NASICON)-like structures. Among them, NASICON-type materials have been widely developed as prospective cathodes for NIBs. This class of materials was discovered in 1976 by Goodenough et al.^{191,192} and its general chemical formula can be written as $\text{A}_n\text{M}_2(\text{XO}_4)_3$ (where A stands for alkali metal ions or vacancies, M stands for transition or main-group metals, and X stands for sulfur (S), phosphor (P), silicon (Si), or arsenic (As)). The structure possesses a robust tridimensional network due to the strong covalent bonds between XO_4 tetrahedra and MO_6 octahedra.

Despite its early discovery, the electrochemical activity of NASICON in Na-based batteries had not been demonstrated till the mid-1980s with the pioneering work of Delmas et al.¹⁹³ on $\text{NaTi}_2(\text{PO}_4)_3$. Later, PBAs as another type of NIB cathode materials with the general formula of $\text{A}_x\text{M}_y[\text{M}'(\text{CN})_6]_z \cdot n\text{G}$ (where A stands for an alkali metal, M and M' stands for transition metals, and G stands for neutral molecules such as H_2O) were developed.^{194–201} They were first introduced in the 1980s and 1990s, but their applications as cathode materials for NIBs using a non-aqueous electrolyte were demonstrated by Goodenough et al. in 2012.^{202,203} As this perspective discusses

the future development of cathode materials for NIBs, they will be focused in more detail in later sections.

The discoveries and developments in anode structures also catalyzed the improved performance of NIBs. Graphite has been historically known as a prevailing anode in LIBs and many early works in the field of NIBs attempted to employ graphite to this new technology.^{95,204,205} However, Na⁺ ions cannot be intercalated into graphite due to the instability of the Na⁺-graphite intercalation (Na-GIC) and the low potentials of the reaction, which hinder the application of graphite in NIBs.^{24,25,206–208} Na⁺ can only be inserted into graphite as a solvated form in diglyme (or bis(2-methoxyethyl) ether) solvent, but the capacity of the reaction is too low, which is not suitable for practical applications.^{26,27} Hard carbon, also known as non-graphitizable carbon, was initially introduced by Dahn et al.²⁸ as anodes for NIBs in 2000. Hard carbon (with a gravimetric theoretical capacity of 300 mAh·g⁻¹ and volumetric theoretical capacity of 420 mAh·cm⁻³)²⁹ can be synthesized by a wide range of methods such as chemical, thermal, or biomass-derived processes from various organic compounds at elevated temperatures (700–2000°C).²⁹ Low-cost precursors and easy synthesis procedures have made hard carbon a promising anode material for NIBs.

However, there are still some fundamental challenges for the implantation of hard carbon in NIBs: (i) its limited practical storage capacity (around 300 mAh·g⁻¹), (ii) the electrochemical performance of hard carbon depends strongly on the nature of the precursors as well as processing temperature, which requires a careful optimization, and (iii) the Na⁺ storage mechanism needs to be better understood by employing advanced characterization techniques.^{209,210}

Besides hard carbon, non-carbonaceous anodes for NIBs were also developed in the last few years.³⁰ Depending on the reaction mechanism with Na⁺, they can be classified as conversion

(metal oxides^{31,32}, sulfides^{33,34}, and selenides^{35,36}), alloying (tin (Sn)^{37–39}, bismuth (Bi)⁴⁰, phosphorus (P)^{41,42}, and antimony (Sb)^{43,44}), or insertion materials (titanium-based oxides^{45–47}, transition metal chalcogenides^{48,49}, and MXenes⁵⁰). Among them, Sn and Sb have shown the greatest promises^{51–55} due to their high theoretical capacities (with a theoretical gravimetric capacity of 847 mAh·g⁻¹ for Sn and 660 mAh·g⁻¹ for Sb)^{56,57}, good electrical conductivity (8.7×10⁶ S·m⁻¹ for Sn and 2.55×10⁶ S·m⁻¹ for Sb at 20°C), low reaction potentials vs. Na⁺/Na (0.2–0.4V for Sn and 0.4–0.8V for Sb)⁵⁷, and less safety concerns associated with them. However, both Sn and Sb suffer significant volume expansions during sodiation process (~ 420% for Sn and ~ 390% for Sb)^{40,58}, which might lead to contact loss and substantial irreversible capacities upon long-term cycling. Furthermore, the high price and the low abundance in the earth's crust of these two elements (0.00023% for Sn and 0.00002% for Sb)⁵⁹ have prevented their wide implementation in NIBs.

Beyond research level prototypes, the advances in this field have enabled some commercialized energy storage systems based on NIB technology in the past few decades. In the 1980s, prior to the commercialization of LIBs, Elsenbaumer et al.^{211–213} from Allied Corp. (USA) and Takeuchi et al.^{214,215} from Hitachi Ltd. (Japan) have introduced the first full-cell model for NIBs with P2-Na_xCoO₂ as cathode and sodium-lead alloy as anode. The cell could operate up to 300 cycles with no failure. However, the low energy density due to the low operational voltage (< 3 V) did not help these systems compete with the relatively high energy density LIBs available at that time (3.7 V for a Graphite||LiCoO₂ cell).

Many years later, the first non-aqueous NIB system was introduced by Faradion Limited in 2015. The company, established in 2011 in the United Kingdom (UK), showcased their first product as an e-bike, powered by NIBs with an energy greater 400Wh per pack. Faradion batteries

utilized O3/P2-type $\text{Na}_a\text{Ni}_{1-x-y-z}\text{Mn}_x\text{Mg}_y\text{Ti}_z\text{O}_2$ layered oxides ($130 \text{ mAh}\cdot\text{g}^{-1}$) as the cathode and hard carbon anode ($230 \text{ mAh}\cdot\text{g}^{-1}$). The cells utilized non-aqueous electrolyte and could operate from -20°C to 60°C .²¹⁶⁻²¹⁸ In the next few years, several start-ups and companies aiming at commercializing NIBs were created all around the world with a great diversity in the choice of chemistry in the commercialized products. In 2017, the start-up Tiamat²¹⁹⁻²²¹ (France) introduced their first Hard carbon|| $\text{Na}_3\text{V}_2(\text{PO}_4)_2\text{F}_3$ cylindrical 18650 cells, which could deliver an energy density of $100\text{-}120 \text{ Wh}\cdot\text{kg}^{-1}$. At the same time, HiNa company²²² (China) developed power banks ($120 \text{ Wh}\cdot\text{kg}^{-1}$) using O3-type $\text{Na}_x[\text{Cu,Fe,Mn}]\text{O}_2$ layered oxide cathode. Altris AB (Sweden) and Natron Energy^{223,224} (USA) have also developed prototypes using PBA cathode materials. Recently, Contemporary Amperex Technology Co., Ltd. (CATL)²²⁵ (China) announced a NIB prototype ($160 \text{ Wh}\cdot\text{kg}^{-1}$) for electric vehicles (EVs) with a plan for supply chain (target to $200 \text{ Wh}\cdot\text{kg}^{-1}$) with a cost \$40 per kWh in 2023.

So far, we provided a historical timeline on the advances in the field of NIBs with examples on efforts on both cathode and anode materials as well as some commercialization attempts. A roadmap of NIBs over the years is shown in Figure 5.1.

While all these efforts have pushed the performance boundaries of NIBs and highlighted their promise as a complement to LIBs, most of the current reports in the literature are rather scattered on different electrode materials with different cycling conditions. Therefore, there remains the need to a clearer roadmap on the design and required performance metrics for NIBs to meet the current market goals.

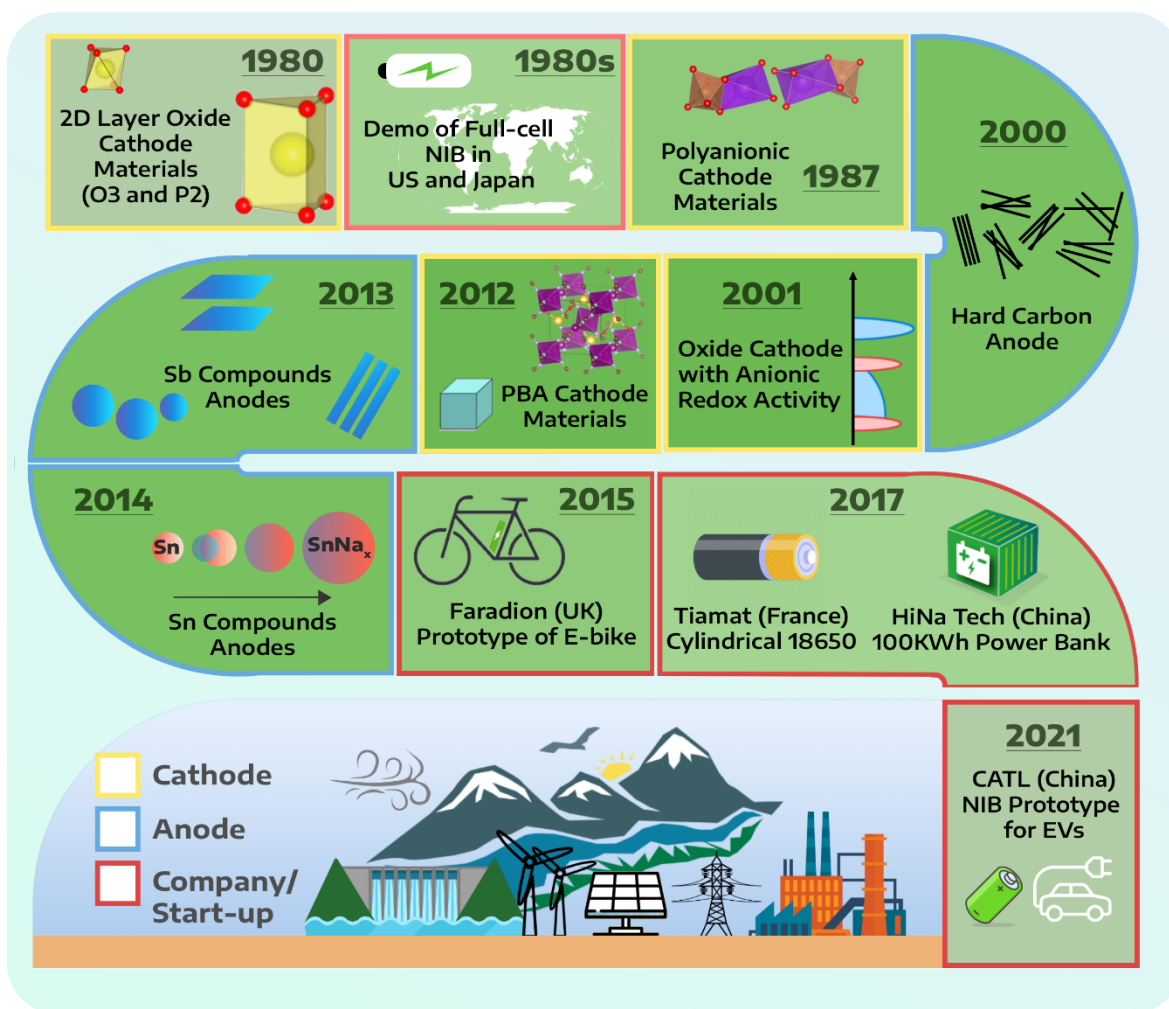


Figure 5-1. The schematic roadmap of sodium-ion batteries over years, highlighting the discovery of key materials and the relevant prototypes.

Amongst various components of NIBs, cathode materials are widely considered as the primary limiting factor in part because of their restraint energy density and substantial structural complexity; leading to challenging stability over long cycle life.⁵⁸ Given the critical role of cathode material in the cost efficacy and performance of NIB systems^{13,226}, we first discuss the important metrics in the key metals in cathode materials that will impact the supply risk and market price in near future. Next, we provide a perspective on design metrics of cathode materials based on an

extensive survey on 295 reports in the past 10 years with the focus on the implemented chemistry and composition, and its correlation to battery performance. An outlook on supply risk factor for NIB technology along with performance insights based on a large experimental data set as shown in this work, can set clear directions for future research efforts and pave the path for design of next generations of NIB cathode materials from sustainable and abundance resources.

5.2. Elements Applied in Cathode Materials for NIBs

The research on NIBs has been on the rise since 2010, mainly due to their high-power density and cost-effectiveness. Even though there have been several studies on cathode materials with different structures and elemental compositions^{22,60,173,227}, no benchmark NIB cathode is considered in the battery community. Designing new cathode materials with high energy density, sustainability, and long cycle-life is crucial for NIBs to compete with current LIBs. Habib et al. reported²²⁸ a study on the resource assessment for passenger EVs based on the baseline, moderate, and stringent scenarios. They estimated an increase to a total number of 2.25–2.6 billion passenger vehicles in 2050 compared to 1.13 billion in 2011 and EVs will take over from 24% up to 73% of these passenger vehicles. The authors also pointed out that the use of critical elements in batteries might be the possible limiting factor, impeding the transition to EVs in the near future.²²⁹ In this context, a sustainable design of cathode materials is crucial as all cathodes contain transition metal ions^{230–232} and many of which are considered as “critical” due to natural or geopolitical constraints. The main transition metals used in sodium cathode materials are manganese (Mn), Iron (Fe), Aluminum (Al), Titanium (Ti), Nickel (Ni), Vanadium (V), and Cobalt (Co). The metals are sorted in order of their price per ton and are shown in Figure 5.2(a). The overall abundance of the elements

in the earth's crust⁵⁹ is shown in Figure 5.2(a). Among these elements, Al and Fe are the most abundant, while Ni and Co have the lowest abundance in the earth's crust.

Metals can be extracted from ores and rocks as the naturally formed compounds in the Earth's crust. The minerals with high enough concentrations of desired metals can be considered as a source of metals. There are four common mining methods for the extraction of metals: underground mining, open surface (pit) mining, placer mining, and in-situ mining.²³³ Underground mining requires to dig down (varied between 300-3000m) into the earth with horizontal tunnels and vertical and diagonally sloped shafts to reach the ore deposits. It is considered as a suitable method for minerals located deep under the surface of the earth. The open surface or pit method requires removal of the plant life, soil, and potentially bedrock to access the deposits of ore, which is suitable for minerals located closer to the earth's surface.

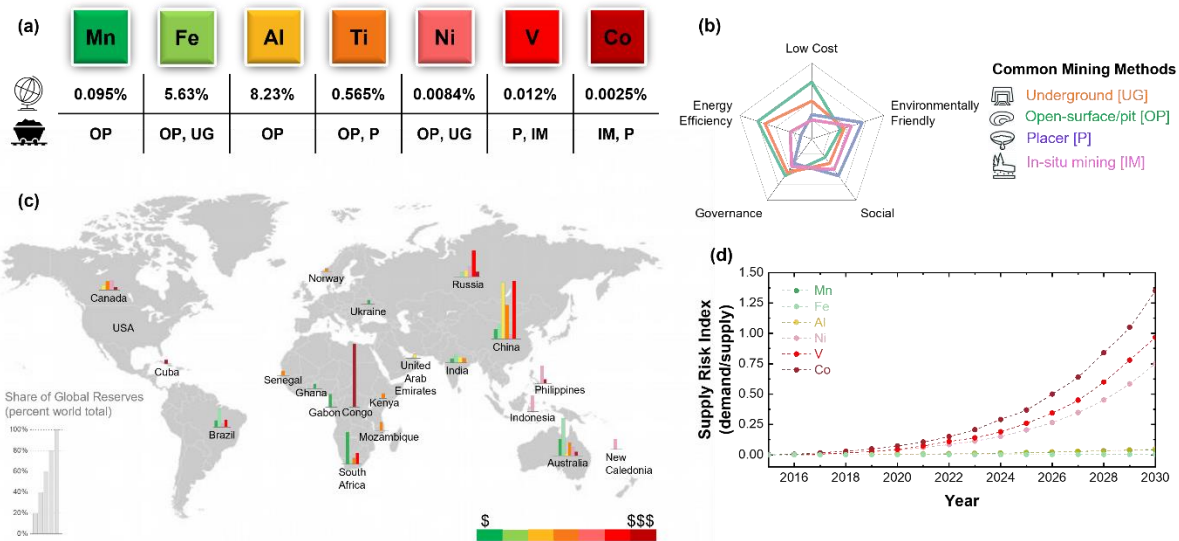


Figure 5-2. (a) The abundance of elements in the earth's crust and the main methods of their mining. (b) Spider plot comparing various desirable parameters for the main mining methods. (c) Share of global reserves for the main metal elements presented on the world's map. (d) Supply risk for the main metal elements from 2015 to 2030.

Placer and in-situ mining are expensive techniques, but they cause minimal disturbance to the surface and minimal waste rock generation. The placer method separates metals from sediments through sifting.²³⁴ In-situ method or solution mining is an in-place extraction approach by injecting a chemical solution to dissolve the minerals in their original location and pumping back the solution including the minerals (known as the pregnant solution) to the surface. There is no extraction of rocks and ore to the surface for any process.²³⁴

From the scientific point of view, the choice of mining method²³³ is usually determined based on four main factors: (i) the location of the mineral, (ii) the financial value of the deposit, (iii) environmental considerations, and (iv) the chemical composition of the mineral. However, other external parameters can also have a great impact, such as (i) energy efficiency, (ii) governance (characterizing the adequacy of national political and regulatory institutions), (iii) cost (including logistic, production, and labor), (iv) social impacts (reflecting the national and regional socioeconomic factors of vulnerability such as poverty, inequalities, and demographic imbalance), and (v) environmental effects (impacting waste containment including climatic and topographic factors, water resources and availability, biodiversity).^{235,236} The impacts of these external factors on the four mining methods are compared in a spider plot in Figure 5.2(b). Open surface and underground mining methods possess higher energy efficiency, lower cost, and better governance compared to placer and in-situ mining methods and are mainly used for Mn, Fe, Al, and Ni. On the other hands, placer and in-situ mining methods are considered as better social and environmentally friendly methods used for V and Co, although exhibiting lower energy efficiency and higher cost.

5.3. Global Reserves and Supply Risk for Critical Elements

The share of global reserves for main metal elements in the world is shown in Figure 5.2(c).¹² These values are presented in percent of the world total and are reported for the countries with above 3% global shares. The unbalanced geographical distribution of some critical metals highlights the limitation of the supply chain around the world. For example, the Democratic Republic of Congo solely retains more than 60% of global reserves for cobalt while Russia, Australia, and Cuba are the following countries with less than 5% of the global share in each country. Another critical element is vanadium, which is distributed mainly in China, Russia, and South Africa with about 56%, 25%, and 11% of the global share, respectively, leading to above 92% of the total global share. On the other hand, manganese is distributed in Australia, Asia, Africa, and South America, yet there is a lack of resources in North America. Overall, the unequal geographical distribution of critical elements leads to long-term economic, ecological, and political challenges over the world especially for countries with no sufficient share reserves.

The limited share of global reserves and the increasing demand for critical metals have a great impact on their economic values around the world.²³⁷⁻²³⁹ Therefore, ensuring a sustainable supply of these metals is the essential key for industrial and large-scale manufacturing. The supply risk index, defined as the ratio between demand over supply, for some critical metals from 2015 to the forecast of 2030 is presented in Figure 5.2(d). Co, V, and Ni are predicted to suffer high supply risks with a rapid demand in the coming years. This risk will be substantial by 2030 and the demand can hit the supply need.

In order to ensure a sustainable supply of critical metals for future applications, recycling could be an essential solution. Direct, pyrometallurgy, and hydrometallurgy recycling methods have been extensively developed for LIBs,^{11,240,241} which can thus be translated to Na-ion

technology. Even though several encouraging achievements have been obtained in the field of NIBs^{242–245}, further studies are required to develop more sustainable recycling methods that can be applied to different types of materials.²⁴⁶ Furthermore, battery recyclability and planning for batteries' end of life (EOL) must be considered in the design step to minimize environmental and economic effects.^{247,248}

5.4. Main Sodium Cathode Categories – Oxides, Polyanions, and PBAs

Over the past 20 years, research for positive electrode materials in NIBs has been mainly centered around layered oxides, polyanions, and PBAs. The representative crystal structure of these materials and their general formulae are given in Figure 5.3(a). In this Figure, M is representative of the transition metals (TMs) in these structures and the most common TMs for each category are listed as well. In LIBs, there is a great interest focusing on high-Ni NMC-based layered oxides ($\text{LiNi}_x\text{Mn}_y\text{Co}_{1-x-y}\text{O}_2$); nevertheless, there is no clear trend on which class of sodium cathode materials should be the main target for successful commercialization.

To gain insight on the most promising candidates for the next generation of sustainable NIBs cathode structures, one needs to hold a full picture of the current experimental results in the literature. Here, we summarized the performance of the 295 Na-ion half-cells using oxide, PBA, or polyanion as cathode materials. The upper cut-off voltage (V) versus the 1st discharge specific capacity ($\text{mAh}\cdot\text{g}^{-1}$) and the capacity retention (%) versus energy density ($\text{Wh}\cdot\text{kg}^{-1}$) are shown in Figure 5.3(b) and Figure 5.3(c), respectively. The size of the circle diameter represents the number of cycles.

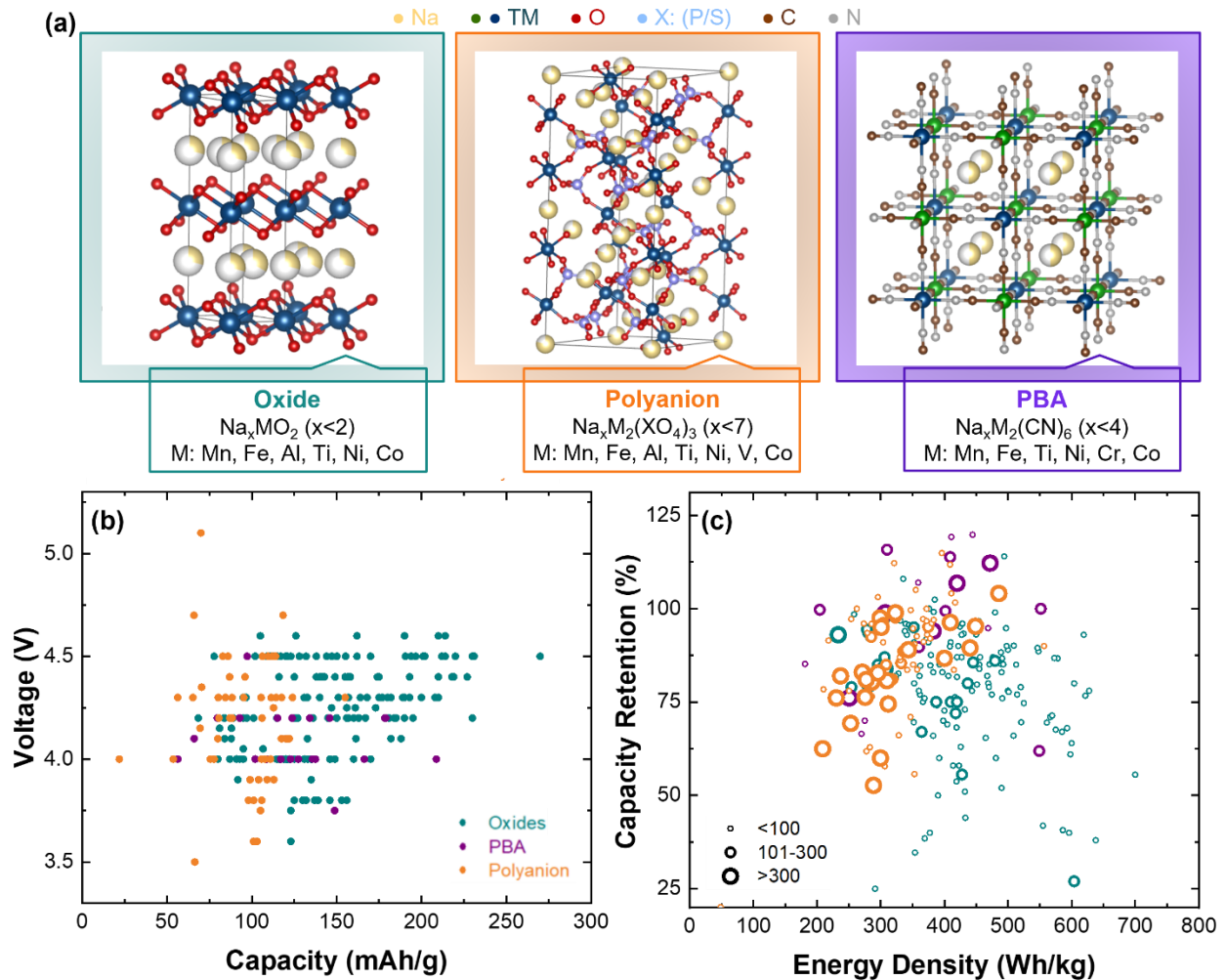


Figure 5-3. The three main types of cathode materials for SIBs. **(a)** A representative crystal structure of oxide, polyanion (NASICON), and PBA. The performance of the 295 NIB system is presented as **(b)** Upper cut off voltage versus capacity, and **(c)** Capacity retention versus energy density.

Overall, we can observe that high energy densities do not lead to high capacity-retentions and long-term cycling. On average, layered oxides exhibit a higher specific capacity and energy density compared to polyanions and PBAs, owing in part to their lower molar mass, but they usually suffer from shorter lifetimes. It should be noted that most layered oxides possess a high electronic conductivity in the pristine or desodiated states, allowing them to exhibit excellent electrochemical performance even without any coatings. On the other hand, polyanions are usually

electronic insulator due to the strong covalent bonds in the structure and thus carbon coating is widely used to help them achieving good electrochemical behaviors, especially at high current rates. In layered oxides, the layer exfoliation and high-volume expansion occur during cycling, leading to capacity loss and short lifetime. The strong covalent bonds in polyanions and PBAs result in a robust network that can support long-term cycling (Figure 5.3(c)).

It is important to note that the operating voltage, stability, and energy density of the oxides strongly depend on the structure, Na-content, and the nature of the transition metals present in the composition. Furthermore, most electrolytes reported in the literature utilize organic carbonate- or ether-based solvents, exhibiting an upper stable voltage at ~4.2-4.5 V vs. Na^+/Na , which also limits the performance of cathode materials.

To achieve a compositional design of a sustainable cathode material, implementation of advanced tools such as machine learning on predictive models with descriptors such as crystal structure of materials, their surface characteristics, and their electrochemical performance is vital.^{249–253} Figure 5.4 summarizes the energy density and capacity retention of different sodium cathode materials depending on their crystal type, space group, and TM-content in the composition.

Layered oxides (Na_xMO_2) are generally classified by the Na crystallographic site and the number of the metal oxide sheets (MO_2) in the stacking sequence. In layered oxides, Na^+ can reside in the prismatic (P) or octahedral (O) sites between MO_2 sheets, and Delmas et al.¹⁷⁵ suggested that the resulted structure should be called as P- or O-type. These characters are followed by an index indicating the number of MO_2 slabs required to generate a repeating unit. While O-type structure is exclusively encountered in Li_xMO_2 , the large ionic radius of Na^+ allows the stability of both O- and P-types in Na_xMO_2 with P2 and O3 are the two common ones.

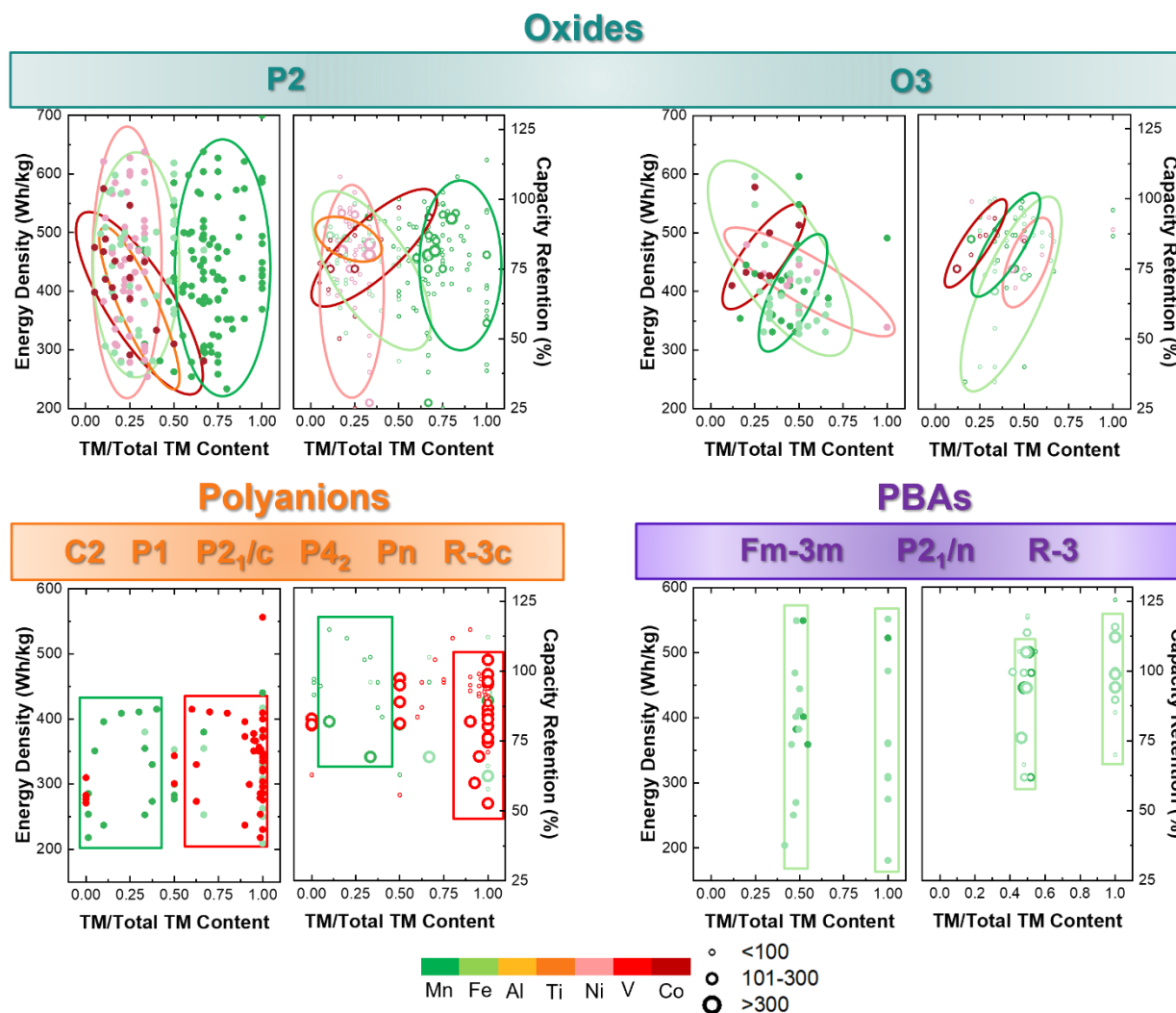


Figure 5-4. Energy density ($\text{Wh}\cdot\text{kg}^{-1}$) and capacity retention (%) for the three main types of cathode materials for the most common phases used in NIBs. The size of the dot represents number of cycles while the color indicates the type of metal.

In $\text{P2-Na}_x\text{MO}_2$ layered oxides, Mn, Fe, Ti, Ni, and Co are the most used TMs. Mn is the most frequent TM used in P2 oxides in the range of (0.5–1) thanks to its low cost, high abundance, and good electrochemical performance that can ensure high energy densities. Many Mn-rich layered oxides (Mn-content of 0.7–0.8) show high capacity-retention and high cycle life as the electroactivity of Mn can be activated in the average potential range with minimal degradation of

the active material. Therefore, Mn-containing layered oxides are usually considered as the main cathode material^{254,255} for NIBs while other substitutions can be implemented to further enhance their performance.

The presence of Ni can increase the operating voltage and thus the energy density; however, high voltages always lead to severe degradation processes. This leads to a limited Ni usage in the layer oxides (usually in the range of 0.1–0.3).^{256–265} Co can increase the intrinsic electronic conductivity of the materials and its usage in a higher amount is desired to optimize the cycling rate and capacity retention. However, our dataset shows that it will be at the cost of energy density.^{266–268}

Ti- and Fe-substitutions are also widely used. The presence of Ti usually lowers the voltage and energy density of the active materials,^{269,270} but its usage at low concentration helps to shift down the operating voltage to the electrochemical window of most currently available electrolytes and to lead to higher energy density and capacity retention.^{271–274} Fe-substitution in Na_xMO_2 usually increases the material's theoretical capacity thanks to the reversible activity of $\text{Fe}^{4+}/\text{Fe}^{3+}$ redox couple at high voltages in sodium layered oxides.^{275,276} Furthermore, a recent study has shown that the presence of Fe^{3+} also helps to obtain reversible anionic activity.²⁵⁶ However, a closer look showed us that higher Fe content can lead to lower capacity retention in a wide range of energy densities.^{277,278} It should be noted that the electrochemical performance of a material does not depend solely on one kind of ion substitution, it depends greatly on the presence of other cations in the structure and the mutual interaction between them. In general, P2- Na_xMO_2 can potentially enable higher rate capability due to the facile sodium ion mobility through the adjacent trigonal prismatic environment.^{181,182,279–281} This feature is unique to P2 sodium materials as a superior advantage compared to LIB cathodes.

Similar analysis on O3-type oxide cathode materials shows that most materials reported in the literature contained an Mn-, Co-, or Ni- content with less than 0.5 ratios while Fe-content was usually in the range of 0.25–0.75. High Mn- and Co-content usually leads to higher energy density and capacity retention^{282,283} while high Fe- and Ni-content tends to result in lower energy density but higher capacity retention.^{284–289} In order to achieve a sustainable supply, Mn-based compositions should be the main focus for layered oxides, where their physical/electrochemical properties can be modulated through the incorporation of other metal ions. The choice of the metal substitution depends on the requirement of the applications, such as voltage, specific capacity, or cycle life.

The second category of the cathodes is polyanions. The crystal structure of polyanions is quite rich and depends strongly on the nature and the interconnection between the polyhedral constituting the framework. The main space groups encountered in this class of materials are *C2*, *P1*, *P2₁/c*, *P4₂*, *Pn*, and *R-3c* (Figure 5.4). For NASICON-based materials, *R-3c* is the dominant space group; nevertheless, Na⁺ ordering can also occur with a symmetry reduction to monoclinic systems.²⁹⁰ Strong covalent bonds between polyhedral units enable this type of material to support long-term cycling with minimal structural degradation.

Figure 5.4 presents that V, Mn, and Fe are the widely used TMs in Na polyanions cathode materials. Fe/V-content is mainly used in the range of 0.5–1 thanks to their great feasibility to reside in the different polyanionic frameworks. Among them, V-based polyanions can enable high capacity and long-term cycling. While Mn, Ni, and Co dominate layered oxides research, their presence in polyanions is quite modest. This could be explained by their specific chemical and crystallochemical properties where Mn, Ni, and Co can hardly be incorporated in the polyanionic framework. Except few structures such as olivine (LiMPO₄), Mn, Ni, and Co can only exist in

polyanionic frameworks at a minor portion (less than 0.5) thanks to the presence of other structural stabilizers. Some important examples of these compounds are $\text{Na}_x\text{MV}(\text{PO}_4)_3$ ($\text{M} = \text{Mn, Ni,}$).^{291,292}

The energy density of polyanions can be engineered by modulating the operating voltage by varying the nature of the electroactive ions or the counterpart anions. For example, incorporating fluorine (the most electronegative element) into some polyanion structures^{293,294} allowed an operating voltage up to 4 V vs Na^+/Na with high energy densities. Despite this feature, the development of polyanion materials with low-cost and earth-abundant elements is necessary and is still an ongoing research challenge.^{295–298}

The third category of sodium cathodes is PBAs with the general formula of $\text{A}_x\text{M}_y[\text{M}'(\text{CN})_6]_z \cdot n\text{G}$. PBAs structures include one or more transition metal ions (in M and M' sites) coordinated by CN^- ions to form hexacyano complex. The connection between $[\text{M}'(\text{CN})_6]^{n-}$ units results in opened channels allowing a fast ionic diffusion process inside the structure. Their crystal structure can be indexed in the *Fm-3m*, *R-3*, or *P2₁/n* space group depending on the degree of distortion induced by the amount of Na^+ , water molecules, and the nature of the electroactive center. Most PBAs utilize abundant elements such as Mn and Fe, making this class of cathode materials one of the best price-to-performance ratios reported to date.^{224,299} Mn- and Fe-based PBAs can provide a wide range of energy densities (200–600 $\text{Wh}\cdot\text{kg}^{-1}$) and capacity retentions over relatively high number of cycles in non-aqueous electrolytes (Figure 5.4).

The accessible specific capacity strongly depends on the stoichiometry of the structure and the initial Na^+ concentration. Generally, the electrochemical cycling of the PBAs is categorized into two main classes: (i) only hexacyanometallate active group, and (ii) active M site TM as well as the hexacyanometallate active group.²²⁴ The class (ii) with higher electron transfer reactions is more favorable in practical batteries by enabling higher specific capacity. Manganese

hexacyanoferrate is the most well-known and commonly used PBA cathode material with two active sites of transition metals offering two electron transfers. Recently, cobalt hexacyanoferrate is also introduced as another type of the PBA cathode material with this property^{300,301}, yet low yield of synthesis considering the high cost of cobalt suppresses the large-scale applications. The number of the electrochemical active TM also affects the operating potentials. For example, an active polarized M site TM can tune the inductive effect on $M'(CN)_6$ leading to higher operating potentials. These cathodes with two electron transfers are considered among the highest energy density cathode materials with more than $150 \text{ mAh}\cdot\text{g}^{-1}$ specific capacities in above 3 V operating voltages in NIBs.

One of the limiting factors in TM selection in PBAs is originated from the synthesis procedure to obtain a stable and insoluble PBA material. Most common bulk synthesis methods are from the reaction of a transition metal salt (M^{m+}) with a simple cyanide (CN^-) or with a hexacyanometallate salt ($[M'(CN)_6]^{n-}$). Although using the simple cyanide results in high yield production, but it limits the material to only one type of the transition metal resulting in lower specific capacity. On the other hand, utilization of hexacyanometallate salt is considered as a flexible and high yield method and is the main method used in the most patent documents using PBA cathode materials. One of the well-studied materials with this method is manganese hexacyanoferrate with sodium-rich initial composition enabling full two electron transfers.³⁰² Another synthesis method for PBAs is through the decomposition products of a hexacyanometallate salt.^{303,304} This method leads to a highly crystalline and fine primary crystal grain size; however, it is not a suitable method for large batch production and scalability due to the required high temperature or pH and large quantity of HCN as the by-product.^{305,306}

Moreover, the long cycle-life of PBA materials is mainly limited by the electronic conductivity in the bulk of the active materials due to the limited reversible sodium intercalation into the bulk structure.³⁰⁷ This point highlights the importance of the size and morphology control in this type of materials. Many on-going researches have focused on the employment of multi-electroactive centers to enhance the stability and the electrochemical performance of this class of materials. For example, Moritomo et al.³⁰⁸ showed lower capacity loss by partial substitution of the Mn with Fe or Ni in manganese hexacyanoferrate.

In general, the energy density of polyanions and PBAs are not as high as those of layered oxides, which is a penalty of the high weight of the anionic part. However, the cyclability of polyanions and PBAs are greatly higher than oxides with the average number of cycles for oxides, PBA, and polyanions are 93, 257, and 686, respectively. The robustness of polyanions and PBAs helps them to find their place in applications where energy density is not the critical criterion, such as large-scale applications in grid storage or aqueous batteries.

Yet, the cyclability of NIBs is inferior to LIBs at the moment. This can be due to several factors such as (i) less advancement in design and structure of the sodium cathode materials, (ii) more sensitivity of the cathode materials to moisture and carbonates which results in more limitations in preparing and handling of the cathode materials, and (iii) limited electrolyte study and development in NIBs. Majority of the studies in NIBs are still in discovery stage with the focus on the synthesis and development of materials with different compositions and their electrochemical performance in limited time and conditions. Moreover, there is a very limited attention to the long cycling performance and the mitigation of the degradation mechanisms. In overall, as suggested, development of next generation of NIBs for large-scale production, require a comprehensive investigation with more than thousands of cycles.

It is important to note that to reach a sustainable design for NIBs, one needs to hold a full picture of all battery components including anode and electrolyte. As such, while the current work provides a practical framework to screen and design of the cathode structures, it is crucial to develop similar datasets with a focus on the anode and on the electrolyte.

5.5. Data Reporting Standard for NIBs

In the literature, P2- and O3-layered oxides have generally shown comparable energy densities and capacity retention, however, it is noteworthy that P2 materials have often been tested under more rigorous conditions compared with O3 (higher applied current densities, longer cycle numbers, and deep discharge). On the other hand, PBAs and polyanions have shown noticeably longer cyclability than layered oxides. Unfortunately, due to large variations in these testing conditions, it is difficult to accurately evaluate the overall performance across all materials.

As outlined in this manuscript, the sustainable design of the cathode materials is crucial for feasibility studies of next generation of sodium ion batteries. Our in-depth review demonstrated that there several topics that are not well explored in current NIB studies such as, (i) cathode degradation mechanism, (ii) cathode-electrolyte interphase (CEI) design, and (iii) SEI engineering. Despite their vital importance, there has been very limited studies on these topics that requires more in-deep fundamental investigations using advanced characterization techniques. Future studies on these can provide a better outlook on the next generation NIBs.

Commercialization and manufacturing of batteries are mostly not considered at laboratory-level research. Investigations at cell-level are necessary for the materials level evaluations, however, scale-up needs investigation for optimal parameters and conditions at large-scale formats.³⁰⁹ Academia with laboratory-scale studies needs to be linked to the industry with large-

scale applications. This approach saves the extra costs in research and facilities and helps to facilitate the path towards manufacturing.

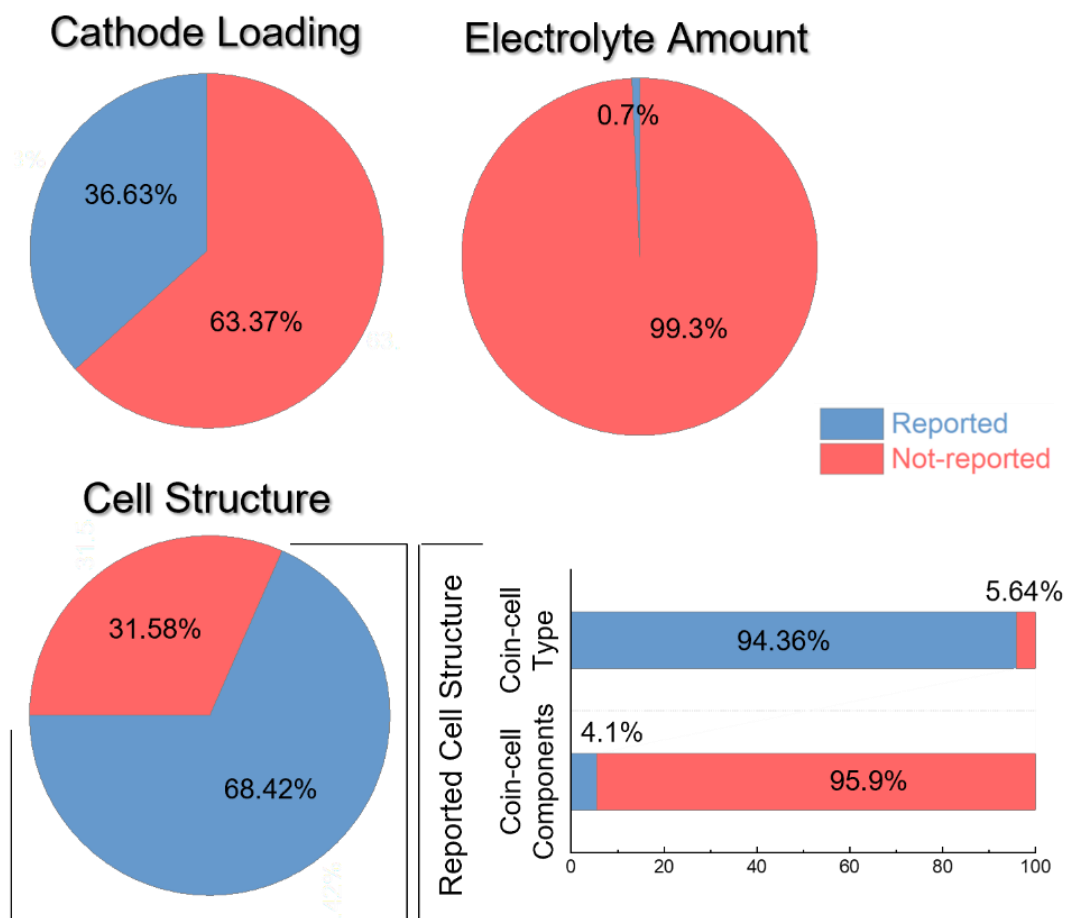


Figure 5-5. Statistical summary of reported data from 295 sodium-ion half-cells reported in the literature.

The statistical summary of reported data from 295 sodium-ion half-cells published in the literature is shown in **Figure 5.5**. The data shows that only about 37% of the studies reported the cathode loading (data varies between less than 1 mg/cm² (0.8 mg/cm²) to 10 mg/cm²) and only less than 1% of them reported the electrolyte amount. It is also observed that about 69% of the studies reported the cell structure. Among these, the coin-cell type (CR2016 or CR2032) is the

main information stated while the coin-cell components are not commonly mentioned. Only about 2.8% of the total systems have reported details about coin-cell components.

To this end, it is necessary to have a standardized and transparent data reporting in the battery community. It is also important to develop a common set of testing protocols among NIB battery researchers and developers to regulate common testing parameters. The following information is vital in battery data reporting: areal capacity, cathode loading and composition, conductive agent and binder types and contents, electrolyte amount, cathode to anode ratio, separator type, cycle number, applied current density, operating temperature, and cell configuration. Similar sets of protocols have already been laid out by the Battery500 Consortium led by the US Office of Energy Efficiency & Renewable Energy for LIBs as it was followed in the work of Niu et al³¹⁰. These protocols mandate participating researchers in order to facilitate the evaluation of LIBs. If applied to NIB research, it can serve to both create transparency across reports in the literature, as well as streamline resources toward the most urgent challenges faced by NIBs.

5.6. Conclusions

Manufacturing sustainable green and low-cost NIBs with high energy density based on earth-abundant elements can play a significant role in the next generation of energy storage systems. In order to establish a material design outlook for this goal, here we critically evaluated 295 research articles based on various cathode structures for NIBs, published in the past ten years. Given the importance of future material supply in such perspective, we evaluated main metal elements (Mn, Fe, Al, Ti, Ni, V, and Co) used in sodium cathode materials using the following metric: abundance in the earth's crust, global share reserves, side-effects of their mining methods,

and their supply risk. Our perspective shows that Mn and Fe satisfy most promising criteria for sustainable designs.

While the recent studies show encouraging results of enhanced energy density and overall cycle performance in oxides, polyanions, and PBA cathode materials, cross analyzing all reported results suggest that higher energy density does not lead to higher capacity retention and cycle life in all cases. Considering this broad outlook suggests that a cathode metal needs to be tailored in detail for optimum capacity and electrochemical cell performance.

We acknowledge that this data set still has some limitations including the lack of data scalability from the half-cell to full-cell or consistent and coherent reporting of testing parameters. Thus, the analysis conducted here is not a universal standard for adoption but rather an example of a common database for NIBs which may be used to accelerate research efforts on this front. We believe such an effort would promote a more collaborative research environment, avoid unnecessary repetition of work, and benefit the entire battery community to advance the next generation of NIBs.

5.7. Acknowledgements

Chapter 5, in full, is a reprint of the material as it appears in the MRS Energy & Sustainability Journal. “Perspective: Design of Cathode Materials for Sustainable Sodium-ion Batteries” by Baharak Sayahpour, Hayley Hirsh, Saurabh Parab, Long Hoang Bao Nguyen, Minghao Zhang, Ying Shirley Meng 9.2 (2022): 183-197. The dissertation author was the primary investigator and author of this paper.

6. CHAPTER 6 – QUANTITATIVE ANALYSIS OF SODIUM METAL DEPOSITION AND INTERPHASE

6.1. Introduction

Recent increase in global energy consumption and environmental deterioration has accelerated the demand for clean energy storage systems. Currently, lithium-based energy storage technologies, such as lithium-ion batteries (LIBs), are known as leading technologies for a wide range of applications from small portable electronics to electric vehicles.³¹¹ This high demand of lithium resources and its increasing cost highlights the need for the exploration of alternatives/complementarities clean technologies to lithium-based systems.^{165,312} During the past decade, sodium-ion batteries (SIBs) have shown great promise for sustainable and cost-effective energy storage systems in grid-scale and transportation applications.^{13,20,21,226,313–315}

Despite advances in cathode materials for sodium-ion systems^{19–21}, development of a stable anode and electrolyte is still the key limiting factor in large-scale utilization of this battery technology.^{17,22,23} Unlike LIBs, graphite cannot be used as anode material for SIBs due to its incapability to intercalate Na^+ into the structure.^{24,25} Only Na^+ in the solvated state with diglyme (bis(2- methoxyethyl) ether) can be co-intercalated into graphite; however, the capacity of the reaction is too low that it can hardly find any practical applications.^{26,27} Hard carbon was introduced as a carbon-based negative electrode alternative to graphite; however, hard carbon is not an impeccable anode for SIBs due to several drawbacks: (i) relatively low specific capacity ($\sim 300 \text{ mAh}\cdot\text{g}^{-1}$), (ii) high irreversible capacity loss due to Na trapping in the first sodiation, and (iii) poor understanding of the sodiation mechanism.^{28,29}

Among a wide range of possible anode materials for SIBs, sodium metal is the ultimate one thanks to its high theoretical specific capacity ($1166 \text{ mAh}\cdot\text{g}^{-1}$) and low reduction potential (-2.73 V vs. standard hydrogen electrode) (Table 1.1).¹⁶ Nonetheless, there exist several challenges

hindering the large-scale utilization of sodium metal as a practical anode, mainly associated to its low melting point and high reactivity. Consequently, a considerable amount of electrolyte is consumed in the first cycle, leading to a significant solid electrolyte interphase (SEI) formation process as well as low initial coulombic efficiency (ICE) and poor cyclability.^{61–63}

To overcome these challenges, several strategies have been proposed: (i) current collector modification by employing a porous three-dimensional structuring or an artificial coating that helps to lower the nucleation overpotential to enable a uniform electric field and ion-flux distribution on the electrode surface^{316–322}, (ii) electrolyte engineering to enable a stable and robust SEI layer that can enable a uniform sodium nucleation^{323–328}, and (iii) application of an artificial SEI layer as a protective coating on sodium surface^{329–333}. Whatever the nature of the utilized approach is, the key factor to enable sodium anode is the synergistic effect of the electrolyte, SEI, and sodium metal itself. It is vital to consider that electrolyte as the unique component with direct physical contact to all cell components requires to be particularly taken into account in the investigation of anode or cathode, separately.¹⁸

Applying stack pressure is another approach that has previously been discussed for lithium metal systems for a long time. Moly Energy Limited published a patent in 1985 on methods for making a battery that mentioned the stack pressure as a factor to control the preferable Li deposition.³³⁴ Later, Hirai et al. showed that Li dendrite formation in Li metal anode can be controlled by applying uniaxial pressure using a coin-cell setup which leads to improve ICE and cycle life.³³⁵ Recently, our group extensively established the concept of “Pressure–Morphology–Performance” correlation as a rational design for improving the performance of Li metal batteries.^{81,336–338}

Similar behavior is expected to be observed for all metal anodes; nonetheless, no systematic study has been reported for Na metal anode at the present time. An investigation on the effects of applied pressure can open another possibility to control the performance of Na metal to enable high energy density SIBs.

In this chapter, the effect of pressure on the morphology, the electrochemical performance, as well as the mechanism of capacity loss of Na metal anode in ether- and carbonate-based electrolytes is comprehensively investigated. For the first time, the sodium capacity usage and loss in the first cycle at different applied pressures was evaluated by titration gas chromatography. Interestingly, the obtained results indicate that SEI formation is main cause of capacity loss for Na metal anode; nonetheless, this phenomenon can be mitigated by applying a suitable pressure on the cell.

Through X-ray photoelectron spectroscopy (XPS), cryogenic scanning transmission electron microscopy (cryo-STEM), and cryogenic electron energy loss spectroscopy (cryo-EELS) a dense and uniform SEI layer with a dominant presence of organic species on the surface and inorganic species underneath is detected in ether-based electrolyte. On the other hand, the SEI layer in carbonate-based electrolytes is rather thick with a fluffy structure consisting of organic carbonyl and carboxyl species. Finally, a long-term cycling of Na||NaCrO₂ cell possessing a controlled amount Na metal is demonstrated with ether-based electrolytes. The cells exhibit excellent performance even at elevated temperatures. The great achievement reported in this study can pave the way in the development of high energy SIBs using Na metal anode.

6.2. Materials and Methods

Synthesis of NaCrO₂ Electrode Materials: NaCrO₂ (NCO) was synthesized from a stoichiometric ratio of Cr₂O₃ (99.97%, Alfa Aesar) and Na₂CO₃ (99.5%, Alfa Aesar). The mixture was pelletized and then calcinated under Ar at 900 °C for 10 h before being naturally cooled to room temperature. The purity of the powder was evaluated using X-ray diffraction (XRD) technique and showed as pure O3-type powder.

X-ray Photoelectron Spectroscopy (XPS): XPS was performed using an AXIS Supra by Kratos Analytica. XPS electrode samples were prepared inside an Ar-filled glovebox with < 0.1 ppm H₂O level. Unwashed samples were directly dried under vacuum before measurements. The XPS was operated using an Al anode source at 15 kV, scanning with a step size of 0.1 eV and 200 ms dwell time. The etching condition used was Ar⁺ mono mode, 5 keV voltage. The etching intervals was 60 s. XPS spectra was analyzed with CasaXPS software to identify the chemical composition on the surface of the electrodes.

Titration Gas Chromatography (TGC): TGC was performed using a Shimadzu GC instrument equipped with a BID detector and ultra-high purity Helium (99.999%) as the carrier gas. The samples were prepared in an Ar-filled glovebox with < 0.1 ppm H₂O level. Each sample was immediately transferred to a glass flask after disassembling and sealed using a septum under Ar. A 0.5 mL of ethanol was injected into the container to fully react with metallic sodium. After reaction completion, a 30 µL gas sample was taken from the container using a gastight Hamilton syringe and immediately injected into the GC. The amount of metallic sodium was quantified based on the amount of detected H₂ gas by the GC.

Cryogenic Focused Ion Beam Scanning Electron Microscopy (Cryo-FIB-SEM): The FIB-SEM was conducted on the FEI Scios Dual-beam microscopy; the discharged cells were

disassembled in the Ar-filled glovebox after cycling. The samples were transferred to the FIB chamber via quick loader without any exposure to air. The electron beam operating voltage was 5 kV, and the stage was cooled with liquid nitrogen to -180 °C or below. Sample cross-sections were exposed using a 1 nA ion beam current and cleaned at 0.1 nA.

Cryogenic Scanning Transmission Electron Microscopy (STEM) and Electron Energy Loss Spectroscopy (EELS): The sample was mounted to an airtight cooling holder from Melbuild to eliminate any contaminations to the Na metal-containing samples and transferred to the TEM column directly. HR-TEM results were obtained on ThermoFisher Talos X200 equipped with a Gatan Oneview camera operated at 200 kV with low dose capability. The image was acquired with minimum beam damage at spot size 6 with a dose rate of $\sim 200 \text{ electrons} \cdot \text{\AA}^{-2} \cdot \text{s}^{-1}$. The STEM-EELS data was collected through UltraFast DualEELS Spectrum Imaging detector with an exposure time of 0.02 s, and the dispersion energy was 0.25 eV per channel.

Electrochemical Impedance Spectroscopy (EIS): EIS was performed with an applied AC potential of 10 mV in the frequency range of 1 MHz to 0.01 Hz, using a Solartron 1260 impedance analyzer. The EIS measurements for each case were performed on the same coin cell in the three steps.

Electrochemical Tests: The electroplating was performed in a custom-made pressure setup with Aluminum foil (MTI Corp.) as the current collector, rolled sodium metal as the counter electrode (Sigma Aldrich, $\geq 99\%$), and Celgard 2325 as the separator. The electrolytes were made using battery-grade sodium hexafluorophosphate (NaPF_6) salt from STREM Chemicals dissolved in dimethoxyethane (DME) from Sigma Aldrich (anhydrous, 99.5%), and in 1:1 wt.% ratio ethylene carbonate (EC) and dimethyl carbonate (DMC) solvent from GOTION (battery-grade). The molar concentration of NaPF_6 was kept constant at 1 M for all electrolytes. The sodium was

plated at a current rate of $0.5 \text{ mA}\cdot\text{cm}^{-2}$ for a total capacity of $1 \text{ mA}\cdot\text{cm}^{-2}$ and was stripped at the same current rate with a cut-off voltage of 1 V.

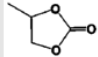
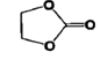
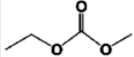
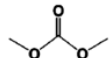
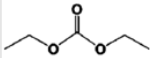
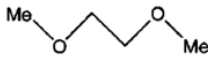
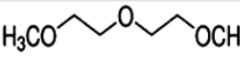
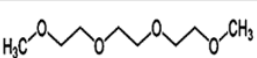
The electrochemical performance of electroplated sodium versus NCO cathode was tested using CR2032 coin cells. The electroplated sodium initially was prepared in our custom-made pressure setup and then used as anode in the coin-cell setup. Pure O3-type NCO powder was synthesized using a solid-state synthesis method and used as the active material in cathode electrode. The cathode electrodes were prepared by casting the slurry (80 wt% NCO, 10 wt% super C65 conductive agent, and 10 wt% polyvinylidene fluoride (PVDF) binder) on Al foil and then dried overnight at 80°C under vacuum. The NCO theoretical capacity was considered as $120 \text{ mAh}\cdot\text{cm}^{-2}$ in C-rate study. A controlled amount of $55 \mu\text{L}$ of 1M NaPF_6 in DME was used as the electrolyte. Detailed summary information of the coin-cell testing specifications are presented in Table 6.2.

6.3. Results and Discussion

6.3.1. Impact of electrolyte compositions on ICE of Na metal anode

Current battery research depends heavily on the use of ether- and carbonate-based electrolytes. Some of the most used carbonate solvents are propylene carbonate (PC), ethylene carbonate (EC), dimethyl carbonate (DMC) or fluoroethylene carbonate (FEC), while dimethoxyethane (DME), diethylene glycol dimethyl ether (DEGDME/diglyme), and tetraethylene glycol dimethyl ether (TEGDME) are widely used ethers. A summary of some physical properties of common carbonate- and ether- based solvents are presented in Table 6.1.

Table 6-1. The physical properties of the common carbonate- and ether- based solvents. Abbreviations: PC, EC, EMC, DMC, DEC, DME, DEGDME, TEGDME.

		Chemical Structure	Viscosity (η) [cP at 25°C]	Dielectric Constant (ϵ at 25°C)	Melting Point (T_m) [°C]	Boiling Point (T_b) [°C]	Flash Point (T_f) [°C]
Carbonate-based	PC		2.53	64.92	-48.8	242	132
	EC		1.9	89.78	36.4	248	160
	EMC		0.65	2.958	-53	110	
	DMC		0.59	3.107	4.6	91	18
	DEC		0.75	2.805	-74.3	126	31
Ether-based	DME		0.46	7.18	-58	84	0
	DEGDME		1.06	7.4	-61	162	57
	TEGDME		3.39	7.53	-46	216	111

As these solvents possess different dielectric constant, viscosity, and chain length, the solvation energy and thus the reactivity of solvated Na^+ would be different. In order to investigate the impact of solvents and salts on the ICE of Na metal anode, Na plating and stripping was performed with different solvent and salt combinations. Aluminum foil was used as the current collector for the Na plating/stripping experiment with rolled Na metal as the counter electrode. All the experiments were performed in the coin-cell configuration with an expected internal pressure of about 150 kPa. The obtained results reveal that ether-based electrolytes can enable high ICE (~60–80%), regardless the nature of the salt.

On the other hand, the ICE in carbonate electrolytes is rather poor and an additive, e.g., FEC, is required to improve the performance of the cell. In a recent study on Li metal system, our group has reported that the irreversible capacity loss in the first cycle is mainly related to the dead

lithium metal due to the loss of contact with the current collector rather than SEI formation.⁸¹ These two contributions can be deconvoluted using TGC technique, in which the amount of dead metal can be quantified by measuring the amount of hydrogen gas released in the reaction with a proton source, such as water or ethanol, $M^0 + H^+ \rightarrow M^+ + \frac{1}{2} H_2 (g)$.

One major difference in the case of sodium metal compared to lithium metal is the use of aluminum (Al) as the current collector instead of copper (Cu). Al is not reactive with sodium at the reduced potentials despite the case of lithium and is widely used as the current collector in sodium ion batteries due to its higher abundance (abundance in earth's crust: 8.23% for Al and 0.0068% for Cu)⁵⁹ and lower cost than Cu. However, Al cannot be used in TGC method with water as the solvent because of the formation of the hydrofluoric (HF) acid as a side reaction of water with NaPF₆ salt or possible SEI components, such as sodium fluoride (NaF), that further can generate H₂ gas in reaction with Al.⁸² Because of this matter, we utilized ethanol (EtOH) as the solvent in TGC study for the case of sodium metal.

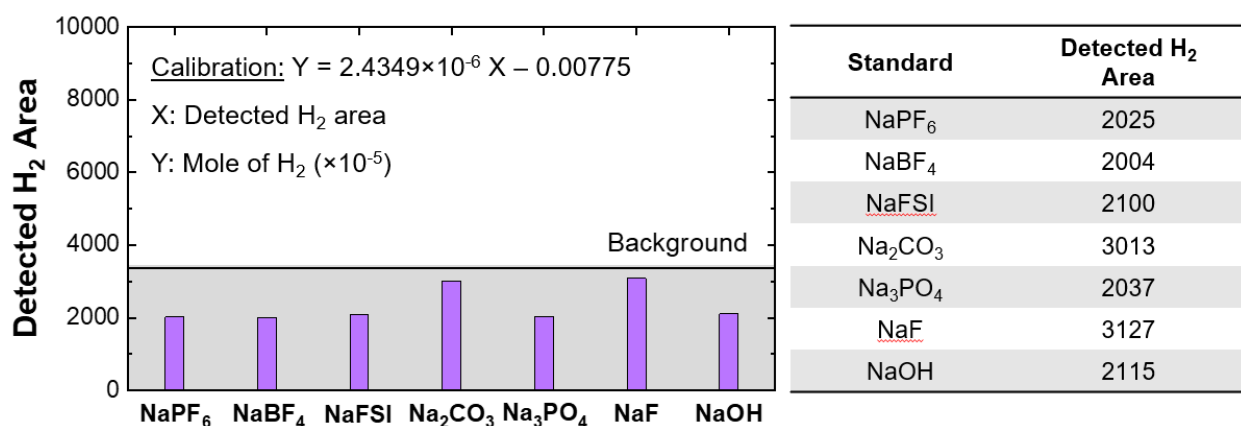


Figure 6-1. The controlled TGC experiment on standard commercial powders showed no hydrogen generation. This test was performed using ethanol as the solvent.

Furthermore, a set of controlled experiments were performed on the available commercial sodium powder standards and salts to evaluate the possible formation of H₂ gas from the other sources. The results of these controlled tests are shown in Figure 6.1.

The TGC quantification after one cycle of plating and stripping reveals that SEI formation is the main cause (~75–85%) of capacity loss for Na metal anode regardless of the solvents or salts (Figure 6.2), which is consistent with the discussions reported in previous studies.^{48,219,339}

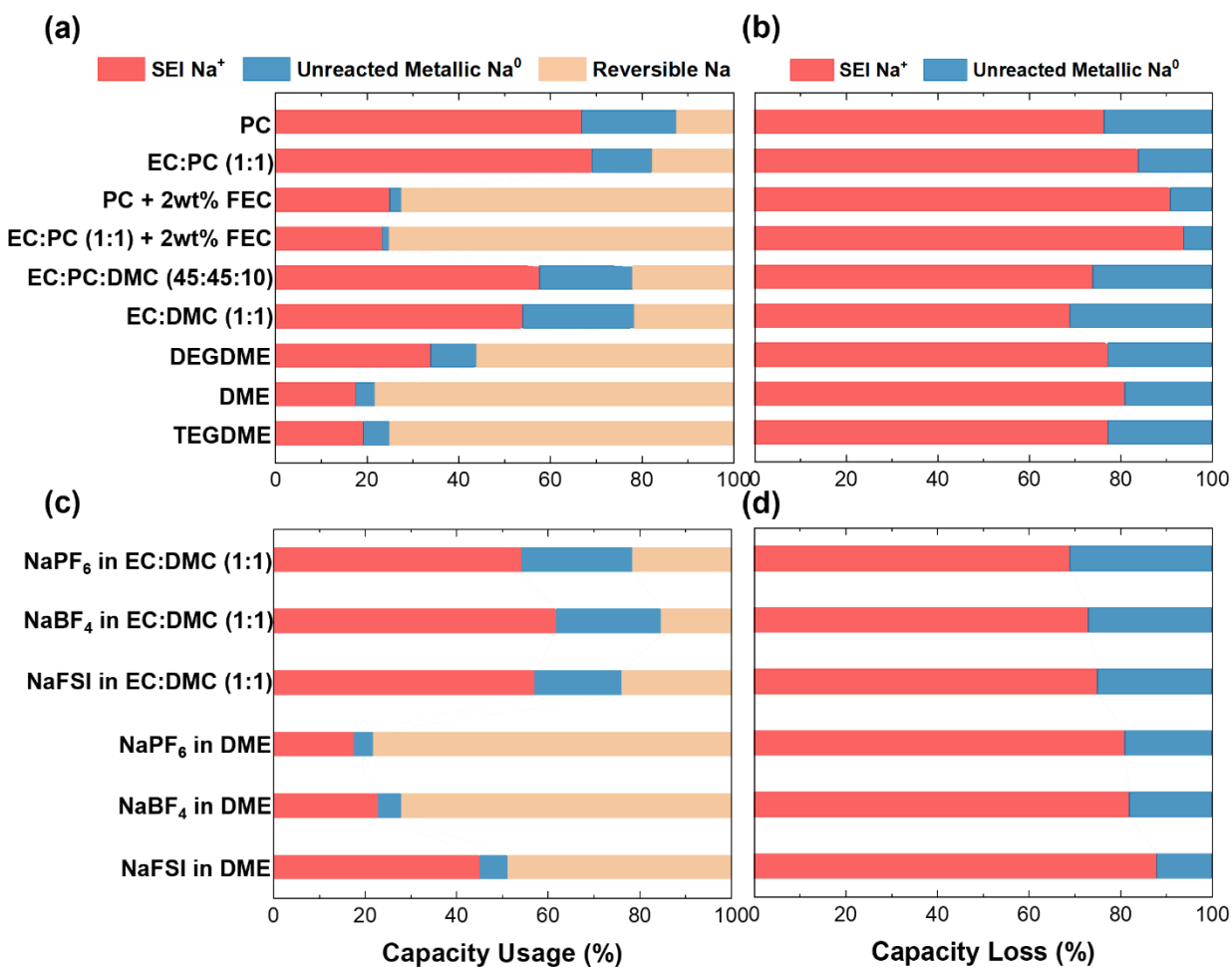


Figure 6-2. Quantification of capacity usage and capacity loss using TGC method. Analysis of capacity usage and capacity loss are shown in (a-b) using 1 M NaPF₆ in different solvents; carbonate-based and ether-based, and (c-d) using 1 M of the different salts in EC:DMC and in DME.

This behavior is completely different to that of Li, in which dead metallic Li is the main source of capacity loss. The difference is the capacity loss mechanism agrees completely with the chemistry of Li and Na, in which Na is highly reactive that can react rapidly with the electrolyte components to form SEI.

Our previous studies showed that the applied pressure can play an essential role on the ICE value of Li metal anode, two representative electrolytes for the ether- and carbonate-based families, e.g. 1M NaPF₆ in DME and 1M NaPF₆ in EC:DMC (1:1), are here chosen to demonstrate the effects of pressure on the performance of Na metal.

6.3.2. Pressure effect on the morphology and capacity usage of plated Na metal anode

In order to investigate the impact of stacking pressure, Na plating and stripping under controlled uniaxial pressure were performed using our custom-made setup^{338,340} (shown un Figure 6.3) with the applied pressure varied in the range of 10–375 kPa. After one plating and stripping cycle, the Al current collector was recovered for TGC measurement. The obtained results show a correlation between the applied axial pressure with the ICE, in which an optimum applied pressure is required to maximize the ICE values (Figures 6.4(a-b)).

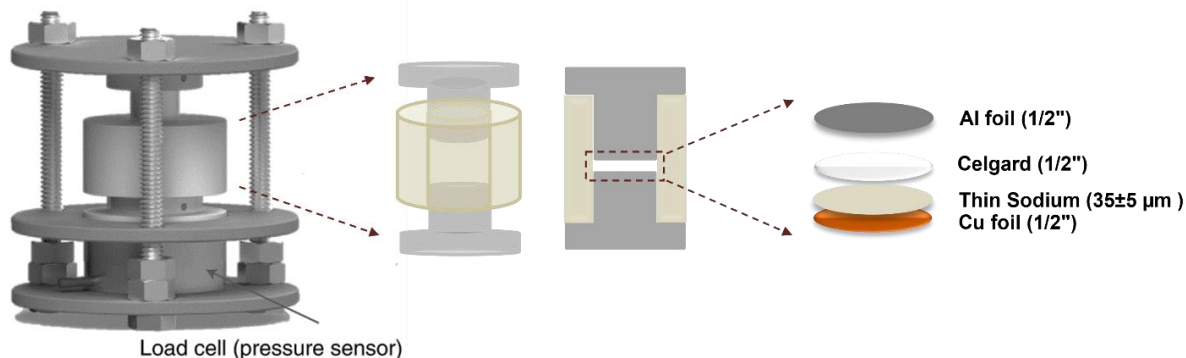


Figure 6-3. The schematic of the pressure setup and the cell components used in this study. The axial pressure was controlled using the load cell.

It should be mentioned that the increase of the uniaxial pressure above the optimal values did not help to improve the ICE. Interestingly, the optimum uniaxial stack pressure for ether-based electrolyte is lower than carbonate one, e.g., ~180 kPa vs. ~250 kPa (Figures 6.4(a–b)).

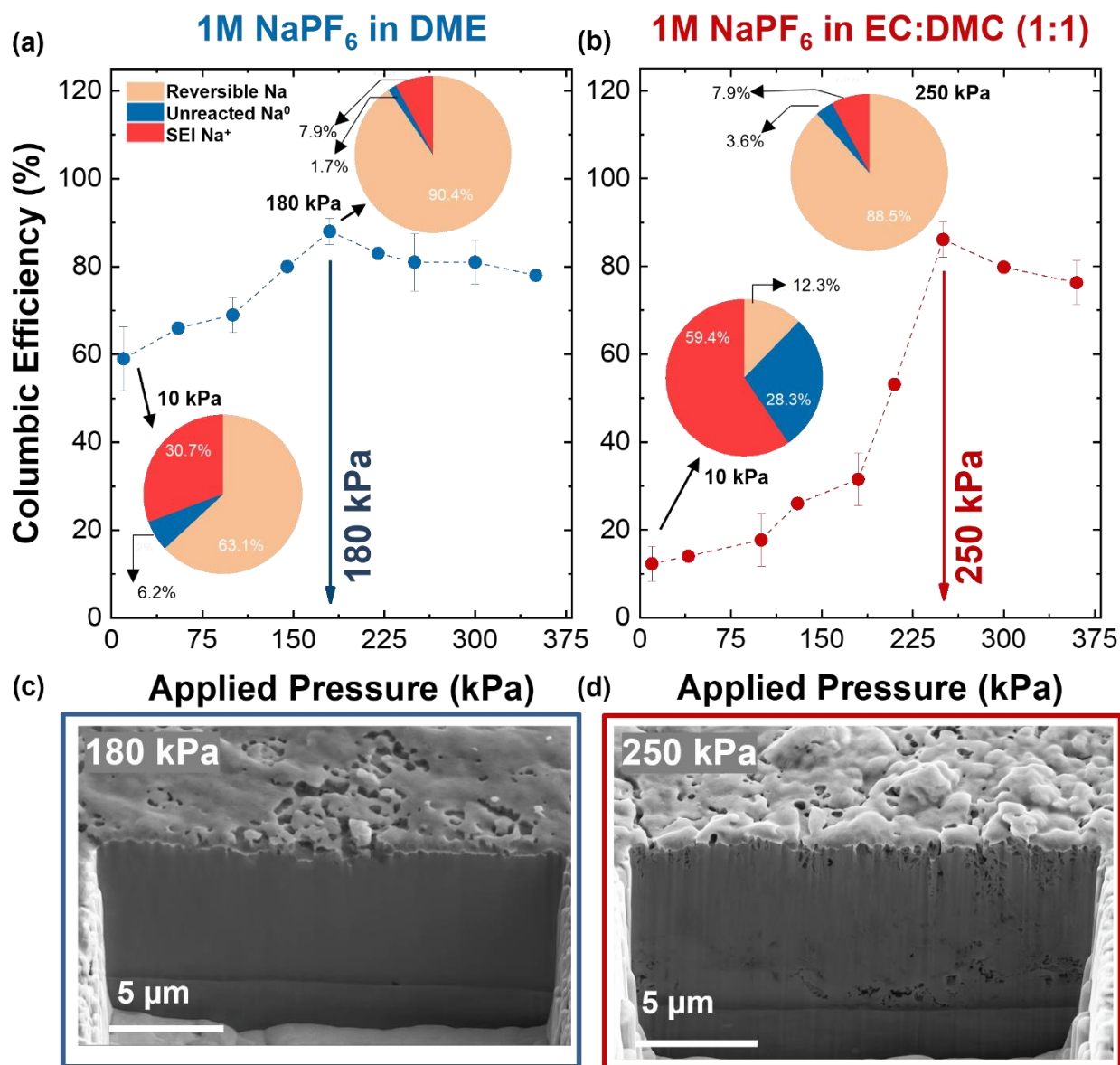
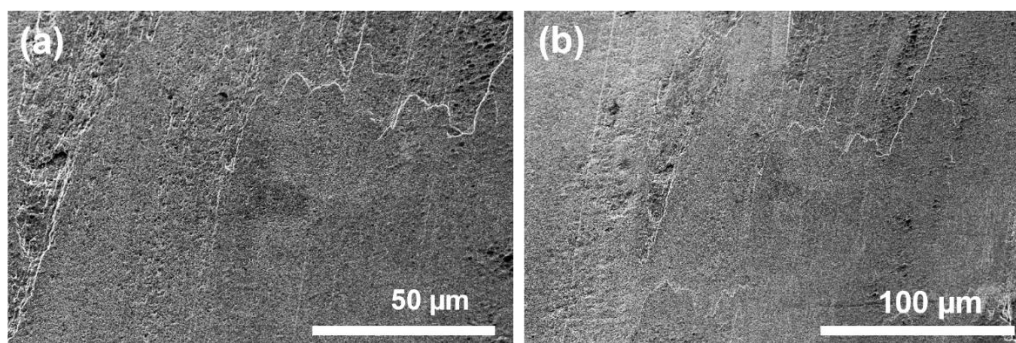


Figure 6-4. The first cycle columbic efficiency of sodium on Al foil under different applied axial pressure (a) in DME and (b) in EC:DMC electrolytes. Analysis of the capacity usage for applied axial pressures using TGC method are also shown. Cross-sectional cryo-FIB-SEM images of the plated Na at opt. pressures (c) in DME and (d) in EC:DMC.

The origin of this difference could be related to the physical and transport properties of the electrolytes, such as viscosity, solvation energy, and diffusion coefficient of Na^+ , as well as the morphology of the deposited sodium. Even at the optimum pressure, SEI formation is still the main cause of the capacity loss, which is the intrinsic property of Na metal due to its high reactivity.

The morphology of sodium metal deposited at the optimal pressure was evaluated using cryogenic focus ion beam scanning electron microscopy (cryo-FIB-SEM). Comparing to lithium, sodium is highly reactive and beam (thermal) sensitive. The beam sensitivity has been extensively discussed as one of the main limiting parameters in using electron microscopy for lithium.^{106,341,342} This extreme instability is more severe for sodium element with a lower melting point (97.7°C for sodium versus 180.5°C for lithium) and weaker atomic bonding than lithium.^{22,343}

Top view – Before Milling



Top and cross-sectional view – After Milling

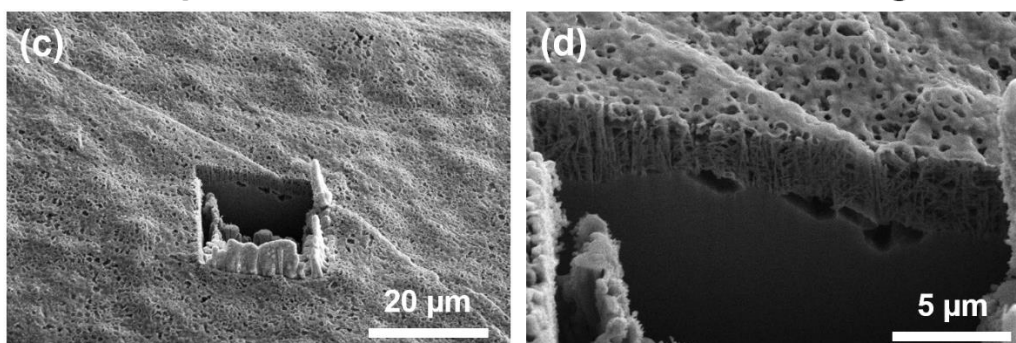
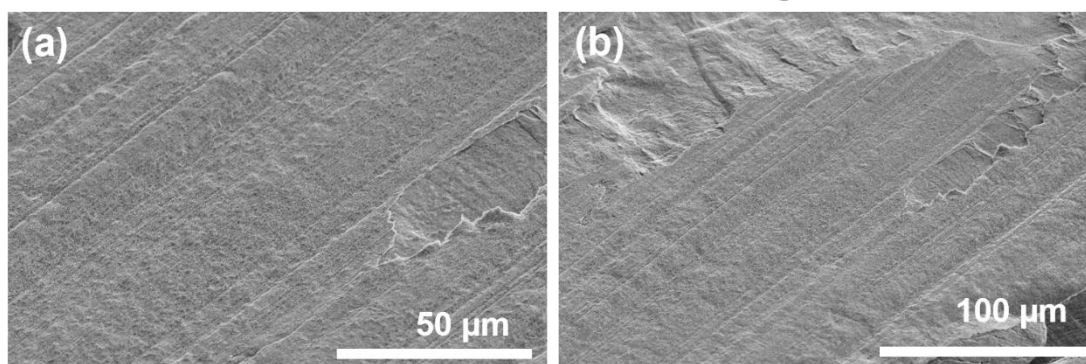


Figure 6-5. The surface of sodium is unstable at room temperature. The images at room temperature are shown for (a-b) top-view before milling, (c) top-view after milling, and (d) cross-sectional view after milling. The sample is freshly cut commercial sodium metal.

Top view – Before Milling



Top and cross-sectional view – After Milling

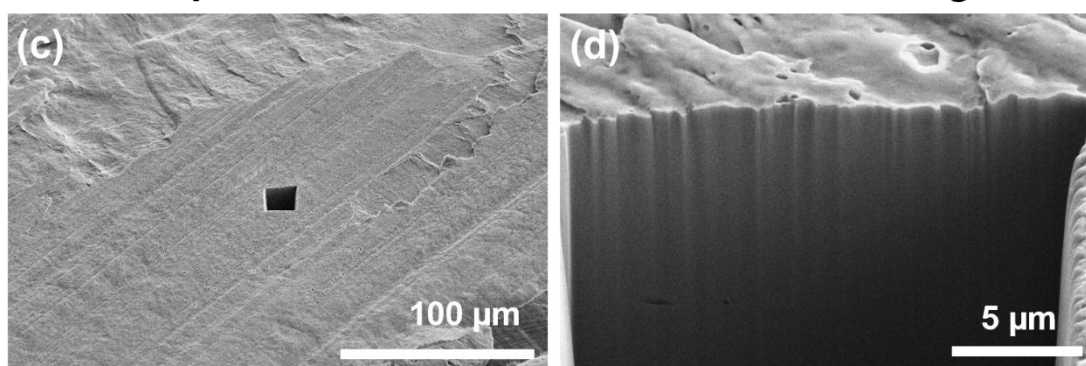


Figure 6-6. The surface of sodium is stable at cryogenic temperature. The images at cryogenic temperature are shown for (a-b) top-view before milling, (c) top-view after milling, and (d) cross-sectional view after milling. The sample is freshly cut commercial sodium metal.

Initial assessments and precautions on the necessity of using cryogenic condition for sodium metal imaging is discussed in Figures 6.5 and Figure 6.6.

The cross-sectional image of Na metal plated under optimum pressure in ether-based electrolyte shows a dense structure with no voids or porosity (Figure 6.4(c)). Similar morphology was also observed for deposited sodium in carbonate-based electrolyte under optimum pressure; however, the structure was less dense with the presence of small voids at certain areas (Figure 6.4(d)). The energy dispersive x-ray spectroscopy (EDS) elemental mappings on the cross-sectional cryo-FIB-SEM images are shown in Figure 6.7.

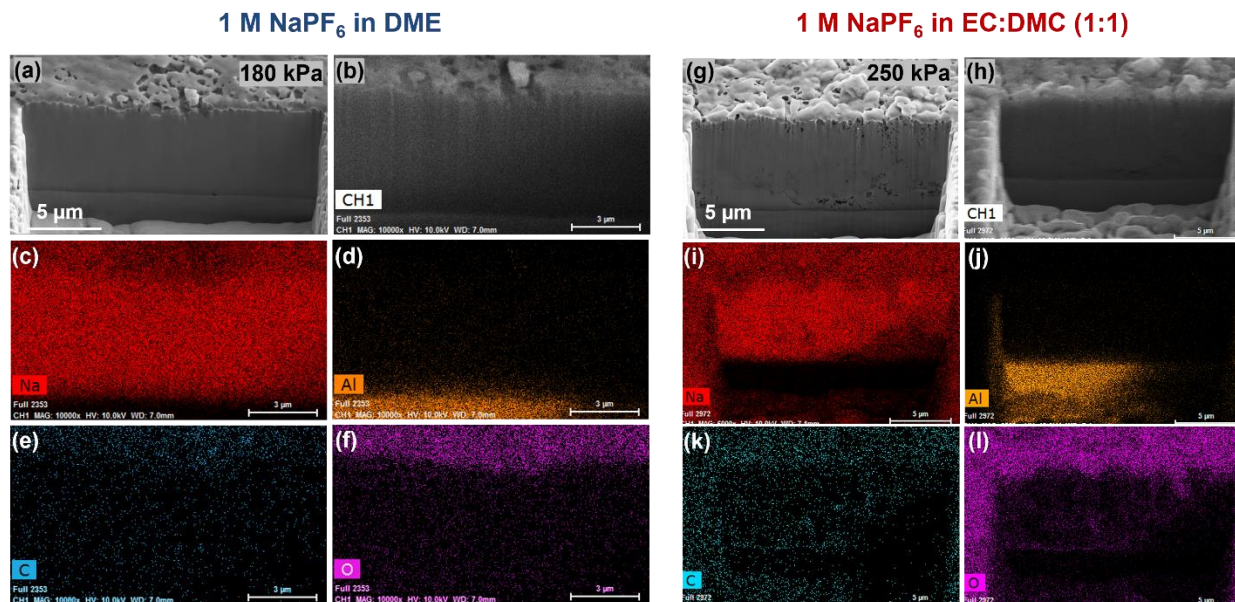


Figure 6-7. The cross-sectional cryogenic (a) FIB-SEM image of the deposited sodium in DME under 180 kPa and (b) the EDS elemental mapping in (c) Na, (d) Al, (e) C, (f) O regions. The cross-sectional cryogenic (g) FIB-SEM image of the deposited sodium in EC:DMC under 250 kPa and (h) the EDS mapping in (i) Na, (j) Al, (k) C, (l) O regions.

The top-view images of the plated sodium corresponding to Figure 6.4(c-d) are shown in Figure 6.8.

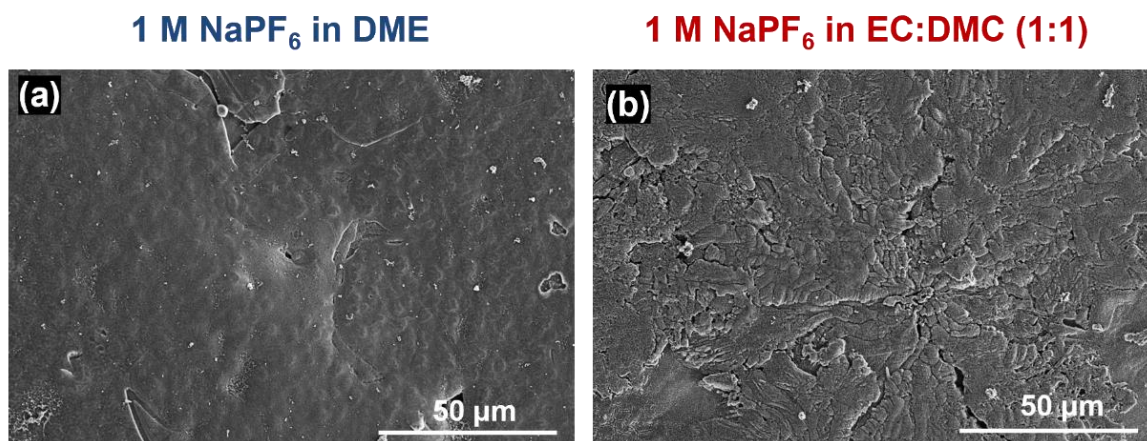


Figure 6-8. Top-view cryogenic FIB-SEM images of plated sodium surface (a) in 1M NaPF₆ in DME electrolyte under 180 kPa uniaxial pressure and (b) in 1M NaPF₆ in EC:DMC (1:1) electrolyte under 250 kPa uniaxial pressure.

The cryo-FIB-SEM image of Na metal deposited at 10 kPa shows a dense sodium metal deposition in ether-based electrolyte, however, it shows a porous structure with whisker shape sodium deposition in the carbonate-based electrolyte (Figures 6.9), which agrees with the results reported by Hong et al.³⁴⁴ for the sodium plating without applied pressure.

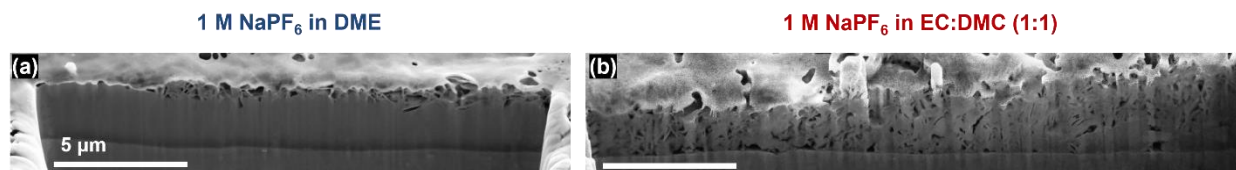


Figure 6-9. Cross-sectional cryogenic FIB-SEM images of the plated sodium at 10 kPa uniaxial pressures (a) in 1M NaPF₆ in DME electrolyte and (b) in 1M NaPF₆ in EC:DMC (1:1) electrolyte. The sodium was plated at 0.5 mA/cm² for 0.1 mAh/cm² on Al foil.

Further at 10 kPa, thick sodium leftovers were visible after the stripping (Figure 6.10 for the case of 1M NaPF₆ in EC:DMC (1:1) and Figure 6.11 for the case of 1M NaPF₆ in DME) in carbonate-based electrolyte which agrees with the low ICE of the cell (<20%). At 250 kPa, less sodium leftovers and more porous structure were observed after the stripping in agreement with higher ICE of the cell (~85%) (Figure 6.4). The porous network after stripping was a consequence of inhomogeneous SEI distribution in the plated Na layer. This porous structure and considerable residues at low pressures indicate a poor connection to Al current collector and further leads to the loss of the electronic conductive pathway.

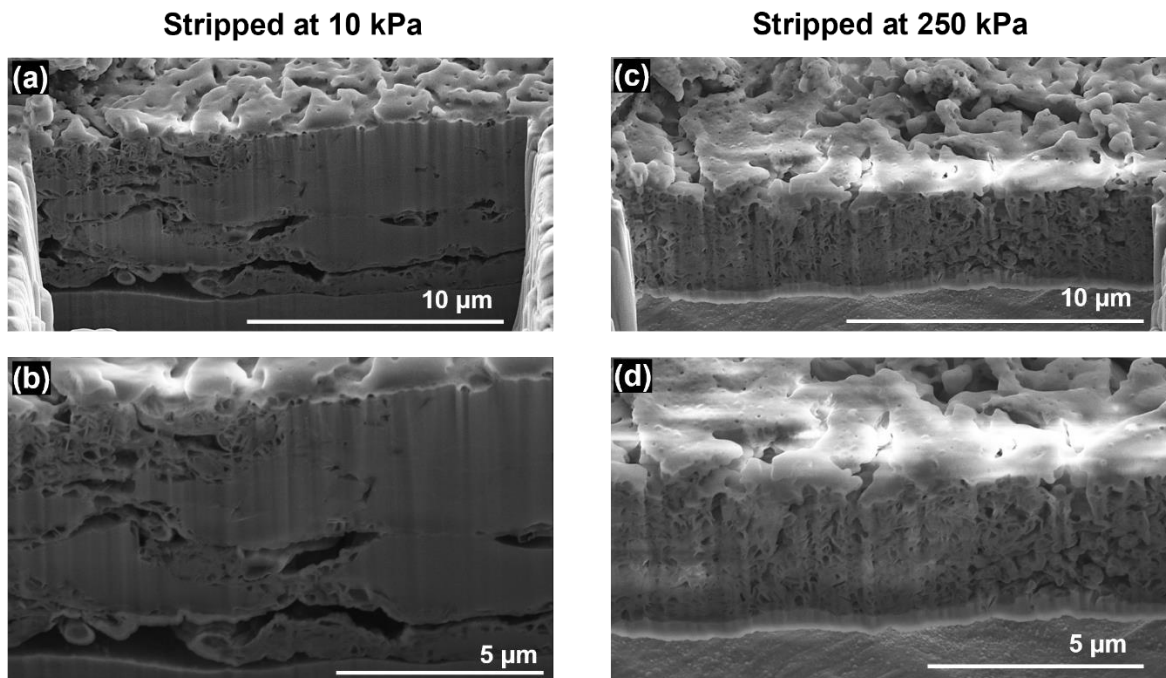


Figure 6-10. Top-view and cross-sectional cryogenic FIB-SEM images of stripped sodium in 1M NaPF₆ in EC:DMC (1:1) electrolyte at (a-b) 10 kPa and (c-d) 250 kPa. The sodium was plated at 0.5 mA/cm² for 1 mAh/cm² on Al foil at 250 kPa uniaxial pressure and stripped to 1V at 0.5 mA/cm².

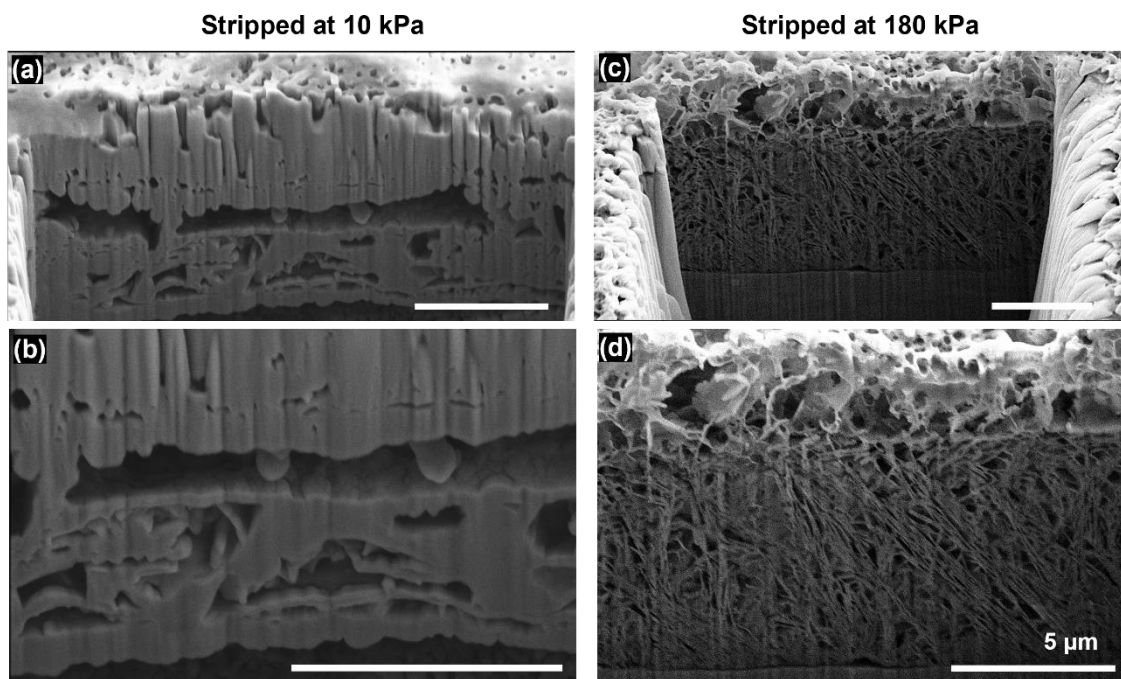


Figure 6-11. The cross-sectional cryogenic FIB-SEM images of the stripped sodium in 1M NaPF₆ in DME electrolyte under 180 kPa. The sodium was plated at 0.5 mA/cm² for 1 mAh/cm² on Al foil at 180 kPa uniaxial pressure and stripped to 1V at 0.5 mA/cm².

These observations indicate that applied uniaxial pressure greatly impacted the sodium nucleation and further facilitated the lateral growth on the surface of Al current collector (Figure 6.12, case of plated sodium at 10 kPa). One of the reasons for the difference in the morphology of the plated sodium at controlled pressure is the change of free energy stimulated by the compressive stress between nuclei and electrolyte/separator interface.³⁴⁵

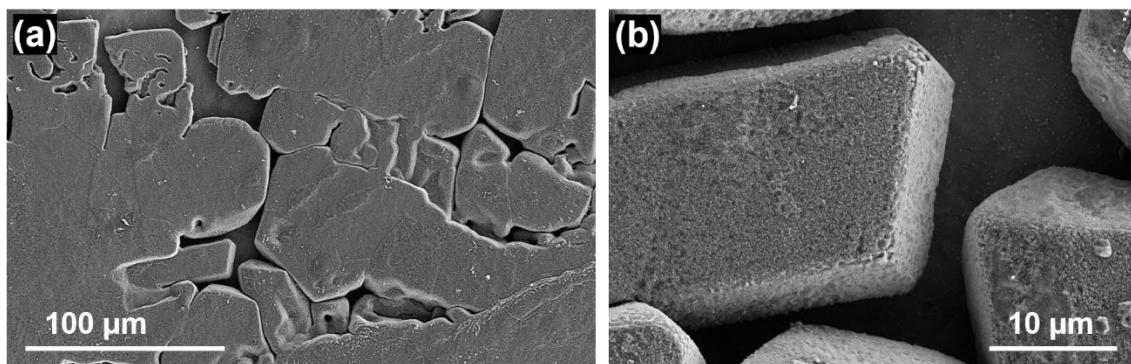


Figure 6-12. Top-view cryogenic FIB-SEM images of plated sodium in 1M NaPF₆ in DME electrolyte under 10 kPa. The sodium was plated at 0.5 mA/cm² for 1 mAh/cm² on Al foil at 10 kPa uniaxial pressure.

The cross-sectional cryogenic FIB-SEM images of plated sodium under different applied uniaxial pressure are shown in Figure 6.13 for 1M NaPF₆ in DME and in Figure 6.14 for 1M NaPF₆ in EC:DMC (1:1).

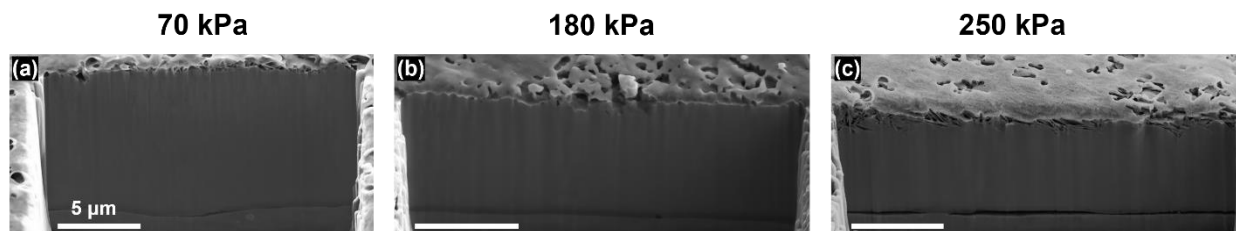


Figure 6-13. Cross-sectional cryogenic FIB-SEM images of the plated sodium in 1M NaPF₆ in DME electrolyte under the uniaxial pressures of (a) 10 kPa, (b) 70 kPa, (c) 120 kPa, (d) 180 kPa, and (e) 250 kPa. The sodium was plated on Al foil at 0.5 mA/cm² for 0.1 mAh/cm² in (a) and for 1 mAh/cm² in (b-e). The scale bars are 5 μm.

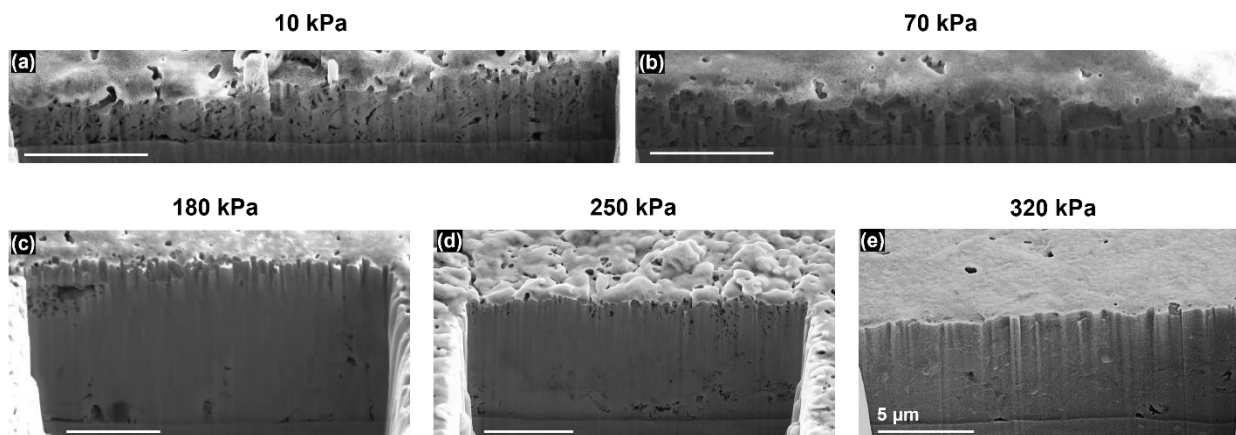


Figure 6-14. Cross-sectional cryogenic FIB-SEM images of the plated sodium in 1M NaPF₆ in EC:DMC electrolyte under the uniaxial pressures of (a) 10 kPa, (b) 70 kPa, (c) 120 kPa, (d) 180 kPa, (e) 250 kPa, and (f) 320 kPa. The sodium was plated on Al foil at 0.5 mA/cm² for 0.1 mAh/cm² in (a-b) and for 1 mAh/cm² in (c-f). The scale bars are 5 μm.

Electrochemical impedance spectroscopy (EIS) was performed to grasp a better idea of the charge transfer resistance and Na⁺ diffusion in the first cycle under different stack pressures.^{346–348} EIS measurements were compared after the first plating and then the first stripping for both lowest (10 kPa) and optimum pressures (180 kPa for 1M NaPF₆ in DME and 250 kPa for 1M NaPF₆ in EC:DMC (1:1)). The results show a significant change in the charge transfer resistance under uniaxial applied pressure, implying a difference in the thickness and composition of the SEI layer. The Nyquist plots for the as assembled, after the 1st plating, and after the 1st stripping steps at 10 kPa and optimum pressures are shown in Figure 6.15.

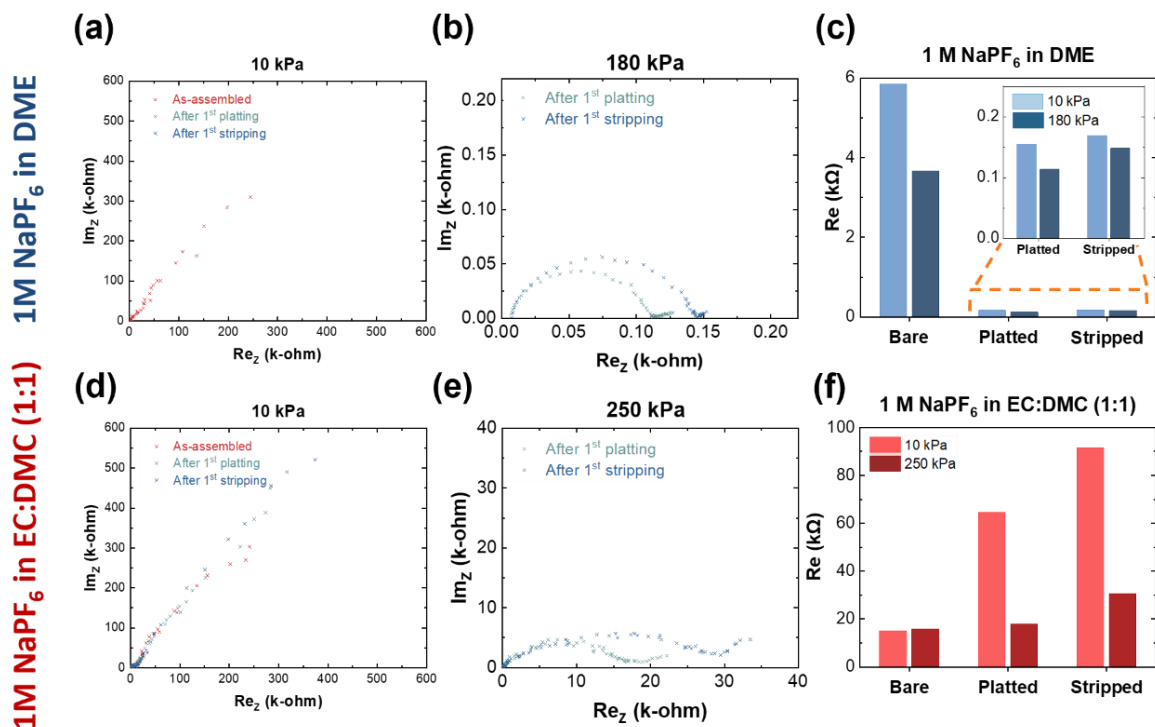


Figure 6-15. EIS measurement of Na||Al cells using both electrolytes at min. and opt. pressures at three stages. The data for DME is shown for (a) 10 kPa and (b) 180 kPa, and (c) compared in overall. The data for EC:DMC is shown for (d) 10 kPa and (e) 250 kPa, and (f) compared in overall.

The sharp increase of charge transfer resistance (from as-assembled to platted to striped) at 10 kPa in EC:DMC should be mainly due to the porous sodium deposition that makes a stronger barrier for charge transfer and can be better controlled at 250 kPa applied uniaxial pressure (Figure 6.15(f)). However, a distinct decrease in charge transfer resistance (from as-assembled to platted) in DME is more in line with the dense morphology of platted sodium. Further analysis of EIS data for Na⁺ diffusion demonstrates about 10⁵–10⁶ times better diffusion process in EC:DMC under optimum pressure versus about 10 times better in DME.

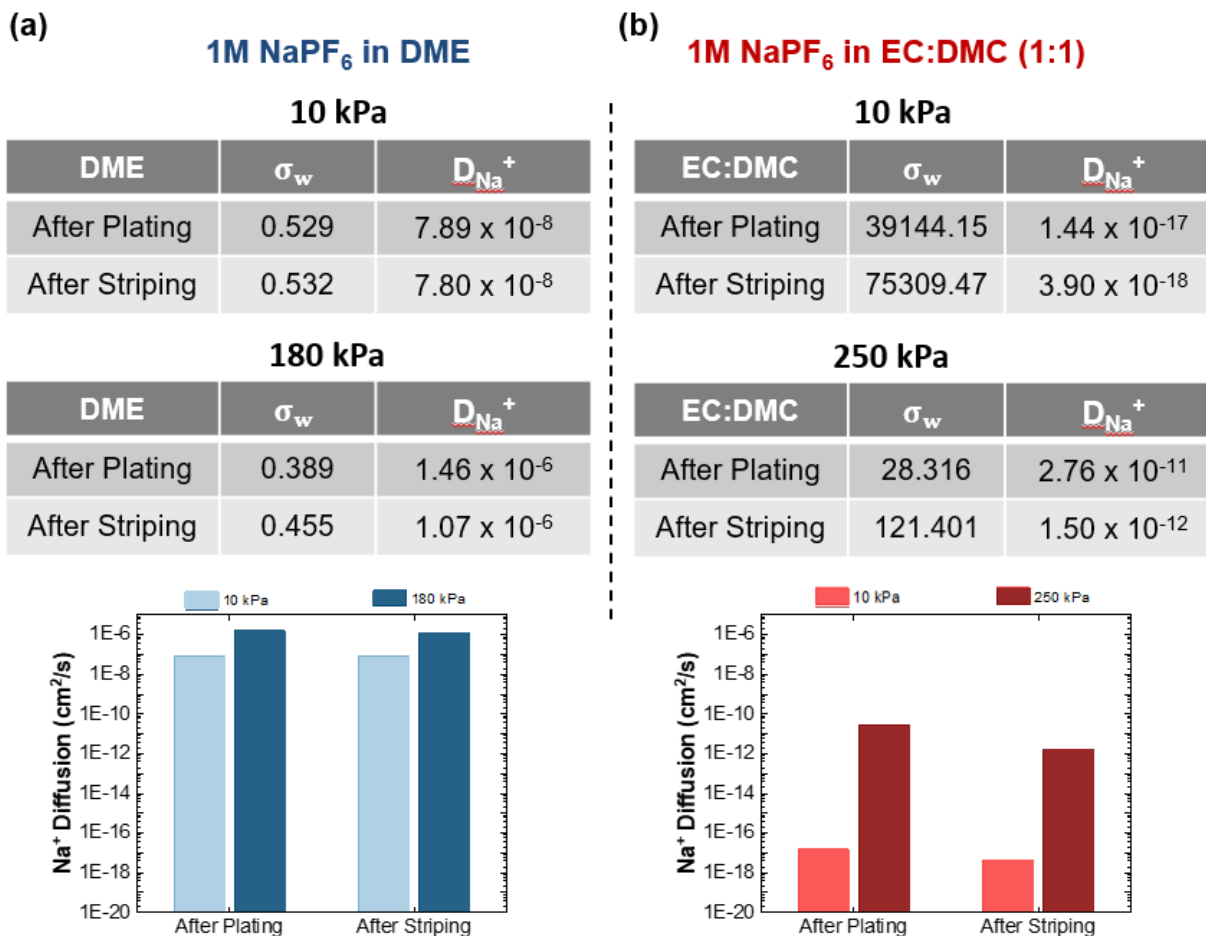


Figure 6-16. Change of ion diffusion under applied axial pressure. The results are shown for (a) 1 M NaPF₆ in DME and (b) 1 M NaPF₆ in EC:DMC (1:1) at the minimum and optimum pressures after the first plating and after the first stripping.

The details of ion diffusion calculations and results are presented in Figure 6.16. In overall, lower charge transfer resistance and better ion diffusion were observed under stack pressure for both electrolytes, with a more significant effect in carbonate-based electrolyte. This observation may also be a result of the difference in the morphology of the plated Na and the SEI compositions.

6.3.3. Chemical composition of the SEI layer

Cryo-STEM, cryo-EELS, and depth profiling XPS were used to evaluate the SEI thickness and its chemical composition in both electrolytes. Depth profiling XPS was performed on the surface of the stripped sodium (after the first cycle) in both electrolytes, 1M NaPF₆ in DME and 1M NaPF₆ in EC:DMC (1:1) at the optimum pressures. The results at the core levels of carbon (C), sodium (Na), oxygen (O), fluorine (F), and phosphorus (P) are shown in Figure 6.17.

The survey spectra presented in Figure 6.18 show no other elements as contamination or impurities on the samples. The aluminum (Al) signal is generated from the current collector used in the plating/stripping experiment. The atomic ratio of each element through the depth of etching on the SEI layer is summarized in Figure 6.17(a) for 1M NaPF₆ in DME and in Figure 6.17(b) for 1M NaPF₆ in EC:DMC (1:1). The data for the first step (surface) and the last step (after five steps of etching with 60s duration of etching in each step) are shown in these figures.

Elemental evaluation in both electrolytes demonstrates a decrease in carbon content versus an increase in sodium content when moving away from the top layer of the SEI. In carbonate-based electrolyte, the presence of carbon-containing species in the SEI is more important than in ether-based one (~30% vs. ~12% for the top surface layer). More carbonyl and carboxyl species are detected in carbonate-based electrolyte, specifically at the surface of the SEI layer.

Similar amounts of fluorine were detected in the underneath layers of SEI in both electrolytes (~26% in ether- and ~29% in carbonate-based electrolyte). This content increases toward the surface of the SEI layer in ether-based electrolyte to 37% while decreases in carbonate-based electrolyte to 24%. Phosphorus content also shows higher content (~11%) closer to the surface of SEI layer in ether-based electrolyte with similar underneath content (~5-6%) in both electrolytes. In overall, the main species in fluorine and phosphorus regions are Na-F, Na-PO_xF_y, and POF₃, and PF₅. The Na-F and PF₅ species mainly originate from the direct salt decomposition of NaPF₆ through the dissociation reaction ($\text{NaPF}_6 \rightarrow \text{NaF} + \text{PF}_5$).

On the other hand, Na-PO_xF_y, -PO₄ and POF₃ are largely resulted from the decomposition of carbonyl and carboxyl groups from the solvent and the complete or incomplete hydrolysis reaction of the salt with water residues. Higher contribution of Na-F, Na-PO_xF_y, and PF₅ in SEI layer confirms a more favorable salt participation that is observed for ether-based electrolyte in sodium, fluorine, and phosphorus regions.

Moreover, despite the similar amounts of fluorine and oxygen in the inner layers of SEI in both electrolytes, the trend of the atomic ratio in these two elements is reversed. It is observed that fluorine increases while oxygen decreases toward the SEI surface in ether-based electrolyte and, in reverse; fluorine decreases and oxygen increases toward the SEI surface in carbonate-based electrolyte. The contribution of species in oxygen and fluorine regions is in good agreement with carbon and phosphorus regions.

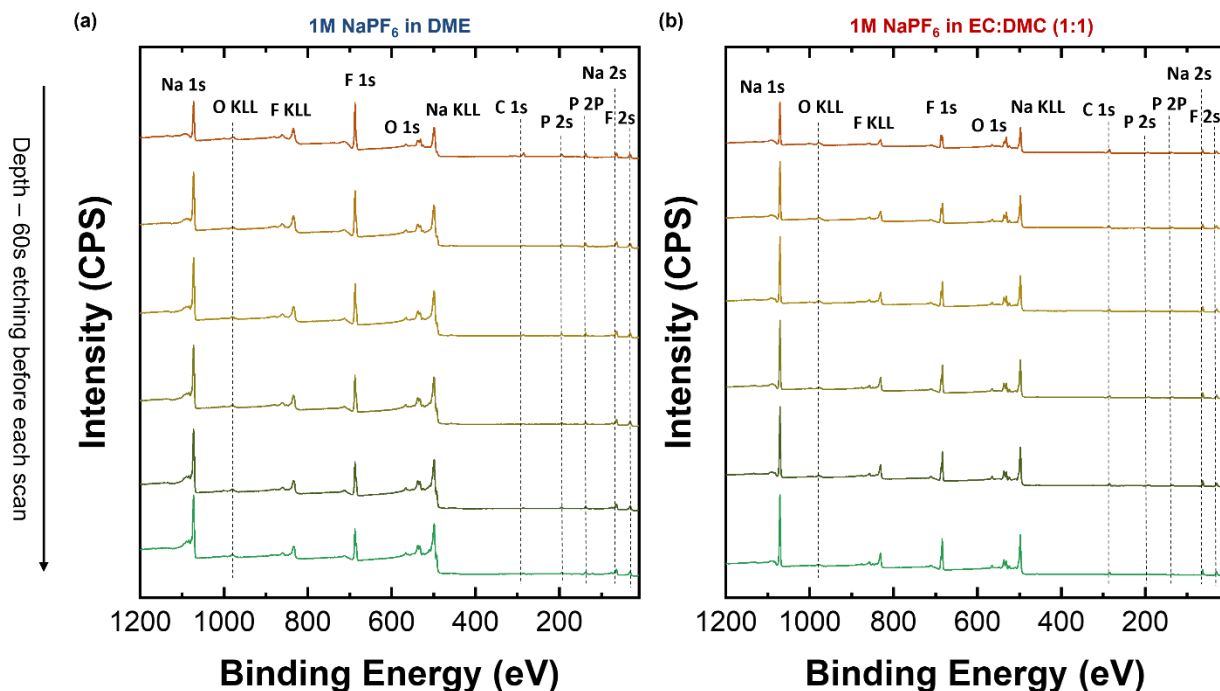


Figure 6-18. XPS spectra at different depth of etching on the stripped sodium in the binding energy range of 1200-10 eV. The spectra show the presence of Na, C, F, O, and P bonding and there is no impurity from any other elements. The data is shown for (a) 1M NaPF₆ in DME electrolyte and (b) 1M NaPF₆ in EC:DMC electrolyte.

In order to further evaluate SEI structure and chemical compositions, cryo-STEM and cryo-EELS are also performed on the stripped sodium samples. The cryo-STEM images recorded on the stripped sodium under optimum pressures show a uniform and thin SEI layer (~25–30 nm) in DME (Figures 6.19a), which is completely different to a thick and fluffy SEI layer (~1500-2000 nm) in EC:DMC (Figures 6.19b).

This observation is also in line with the difference in the charge transfer valued obtained from EIS measurements. Thicker SEI layer in carbonate-based electrolyte causes a long diffusion pathway that leads to a slow diffusion kinetic for electroplating. On the other hand, the uniform and thin SEI layer in ether-based electrolyte shortens the diffusion pathway that is a favorable factor of the system to enable efficient Na plating process. The thickness and porosity of the SEI

depends directly on the chemical composition of the layer as the components consisting of the SEI possess different stabilities, densities, and preferential growing directions of the lattice plane.

The polycrystalline nature of SEI components was analyzed by the selected area diffraction (SAED) pattern in both electrolytes (Figure 6.19(c) and Figure 6.19(d)). Crystalline Na_2CO_3 , Na_3PO_4 , NaF , NaOH/Na , and Na_2O were detected in the SEI structures.

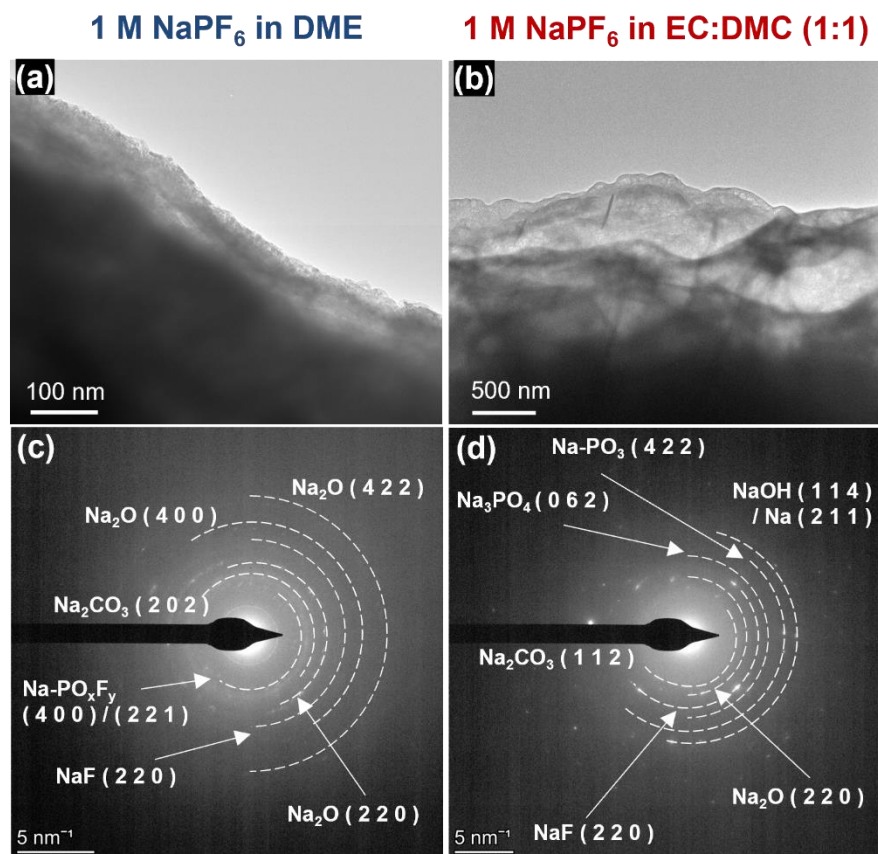


Figure 6-19. The surface characterization of SEI layer on the stripped sodium sample. The cryo-TEM of the stripped sodium (a) in 1M NaPF_6 in DME, and (b) in 1M NaPF_6 in EC:DMC (1:1). The SAED patterns show the crystalline structure of SEI components are shown in (c) 1M NaPF_6 in DME, and (d) 1M NaPF_6 in EC:DMC (1:1).

EDS chemical mapping was also performed on the SEI structures. SEI elemental composition in ether-based electrolyte (Figure 6.20) and carbonate-based electrolyte (Figure 6.21) show dominant carbon on the surface while sodium was detected more in-depth. These data are in a well agreement with depth profiling XPS results discussed earlier.

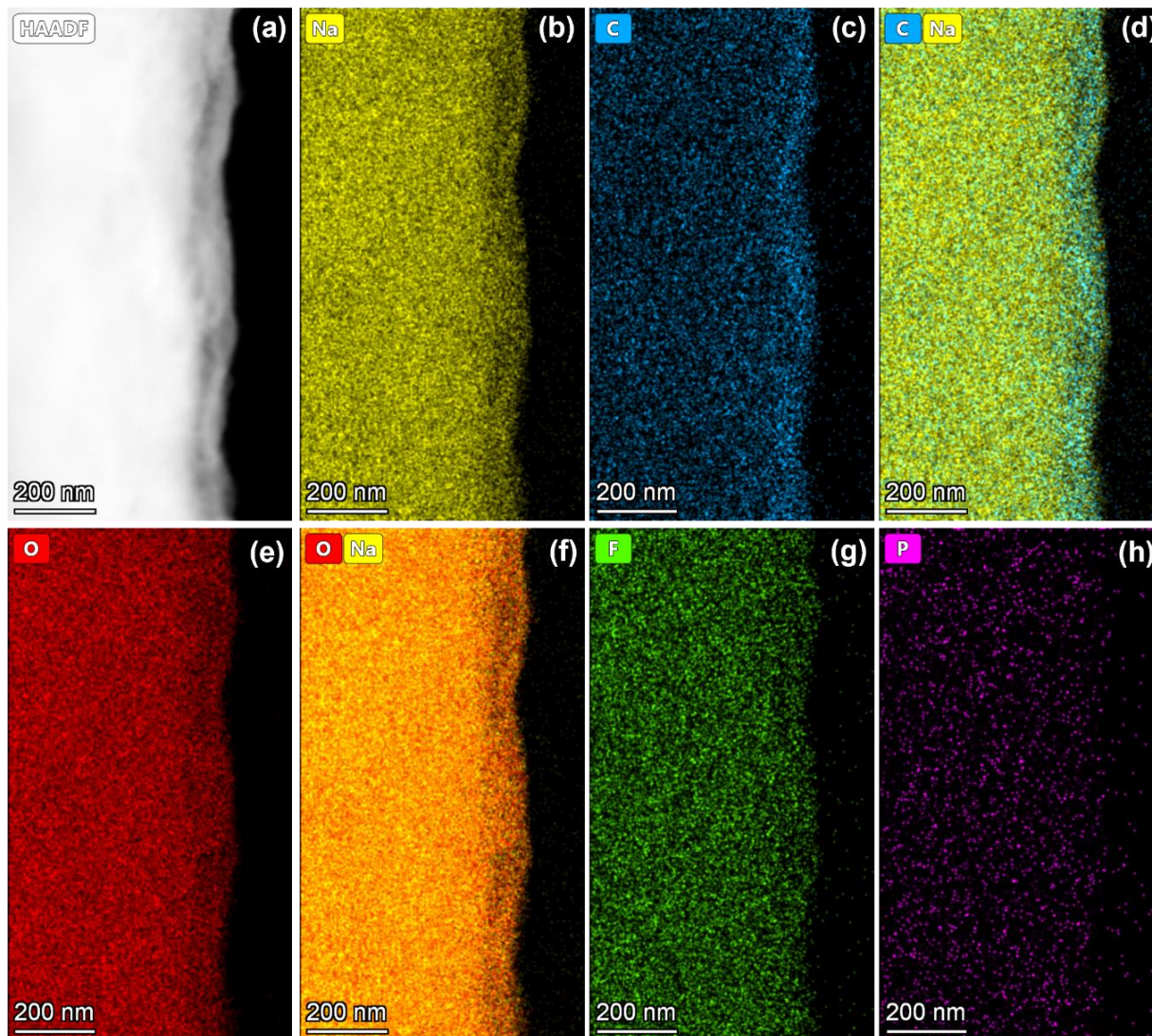


Figure 6-20. The EDS elemental mapping on the stripped sodium in 1M NaPF₆ in DME. (a) HAADF image, and elemental composition scans in (b) Na, (c) C, (d) overlaid of Na and C, (e) O, (f) overlaid of Na and O, (g) F, and (h) P regions. The sodium was plated at 0.5 mA/cm² for 1 mAh/cm² on TEM grid at 180 kPa and stripped to 1V at 0.5 mA/cm².

A detailed analysis of the SEI chemical compositions will give a better understanding on the surface chemistry of the SEI and indications on the design of new electrolytes to enable Na metal anode.

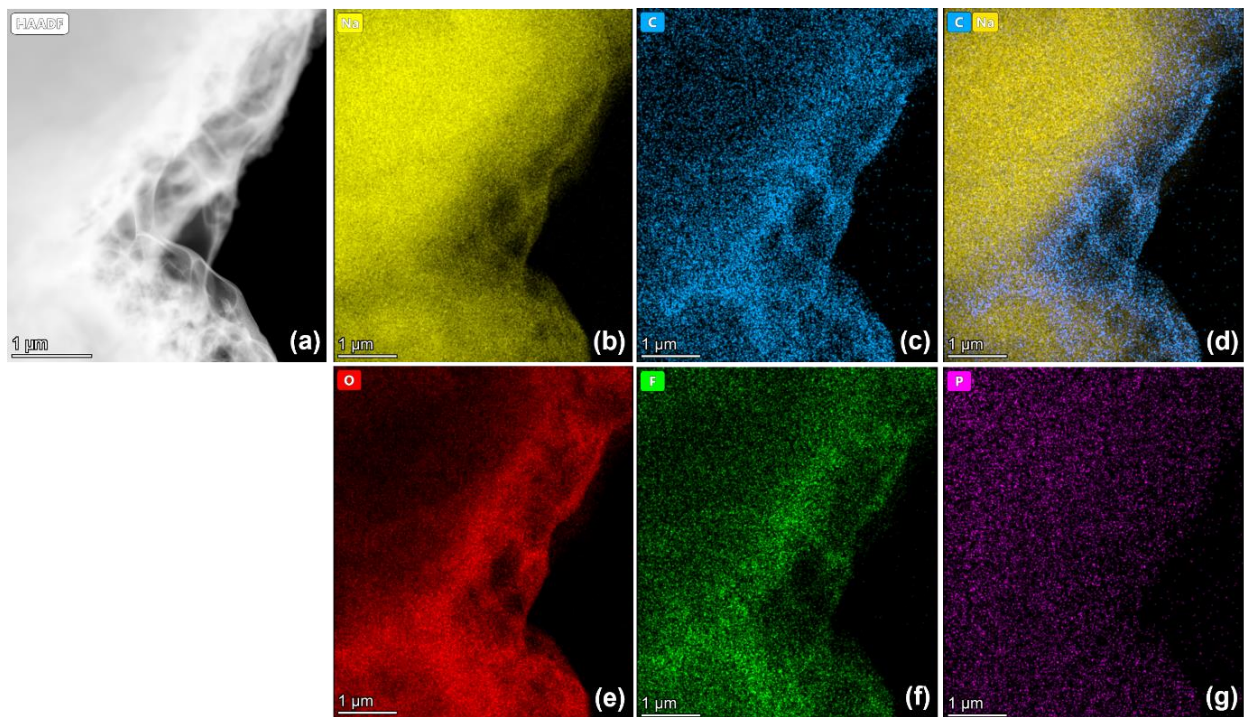


Figure 6-21. The EDS elemental mapping on the stripped sodium in 1M NaPF₆ in EC:DMC (1:1). (a) HAADF image, and elemental composition scans in (b) Na, (c) C, (d) overlaid of Na and C, (e) O, (f) F, and (g) P regions. The sodium was plated at 0.5 mA/cm² for 1 mAh/cm² on TEM grid at 250 kPa uniaxial pressure and stripped to 1V at 0.5 mA/cm².

Through the cryo-STEM, cryo-EELS, and depth-profiling XPS measurements, a uniform and thin SEI layer was detected in ether-based electrolyte in comparison with a thick and fluffy structure in carbonate-based electrolyte. Overall, the SEI layer possesses more inorganic components (rich in sodium, fluorine, and oxygen) in ether-based electrolyte as opposed to more organic species (rich in carbon and oxygen) in carbonate-based electrolyte. As most inorganic SEI components, e.g., NaF and Na₂CO₃, crystallize in close-packed structures, a thin and dense SEI

layer was observed in ether-based system. On the other hand, the organic components, e.g., esters, usually possess long organic chains that prevents the material from packing in a dense structure, and thus a fluffy and porous SEI layer was formed in carbonate-based electrolyte.

This idea is also supported by lower ionic conductivity of Na_2CO_3 (5.69×10^{-23} S/cm at 25°C) compared to Na_2O (1.47×10^{-12} S/cm at 25°C) and easier deformation of Na_2CO_3 due to lower Young and Shear Moduli (31.9 and 11.47 GPa for Na_2CO_3 vs. 76.34 and 31.2 GPa for Na_2O).

Table 6-2. Coin-cell testing specifications – Sodium-ion battery using sodium metal anode.

Coin Cell Specifications	
Cell type	CR2032
Cathode active material	NaCrO_2 – 80wt%
Binder	PVDF – 10wt%
Conductive Agent	Super C65 – 10wt%
Counter electrode	Controlled amount of electroplated sodium
Separator	<u>Celgard 2325</u>
Electrolyte	1M NaPF_6 in DME
Electrolyte amount	50 μL
Coin cell setup	0.5 mm thick SS spacer and one spring at the cathode side 0.5 mm thick SS space at the anode side
Voltage range	2-3.6 V
Active material loading	10-15 mg/cm^2
Applied current density	C/3 (based on 120 <u>mAh/g</u> theoretical capacity)

6.3.4. Electrochemical evaluation

Uniaxial pressure has been shown as a powerful knob to control the morphology of plated Na in organic electrolytes. Under the optimum pressure, a dense Na layer with a favorable composition, uniform and thin SEI layer can be obtained from 1M NaPF₆ in DME electrolyte. Such conditions might enable long-term cycling batteries with a controlled amount of Na metal anode. To demonstrate this concept, Na||1M NaPF₆ in DME||NaCrO₂ cells (Table 6.2) were assembled and tested at different conditions. The Na anode was electroplated on a carbon-coated aluminum under the optimum pressure of 180 kPa and the current rate of 0.5 mA·cm⁻² in 1M NaPF₆ in DME electrolyte using our custom-made pressure. Pure O3 NaCrO₂ (Figure 6.22) synthesized by a solid-state synthesis method³⁴⁹ was used as the active material in the cathode.

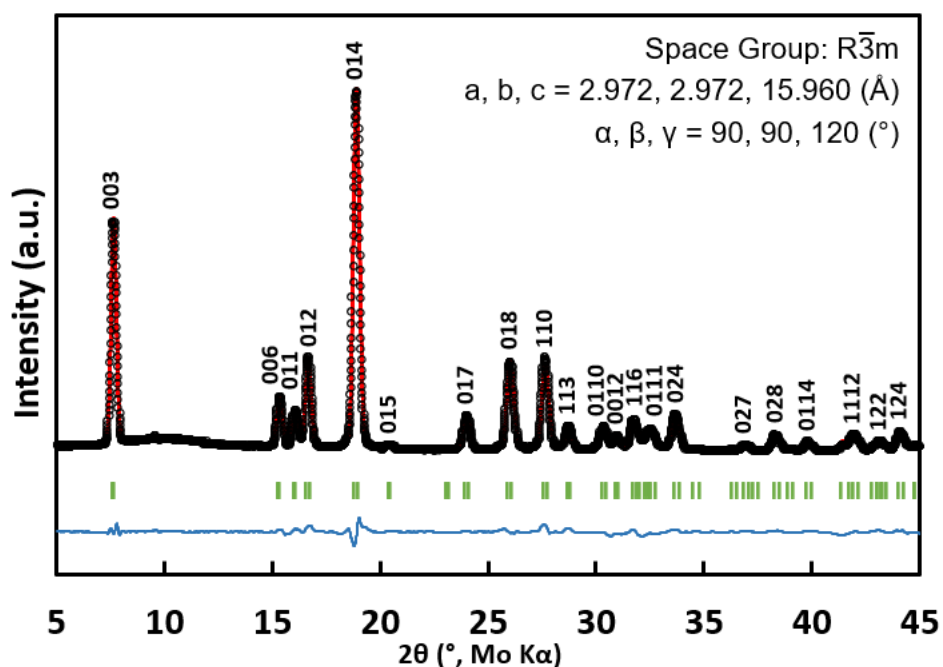


Figure 6-22. The XRD pattern shows the pure O3 phase of NaCrO₂ cathode material.

The amount of electroplated sodium is calculated to meet the sodium metal as 100% excess to cathode active material. The controlled electroplated sodium was then used as anode in a coin-cell with NCO cathode and DME-based electrolyte.

It should be noted that the applied pressure inside a coin-cell is about 150 kPa³³⁸ that is around the optimum value for sodium deposition in the ether-based electrolyte, and an ICE of above 80% should be obtained for Na metal anode in the coin-cell setup. The electrochemical performance of the cell over 500 cycles (at C/3 current rate) is presented in Figure 6.23. The cell shows an average columbic efficiency of 99.69% and capacity retention of 83.1%.

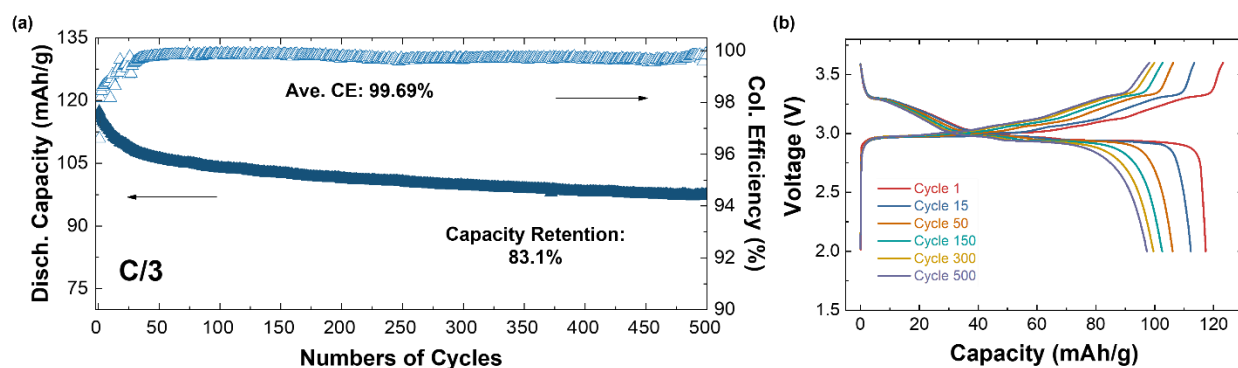


Figure 6-23. The electrochemical performance of the cell. The cells have controlled 100% excess sodium anode. **(a)** Discharge capacity (mAh/g) and columbic efficiency (%) versus numbers of cycles at the rate of C/3. **(b)** The representative voltage profiles.

At 40°C, the cell shows an ICE of 95.08% at C/3 and an average columbic efficiency of 99.68% with capacity retention of 96.29% (Figure 6.24).

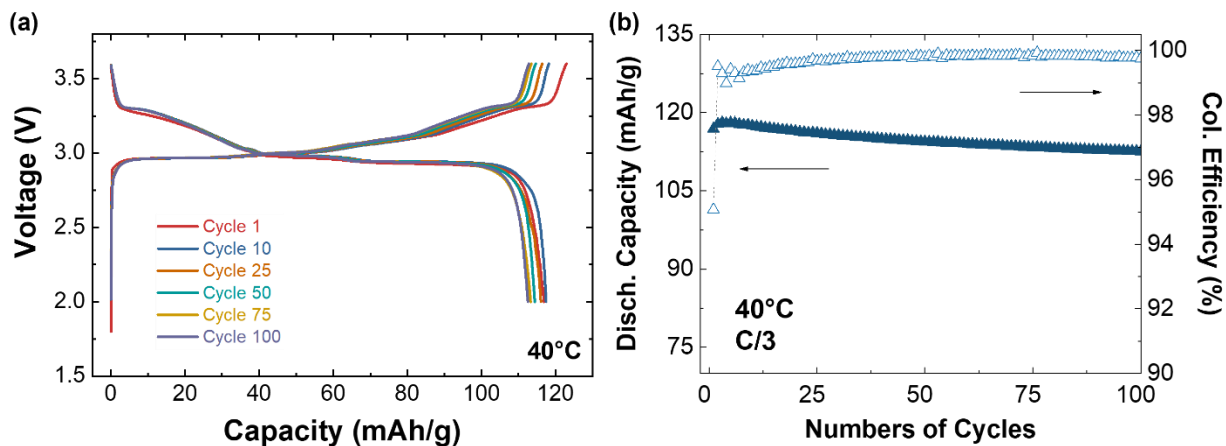


Figure 6-24. The electrochemical performance of the cell. (a) Discharge capacity (mAh/g) and columbic efficiency (%) versus numbers of cycles at 40°C temperature at the rate of C/3. (b) The representative voltage profiles.

The electrochemical performance of this system was evaluated at different current rates (at C/10, C/5, C/3, C/2, 1C, and 2C) and the voltage profiles are presented in Figure 6.25. The obtained results indicate that the cells can operate at high current rates with negligible capacity loss.

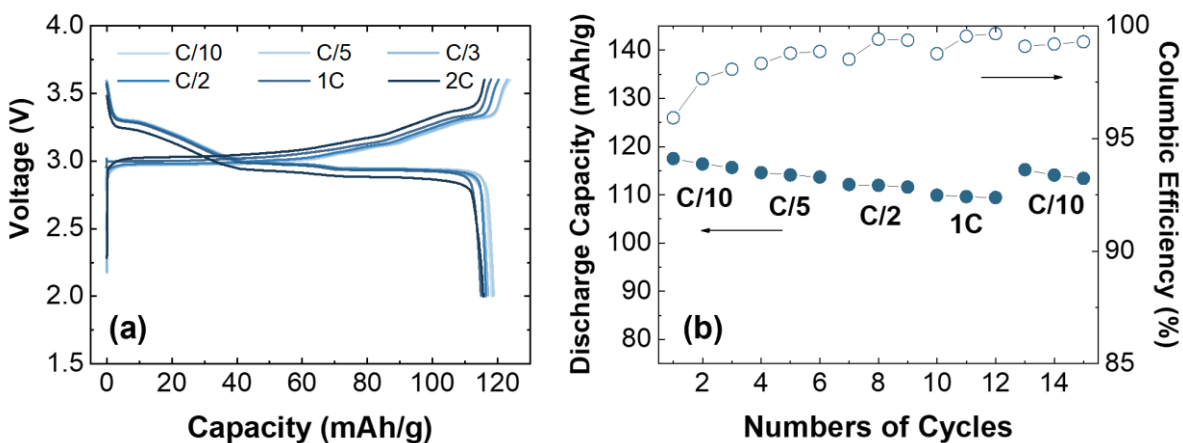


Figure 6-25. The electrochemical performance of the cell. The cells have controlled 100% excess sodium anode. (a) The first cycle voltage profiles of cell at different C rates of C/10, C/5, C/3, C/2, 1C, and 2C. (b) Rate capability evaluation at room-temperature.

The self-discharge was also evaluated for the system. The details and the rate of self-discharge is presented in Figure 6.26. The results show a sharp drop in the capacity in the first 10–20 days of the test and then this drop goes slower. An 11% of self-discharge rate observed in the first 30 days and the value was raised to about 17% after 90 days.

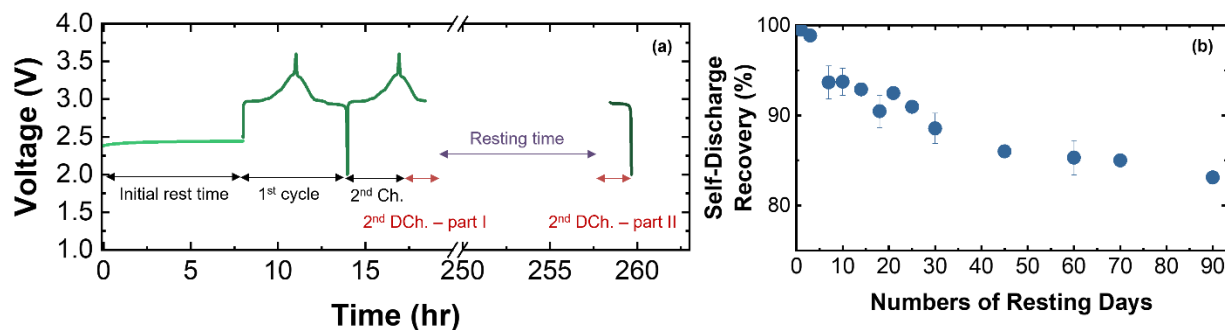


Figure 6-26. The electrochemical performance of the cell consisting of controlled electroplated sodium as the anode, NaCrO_2 as the cathode, and 1M NaPF_6 in DME as the electrolyte. The cells have controlled 100% excess sodium anode. **(a)** The self-discharge protocol. **(b)** The Self-discharge recovery of the cell at room-temperature.

6.4. Conclusions

In this study, the impact of uniaxial pressure on the growth of sodium metal in carbonate- and ether-based electrolytes were carefully investigated. For each system, there exists an optimum pressure, at which the best ICE for the Na plating and stripping can be achieved. Regardless of the nature of the solvent, the optimum pressure for Na is much lower than Li, which could be attributed to the low Young's modulus of Na metal. As indicated by cryogenic FIB-SEM images, this improved performance was enabled through the formation of a dense electroplated Na layer at the optimum pressure.

Regardless of the applied pressure value, it has been elucidated that SEI formation was the main cause of capacity loss for Na metal anode, which is consistent with the high reactivity of Na

metal. Through the use of cryogenic TEM and depth profiling XPS, the SEI thickness and its chemical compositions have been shown to depend strongly on the type of salt and solvent employed in the electrolyte. Ether-based electrolytes will enable a thin and dense SEI while a fluffy and porous SEI is formed in carbonate-based ones. In order to enable Na metal anode for practical applications, two essential parameters must be taken into account: (i) uniaxial pressure which controls the thickness of the electroplated Na layer, and (ii) nature of the solvent and salt which has direct impact on the thickness and chemical compositions of the SEI layer. With this approach in mind, the performance of sodium ion batteries using a controlled amount of sodium metal anode was demonstrated. The system exhibits a long cycle life with excellent capacity retention and rate capability. Such findings contribute significantly to the practical development of the next generation of sodium ion technologies.

6.5. Acknowledgment

Chapter 6 in part is currently being prepared for submission for publication of the material. Sayahpour, Baharak; Lu, Bingyu; Bai, Shuang; Han, Bing; Chen, Yu-Ting; Li, Weikang; Deysheer, Grayson; Chouchane; Mehdi, Parab, Saurabh; Ridley, Phillip; Raghavendran, Ganesh; Nguyen, Long H. B.; Zhang, Minghao; Meng, Ying Shirley. The dissertation author was the primary researcher and author of this material.

REFERENCES

- (1) Linden, D.; Reddy, T. B. *Handbook of Batteries*; McGraw-Hill books, 2001.
- (2) Zhang, Q.; Takeuchi, K. J.; Takeuchi, E. S.; Marschilok, A. C. Progress towards High-Power Li/CF_x Batteries: Electrode Architectures Using Carbon Nanotubes with CF_x. *Phys. Chem. Chem. Phys.* **2015**, *17* (35), 22504–22518. <https://doi.org/10.1039/C5CP03217B>.
- (3) Bock, D. C.; Marschilok, A. C.; Takeuchi, K. J.; Takeuchi, E. S. Batteries Used to Power Implantable Biomedical Devices. *Electrochim. Acta* **2012**, *84*, 155–164. <https://doi.org/10.1016/j.electacta.2012.03.057>.
- (4) Wang, D.; Wang, G.; Zhang, M.; Cui, Y.; Yu, J.; Shi, S. Composite Cathode Materials for Next-Generation Lithium Fluorinated Carbon Primary Batteries. *J. Power Sources* **2022**, *541* (May), 231716. <https://doi.org/10.1016/j.jpowsour.2022.231716>.
- (5) Linden, D.; Reddy, T. *Handbook of Batteries - 3rd Ed.*; 2002. <https://doi.org/10.5860/choice.33-2144>.
- (6) Yue, H.; Zhang, W.; Liu, H.; Liu, Z.; Zhong, G.; Yang, Y. Synthesis and Characterization of Fluorinated Carbon Nanotubes for Lithium Primary Batteries with High Power Density. *Nanotechnology* **2013**, *24* (42), 424003. <https://doi.org/10.1088/0957-4484/24/42/424003>.
- (7) Lam, P.; Yazami, R. Physical Characteristics and Rate Performance of (CF_x)_n (0.33 < x < 0.66) in Lithium Batteries. *J. Power Sources* **2006**, *153* (2), 354–359. <https://doi.org/10.1016/j.jpowsour.2005.05.022>.
- (8) Zhang, S. S.; Foster, D.; Read, J. A Low Temperature Electrolyte for Primary Li/CF_x Batteries. *J. Power Sources* **2009**, *188* (2), 532–537. <https://doi.org/10.1016/j.jpowsour.2008.12.030>.
- (9) U.S. Geological Survey. *Mineral Commodity Summaries 2021*; 2021.
- (10) Mayyas, A.; Steward, D.; Mann, M. The Case for Recycling: Overview and Challenges in the Material Supply Chain for Automotive Li-Ion Batteries. *Sustain. Mater. Technol.* **2019**, *19*, 1–26. <https://doi.org/10.1016/j.susmat.2018.e00087>.
- (11) Harper, G.; Sommerville, R.; Kendrick, E.; Driscoll, L.; Slater, P.; Stolkin, R.; Walton, A.; Christensen, P.; Heidrich, O.; Lambert, S.; Abbott, A.; Ryder, K.; Gaines, L.; Anderson, P. Recycling Lithium-Ion Batteries from Electric Vehicles. *Nature* **2019**, *575* (7781), 75–86. <https://doi.org/10.1038/s41586-019-1682-5>.
- (12) Minerals Yearbook - Volume 1: Metals and Minerals. *National Minerals Information Center*; 2019.
- (13) Hirsh, H. S.; Li, Y.; Tan, D. H. S.; Zhang, M.; Zhao, E.; Meng, Y. S. Sodium-Ion Batteries

- Paving the Way for Grid Energy Storage. *Adv. Energy Mater.* **2020**, 2001274, 1–8. <https://doi.org/10.1002/aenm.202001274>.
- (14) Tarascon, J. M. Na-Ion versus Li-Ion Batteries: Complementarity Rather than Competitiveness. *Joule* **2020**, 4 (8), 1616–1620. <https://doi.org/10.1016/j.joule.2020.06.003>.
- (15) Usiskin, R.; Lu, Y. Fundamentals, Status and Promise of Sodium-Based Batteries. **2021**, 6 (November). <https://doi.org/10.1038/s41578-021-00324-w>.
- (16) Slater, M. D.; Kim, D.; Lee, E.; Johnson, C. S. Sodium-Ion Batteries. *Adv. Funct. Mater.* **2013**, 23 (8), 947–958. <https://doi.org/10.1002/adfm.201200691>.
- (17) Zhao, Y.; Adair, K. R.; Sun, X. Recent Developments and Insights into the Understanding of Na Metal Anodes for Na-Metal Batteries. *Energy Environ. Sci.* **2018**, 11 (10), 2673–2695. <https://doi.org/10.1039/c8ee01373j>.
- (18) Meng, Y. S.; Srinivasan, V.; Xu, K. Designing Better Electrolytes. *Science* **2022**, 378 (6624), eabq3750. <https://doi.org/10.1126/science.abq3750>.
- (19) You, Y.; Manthiram, A. Progress in High-Voltage Cathode Materials for Rechargeable Sodium-Ion Batteries. *Adv. Energy Mater.* **2018**, 8 (2), 1–11. <https://doi.org/10.1002/aenm.201701785>.
- (20) Sayahpour, B.; Parab, S.; Science, M. LARGE-SCALE ENERGY STORAGE — PERSPECTIVE Perspective : Design of Cathode Materials for Sustainable Sodium - Ion Batteries. *MRS Energy Sustain.* **2022**, XX (0123456789), 1–15. <https://doi.org/10.1557/s43581-022-00029-9>.
- (21) Monconduit, L.; Croguennec, L. *Na-Ion Batteries*; John Wiley & Sons, Inc., 2021.
- (22) Yabuuchi, N.; Kubota, K.; Dahbi, M.; Komaba, S. Research Development on Sodium-Ion Batteries. *Chem. Rev.* **2014**, 114 (23), 11636–11682. <https://doi.org/10.1021/cr500192f>.
- (23) Lee, B.; Paek, E.; Mitlin, D.; Lee, S. W. Sodium Metal Anodes: Emerging Solutions to Dendrite Growth. *Chem. Rev.* **2019**. <https://doi.org/10.1021/acs.chemrev.8b00642>.
- (24) Liu, Y.; Merinov, B. V.; Goddard, W. A. Origin of Low Sodium Capacity in Graphite and Generally Weak Substrate Binding of Na and Mg among Alkali and Alkaline Earth Metals. *Proc. Natl. Acad. Sci. U. S. A.* **2016**, 113 (14), 3735–3739. <https://doi.org/10.1073/pnas.1602473113>.
- (25) Moriwake, H.; Kuwabara, A.; Fisher, C. A. J.; Ikuhara, Y. Why Is Sodium-Intercalated Graphite Unstable? *RSC Adv.* **2017**, 7 (58), 36550–36554. <https://doi.org/10.1039/c7ra06777a>.
- (26) Westman, K.; Dugas, R.; Jankowski, P.; Wiczorek, W.; Gachot, G.; Morcrette, M.; Irisarri, E.; Ponrouch, A.; Palac, M. R.; Tarascon, J.; Johansson, P. Diglyme Based Electrolytes for

- Sodium-Ion Batteries. **2018**. <https://doi.org/10.1021/acsaem.8b00360>.
- (27) Jache, B.; Adelhelm, P. Use of Graphite as a Highly Reversible Electrode with Superior Cycle Life for Sodium-Ion Batteries by Making Use of Co-Intercalation Phenomena. *Angew. Chemie* **2014**, *126* (38), 10333–10337. <https://doi.org/10.1002/ange.201403734>.
- (28) Stevens, D. A.; Dahn, J. R. High Capacity Anode Materials for Rechargeable Sodium-Ion Batteries. *J. Electrochem. Soc.* **2000**, *147* (4), 1271. <https://doi.org/10.1149/1.1393348>.
- (29) Dou, X.; Hasa, I.; Saurel, D.; Vaalma, C.; Wu, L.; Buchholz, D.; Bresser, D.; Komaba, S.; Passerini, S. Hard Carbons for Sodium-Ion Batteries: Structure, Analysis, Sustainability, and Electrochemistry. *Mater. Today* **2019**, *23* (March), 87–104. <https://doi.org/10.1016/j.mattod.2018.12.040>.
- (30) Gabaudan, V.; Sougrati, M. T.; Stievano, L.; Monconduit, L. Chapter 4. Non-Carbonaceous Negative Electrodes in Sodium Batteries. In *Na-ion Batteries*; 2020; pp 147–204.
- (31) Wang, S.; Zhang, X.-B. N-Doped C@Zn₃B₂O₆ as a Low Cost and Environmentally Friendly Anode Material for Na-Ion Batteries: High Performance and New Reaction Mechanism. *Adv. Mater.* **2019**, *31* (5), 1805432. <https://doi.org/10.1002/adma.201805432>.
- (32) Yang, C. C.; Zhang, D. M.; Du, L.; Jiang, Q. Hollow Ni–NiO Nanoparticles Embedded in Porous Carbon Nanosheets as a Hybrid Anode for Sodium-Ion Batteries with an Ultra-Long Cycle Life. *J. Mater. Chem. A* **2018**, *6* (26), 12663–12671. <https://doi.org/10.1039/C8TA03692F>.
- (33) Fang, Y.; Guan, B. Y.; Luan, D.; Lou, X. W. (David). Synthesis of CuS@CoS₂ Double-Shelled Nanoboxes with Enhanced Sodium Storage Properties. *Angew. Chemie* **2019**, *131* (23), 7821–7825. <https://doi.org/10.1002/ange.201902583>.
- (34) Fang, Y.; Yu, X.; Lou, X. W. (David). Bullet-like Cu₉S₅ Hollow Particles Coated with Nitrogen-Doped Carbon for Sodium-Ion Batteries. *Angew. Chemie* **2019**, *131* (23), 7826–7830. <https://doi.org/10.1002/ange.201902988>.
- (35) Zhang, D. M.; Jia, J. H.; Yang, C. C.; Jiang, Q. Fe₇Se₈ Nanoparticles Anchored on N-Doped Carbon Nanofibers as High-Rate Anode for Sodium-Ion Batteries. *Energy Storage Mater.* **2020**, *24*, 439–449. <https://doi.org/10.1016/j.ensm.2019.07.017>.
- (36) Fang, Y.; Yu, X.-Y.; Lou, X. W. D. Formation of Polypyrrole-Coated Sb₂Se₃ Microclips with Enhanced Sodium-Storage Properties. *Angew. Chemie* **2018**, *130* (31), 10007–10011. <https://doi.org/10.1002/ange.201805552>.
- (37) Liu, Y.; Zhang, N.; Jiao, L.; Tao, Z.; Chen, J. Ultrasmall Sn Nanoparticles Embedded in Carbon as High-Performance Anode for Sodium-Ion Batteries. *Adv. Funct. Mater.* **2015**, *25* (2), 214–220. <https://doi.org/10.1002/adfm.201402943>.
- (38) Liu, Y.; Zhang, N.; Jiao, L.; Chen, J. Tin Nanodots Encapsulated in Porous Nitrogen-Doped Carbon Nanofibers as a Free-Standing Anode for Advanced Sodium-Ion Batteries. *Adv.*

- Mater.* **2015**, 27 (42), 6702–6707. <https://doi.org/10.1002/adma.201503015>.
- (39) Zhou, X.; Yu, L.; Yu, X.-Y.; Lou, X. W. D. Encapsulating Sn Nanoparticles in Amorphous Carbon Nanotubes for Enhanced Lithium Storage Properties. *Adv. Energy Mater.* **2016**, 6 (22), 1601177. <https://doi.org/10.1002/aenm.201601177>.
- (40) Li, X.; Ni, J.; Savilov, S. V.; Li, L. Materials Based on Antimony and Bismuth for Sodium Storage. *Chem. - A Eur. J.* **2018**, 24 (52), 13719–13727. <https://doi.org/10.1002/chem.201801574>.
- (41) Kim, Y.; Park, Y.; Choi, A.; Choi, N.-S.; Kim, J.; Lee, J.; Ryu, J. H.; Oh, S. M.; Lee, K. T. An Amorphous Red Phosphorus/Carbon Composite as a Promising Anode Material for Sodium Ion Batteries. *Adv. Mater.* **2013**, 25 (22), 3045–3049. <https://doi.org/10.1002/adma.201204877>.
- (42) Fan, X.; Mao, J.; Zhu, Y.; Luo, C.; Suo, L.; Gao, T.; Han, F.; Liou, S.-C.; Wang, C. Superior Stable Self-Healing SnP₃ Anode for Sodium-Ion Batteries. *Adv. Energy Mater.* **2015**, 5 (18), 1500174. <https://doi.org/10.1002/aenm.201500174>.
- (43) Seng, K. H.; Guo, Z. P.; Chen, Z. X.; Liu, H. K. SnSb/Graphene Composite as Anode Materials for Lithium Ion Batteries. *Adv. Sci. Lett.* **2011**, 4 (1), 18–23. <https://doi.org/10.1166/asl.2011.1198>.
- (44) Baggetto, L.; Allcorn, E.; Unocic, R. R.; Manthiram, A.; Veith, G. M. Mo₃Sb₇ as a Very Fast Anode Material for Lithium-Ion and Sodium-Ion Batteries. *J. Mater. Chem. A* **2013**, 1 (37), 11163. <https://doi.org/10.1039/c3ta12040f>.
- (45) Sun, Y.; Zhao, L.; Pan, H.; Lu, X.; Gu, L.; Hu, Y.-S.; Li, H.; Armand, M.; Ikuhara, Y.; Chen, L.; Huang, X. Direct Atomic-Scale Confirmation of Three-Phase Storage Mechanism in Li₄Ti₅O₁₂ Anodes for Room-Temperature Sodium-Ion Batteries. *Nat. Commun.* **2013**, 4 (1), 1870. <https://doi.org/10.1038/ncomms2878>.
- (46) Senguttuvan, P.; Rousse, G.; Seznec, V.; Tarascon, J.-M.; Palacín, M. R. Na₂Ti₃O₇: Lowest Voltage Ever Reported Oxide Insertion Electrode for Sodium Ion Batteries. *Chem. Mater.* **2011**, 23 (18), 4109–4111. <https://doi.org/10.1021/cm202076g>.
- (47) Rudola, A.; Saravanan, K.; Devaraj, S.; Gong, H.; Balaya, P. Na₂Ti₆O₁₃: A Potential Anode for Grid-Storage Sodium-Ion Batteries. *Chem. Commun.* **2013**, 49 (67), 7451. <https://doi.org/10.1039/c3cc44381g>.
- (48) Liu, Y.; Zhang, N.; Kang, H.; Shang, M.; Jiao, L.; Chen, J. WS₂ Nanowires as a High-Performance Anode for Sodium-Ion Batteries. *Chem. - A Eur. J.* **2015**, 21 (33), 11878–11884. <https://doi.org/10.1002/chem.201501759>.
- (49) Gao, P.; Wang, L.; Zhang, Y.; Huang, Y.; Liu, K. Atomic-Scale Probing of the Dynamics of Sodium Transport and Intercalation-Induced Phase Transformations in MoS₂. *ACS Nano* **2015**, 9 (11), 11296–11301. <https://doi.org/10.1021/acsnano.5b04950>.

- (50) Yu, Y. X. Prediction of Mobility, Enhanced Storage Capacity, and Volume Change during Sodiation on Interlayer-Expanded Functionalized Ti₃C₂ MXene Anode Materials for Sodium-Ion Batteries. *J. Phys. Chem. C* **2016**, *120* (10), 5288–5296. <https://doi.org/10.1021/acs.jpcc.5b10366>.
- (51) Liu, Z.; Song, T.; Paik, U. Sb-Based Electrode Materials for Rechargeable Batteries. *J. Mater. Chem. A* **2018**, *6* (18), 8159–8193. <https://doi.org/10.1039/c8ta01782d>.
- (52) Lao, M.; Zhang, Y.; Luo, W.; Yan, Q.; Sun, W.; Dou, S. X. Alloy-Based Anode Materials toward Advanced Sodium-Ion Batteries. *Adv. Mater.* **2017**, *29* (48), 1–23. <https://doi.org/10.1002/adma.201700622>.
- (53) Song, K.; Liu, C.; Mi, L.; Chou, S.; Chen, W.; Shen, C. Recent Progress on the Alloy-Based Anode for Sodium-Ion Batteries and Potassium-Ion Batteries. *Small* **2021**, *17* (9), 1–26. <https://doi.org/10.1002/smll.201903194>.
- (54) Ying, H.; Han, W. Q. Metallic Sn-Based Anode Materials: Application in High-Performance Lithium-Ion and Sodium-Ion Batteries. *Adv. Sci.* **2017**, *4* (11). <https://doi.org/10.1002/advs.201700298>.
- (55) Jing, W. T.; Yang, C. C.; Jiang, Q. Recent Progress on Metallic Sn- And Sb-Based Anodes for Sodium-Ion Batteries. *J. Mater. Chem. A* **2020**, *8* (6), 2913–2933. <https://doi.org/10.1039/c9ta11782b>.
- (56) Wu, H.; Cui, Y. Designing Nanostructured Si Anodes for High Energy Lithium Ion Batteries. *Nano Today* **2012**, *7* (5), 414–429. <https://doi.org/10.1016/j.nantod.2012.08.004>.
- (57) Li, L.; Zheng, Y.; Zhang, S.; Yang, J.; Shao, Z.; Guo, Z. Recent Progress on Sodium Ion Batteries: Potential High-Performance Anodes. *Energy Environ. Sci.* **2018**, *11* (9), 2310–2340. <https://doi.org/10.1039/C8EE01023D>.
- (58) Hwang, J. Y.; Myung, S. T.; Sun, Y. K. Sodium-Ion Batteries: Present and Future. *Chem. Soc. Rev.* **2017**, *46* (12), 3529–3614. <https://doi.org/10.1039/c6cs00776g>.
- (59) Carmichael, R. S. *Practical Handbook of Physical Properties of Rocks and Minerals*; CRC Press, 1988.
- (60) Sun, Y.; Shi, P.; Chen, J.; Wu, Q.; Liang, X.; Rui, X.; Xiang, H.; Yu, Y. Development and Challenge of Advanced Nonaqueous Sodium Ion Batteries. *EnergyChem* **2020**, *2* (2), 100031. <https://doi.org/10.1016/j.enchem.2020.100031>.
- (61) Sun, B.; Li, P.; Zhang, J.; Wang, D.; Munroe, P.; Wang, C.; Notten, P. H. L.; Wang, G. Dendrite-Free Sodium-Metal Anodes for High-Energy Sodium-Metal Batteries. <https://doi.org/10.1002/adma.201801334>.
- (62) Tian, Y.; An, Y.; Wei, C.; Jiang, H.; Xiong, S.; Feng, J.; Qian, Y. Recently Advances and Perspectives of Anode-Free Rechargeable Batteries. *Nano Energy* **2020**, *78* (September), 105344. <https://doi.org/10.1016/j.nanoen.2020.105344>.

- (63) Liu, T.; Yang, X.; Nai, J.; Wang, Y.; Liu, Y.; Liu, C.; Tao, X. Recent Development of Na Metal Anodes: Interphase Engineering Chemistries Determine the Electrochemical Performance. *Chem. Eng. J.* **2021**, *409* (November 2020), 127943. <https://doi.org/10.1016/j.cej.2020.127943>.
- (64) Higgins, R. L.; Erisman, L. R. Applications of the Lithium/Carbon Monofluoride Battery. In *Proc. 28th Power Sources Symposium*; The Electrochemical Society, Atlantic City, N.J.: Atlantic City, NJ, USA, 1978; pp 208–210.
- (65) Watanabe, N.; Nakajima, T.; Touhara, H. *Graphite Fluorides*; Elsevier, Japan: Japan, 1988.
- (66) Han, S. S.; Yu, T. H.; Merinov, B. V.; Van Duin, A. C. T.; Yazami, R.; Goddard, W. A. Unraveling Structural Models of Graphite Fluorides by Density Functional Theory Calculations. *Chem. Mater.* **2010**, *22* (6), 2142–2154. <https://doi.org/10.1021/cm903760t>.
- (67) Leung, K.; Schorr, N. B.; Mayer, M.; Lambert, T. N.; Shirley Meng, Y.; Harrison, K. L. Edge-Propagation Discharge Mechanism in CFX Batteries—a First-Principles and Experimental Study. *Chem. Mater.* **2021**, *33*, 1760–1770. <https://doi.org/10.1021/acs.chemmater.0c04676>.
- (68) Nakajima, T. *Lithium-Graphite Fluoride Battery-History and Fundamentals*; Elsevier, Japan, 2016. <https://doi.org/10.1016/B978-0-12-803479-8.00013-9>.
- (69) Watanabe, N.; Fukuda, M. US Patent US3536532A - Primary Cell for Electric Batteries, 1970.
- (70) Fukuda, M.; Iijima, T. Extended Abstract No. 41; The Electrochemical Society Fall Meeting, Cleveland, OH: Cleveland, OH, 1971; p p 100.
- (71) Watanabe, N.; Takashima, M. Proceedings of the 7th International Symposium on Fluorine Chemistry; International Symposium on Fluorine Chemistry (ISFC), Santa Cruz, CA: Santa Cruz, CA, 1973; p P. 19.
- (72) Whittingham, M. S. Mechanism of Reduction of the Fluorographite Cathode. *J. Electrochem. Soc.* **1975**, *122* (4), 526. <https://doi.org/10.1149/1.2134252>.
- (73) Ueno, K.; Watanabe, N.; Nakajima, T. Thermodynamic Studies of Discharge Reaction of Graphite Fluoride-Lithium Battery. *J. Fluor. Chem.* **1982**, *19* (3–6), 323–332. [https://doi.org/10.1016/S0022-1139\(00\)83135-8](https://doi.org/10.1016/S0022-1139(00)83135-8).
- (74) Watanabe, N.; Nakajima, T.; Hagiwara, R. Discharge Reaction and Overpotential of the Graphite Fluoride Cathode in a Nonaqueous Lithium Cell. *J. Power Sources* **1987**, *20* (1–2), 87–92. [https://doi.org/10.1016/0378-7753\(87\)80095-2](https://doi.org/10.1016/0378-7753(87)80095-2).
- (75) Wood, J. L.; Valerga, A. J.; Badachhape, R. B.; Margrave, J. L. *R&D Tech. Report: ECOM-0105-F; Contract DAAB 07-72-C-0105*; 1972.
- (76) Watanabe, N.; Hagiwara, R.; Nakajima, T.; Touhara, H.; Ueno, K. Solvents Effects on

- Electrochemical Characteristics of Graphite Fluoride-Lithium Batteries. *Electrochim. Acta* **1982**, 27 (11), 1615–1619. [https://doi.org/10.1016/0013-4686\(82\)80088-1](https://doi.org/10.1016/0013-4686(82)80088-1).
- (77) Zhang, S. S.; Foster, D.; Wolfenstine, J.; Read, J. Electrochemical Characteristic and Discharge Mechanism of a Primary Li/CF_x Cell. *J. Power Sources* **2009**, 187 (1), 233–237. <https://doi.org/10.1016/j.jpowsour.2008.10.076>.
- (78) Ding, Z.; Yang, C.; Zou, J.; Chen, S.; Qu, K.; Ma, X.; Zhang, J.; Lu, J.; Wei, W.; Gao, P.; Wang, L. Reaction Mechanism and Structural Evolution of Fluorographite Cathodes in Solid-State K/Na/Li Batteries. <https://doi.org/10.1002/adma.202006118>.
- (79) Pang, C.; Ding, F.; Sun, W.; Liu, J.; Hao, M.; Wang, Y.; Liu, X.; Xu, Q. A Novel Dimethyl Sulfoxide/1,3-Dioxolane Based Electrolyte for Lithium/Carbon Fluorides Batteries with a High Discharge Voltage Plateau. *Electrochim. Acta* **2015**, 174, 230–237. <https://doi.org/10.1016/j.electacta.2015.06.004>.
- (80) Jiang, C.; Wang, B.; Wu, Z.; Qiu, J.; Ding, Z.; Zou, J.; Chen, S.; Gao, P.; Niu, X.; Wang, L.; Li, H. Nano Energy Electrolyte-Assisted Dissolution-Recrystallization Mechanism towards High Energy Density and Power Density CF Cathodes in Potassium Cell. *Nano Energy* **2020**, 70 (January), 104552. <https://doi.org/10.1016/j.nanoen.2020.104552>.
- (81) Fang, C.; Li, J.; Zhang, M.; Zhang, Y.; Yang, F.; Lee, J. Z.; Lee, M. H.; Alvarado, J.; Schroeder, M. A.; Yang, Y.; Lu, B.; Williams, N.; Ceja, M.; Yang, L.; Cai, M.; Gu, J.; Xu, K.; Wang, X.; Meng, Y. S. Quantifying Inactive Lithium in Lithium Metal Batteries. *Nature* **2019**, 572 (7770), 511–515. <https://doi.org/10.1038/s41586-019-1481-z>.
- (82) Department of Energy, U. *Reaction of Aluminum with Water to Produce Hydrogen, A Study of Issues Related to the Use of Aluminum for On-Board Vehicular Hydrogen Storage*; 2008.
- (83) Besenhard, J. O. *Handbook of Battery Materials*; Wiley-VCH Austria: Weinheim, Germany, 1999.
- (84) Asenbauer, J.; Eisenmann, T.; Kuenzel, M.; Kazzazi, A.; Chen, Z.; Bresser, D. Insights into the Lithiation Mechanism Of. *Sustain. Energy Fuels* **2020**, 4 (11), 5387–5416. <https://doi.org/10.1039/d0se00175a>.
- (85) Wang, N.; Liu, Q.; Sun, B.; Gu, J.; Yu, B.; Zhang, W.; Zhang, D. N-Doped Catalytic Graphitized Hard Carbon for High-Performance Lithium/Sodium-Ion Batteries. *Sci. Rep.* **2018**, 8 (1), 1–8. <https://doi.org/10.1038/s41598-018-28310-3>.
- (86) Guérin, K.; Dubois, M.; Hamwi, A. Electrochemical Discharge Mechanism of Fluorinated Graphite Used as Electrode in Primary Lithium Batteries. *J. Phys. Chem. Solids* **2006**, 67 (5–6), 1173–1177. <https://doi.org/10.1016/j.jpccs.2006.01.043>.
- (87) Zhong, G.; Chen, H.; Cheng, Y.; Meng, L.; Liu, H.; Liu, Z.; Zheng, G.; Xiang, Y.; Liu, X.; Li, Q.; Zhang, Q.; Yue, H.; Lu, C.; Yang, Y. Insights into the Lithiation Mechanism of CF_x by a Joint High-Resolution 19F NMR, in Situ TEM and 7Li NMR Approach. *J. Mater. Chem. A* **2019**, 7 (34), 19793–19799. <https://doi.org/10.1039/c9ta06800g>.

- (88) Li, Y. R.; Bruck, A. M.; Brady, A. B.; Bock, D.; Takeuchi, K. J.; Takeuchi, E. S.; Marschilok, A. C. Hybrid Ag₂VO₂PO₄/CF_x as a High Capacity and Energy Cathode for Primary Batteries. *J. Electrochem. Soc.* **2017**, *164* (12), A2457–A2467. <https://doi.org/10.1149/2.0991712jes>.
- (89) Ahmad, Y.; Guérin, K.; Dubois, M.; Zhang, W.; Hamwi, A. Enhanced Performances in Primary Lithium Batteries of Fluorinated Carbon Nanofibers through Static Fluorination. *Electrochim. Acta* **2013**, *114*, 142–151. <https://doi.org/10.1016/j.electacta.2013.09.140>.
- (90) Rodriguez, M. A.; Keenan, M. R.; Nagasubramanian, G. In Situ X-Ray Diffraction Analysis of (CF_x)_n Batteries: Signal Extraction by Multivariate Analysis. *J. Appl. Crystallogr.* **2007**, *40* (6), 1097–1104. <https://doi.org/10.1107/S0021889807042045>.
- (91) Hai-Yang, D.; Li-Wu, W.; Hui, J.; Ning-Kang, H. A New Empirical Model for Estimation of Sp³ Fraction in Diamond-Like Carbon Films. *Chinese Phys. Lett.* **2007**, *24* (7), 2122–2124.
- (92) Childres, I.; Jauregui, L. A.; Park, W.; Caoa, H.; Chena, Y. P. Raman Spectroscopy of Graphene and Related Materials. In *New Developments in Photon and Materials Research*; Nova Science Publishers, New York, 2013; pp 403–418.
- (93) Ferrari, A.; Robertson, J. Interpretation of Raman Spectra of Disordered and Amorphous Carbon. *Phys. Rev. B - Condens. Matter Mater. Phys.* **2000**, *61* (20), 14095–14107. <https://doi.org/10.1103/PhysRevB.61.14095>.
- (94) Inaba, M. In Situ Raman Study on Electrochemical Li Intercalation into Graphite. *J. Electrochem. Soc.* **1995**, *142* (1), 20. <https://doi.org/10.1149/1.2043869>.
- (95) Fong, R.; von Sacken, U.; Dahn, J. R. Studies of Lithium Intercalation into Carbons Using Nonaqueous Electrochemical Cells. *J. Electrochem. Soc.* **1990**, *137* (7), 2009–2013. <https://doi.org/10.1149/1.2086855>.
- (96) Stancovski, V.; Badilescu, S. In Situ Raman Spectroscopic-Electrochemical Studies of Lithium-Ion Battery Materials: A Historical Overview. *J. Appl. Electrochem.* **2014**, *44* (1), 23–43. <https://doi.org/10.1007/s10800-013-0628-0>.
- (97) Sole, C.; Drewett, N. E.; Hardwick, L. J. In situ Raman Study of Lithium-Ion Intercalation into Microcrystalline Graphite. *Faraday Discuss.* **2014**, *172*, 223–237. <https://doi.org/10.1039/c4fd00079j>.
- (98) Ferrari, A. C. Determination of Bonding in Diamond-like Carbon by Raman Spectroscopy. *Diam. Relat. Mater.* **2002**, *11* (3–6), 1053–1061. [https://doi.org/10.1016/S0925-9635\(01\)00730-0](https://doi.org/10.1016/S0925-9635(01)00730-0).
- (99) Pal, U.; Rakov, D.; Lu, B.; Sayahpour, B.; Chen, F.; Roy, B.; MacFarlane, D. R.; Armand, M.; Howlett, P. C.; Meng, Y. S.; Forsyth, M. Interphase Control for High Performance Lithium Metal Batteries Using Ether Aided Ionic Liquid Electrolyte. *Energy Environ. Sci.* **2022**, *15* (5), 1907–1919. <https://doi.org/10.1039/d1ee02929k>.

- (100) Chung, H.; Lebens-Higgins, Z.; Sayahpour, B.; Mejia, C.; Grenier, A.; Kamm, G. E.; Li, Y.; Huang, R.; Piper, L. F. J.; Chapman, K. W.; Doux, J. M.; Meng, Y. S. Experimental Considerations to Study Li-Excess Disordered Rock Salt Cathode Materials. *J. Mater. Chem. A* **2021**, *9* (3), 1720–1732. <https://doi.org/10.1039/d0ta07836k>.
- (101) Read, J.; Collins, E.; Piekarski, B.; Zhang, S. LiF Formation and Cathode Swelling in the Li/CF_x Battery. *J. Electrochem. Soc.* **2011**, *158* (5), A504. <https://doi.org/10.1149/1.3561429>.
- (102) Mar, M.; Ahmad, Y.; Guérin, K.; Dubois, M.; Batische, N. Fluorinated Exfoliated Graphite as Cathode Materials for Enhanced Performances in Primary Lithium Battery. *Electrochim. Acta* **2017**, *227*, 18–23. <https://doi.org/10.1016/j.electacta.2016.12.137>.
- (103) Desilva, J. H. S. R.; Vazquez, R.; Stallworth, P. E.; Reddy, T. B.; Lehnes, J. M.; Guo, R.; Gan, H.; Muffoletto, B. C.; Greenbaum, S. G. Solid-State Nuclear Magnetic Resonance Studies of Electrochemically Discharged CF_x. *J. Power Sources* **2011**, *196* (13), 5659–5666. <https://doi.org/10.1016/j.jpowsour.2011.02.036>.
- (104) Nanoparticles, L. O. Lithium Oxide - Specification Sheet - Intelligent Materials Pvt. Ltd. *Schmierungstechnik* **1988**, *19* (2, 1988), 61–63.
- (105) Chen, N.; Zhou, E.; Duan, D. ping; Yang, X. min. Mechanochemistry Synthesis of High Purity Lithium Carbonate. *Korean J. Chem. Eng.* **2017**, *34* (10), 2748–2755. <https://doi.org/10.1007/s11814-017-0172-4>.
- (106) Lee, J. Z.; Wynn, T. A.; Schroeder, M. A.; Alvarado, J.; Wang, X.; Xu, K.; Meng, Y. S. Cryogenic Focused Ion Beam Characterization of Lithium Metal Anodes. *ACS Energy Lett.* **2019**, *4* (2), 489–493. <https://doi.org/10.1021/acseenergylett.8b02381>.
- (107) Langenhorst, F.; Solozhenko, V. L. ATEM-EELS Study of New Diamond-like Phases in the B-C-N System. *Phys. Chem. Chem. Phys.* **2002**, *4* (20), 5183–5188. <https://doi.org/10.1039/b206691b>.
- (108) Cheng, D.; Wynn, T. A.; Wang, X.; Wang, S.; Zhang, M.; Shimizu, R.; Bai, S.; Nguyen, H.; Fang, C.; Kim, M.; Li, W.; Lu, B.; Kim, S. J.; Meng, Y. S. Unveiling the Stable Nature of the Solid Electrolyte Interphase between Lithium Metal and LiPON via Cryogenic Electron Microscopy. *Joule* **2020**, *4* (11), 2484–2500. <https://doi.org/10.1016/j.joule.2020.08.013>.
- (109) Sayahpour, B.; Hirsh, H.; Bai, S.; Schorr, N. B.; Lambert, T. N.; Mayer, M.; Bao, W.; Cheng, D.; Zhang, M.; Leung, K.; Harrison, K. L.; Li, W.; Meng, Y. S. Revisiting Discharge Mechanism of CF_x as a High Energy Density Cathode Material for Lithium Primary Battery. *Adv. Energy Mater.* **2022**, *12* (5), 2103196. <https://doi.org/10.1002/aenm.202103196>.
- (110) Sayahpour, B.; Bai, S.; Cheng, D.; Zhang, M.; Li, W.; Meng, Y. S. Elucidation of Discharge Mechanism in CF_x As a High Energy Density Cathode Material for Lithium Primary Battery. *ECS Meet. Abstr.* **2022**, *MA2022-01* (2), 335–335.

<https://doi.org/10.1149/MA2022-012335mtgabs>.

- (111) Hernandez, Y.; Nicolosi, V.; Lotya, M.; Blighe, F. M.; Sun, Z.; De, S.; McGovern, I. T.; Holland, B.; Byrne, M.; Gun'Ko, Y. K.; Boland, J. J.; Niraj, P.; Duesberg, G.; Krishnamurthy, S.; Goodhue, R.; Hutchison, J.; Scardaci, V.; Ferrari, A. C.; Coleman, J. N. High-Yield Production of Graphene by Liquid-Phase Exfoliation of Graphite. *Nat. Nanotechnol.* **2008**, *3* (9), 563–568. <https://doi.org/10.1038/nnano.2008.215>.
- (112) Halim, U.; Zheng, C. R.; Chen, Y.; Lin, Z.; Jiang, S.; Cheng, R.; Huang, Y.; Duan, X. A Rational Design of Cosolvent Exfoliation of Layered Materials by Directly Probing Liquid–Solid Interaction. *Nat. Commun.* **2013**, *4* (1), 2213. <https://doi.org/10.1038/ncomms3213>.
- (113) Tao, H.; Zhang, Y.; Gao, Y.; Sun, Z.; Yan, C.; Texter, J. Scalable Exfoliation and Dispersion of Two-Dimensional Materials – an Update. *Phys. Chem. Chem. Phys.* **2017**, *19* (2), 921–960. <https://doi.org/10.1039/C6CP06813H>.
- (114) Verger, L.; Xu, C.; Natu, V.; Cheng, H.-M.; Ren, W.; Barsoum, M. W. Overview of the Synthesis of MXenes and Other Ultrathin 2D Transition Metal Carbides and Nitrides. *Curr. Opin. Solid State Mater. Sci.* **2019**, *23* (3), 149–163. <https://doi.org/10.1016/j.cossms.2019.02.001>.
- (115) Hua, X.; Eggeman, A. S.; Castillo-Martínez, E.; Robert, R.; Geddes, H. S.; Lu, Z.; Pickard, C. J.; Meng, W.; Wiaderek, K. M.; Pereira, N.; Amatucci, G. G.; Midgley, P. A.; Chapman, K. W.; Steiner, U.; Goodwin, A. L.; Grey, C. P. Revisiting Metal Fluorides as Lithium-Ion Battery Cathodes. *Nat. Mater.* **2021**. <https://doi.org/10.1038/s41563-020-00893-1>.
- (116) Liu, L.; Guo, H.; Zhou, M.; Wei, Q.; Yang, Z.; Shu, H.; Yang, X.; Tan, J.; Yan, Z.; Wang, X. A Comparison among FeF₃·3H₂O, FeF₃·0.33H₂O and FeF₃ Cathode Materials for Lithium Ion Batteries: Structural, Electrochemical, and Mechanism Studies. *J. Power Sources* **2013**, *238*, 501–515. <https://doi.org/10.1016/j.jpowsour.2013.04.077>.
- (117) Doe, R. E.; Persson, K. A.; Meng, Y. S.; Ceder, G. First-Principles Investigation of the Li-Fe-F Phase Diagram and Equilibrium and Nonequilibrium Conversion Reactions of Iron Fluorides with Lithium. *Chem. Mater.* **2008**, *20* (16), 5274–5283. <https://doi.org/10.1021/cm801105p>.
- (118) Hua, X.; Eggeman, A. S.; Castillo-Martínez, E.; Robert, R.; Geddes, H. S.; Lu, Z.; Pickard, C. J.; Meng, W.; Wiaderek, K. M.; Pereira, N.; Amatucci, G. G.; Midgley, P. A.; Chapman, K. W.; Steiner, U.; Goodwin, A. L.; Grey, C. P. Revisiting Metal Fluorides as Lithium-Ion Battery Cathodes. *Nat. Mater.* **2021**, *20* (6), 841–850. <https://doi.org/10.1038/s41563-020-00893-1>.
- (119) Karki, K.; Wu, L.; Ma, Y.; Armstrong, M. J.; Holmes, J. D.; Garofalini, S. H.; Zhu, Y.; Stach, E. A.; Wang, F. Revisiting Conversion Reaction Mechanisms in Lithium Batteries: Lithiation-Driven Topotactic Transformation in FeF₂. *J. Am. Chem. Soc.* **2018**, *140* (51), 17915–17922. <https://doi.org/10.1021/jacs.8b07740>.
- (120) Wang, F.; Robert, R.; Chernova, N. A.; Pereira, N.; Omenya, F.; Badway, F.; Hua, X.;

- Ruotolo, M.; Zhang, R.; Wu, L.; Volkov, V.; Su, D.; Key, B.; Stanley Whittingham, M.; Grey, C. P.; Amatucci, G. G.; Zhu, Y.; Graetz, J. Conversion Reaction Mechanisms in Lithium Ion Batteries: Study of the Binary Metal Fluoride Electrodes. *J. Am. Chem. Soc.* **2011**, *133* (46), 18828–18836. <https://doi.org/10.1021/ja206268a>.
- (121) Li, L.; Jacobs, R.; Gao, P.; Gan, L.; Wang, F.; Morgan, D.; Jin, S. Origins of Large Voltage Hysteresis in High-Energy-Density Metal Fluoride Lithium-Ion Battery Conversion Electrodes. *J. Am. Chem. Soc.* **2016**, *138* (8), 2838–2848. <https://doi.org/10.1021/jacs.6b00061>.
- (122) Li, T.; Li, L.; Cao, Y. L.; Ai, X. P.; Yang, H. X. Reversible Three-Electron Redox Behaviors of FeF₃ Nanocrystals as High-Capacity Cathode-Active Materials for Li-Ion Batteries. *J. Phys. Chem. C* **2010**, *114* (7), 3190–3195. <https://doi.org/10.1021/jp908741d>.
- (123) Yin, Y.; Holoubek, J.; Liu, A.; Sayahpour, B.; Raghavendran, G.; Cai, G.; Han, B.; Mayer, M.; Schorr, N. B.; Lambert, T. N.; Harrison, K. L.; Li, W.; Chen, Z.; Meng, Y. S. Ultra-Low Temperature Li/CF_x Batteries Enabled by Fast-transport and Anion-pairing Liquefied Gas Electrolytes. *Adv. Mater.* **2022**, 2207932, 2207932. <https://doi.org/10.1002/adma.202207932>.
- (124) Ehrlich, G. M. *Handbook of Batteries*; 2002. [https://doi.org/10.1016/0378-7753\(86\)80059-3](https://doi.org/10.1016/0378-7753(86)80059-3).
- (125) Guérin, K.; Dubois, M.; Houdayer, A.; Hamwi, A. Applicative Performances of Fluorinated Carbons through Fluorination Routes: A Review. *J. Fluor. Chem.* **2012**, *134*, 11–17. <https://doi.org/10.1016/j.jfluchem.2011.06.013>.
- (126) Zhang, Q.; Takeuchi, K. J.; Takeuchi, E. S.; Marschlok, A. C. Progress towards High-Power Li/CF_x Batteries: Electrode Architectures Using Carbon Nanotubes with CF_x. *Phys. Chem. Chem. Phys.* **2015**, *17* (35), 22504–22518. <https://doi.org/10.1039/c5cp03217b>.
- (127) Groult, H.; Tressaud, A. Use of Inorganic Fluorinated Materials in Lithium Batteries and in Energy Conversion Systems. *Chem. Commun.* **2018**, *54* (81), 11375–11382. <https://doi.org/10.1039/C8CC05549A>.
- (128) Li, Q.; Liu, G.; Cheng, H.; Sun, Q.; Zhang, J.; Ming, J. Low-Temperature Electrolyte Design for Lithium-Ion Batteries: Prospect and Challenges. *Chem. - A Eur. J.* **2021**, *27* (64), 15842–15865. <https://doi.org/10.1002/chem.202101407>.
- (129) Li, Q.; Lu, D.; Zheng, J.; Jiao, S.; Luo, L.; Wang, C.-M.; Xu, K.; Zhang, J.-G.; Xu, W. Li + -Desolvation Dictating Lithium-Ion Battery's Low-Temperature Performances. *ACS Appl. Mater. Interfaces* **2017**, *9* (49), 42761–42768. <https://doi.org/10.1021/acsami.7b13887>.
- (130) Zhang, L. Facile Fabrication of CF_x-Pt Composites as a High-Performance Cathode for Primary Lithium Batteries. *Int. J. Electrochem. Sci.* **2019**, *14*, 5738–5747. <https://doi.org/10.20964/2019.06.02>.

- (131) Zhang, S.; Foster, D. L.; Wolfenstine, J.; Read, J. A. FLUORINATED CARBON COMPOSITE CATHODE FOR A HIGH ENERGY LITHIUM BATTERY. US 8,961,833 B2, 2015.
- (132) Zhu, Y.; Zhang, L.; Zhao, H.; Fu, Y. Significantly Improved Electrochemical Performance of CF_x Promoted by SiO₂ Modification for Primary Lithium Batteries. *J. Mater. Chem. A* **2017**, *5* (2), 796–803. <https://doi.org/10.1039/c6ta07919a>.
- (133) Li, Y.; Feng, W. The Tunable Electrochemical Performances of Carbon Fluorides/Manganese Dioxide Hybrid Cathodes by Their Arrangements. *J. Power Sources* **2015**, *274*, 1292–1299. <https://doi.org/10.1016/j.jpowsour.2014.10.150>.
- (134) Meduri, P.; Chen, H.; Chen, X.; Xiao, J.; Gross, M. E.; Carlson, T. J.; Zhang, J. G.; Deng, Z. D. Hybrid CF_x-Ag₂V₄O₁₁ as a High-Energy, Power Density Cathode for Application in an Underwater Acoustic Microtransmitter. *Electrochem. commun.* **2011**, *13* (12), 1344–1348. <https://doi.org/10.1016/j.elecom.2011.08.006>.
- (135) Li, Y.; Feng, Y.; Feng, W. Deeply Fluorinated Multi-Wall Carbon Nanotubes for High Energy and Power Densities Lithium/Carbon Fluorides Battery. *Electrochim. Acta* **2013**, *107*, 343–349.
- (136) Ahmad, Y.; Dubois, M.; Guérin, K.; Hamwi, A.; Zhang, W. Pushing the Theoretical Limit of Li–CF_x Batteries Using Fluorinated Nanostructured Carbon Nanodiscs. *Carbon N. Y.* **2015**, *94*, 1061–1070.
- (137) Yazami, R.; Hamwi, A.; Guérin, K.; Ozawa, Y.; Dubois, M.; Giraudet, J.; Masin, F. Fluorinated Carbon Nanofibres for High Energy and High Power Densities Primary Lithium Batteries. *Electrochem. commun.* **2007**, *9* (7), 1850–1855. <https://doi.org/10.1016/j.elecom.2007.04.013>.
- (138) Wang, L.; Li, Y.; Wang, S.; Zhou, P.; Zhao, Z.; Li, X.; Zhou, J.; Zhuo, S. Fluorinated Nanographite as a Cathode Material for Lithium Primary Batteries. *ChemElectroChem* **2019**, *6* (8), 2201–2207. <https://doi.org/10.1002/celec.201900194>.
- (139) Ahmad, Y.; Dubois, M.; Guérin, K.; Hamwi, A.; Zhang, W. Pushing the Theoretical Limit of Li-CF_x Batteries Using Fluorinated Nanostructured Carbon Nanodiscs. *Carbon N. Y.* **2015**, *94*, 1061–1070. <https://doi.org/10.1016/j.carbon.2015.07.073>.
- (140) Ahmad, Y.; Dubois, M.; Guerin, K.; Hamwi, A.; Flahaut, E. High Energy Density of Primary Lithium Batteries Working with Sub-Fluorinated Few Walled Carbon Nanotubes Cathode. *J. Alloys Compd.* **2017**, *726*, 852–859. <https://doi.org/10.1016/j.jallcom.2017.08.001>.
- (141) Damien, D.; Sudeep, P. M.; Narayanan, T. N.; Anantharaman, M. R.; Ajayan, P. M.; Shaijumon, M. M. Fluorinated Graphene Based Electrodes for High Performance Primary Lithium Batteries. *RSC Adv.* **2013**, *3* (48), 25702–25706. <https://doi.org/10.1039/c3ra45377d>.

- (142) Bi, X.; Li, Y.; Qiu, Z.; Liu, C.; Zhou, T.; Zhuo, S.; Zhou, J. Fluorinated Graphene Prepared by Direct Fluorination of N, O-Doped Graphene Aerogel at Different Temperatures for Lithium Primary Batteries. *Materials (Basel)*. **2018**, *11* (7), 1072. <https://doi.org/10.3390/ma11071072>.
- (143) Li, Y.; Wu, X.; Liu, C.; Wang, S.; Zhou, P.; Zhou, T.; Miao, Z.; Xing, W.; Zhuo, S.; Zhou, J. Fluorinated Multi-Walled Carbon Nanotubes as Cathode Materials of Lithium and Sodium Primary Batteries: Effect of Graphitization of Carbon Nanotubes. *J. Mater. Chem. A* **2019**, *7* (12), 7128–7137. <https://doi.org/10.1039/c8ta12074a>.
- (144) Gunther, R. G. No Title. In *Proceedings of the 9th International Power Sources Symposium, Brighton, Sussex, England*; Brighton, Sussex, England, 1974; p 11.
- (145) Tan, T.; Lam, P.; Yumoto, H. No Title. In *Proceedings of the 208th Electrochemical Society Meeting, Los Angeles, CA*; Los Angeles, CA, 2005.
- (146) Tan, T.; Lam, P.; Yumoto, H. No Title. In *Proceedings of the Fifth Power Sources Conference*; 1975; pp 713–728.
- (147) Whitacre, J.; Yazami, R.; Hamwi, A.; Smart, M. C.; Bennett, W.; Surya Prakash, G. K.; Miller, T.; Bugga, R. Low Operational Temperature Li-CFx Batteries Using Cathodes Containing Sub-Fluorinated Graphitic Materials. *J. Power Sources* **2006**, *160* (1), 577–584. <https://doi.org/10.1016/j.jpowsour.2006.01.045>.
- (148) Whitacre, J. F.; West, W. C.; Smart, M. C.; Yazami, R.; Surya Prakash, G. K.; Hamwi, A.; Ratnakumar, B. V. Enhanced Low-Temperature Performance of Li-CFx Batteries. *Electrochem. Solid-State Lett.* **2007**, *10* (7), A166. <https://doi.org/10.1149/1.2735823>.
- (149) Whitacre, J.; Yazami, R.; Hamwi, A.; Smart, M. C.; Bennett, W.; Surya Prakash, G. K.; Miller, T.; Bugga, R. Low Operational Temperature Li-CFx Batteries Using Cathodes Containing Sub-Fluorinated Graphitic Materials. *J. Power Sources* **2006**, *160* (1), 577–584. <https://doi.org/10.1016/j.jpowsour.2006.01.045>.
- (150) Jones, J.-P.; Jones, S. C.; Krause, F. C.; Pasalic, J.; Smart, M. C.; Bugga, R. V.; Brandon, E. J.; West, W. C. Additive Effects on Li||CFx and Li||CFx -MnO₂ Primary Cells at Low Temperature. *J. Electrochem. Soc.* **2017**, *164* (13), A3109–A3116. <https://doi.org/10.1149/2.0831713jes>.
- (151) Nagasubramanian, G.; Rodriguez, M. Performance Enhancement at Low Temperatures and in Situ X-Ray Analyses of Discharge Reaction of Li/(CFx)_n Cells. *J. Power Sources* **2007**, *170* (1), 179–184. <https://doi.org/10.1016/j.jpowsour.2007.04.023>.
- (152) Zhou, K.-G.; Mao, N.-N.; Wang, H.-X.; Peng, Y.; Zhang, H.-L. A Mixed-Solvent Strategy for Efficient Exfoliation of Inorganic Graphene Analogues. *Angew. Chemie Int. Ed.* **2011**, *50* (46), 10839–10842. <https://doi.org/10.1002/anie.201105364>.
- (153) Dong, L.; Chen, Z.; Zhao, X.; Ma, J.; Lin, S.; Li, M.; Bao, Y.; Chu, L.; Leng, K.; Lu, H.; Loh, K. P. A Non-Dispersion Strategy for Large-Scale Production of Ultra-High

- Concentration Graphene Slurries in Water. *Nat. Commun.* **2018**, *9* (1), 76. <https://doi.org/10.1038/s41467-017-02580-3>.
- (154) Varrla, E.; Backes, C.; Paton, K. R.; Harvey, A.; Gholamvand, Z.; McCauley, J.; Coleman, J. N. Large-Scale Production of Size-Controlled MoS₂ Nanosheets by Shear Exfoliation. *Chem. Mater.* **2015**, *27* (3), 1129–1139. <https://doi.org/10.1021/cm5044864>.
- (155) Sherwood, J.; De bruyn, M.; Constantinou, A.; Moity, L.; McElroy, C. R.; Farmer, T. J.; Duncan, T.; Raverty, W.; Hunt, A. J.; Clark, J. H. Dihydrolevoglucosenone (Cyrene) as a Bio-Based Alternative for Dipolar Aprotic Solvents. *Chem. Commun.* **2014**, *50* (68), 9650–9652. <https://doi.org/10.1039/c4cc04133j>.
- (156) De Bruyn, M.; Fan, J.; Budarin, V. L.; Macquarrie, D. J.; Gomez, L. D.; Simister, R.; Farmer, T. J.; Raverty, W. D.; McQueen-Mason, S. J.; Clark, J. H. A New Perspective in Bio-Refining: Levoglucosenone and Cleaner Lignin from Waste Biorefinery Hydrolysis Lignin by Selective Conversion of Residual Saccharides. *Energy Environ. Sci.* **2016**, *9* (8), 2571–2574. <https://doi.org/10.1039/c6ee01352j>.
- (157) Clark, J. H.; Shuttleworth, P. S. Identification of High Performance Solvents for the Sustainable Processing of Graphene. **2017**, *19* (11). <https://doi.org/10.1039/c7gc00112f>.
- (158) Zhou, P.; Meng, H.; Zhang, Z.; Chen, C.; Lu, Y.; Cao, J.; Cheng, F.; Chen, J. Stable Layered Ni-Rich LiNi_{0.9}Co_{0.07}Al_{0.03}O₂ Microspheres Assembled with Nanoparticles as High-Performance Cathode Materials for Lithium-Ion Batteries. *J. Mater. Chem. A* **2017**, *5* (6), 2724–2731. <https://doi.org/10.1039/c6ta09921a>.
- (159) Weppner, W.; Huggins, R. A. Determination of the Kinetic Parameters of Mixed-Conducting Electrodes and Application to the System Li₃Sb. *J. Electrochem. Soc.* **1977**, *124* (10), 1569–1578. <https://doi.org/10.1149/1.2133112>.
- (160) Whitacre, J. F.; West, W. C.; Smart, M. C.; Yazami, R.; Surya Prakash, G. K.; Hamwi, A.; Ratnakumar, B. V. Enhanced Low-Temperature Performance of Li- CFX Batteries. *Electrochem. Solid-State Lett.* **2007**, *10* (7), 166–170. <https://doi.org/10.1149/1.2735823>.
- (161) Zhang, S. S.; Foster, D.; Read, J. A Low Temperature Electrolyte for Primary Li/CFX Batteries. *J. Power Sources* **2009**, *188* (2), 532–537. <https://doi.org/10.1016/j.jpowsour.2008.12.030>.
- (162) Ignatova, A. A.; Yarmolenko, O. V.; Tulibaeva, G. Z.; Shestakov, A. F.; Fateev, S. A. Influence of 15-Crown-5 Additive to a Liquid Electrolyte on the Performance of Li/CFX - Systems at Temperatures up to -50 °C. *J. Power Sources* **2016**, *309*, 116–121. <https://doi.org/10.1016/j.jpowsour.2016.01.075>.
- (163) Read, J.; Soc, J. E.; Read, J.; Collins, E.; Piekarski, B.; Zhang, S. LiF Formation and Cathode Swelling in the Li / CF_x Battery LiF Formation and Cathode Swelling in the Li / CF_x Battery. **2011**. <https://doi.org/10.1149/1.3561429>.
- (164) Yao, W.; Chouchane, M.; Li, W.; Bai, S.; Liu, Z.; Li, L.; Chen, A. X.; Sayahpour, B.;

- Shimizu, R.; Raghavendran, G.; Schroeder, M. A.; Chen, Y.-T.; Tan, D. H. S.; Sreenarayanan, B.; Waters, C. K.; Sichler, A.; Gould, B.; Kountz, D. J.; Lipomi, D. J.; Zhang, M.; Meng, Y. S. A 5 V-Class Cobalt-Free Battery Cathode with High Loading Enabled by Dry Coating. *Energy Environ. Sci.* **2023**. <https://doi.org/10.1039/D2EE03840D>.
- (165) Tarascon, J. Na-Ion versus Li-Ion Batteries: Complementarity Rather than Competitiveness. *Joule* **2020**, *4* (8), 1616–1620. <https://doi.org/10.1016/j.joule.2020.06.003>.
- (166) Tan, D. H. S.; Chen, Y. T.; Yang, H.; Bao, W.; Sreenarayanan, B.; Doux, J. M.; Li, W.; Lu, B.; Ham, S. Y.; Sayahpour, B.; Scharf, J.; Wu, E. A.; Deysheer, G.; Han, H. E.; Hah, H. J.; Jeong, H.; Lee, J. B.; Chen, Z.; Meng, Y. S. Carbon-Free High-Loading Silicon Anodes Enabled by Sulfide Solid Electrolytes. *Science* (80-.). **2021**, *373* (6562), 1494–1499. <https://doi.org/10.1126/science.abg7217>.
- (167) Iermakova, D. I.; Dugas, R.; Palacín, M. R.; Ponrouch, A. On the Comparative Stability of Li and Na Metal Anode Interfaces in Conventional Alkyl Carbonate Electrolytes. *J. Electrochem. Soc.* **2015**, *162* (13), A7060–A7066. <https://doi.org/10.1149/2.0091513jes>.
- (168) Song, J.; Xiao, B.; Lin, Y.; Xu, K.; Li, X. Interphases in Sodium-Ion Batteries. *Adv. Energy Mater.* **2018**, *8* (17). <https://doi.org/10.1002/aenm.201703082>.
- (169) Matios, E.; Wang, H.; Wang, C.; Li, W. Enabling Safe Sodium Metal Batteries by Solid Electrolyte Interphase Engineering: A Review. *Ind. Eng. Chem. Res.* **2019**, *58* (23), 9758–9780. <https://doi.org/10.1021/acs.iecr.9b02029>.
- (170) Fang, Y.; Xiao, L.; Ai, X.; Cao, Y.; Yang, H. Hierarchical Carbon Framework Wrapped Na₃V₂(PO₄)₃ as a Superior High-Rate and Extended Lifespan Cathode for Sodium-Ion Batteries. *Adv. Mater.* **2015**, *27* (39), 5895–5900. <https://doi.org/10.1002/adma.201502018>.
- (171) Bordeaux, U.; Cedex, T.; Cedex, T. The Role of the Inductive Effect in Solid State Chemistry: How the Chemist Can Use It to Modify Both the Structural and the Physical Properties of the Materials. **1992**, *188*, 0–6.
- (172) Society, T. E. Effect of Structure on the Fe³⁺/Fe²⁺ Redox Couple in Iron Phosphates. **1997**, 3–8.
- (173) Masquelier, C.; Croguennec, L. Polyanionic (Phosphates, Silicates, Sulfates) Frameworks as Electrode Materials for Rechargeable Li (or Na) Batteries. *Chem. Rev.* **2013**, *113* (8), 6552–6591. <https://doi.org/10.1021/cr3001862>.
- (174) Newman, G. H.; Klemann, L. P. Ambient Temperature Cycling of an Na - TiS₂ Cell. *J. Electrochem. Soc.* **1980**, *127* (10), 2097–2099. <https://doi.org/10.1149/1.2129353>.
- (175) Delmas, C.; Fouassier, C.; Hagenmuller, P. Structural Classification and Properties of the Layered Oxides. *Phys. B+C* **1980**, *99* (1), 81–85. [https://doi.org/10.1016/0378-4363\(80\)90214-4](https://doi.org/10.1016/0378-4363(80)90214-4).

- (176) Fouassier, C.; Matejka, G.; Reau, J. M.; Hagenmuller, P. Sur de Nouveaux Bronzes Oxygénés de Formule Na_xCoO_2 (X1). Le Système Cobalt-Oxygène-Sodium. *J. Solid State Chem.* **1973**, *6* (4), 532–537. [https://doi.org/10.1016/S0022-4596\(73\)80011-8](https://doi.org/10.1016/S0022-4596(73)80011-8).
- (177) Fouassier, C.; Delmas, C.; Hagenmuller, P. Evolution Structurale et Propriétés Physiques Des Phases AXMO_2 (A = Na, K; M = Cr, Mn, Co) ($x \leq 1$). *Mater. Res. Bull.* **1975**, *10* (6), 443–449. [https://doi.org/10.1016/0025-5408\(75\)90166-X](https://doi.org/10.1016/0025-5408(75)90166-X).
- (178) Braconnier, J. J.; Delmas, C.; Fouassier, C.; Hagenmuller, P. Comportement Electrochimique Des Phases Na_xCoO_2 . *Mater. Res. Bull.* **1980**, *15* (12), 1797–1804. [https://doi.org/10.1016/0025-5408\(80\)90199-3](https://doi.org/10.1016/0025-5408(80)90199-3).
- (179) Delmas, C.; Braconnier, J.-J.; Fouassier, C.; Hagenmuller, P. Electrochemical Intercalation of Sodium in Na_xCoO_2 Bronzes. *Solid State Ionics* **1981**, *3–4*, 165–169. [https://doi.org/10.1016/0167-2738\(81\)90076-X](https://doi.org/10.1016/0167-2738(81)90076-X).
- (180) Komaba, S.; Kubota, K. Chapter 1. Layered NaMO_2 for the Positive Electrode. In *Na-ion Batteries*; Tokyo University of Science, Japan, 2020; pp 1–46.
- (181) Lu, Z.; Dahn, J. R. In Situ X-Ray Diffraction Study of $\text{P}_2\text{-Na}_{2/3}[\text{Ni}_{1/3}\text{Mn}_{2/3}]\text{O}_2$. *J. Electrochem. Soc.* **2001**, *148* (11), A1225. <https://doi.org/10.1149/1.1407247>.
- (182) Du, K.; Zhu, J.; Hu, G.; Gao, H.; Li, Y.; Goodenough, J. B. Exploring Reversible Oxidation of Oxygen in a Manganese Oxide. *Energy Environ. Sci.* **2016**, *9* (8), 2575–2577. <https://doi.org/10.1039/c6ee01367h>.
- (183) Rozier, P.; Sathiya, M.; Paulraj, A.; Foix, D.; Desautay, T.; Taberna, P.; Simon, P.; Tarascon, J. Electrochemistry Communications Anionic Redox Chemistry in Na-Rich $\text{Na}_2\text{Ru}_{1-y}\text{Sn}_y\text{O}_3$ Positive Electrode Material for Na-Ion Batteries. *Electrochem. commun.* **2015**, *53*, 29–32. <https://doi.org/10.1016/j.elecom.2015.02.001>.
- (184) Nam, K.; Chung, K. Y. Polythiophene-Wrapped Olivine NaFePO_4 as a Cathode for Na-Ion Batteries. **2016**, 4–11. <https://doi.org/10.1021/acsami.6b04014>.
- (185) Trad, K.; Carlier, D.; Croguennec, L.; Wattiaux, A.; Amara, M. Ben; Delmas, C. $\text{NaMnFe}_2(\text{PO}_4)_3$ Alluaudite Phase: Synthesis, Structure, and Electrochemical Properties As Positive Electrode in Lithium and Sodium Batteries. *Chem. Mater.* **2010**, *2* (12), 5554–5562. <https://doi.org/10.1021/cm1015614>.
- (186) Daidouh, A.; Durio, C.; Pico, C.; Veiga, M. L.; Chouaibi, N.; Ouassini, A. Structural and Electrical Study of the Alluaudites. **2002**, *4*, 541–548.
- (187) Serras, P.; Croguennec, L. Vanadyl-Type Defects in Tavorite-like NaVPO_4F : From the Average Long Range Structure to Local Environments. *Mater. Chem. A* **2017**, *5*, 25044–25055. <https://doi.org/10.1039/c7ta08733k>.
- (188) Tsirlin, A. A.; Nath, R.; Abakumov, A. M.; Furukawa, Y.; Johnston, D. C.; Hemmida, M.; Nidda, H. K. Von; Loidl, A.; Geibel, C.; Rosner, H. Phase Separation and Frustrated Square

- Lattice Magnetism of $\text{Na}_{1.5}\text{VOPO}_4\text{F}_{0.5}$. **2011**, *84* (014429), 1–16. <https://doi.org/10.1103/PhysRevB.84.014429>.
- (189) Po, N. V. O. F.; Massa, W.; Yakubovich, O. V.; Dimitrova, O. V. Crystal Structure of a New Sodium Vanadyl (IV) Fluoride Phosphate $\text{Na}_3(\text{V}_2\text{O}_2\text{F}[\text{PO}_4]_2)$. **2002**, *4*, 495–501.
- (190) Meins, J. Le; Courbion, G. Phase Transitions in the $\text{Na}_3\text{M}_2(\text{PO}_4)_2\text{F}_3$ Family ($\text{M}=\text{Al}^{3+}, \text{V}^{3+}, \text{Cr}^{3+}, \text{Fe}^{3+}, \text{Ga}^{3+}$): Synthesis, Thermal, Structural, and Magnetic Studies. *J. Solid State Chem.* **1999**, *277*, 260–277.
- (191) Goodenough, J. B.; Hong, H. Y.; Kafalas, J. A. R. G. Graves and J. B. Smathers. *Mater. Res. Bull.* **1976**, *5* (5), 77843.
- (192) Manthiram, A.; Goodenough, J. B. Lithium Insertion into $\text{Fe}_2(\text{SO}_4)_3$ Frameworks. *J. Power Sources* **1989**, *26* (3–4), 403–408. [https://doi.org/10.1016/0378-7753\(89\)80153-3](https://doi.org/10.1016/0378-7753(89)80153-3).
- (193) Delmas, C.; Cherkaoui, F.; Nadiri, A.; Hagenmuller, P. A Nasicon-Type Phase as Intercalation Electrode: $\text{NaTi}_2(\text{PO}_4)_3$. *Mater. Res. Bull.* **1987**, *22* (5), 631–639. [https://doi.org/10.1016/0025-5408\(87\)90112-7](https://doi.org/10.1016/0025-5408(87)90112-7).
- (194) Sato, O.; Einaga, Y.; Iyoda, T.; Fujishima, A.; Hashimoto, K. Reversible Photoinduced Magnetization. *J. Electrochem. Soc.* **1997**, *144* (1), L11–L13. <https://doi.org/10.1149/1.1837356>.
- (195) Entley, W. R.; Treadway, C. R.; Girolami, G. S. Molecular Magnets Constructed from Cyanometalate Building Blocks. *Mol. Cryst. Liq. Cryst. Sci. Technol. Sect. A. Mol. Cryst. Liq. Cryst.* **1995**, *273* (1), 153–166. <https://doi.org/10.1080/10587259508031851>.
- (196) Ferlay, S.; Mallah, T.; Ouahès, R.; Veillet, P.; Verdager, M. A Room-Temperature Organometallic Magnet Based on Prussian Blue. *Nature* **1995**, *378* (6558), 701–703. <https://doi.org/10.1038/378701a0>.
- (197) Ziegler, J. P.; Howard, B. M. Applications of Reversible Electrodeposition Electrochromic Devices. *Sol. Energy Mater. Sol. Cells* **1995**, *39* (2–4), 317–331. [https://doi.org/10.1016/0927-0248\(95\)00067-4](https://doi.org/10.1016/0927-0248(95)00067-4).
- (198) Ellis, D.; Eckhoff, M.; Neff, V. D. Electrochromism in the Mixed-Valence Hexacyanides. 1. Voltammetric and Spectral Studies of the Oxidation and Reduction of Thin Films of Prussian Blue. *J. Phys. Chem.* **1981**, *96* (14), 1225–1231.
- (199) Rajan, K. P.; Neff, V. D. Electrochromism in the Mixed-Valence Hexacyanides. 2. Kinetics of the Reduction of Ruthenium Purple and Prussian Blue. *J. Phys. Chem.* **1982**, *86* (22), 4361–4368. <https://doi.org/10.1021/j100219a017>.
- (200) Imanishi, N.; Morikawa, T.; Kondo, J.; Takeda, Y.; Yamamoto, O.; Kinugasa, N.; Yamagishi, T. Lithium Intercalation Behavior into Iron Cyanide Complex as Positive Electrode of Lithium Secondary Battery. *J. Power Sources* **1999**, *79* (2), 215–219. [https://doi.org/10.1016/S0378-7753\(99\)00061-0](https://doi.org/10.1016/S0378-7753(99)00061-0).

- (201) Eftekhari, A. Potassium Secondary Cell Based on Prussian Blue Cathode. *J. Power Sources* **2004**, *126* (1–2), 221–228. <https://doi.org/10.1016/j.jpowsour.2003.08.007>.
- (202) Lu, Y.; Wang, L.; Cheng, J.; Goodenough, J. B. Prussian Blue: A New Framework of Electrode Materials for Sodium Batteries. *Chem. Commun.* **2012**, *48* (52), 6544–6546. <https://doi.org/10.1039/c2cc31777j>.
- (203) Wang, L.; Lu, Y.; Liu, J.; Xu, M.; Cheng, J.; Zhang, D.; Goodenough, J. B. A Superior Low-Cost Cathode for a Na-Ion Battery. *Angew. Chemie* **2013**, *125* (7), 2018–2021. <https://doi.org/10.1002/ange.201206854>.
- (204) Ohzuku, T.; Iwakoshi, Y.; Sawai, K. Formation of Lithium-Graphite Intercalation Compounds in Nonaqueous Electrolytes and Their Application as a Negative Electrode for a Lithium Ion (Shuttlecock) Cell. *J. Electrochem. Soc.* **1993**, *140* (9), 2490–2498. <https://doi.org/10.1149/1.2220849>.
- (205) Sawai, K.; Ohzuku, T.; Hirai, T. Natural Graphite as an Anode for Rechargeable Nonaqueous Cells. *Chem. Express* **1990**, *5* (837).
- (206) Wan, W.; Wang, H. Study on the First-Principles Calculations of Graphite Intercalated by Alkali Metal (Li, Na, K). *Int. J. Electrochem. Sci.* **2015**, *10* (4), 3177–3184.
- (207) Nobuhara, K.; Nakayama, H.; Nose, M.; Nakanishi, S.; Iba, H. First-Principles Study of Alkali Metal-Graphite Intercalation Compounds. *J. Power Sources* **2013**, *243*, 585–587. <https://doi.org/10.1016/j.jpowsour.2013.06.057>.
- (208) Okamoto, Y. Density Functional Theory Calculations of Alkali Metal (Li, Na, and K) Graphite Intercalation Compounds. *J. Phys. Chem. C* **2014**, *118* (1), 16–19. <https://doi.org/10.1021/jp4063753>.
- (209) Rios, C. D. M. S.; Beda, A.; Simonin, L.; Ghimbeu, C. M. Chapter 3. Hard Carbon for Na-Ion Batteries: From Synthesis to Performance and Storage Mechanism. In *Na-ion Batteries*; 2020; pp 101–146.
- (210) Hirsh, H. S.; Sayahpour, B.; Shen, A.; Li, W.; Lu, B.; Zhao, E.; Zhang, M.; Meng, Y. S. Role of Electrolyte in Stabilizing Hard Carbon as an Anode for Rechargeable Sodium-Ion Batteries with Long Cycle Life. *Energy Storage Mater.* **2021**, *42* (July), 78–87. <https://doi.org/10.1016/j.ensm.2021.07.021>.
- (211) Shacklette, L.; Toth, J.; Elsenbaumer, R. Conjugated Polymer as Substrate for the Plating of Alkal Metal in a Nonaqueous Secondary Battery, 1987.
- (212) Shacklette, L.; Jow, T. R.; Townsend, L. Rechargeable Electrodes from Sodium Cobalt Bronzes. *J. Electrochem. Soc.* **1988**, *135* (11), 2669–2674.
- (213) Shacklette, L.; Toth, J. E.; Elsenbaumer, R. L. Conjugated Polymer as Substrate for the Plating of Alkali Metal in a Nonaqueous Secondary Battery. EP Patent Application US 1985-749325. 1985–749325, 1985.

- (214) Shishikura, T.; Takeuchi, M. Secondary Batteries. Patent Application 86109020.7, 1987.
- (215) Shishikura, T.; Takeuchi, M.; Murakoshi, Y.; Konuma, H.; Kameyama, M. Secondary Cobalt Sodium Oxide-Sodium Alloy Battery. EP Patent Application., 1989.
- (216) Barker, J.; Heap, R. J.; Roche, N.; Tan, C.; Sayers, R.; Whitley, J.; Lui, Y.; Faradion Limited. Commercialization of Faradion's High Energy Faradion Density Na-Ion Battery Technology. In *3rd International Conference on Sodium Batteries*; Sheffield, UK, 2016.
- (217) Rudola, A.; Rennie, A. J. R.; Heap, R.; Meysami, S. S.; Lowbridge, A.; Mazzali, F.; Sayers, R.; Wright, C. J.; Barker, J. Commercialisation of High Energy Density Sodium-Ion Batteries: Faradion's Journey and Outlook. *J. Mater. Chem. A* **2021**, *9* (13), 8279–8302. <https://doi.org/10.1039/d1ta00376c>.
- (218) Barker, J.; Heap, R. Doped Nickelate Compounds, 2017.
- (219) Ponrouch, A.; Dedryvère, R.; Monti, D.; Demet, A. E.; Ateba Mba, J. M.; Croguennec, L.; Masquelier, C.; Johansson, P.; Palacín, M. R. Towards High Energy Density Sodium Ion Batteries through Electrolyte Optimization. *Energy Environ. Sci.* **2013**, *6* (8), 2361. <https://doi.org/10.1039/c3ee41379a>.
- (220) Broux, T.; Fauth, F.; Hall, N.; Chatillon, Y.; Bianchini, M.; Bamine, T.; Leriche, J. B.; Suard, E.; Carlier, D.; Reynier, Y.; Simonin, L.; Masquelier, C.; Croguennec, L. High Rate Performance for Carbon-Coated Na₃V₂(PO₄)₂F₃ in Na-Ion Batteries. *Small Methods* **2019**, *3* (4), 1–12. <https://doi.org/10.1002/smt.201800215>.
- (221) Sodium to Boost Batteries by 2020. In *une année avec le CNRS*; 2017.
- (222) Rong, X.; Yaxiang, L.; Xingguo, Q.; Weihe, K.; Kun, T.; Liquan, C.; Yongsheng, H. Na-Ion Batteries: From Fundamental Research to Engineering Exploration. *Energy Storage Sci. Technol.* **2020**, *9* (2). <https://doi.org/10.19799/j.cnki.2095-4239.2020.0054>.
- (223) Datasheet 2019 Natron Energy Blue Tray 4000. In *Distributed at the Battery Show*; 2019.
- (224) Wessells, C. D. Chapter 7. Batteries Containing Prussian Blue Analogue Electrodes. In *Na-ion Batteries*; 2020; pp 265–312.
- (225) *CATL Unveils Its Latest Breakthrough Technology by Releasing Its First Generation of Sodium-Ion Batteries*; China, 2021.
- (226) Vaalma, C.; Buchholz, D.; Weil, M.; Passerini, S. A Cost and Resource Analysis of Sodium-Ion Batteries. *Nat. Rev. Mater.* **2018**, *3*. <https://doi.org/10.1038/natrevmats.2018.13>.
- (227) Chayambuka, K.; Mulder, G.; Danilov, D. L.; Notten, P. H. L. Sodium-Ion Battery Materials and Electrochemical Properties Reviewed. *Adv. Energy Mater.* **2018**, *8* (16), 1–49. <https://doi.org/10.1002/aenm.201800079>.
- (228) Habib, K.; Hansdóttir, S. T.; Habib, H. Critical Metals for Electromobility: Global Demand

- Scenarios for Passenger Vehicles, 2015–2050. *Resour. Conserv. Recycl.* **2020**, *154* (November 2019), 104603. <https://doi.org/10.1016/j.resconrec.2019.104603>.
- (229) Habib, K.; Wenzel, H. Exploring Rare Earths Supply Constraints for the Emerging Clean Energy Technologies and the Role of Recycling. *J. Clean. Prod.* **2014**, *84* (1), 348–359. <https://doi.org/10.1016/j.jclepro.2014.04.035>.
- (230) Wang, P.-F.; You, Y.; Yin, Y.-X.; Guo, Y.-G. Layered Oxide Cathodes for Sodium-Ion Batteries: Phase Transition, Air Stability, and Performance. *Adv. Energy Mater.* **2018**, *8* (8), 1701912. <https://doi.org/10.1002/aenm.201701912>.
- (231) Zhan, C.; Wu, T.; Lu, J.; Amine, K. Dissolution, Migration, and Deposition of Transition Metal Ions in Li-Ion Batteries Exemplified by Mn-Based Cathodes – a Critical Review. *Energy Environ. Sci.* **2018**, *11* (2), 243–257. <https://doi.org/10.1039/C7EE03122J>.
- (232) Delmas, C. Sodium and Sodium-Ion Batteries: 50 Years of Research. *Adv. Energy Mater.* **2018**, *8* (17). <https://doi.org/10.1002/aenm.201703137>.
- (233) Hofstra, A. H.; Kreiner, D. C. *Systems-Deposits-Commodities-Critical Minerals Table for the Earth Mapping Resources Initiative*; 2020.
- (234) Yamatomi, J.; Okubo, S. Surface Mining Methods and Equipment. In *Civil Engineering - Vol. II - Encyclopedia of Life Support Systems*; 2009; pp 155–170.
- (235) Watson, I. Methodology Report 2017. *Responsible Min. Index* **2018**.
- (236) Lèbre, É.; Stringer, M.; Svobodova, K.; Owen, J. R.; Kemp, D.; Côte, C.; Arratia-Solar, A.; Valenta, R. K. The Social and Environmental Complexities of Extracting Energy Transition Metals. *Nat. Commun.* **2020**, *11* (1), 1–8. <https://doi.org/10.1038/s41467-020-18661-9>.
- (237) Watari, T.; Nansai, K.; Nakajima, K. Review of Critical Metal Dynamics to 2050 for 48 Elements. *Resour. Conserv. Recycl.* **2020**, *155* (July 2019), 104669. <https://doi.org/10.1016/j.resconrec.2019.104669>.
- (238) Helbig, C.; Thorenz, A.; Tuma, A. Quantitative Assessment of Dissipative Losses of 18 Metals. *Resour. Conserv. Recycl.* **2020**, *153* (August 2019), 104537. <https://doi.org/10.1016/j.resconrec.2019.104537>.
- (239) Watari, T.; Nansai, K.; Nakajima, K. Major Metals Demand, Supply, and Environmental Impacts to 2100: A Critical Review. *Resour. Conserv. Recycl.* **2021**, *164* (June 2020), 105107. <https://doi.org/10.1016/j.resconrec.2020.105107>.
- (240) Tan, D. H. S.; Xu, P.; Chen, Z. Enabling Sustainable Critical Materials for Battery Storage through Efficient Recycling and Improved Design: A Perspective. *MRS Energy Sustain.* **2020**, *7* (1), 27. <https://doi.org/10.1557/mre.2020.31>.
- (241) Chen, M.; Ma, X.; Chen, B.; Arsenault, R.; Karlson, P.; Simon, N.; Wang, Y. Recycling End-of-Life Electric Vehicle Lithium-Ion Batteries. *Joule* **2019**, *3* (11), 2622–2646.

<https://doi.org/10.1016/j.joule.2019.09.014>.

- (242) Chen, J.; Zhong, S.; Zhang, X.; Liu, J.; Shi, S.; Hu, Y.; Wu, L. High Performance of Hexagonal Plates P2-Na₂/3Fe₁/2Mn₁/2O₂ Cathode Material Synthesized by an Improved Solid-State Method. *Mater. Lett.* **2017**, *202*, 21–24. <https://doi.org/10.1016/j.matlet.2017.05.084>.
- (243) Jin, T.; Wang, P.; Wang, Q.; Zhu, K.; Deng, T.; Zhang, J.; Zhang, W.; Yang, X.; Jiao, L.; Wang, C. Realizing Complete Solid-Solution Reaction in High Sodium Content P2-Type Cathode for High-Performance Sodium-Ion Batteries. *Angew. Chemie* **2020**, *132* (34), 14619–14624. <https://doi.org/10.1002/ange.202003972>.
- (244) Bai, Y.; Zhao, L.; Wu, C.; Li, H.; Li, Y.; Wu, F. Enhanced Sodium Ion Storage Behavior of P2-Type Na₂/3Fe₁/2Mn₁/2O₂ Synthesized via a Chelating Agent Assisted Route. *ACS Appl. Mater. Interfaces* **2016**, *8* (4), 2857–2865. <https://doi.org/10.1021/acsami.5b11848>.
- (245) Liu, T.; Zhang, Y.; Chen, C.; Lin, Z.; Zhang, S.; Lu, J. Sustainability-Inspired Cell Design for a Fully Recyclable Sodium Ion Battery. *Nat. Commun.* **2019**, *10* (1), 1–7. <https://doi.org/10.1038/s41467-019-09933-0>.
- (246) Gaines, L. Lithium-Ion Battery Recycling Processes: Research towards a Sustainable Course. *Sustain. Mater. Technol.* **2018**, *17*, e00068. <https://doi.org/10.1016/j.susmat.2018.e00068>.
- (247) Geis, E. Lazarus Batteries. *Nature* **2015**, *526*, S100–S101.
- (248) Liu, T.; Zhang, Y.; Jiang, Z.; Zeng, X.; Ji, J.; Li, Z.; Gao, X.; Sun, M.; Lin, Z.; Ling, M.; Zheng, J.; Liang, C. Exploring Competitive Features of Stationary Sodium Ion Batteries for Electrochemical Energy Storage. *Energy Environ. Sci.* **2019**, *12* (5), 1512–1533. <https://doi.org/10.1039/c8ee03727b>.
- (249) Hu, X.; Li, S. E.; Yang, Y. Advanced Machine Learning Approach for Lithium-Ion Battery State Estimation in Electric Vehicles. *IEEE Trans. Transp. Electrif.* **2016**, *2* (2), 140–149. <https://doi.org/10.1109/TTE.2015.2512237>.
- (250) Attarian Shandiz, M.; Gauvin, R. Application of Machine Learning Methods for the Prediction of Crystal System of Cathode Materials in Lithium-Ion Batteries. *Comput. Mater. Sci.* **2016**, *117*, 270–278. <https://doi.org/10.1016/j.commatsci.2016.02.021>.
- (251) Houchins, G.; Viswanathan, V. An Accurate Machine-Learning Calculator for Optimization of Li-Ion Battery Cathodes. *J. Chem. Phys.* **2020**, *153* (5), 054124. <https://doi.org/10.1063/5.0015872>.
- (252) Deringer, V. L. Modelling and Understanding Battery Materials with Machine-Learning-Driven Atomistic Simulations Journal of Physics : Energy OPEN ACCESS Modelling and Understanding Battery Materials with Machine-Learning-Driven Atomistic Simulations. *J. Phys. Energy* **2020**, *2*, 041003-1–11.

- (253) Aykol, M.; Gopal, C. B.; Anapolsky, A.; Herring, P. K.; van Vlijmen, B.; Berliner, M. D.; Bazant, M. Z.; Braatz, R. D.; Chueh, W. C.; Storey, B. D. Perspective—Combining Physics and Machine Learning to Predict Battery Lifetime. *J. Electrochem. Soc.* **2021**, *168* (3), 030525. <https://doi.org/10.1149/1945-7111/abec55>.
- (254) Clément, R. J.; Soc, J. E. Review — Manganese-Based P2-Type Transition Metal Oxides as Sodium-Ion Battery Cathode Materials Review — Manganese-Based P2-Type Transition Metal Oxides as Sodium-Ion Battery Cathode Materials. **2015**. <https://doi.org/10.1149/2.0201514jes>.
- (255) Liu, H.; Gao, X.; Hou, H. Manganese-Based Layered Oxide Cathodes for Sodium Ion Batteries. **2020**, No. June, 200–225. <https://doi.org/10.1002/nano.202000030>.
- (256) Zhang, Y.; Wu, M.; Ma, J.; Wei, G.; Ling, Y.; Zhang, R.; Huang, Y. Revisiting the $\text{Na}_2/3\text{Ni}_1/3\text{Mn}_2/3\text{O}_2$ Cathode: Oxygen Redox Chemistry and Oxygen Release Suppression. *ACS Cent. Sci.* **2020**, *6* (2), 232–240. <https://doi.org/10.1021/acscentsci.9b01166>.
- (257) Ma, C.; Alvarado, J.; Xu, J.; Clément, R. J.; Kodur, M.; Tong, W.; Grey, C. P.; Meng, Y. S. Exploring Oxygen Activity in the High Energy P2-Type $\text{Na}_{0.78}\text{Ni}_{0.23}\text{Mn}_{0.69}\text{O}_2$ Cathode Material for Na-Ion Batteries. *J. Am. Chem. Soc.* **2017**, *139* (13), 4835–4845. <https://doi.org/10.1021/jacs.7b00164>.
- (258) Lee, D. H.; Xu, J.; Meng, Y. S. An Advanced Cathode for Na-Ion Batteries with High Rate and Excellent Structural Stability. *Phys. Chem. Chem. Phys.* **2013**, *15* (9), 3304–3312. <https://doi.org/10.1039/c2cp44467d>.
- (259) Mn, L.; Yu, H.; Liu, G.; Li, G.; Zhang, J.; Chen, G.; Wen, L. Electrochimica Acta Study on Enhancing Electrochemical Properties of Li in Layered. *Electrochim. Acta* **2018**, *263*, 474–479. <https://doi.org/10.1016/j.electacta.2017.12.177>.
- (260) Zhao, W.; Kirie, H.; Tanaka, A.; Unno, M.; Yamamoto, S. Material with Enhanced Performance for Na Ion Batteries. *Mater. Lett.* **2014**, *135*, 131–134. <https://doi.org/10.1016/j.matlet.2014.07.153>.
- (261) Liu, Y.; Fang, X.; Zhang, A.; Shen, C.; Liu, Q.; Enaya, H. A. Nano Energy Sodium-Ion Batteries : The Capacity Decay Mechanism and Al_2O_3 Surface Modified Cation. *Nano Energy* **2016**, *27*, 27–34. <https://doi.org/10.1016/j.nanoen.2016.06.026>.
- (262) Manikandan, P.; Ramasubramonian, D.; Shaijumon, M. M. Layered P2-Type $\text{Na}_{0.5}\text{Ni}_{0.25}\text{Mn}_{0.75}\text{O}_2$ as a High Performance Cathode Material for Sodium-Ion Batteries. *Electrochim. Acta* **2016**, *206*, 199–206. <https://doi.org/10.1016/j.electacta.2016.04.138>.
- (263) Somerville, J. W.; House, R. A.; Tapia-ruiz, N.; Sobkowiak, A.; Ramos, S. Identification and Characterisation of High Energy Density P2-Type $\text{Na}_2/3[\text{Ni}_{1/3-y}/2\text{Mn}_{2/3-y}/2\text{Fe}_y]\text{O}_2$ Compounds for Na-Ion Batteries. *Mater. Chem. A* **2018**, *6*, 5271–5275. <https://doi.org/10.5287/bodleian>.

- (264) Ni, N.; Materials, M. O.; Batteries, S.; Palanisamy, M.; Kim, H. W.; Heo, S.; Lee, E.; Kim, Y. Insights into the Dual-Electrode Characteristics of Layered $\text{Na}_{0.5}\text{Ni}_{0.25}\text{Mn}_{0.75}\text{O}_2$ Materials for Sodium-Ion Batteries. *ACS Appl. Mater. Interfaces* **2017**, *2*. <https://doi.org/10.1021/acsami.6b15355>.
- (265) Luo, R.; Wu, F.; Xie, M.; Ying, Y.; Zhou, J.; Huang, Y.; Ye, Y.; Li, L.; Chen, R. Habit Plane-Driven P2-Type Manganese-Based Layered Oxide as Long Cycling Cathode for Na-Ion Batteries. **2018**, *383* (November 2017), 80–86. <https://doi.org/10.1016/j.jpowsour.2018.02.053>.
- (266) Hemalatha, K.; Jayakumar, M.; Prakash, A. S. Influence of the Manganese and Cobalt Content on the Electrochemical Performance of P2- $\text{Na}_{0.67}\text{Mn}_x\text{Co}_{1-x}\text{O}_2$ Cathodes for Sodium-Ion Batteries. **2018**, 1223–1232. <https://doi.org/10.1039/c7dt04372d>.
- (267) Wang, Y. A Study on Electrochemical Properties of P2-Type Na–Mn–Co–Cr–O Cathodes for Sodium-Ion Batteries. *Inorg. Chem. Front.* **2018**, *5*, 577–584. <https://doi.org/10.1039/c7qi00778g>.
- (268) Kang, W.; Yu, D. Y. W.; Lee, P.; Zhang, Z.; Bian, H.; Li, W.; Ng, T.; Zhang, W.; Lee, C. High-Power and Long-Life Sodium-Ion Batteries. **2016**, 0–7. <https://doi.org/10.1021/acsami.6b10841>.
- (269) Wang, P.; Yao, H.; Liu, X.; Yin, Y.; Zhang, J.; Wen, Y.; Yu, X.; Gu, L.; Guo, Y. Na+ Vacancy Disorder Promises High-Rate Na-Ion Batteries. **2018**, 1–10.
- (270) Hu, F.; Jiang, X. Li-Substituted P2- $\text{Na}_{0.66}\text{Li}_x\text{Mn}_{0.5}\text{Ti}_{0.5}\text{O}_2$ as an Advanced Cathode Material and New “bi-Functional” Electrode for Symmetric Sodium-Ion Batteries. *Adv. Powder Technol.* **2018**, *29* (4), 1049–1053. <https://doi.org/10.1016/j.appt.2018.01.027>.
- (271) Li, C.; Zhao, C.; Hu, B.; Tong, W.; Shen, M.; Hu, B. Unraveling the Critical Role of Ti Substitution in P2- $\text{Na}_x\text{Li}_y\text{Mn}_{1-y}\text{O}_2$ Cathodes for Highly Reversible Oxygen Redox Chemistry. *Chem. Mater.* **2020**, *32*. <https://doi.org/10.1021/acs.chemmater.9b03765>.
- (272) Lan, T.; Wei, W.; Xiao, S.; He, G.; Hong, J. P2-type Fe and Mn-based $\text{Na}_{0.67}\text{Ni}_{0.15}\text{Fe}_{0.35}\text{Mn}_{0.3}\text{Ti}_{0.2}\text{O}_2$ as Cathode Material with High Energy Density and Structural Stability for Sodium-ion Batteries. *J. Mater. Sci. Mater. Electron.* **2020**, *31* (12), 9423–9429. <https://doi.org/10.1007/s10854-020-03482-9>.
- (273) Zhao, C. Ti Substitution Facilitating Oxygen Oxidation in $\text{Na}_{2/3}\text{Mg}_{1/3}\text{Ti}_{1/6}\text{Mn}_{1/2}\text{O}_2$ Cathode. *Chem* **2019**, *5*, 2913–2925. <https://doi.org/10.1016/j.chempr.2019.08.003>.
- (274) Milewska, A.; Konrad, Ś.; Zaj, W.; Molenda, J. Overcoming Transport and Electrochemical Limitations in the High-Voltage $\text{Na}_{0.67}\text{Ni}_{0.33}\text{Mn}_{0.67-y}\text{Ti}_y\text{O}_2$ ($0 \leq y \leq 0.33$) Cathode Materials by Ti-Doping. *J. Power Sources* **2018**, *404* (October), 39–46. <https://doi.org/10.1016/j.jpowsour.2018.09.103>.
- (275) Yang, L.; Li, X.; Liu, J.; Xiong, S.; Ma, X.; Liu, P.; Bai, J.; Xu, W.; Tang, Y.; Hu, Y.; Liu, M.; Chen, H. Lithium-Doping Stabilized High-Performance P2–

- Na_{0.66}Li_{0.18}Fe_{0.12}Mn_{0.70}O₂ Cathode for Sodium Ion Batteries. *J. Am. Chem. Soc.* **2019**, *141*, 6680–6689. <https://doi.org/10.1021/jacs.9b01855>.
- (276) Hasa, I.; Buchholz, D.; Passerini, S.; Scrosati, B.; Hassoun, J. High Performance Na_{0.5}[Ni_{0.23}Fe_{0.13}Mn_{0.63}]O₂ Cathode for Sodium-Ion Batteries. *Adv. Energy Mater.* **2014**, *4*, 2–8. <https://doi.org/10.1002/aenm.201400083>.
- (277) Marino, C.; Marelli, E.; Villevieille, C.; Park, S.; He, N. Co-Free P2–Na_{0.67}Mn_{0.6}Fe_{0.25}Al_{0.15}O₂ as Promising Cathode Material for Sodium-Ion Batteries. *ACS Appl. Energy Mater.* **2018**, *1*, 5960–5967. <https://doi.org/10.1021/acsaem.8b01015>.
- (278) Yang, Q.; Wang, P.; Guo, J.; Chen, Z.; Pang, W.; Huang, K.; Guo, Y.; Wu, X.; Zhang, J. Advanced P2–Na_{2/3}Ni_{1/3}Mn_{7/12}Fe_{1/12}O₂ Cathode Material with Suppressed P2–O₂ Phase Transition toward High-Performance Sodium-Ion Battery. *ACS Appl. Mater. Interfaces* **2018**, *10*, 34272–34282. <https://doi.org/10.1021/acsami.8b12204>.
- (279) Stoyanova, R.; Carlier, D.; Sendova-Vassileva, M.; Yoncheva, M.; Zhecheva, E.; Nihtianova, D.; Delmas, C. Stabilization of Over-Stoichiometric Mn⁴⁺ in Layered Na_{2/3}MnO₂. *J. Solid State Chem.* **2010**, *183* (6), 1372–1379. <https://doi.org/10.1016/j.jssc.2010.04.024>.
- (280) Kumakura, S.; Tahara, Y.; Kubota, K.; Chihara, K.; Komaba, S. Sodium and Manganese Stoichiometry of P2-Type Na_{2/3}MnO₂. *Angew. Chemie* **2016**, *128* (41), 12952–12955. <https://doi.org/10.1002/ange.201606415>.
- (281) Zheng, X.; Li, P.; Zhu, H.; Rui, K.; Zhao, G.; Shu, J.; Xu, X.; Sun, W.; Dou, S. X. New Insights into Understanding the Exceptional Electrochemical Performance of P2-Type Manganese-Based Layered Oxide Cathode for Sodium Ion Batteries. *Energy Storage Mater.* **2018**, *15*, 257–265. <https://doi.org/10.1016/j.ensm.2018.05.001>.
- (282) Yoshida, H.; Yabuuchi, N.; Komaba, S. NaFe_{0.5}Co_{0.5}O₂ as High Energy and Power Positive Electrode for Na-Ion Batteries. *Electrochem. commun.* **2013**, *34*, 60–63. <https://doi.org/10.1016/j.elecom.2013.05.012>.
- (283) Wang, J. E.; Han, W. H.; Chang, K. J.; Jung, Y. H.; Kim, D. K. New Insight into Na Intercalation with Li Substitution on Alkali Site and High Performance of O3-Type Layered Cathode Material for Sodium Ion Batteries. *Mater. Chem. A* **2018**, *6*, 22731–22740. <https://doi.org/10.1039/c8ta06159a>.
- (284) Huon, M.; Gonzalo, E.; Casas-cabanias, M. Structural Evolution and Electrochemistry of Monoclinic NaNiO₂ upon the First Cycling Process. *J. Power Sources* **2014**, *258*, 266–271. <https://doi.org/10.1016/j.jpowsour.2014.02.048>.
- (285) Sun, L.; Xie, Y.; Liao, X.; Wang, H.; Tan, G.; Chen, Z.; Ren, Y.; Gim, J.; Tang, W.; He, Y.; Amine, K.; Ma, Z. Insight into Ca-Substitution Effects on O3-Type NaNi_{1/3}Fe_{1/3}Mn_{1/3}O₂ Cathode Materials for Sodium-Ion Batteries Application. *Small* **2018**, *1704523*, 1–7. <https://doi.org/10.1002/smll.201704523>.

- (286) Jung, K.; Choi, J.; Shin, H.; Tran, H.; Bin, W.; Lee, J. Mg-Doped Na[Ni_{1/3}Fe_{1/3}Mn_{1/3}]O₂ with Enhanced Cycle Stability as a Cathode Material for Sodium-Ion Batteries. *Solid State Sci.* **2020**, *106* (June), 106334. <https://doi.org/10.1016/j.solidstatesciences.2020.106334>.
- (287) Zhou, D. Materials The Effect of Na Content on the Electrochemical for Sodium-Ion Batteries. *J. Mater. Sci.* **2019**, *54* (9), 7156–7164. <https://doi.org/10.1007/s10853-018-03277-8>.
- (288) Hwang, J.; Myung, S.; Aurbach, D.; Sun, Y. Effect of Nickel and Iron on Structural and Electrochemical Properties of O3 Type Layer Cathode Materials for Sodium-Ion Batteries. *J. Power Sources* **2016**, *324*, 106–112. <https://doi.org/10.1016/j.jpowsour.2016.05.064>.
- (289) Thorne, J. S.; Electrochem, J.; Soc, A.; Thorne, J. S.; Dunlap, R. A.; Obrovac, M. N. Structure and Electrochemistry of Na_xFe_xMn_{1-x}O₂ (1.0 ≤ x ≤ 0.5) for Na- Ion Battery Positive Electrodes for Na-Ion Battery Positive Electrodes. *J. Electrochem. Soc.* **2013**, *2* (160), 361–367. <https://doi.org/10.1149/2.058302jes>.
- (290) Nguyen, L. H. B.; Chen, F.; Masquelier, C.; Croguennec, L. Chapter 2. Polyanionic-Type Compounds as Positive Electrode for Na-Ion Batteries. In *Na-ion Batteries*; 2020; pp 47–100.
- (291) Zhou, W.; Xue, L.; Gao, H.; Li, Y.; Xin, S.; Fu, G.; Cui, Z.; Zhu, Y.; Goodenough, J. B. Na_xMV(PO₄)₃ (M=Mn, Fe, Ni) Structure and Properties for Sodium Extraction. *Nano Lett.* **2016**, *3*, 3–8. <https://doi.org/10.1021/acs.nanolett.6b04044>.
- (292) Chen, F.; Kovrugin, V. M.; David, R.; Mentré, O.; Fauth, F.; Chotard, J.; Masquelier, C. A NASICON-Type Positive Electrode for Na Batteries with High Energy Density: Na₄MnV(PO₄)₃. **2019**, *1800218*, 1–9. <https://doi.org/10.1002/smt.201800218>.
- (293) Li, H.; Xu, M.; Zhang, Z.; Lai, Y.; Ma, J. Engineering of Polyanion Type Cathode Materials for Sodium-Ion Batteries: Toward Higher Energy/Power Density. *Adv. Funct. Mater.* **2020**, *30* (28), 1–29. <https://doi.org/10.1002/adfm.202000473>.
- (294) Barpanda, P.; Lander, L.; Nishimura, S. I.; Yamada, A. Polyanionic Insertion Materials for Sodium-Ion Batteries. *Adv. Energy Mater.* **2018**, *8* (17), 1–26. <https://doi.org/10.1002/aenm.201703055>.
- (295) Bianchini, M.; Xiao, P.; Wang, Y.; Ceder, G. Additional Sodium Insertion into Polyanionic Cathodes for Higher-Energy Na-Ion Batteries. *Adv. Energy Mater.* **2017**, *7* (18). <https://doi.org/10.1002/aenm.201700514>.
- (296) Kim, M.; Kim, D.; Lee, W.; Jang, H. M.; Kang, B. New Class of 3.7 v Fe-Based Positive Electrode Materials for Na-Ion Battery Based on Cation-Disordered Polyanion Framework. *Chem. Mater.* **2018**, *30* (18), 6346–6352. <https://doi.org/10.1021/acs.chemmater.8b02354>.
- (297) Song, T.; Yao, W.; Kiadkhunthod, P.; Zheng, Y.; Wu, N.; Zhou, X.; Tunmee, S.; Sattayaporn, S.; Tang, Y. A Low-Cost and Environmentally Friendly Mixed Polyanionic Cathode for Sodium-Ion Storage. *Angew. Chemie* **2020**, *132* (2), 750–755.

<https://doi.org/10.1002/ange.201912272>.

- (298) Olchowka, J.; Nguyen, L. H. B.; Broux, T.; Sanz Camacho, P.; Petit, E.; Fauth, F.; Carlier, D.; Masquelier, C.; Croguennec, L. Aluminum Substitution for Vanadium in the $\text{Na}_3\text{V}_2(\text{PO}_4)_2\text{F}_3$ and $\text{Na}_3\text{V}_2(\text{PO}_4)_2\text{FO}_2$ Type Materials. *Chem. Commun.* **2019**, 55 (78), 11719–11722. <https://doi.org/10.1039/C9CC05137F>.
- (299) Liu, Q.; Hu, Z.; Chen, M.; Zou, C.; Jin, H.; Wang, S.; Chou, S. L.; Liu, Y.; Dou, S. X. The Cathode Choice for Commercialization of Sodium-Ion Batteries: Layered Transition Metal Oxides versus Prussian Blue Analogs. *Adv. Funct. Mater.* **2020**, 30 (14), 1–15. <https://doi.org/10.1002/adfm.201909530>.
- (300) Pasta, M.; Wang, R. Y.; Ruffo, R.; Qiao, R.; Lee, H.-W.; Shyam, B.; Guo, M.; Wang, Y.; Wray, L. A.; Yang, W.; Toney, M. F.; Cui, Y. Manganese–Cobalt Hexacyanoferrate Cathodes for Sodium-Ion Batteries. *J. Mater. Chem. A* **2016**, 4 (11), 4211–4223. <https://doi.org/10.1039/C5TA10571D>.
- (301) Wu, X.; Wu, C.; Wei, C.; Hu, L.; Qian, J.; Cao, Y.; Ai, X.; Wang, J.; Yang, H. Highly Crystallized $\text{Na}_2\text{CoFe}(\text{CN})_6$ with Suppressed Lattice Defects as Superior Cathode Material for Sodium-Ion Batteries. *ACS Appl. Mater. Interfaces* **2016**, 8 (8), 5393–5399. <https://doi.org/10.1021/acsami.5b12620>.
- (302) Sottmann, J.; Bernal, F. L. M.; Yussenko, K. V.; Herrmann, M.; Emerich, H.; Wragg, D. S.; Margadonna, S. In Operando Synchrotron XRD/XAS Investigation of Sodium Insertion into the Prussian Blue Analogue Cathode Material $\text{Na}_{1.32}\text{Mn}[\text{Fe}(\text{CN})_6]_{0.83} \cdot z\text{H}_2\text{O}$. *Electrochim. Acta* **2016**, 200, 305–313. <https://doi.org/10.1016/j.electacta.2016.03.131>.
- (303) He, G.; Nazar, L. F. Crystallite Size Control of Prussian White Analogues for Nonaqueous Potassium-Ion Batteries. *ACS Energy Lett.* **2017**, 2 (5), 1122–1127. <https://doi.org/10.1021/acsenergylett.7b00179>.
- (304) You, Y.; Wu, X.-L.; Yin, Y.-X.; Guo, Y.-G. High-Quality Prussian Blue Crystals as Superior Cathode Materials for Room-Temperature Sodium-Ion Batteries. *Energy Environ. Sci.* **2014**, 7 (5), 1643–1647. <https://doi.org/10.1039/C3EE44004D>.
- (305) Su, D.; McDonagh, A.; Qiao, S.; Wang, G. High-Capacity Aqueous Potassium-Ion Batteries for Large-Scale Energy Storage. *Adv. Mater.* **2017**, 29 (1), 1604007. <https://doi.org/10.1002/adma.201604007>.
- (306) Wang, H.; Zhu, Q.; Li, H.; Xie, C.; Zeng, D. Tuning the Particle Size of Prussian Blue by a Dual Anion Source Method. *Cryst. Growth Des.* **2018**, 18 (10), 5780–5789. <https://doi.org/10.1021/acs.cgd.8b00239>.
- (307) Shrivastava, A.; Smith, K. C. Electron Conduction in Nanoparticle Agglomerates Limits Apparent Na^+ Diffusion in Prussian Blue Analogue Porous Electrodes. *J. Electrochem. Soc.* **2018**, 165 (9), A1777–A1787. <https://doi.org/10.1149/2.0861809jes>.
- (308) Moritomo, Y.; Urase, S.; Shibata, T. Enhanced Battery Performance in Manganese

- Hexacyanoferrate by Partial Substitution. *Electrochim. Acta* **2016**, *210*, 963–969. <https://doi.org/10.1016/j.electacta.2016.05.205>.
- (309) Chen, S.; Niu, C.; Lee, H.; Chen, S.; Niu, C.; Lee, H.; Li, Q.; Yu, L.; Xu, W.; Zhang, J. Critical Parameters for Evaluating Coin Cells and Pouch Cells of Rechargeable Li-Metal Batteries. *Energy Storage Mater.* **2019**, *1*, 1094–1105. <https://doi.org/10.1016/j.joule.2019.02.004>.
- (310) Niu, C.; Liu, D.; Lochala, J. A.; Anderson, C. S.; Cao, X.; Gross, M. E.; Xu, W.; Zhang, J. G.; Whittingham, M. S.; Xiao, J.; Liu, J. Balancing Interfacial Reactions to Achieve Long Cycle Life in High-Energy Lithium Metal Batteries. *Nat. Energy* **2021**, *6* (7), 723–732. <https://doi.org/10.1038/s41560-021-00852-3>.
- (311) U.S. Department of Energy. Energy Storage Grand Challenge Energy Storage Market Report 2020. *U.S. Dep. Energy* **2020**, *Technical* (December), 65.
- (312) Wadia, C.; Albertus, P.; Srinivasan, V. Resource Constraints on the Battery Energy Storage Potential for Grid and Transportation Applications. *J. Power Sources* **2011**, *196* (3), 1593–1598. <https://doi.org/10.1016/j.jpowsour.2010.08.056>.
- (313) Nayak, P. K.; Yang, L.; Brehm, W.; Adelhelm, P. From Lithium-Ion to Sodium-Ion Batteries: Advantages, Challenges, and Surprises. *Angew. Chemie - Int. Ed.* **2018**, *57* (1), 102–120. <https://doi.org/10.1002/anie.201703772>.
- (314) Tapia-ruiz, N.; Armstrong, A. R.; Alptekin, H.; Amores, M. A.; Au, H.; Barker, J.; Boston, R.; Brant, W. R.; Brittain, J. M.; Chen, Y.; Chhowalla, M.; Choi, Y.; Costa, S. I. R.; Ribadeneyra, M. C.; Dickson, S. A. M.; Eweka, E. I.; Forero-saboya, J. D.; Grey, C. P.; Li, Z.; Mertens, S. F. L.; Mogensen, R.; Monconduit, L.; Ould, D. M. C.; Palgrave, R. G.; Poizot, P.; Ponrouch, A.; Renault, S.; Reynolds, E. M.; Rudola, A.; Sayers, R.; Scanlon, D. O.; Sen, S.; Seymour, V. R.; Silv, B.; Stone, G. S.; Thomas, C. I.; Titirici, M.; Tong, J.; Wood, T. J.; Wright, D. S.; Younesi, R. 2021 Roadmap for Sodium-Ion Batteries. *J. Phys. Energy* **2021**, *3*, 031503.
- (315) Ridley, P.; Hoang, L.; Nguyen, B.; Sebti, E.; Duong, G.; Chen, Y. Glass-Ceramic Sodium-Deficient Chlorides with High Sodium-Ion Conductivity. *ChemRxiv* **2022**, *2022*, x7llq. <https://doi.org/10.26434/chemrxiv-2022-x7llq>.
- (316) Wang, C.; Wang, H.; Matios, E.; Hu, X.; Li, W. A Chemically Engineered Porous Copper Matrix with Cylindrical Core–Shell Skeleton as a Stable Host for Metallic Sodium Anodes. *Adv. Funct. Mater.* **2018**, *28* (30), 1802282. <https://doi.org/10.1002/adfm.201802282>.
- (317) Chi, S.-S.; Qi, X.-G.; Hu, Y.-S.; Fan, L.-Z. 3D Flexible Carbon Felt Host for Highly Stable Sodium Metal Anodes. *Adv. Energy Mater.* **2018**, *8* (15), 1702764. <https://doi.org/10.1002/aenm.201702764>.
- (318) Zhao, Y.; Yang, X.; Kuo, L.-Y.; Kaghazchi, P.; Sun, Q.; Liang, J.; Wang, B.; Lushington, A.; Li, R.; Zhang, H.; Sun, X. High Capacity, Dendrite-Free Growth, and Minimum Volume Change Na Metal Anode. *Small* **2018**, *14* (20), 1703717.

<https://doi.org/10.1002/sml.201703717>.

- (319) Ye, H.; Wang, C.-Y.; Zuo, T.-T.; Wang, P.-F.; Yin, Y.-X.; Zheng, Z.-J.; Wang, P.; Cheng, J.; Cao, F.-F.; Guo, Y.-G. Realizing a Highly Stable Sodium Battery with Dendrite-Free Sodium Metal Composite Anodes and O₃-Type Cathodes. *Nano Energy* **2018**, *48*, 369–376. <https://doi.org/10.1016/j.nanoen.2018.03.069>.
- (320) Yoon, H. J.; Kim, N. R.; Jin, H.-J.; Yun, Y. S. Macroporous Catalytic Carbon Nanotemplates for Sodium Metal Anodes. *Adv. Energy Mater.* **2018**, *8* (6), 1701261. <https://doi.org/10.1002/aenm.201701261>.
- (321) Cohn, A. P.; Muralidharan, N.; Carter, R.; Share, K.; Pint, C. L. Anode-Free Sodium Battery through in Situ Plating of Sodium Metal. *Nano Lett.* **2017**, *17* (2), 1296–1301. <https://doi.org/10.1021/acs.nanolett.6b05174>.
- (322) Liu, S.; Tang, S.; Zhang, X.; Wang, A.; Yang, Q.-H.; Luo, J. Porous Al Current Collector for Dendrite-Free Na Metal Anodes. *Nano Lett.* **2017**, *17* (9), 5862–5868. <https://doi.org/10.1021/acs.nanolett.7b03185>.
- (323) Lee, J.; Lee, Y.; Lee, J.; Lee, S.-M.; Choi, J.-H.; Kim, H.; Kwon, M.-S.; Kang, K.; Lee, K. T.; Choi, N.-S. Ultraconcentrated Sodium Bis(Fluorosulfonyl)Imide-Based Electrolytes for High-Performance Sodium Metal Batteries. *ACS Appl. Mater. Interfaces* **2017**, *9* (4), 3723–3732. <https://doi.org/10.1021/acsami.6b14878>.
- (324) Wang, H.; Wang, C.; Matios, E.; Li, W. Facile Stabilization of the Sodium Metal Anode with Additives: Unexpected Key Role of Sodium Polysulfide and Adverse Effect of Sodium Nitrate. *Angew. Chemie Int. Ed.* **2018**, *57* (26), 7734–7737. <https://doi.org/10.1002/anie.201801818>.
- (325) Gao, L.; Chen, J.; Liu, Y.; Yamauchi, Y.; Huang, Z.; Kong, X. Revealing the Chemistry of an Anode-Passivating Electrolyte Salt for High Rate and Stable Sodium Metal Batteries. *J. Mater. Chem. A* **2018**, *6* (25), 12012–12017. <https://doi.org/10.1039/C8TA03436B>.
- (326) Lee, Y.; Lee, J.; Lee, J.; Kim, K.; Cha, A.; Kang, S.; Wi, T.; Kang, S. J.; Lee, H.-W.; Choi, N.-S. Fluoroethylene Carbonate-Based Electrolyte with 1 M Sodium Bis(Fluorosulfonyl)Imide Enables High-Performance Sodium Metal Electrodes. *ACS Appl. Mater. Interfaces* **2018**, *10* (17), 15270–15280. <https://doi.org/10.1021/acsami.8b02446>.
- (327) Basile, A.; Makhlooghiyazad, F.; Yunis, R.; MacFarlane, D. R.; Forsyth, M.; Howlett, P. C. Extensive Sodium Metal Plating and Stripping in a Highly Concentrated Inorganic–Organic Ionic Liquid Electrolyte through Surface Pretreatment. *ChemElectroChem* **2017**, *4* (5), 986–991. <https://doi.org/10.1002/celec.201600784>.
- (328) Shi, Q.; Zhong, Y.; Wu, M.; Wang, H.; Wang, H. High-Performance Sodium Metal Anodes Enabled by a Bifunctional Potassium Salt. *Angew. Chemie Int. Ed.* **2018**, *57* (29), 9069–9072. <https://doi.org/10.1002/anie.201803049>.
- (329) Zhang, D.; Li, B.; Wang, S.; Yang, S. Simultaneous Formation of Artificial SEI Film and

- 3D Host for Stable Metallic Sodium Anodes. *ACS Appl. Mater. Interfaces* **2017**, 9 (46), 40265–40272. <https://doi.org/10.1021/acsami.7b12568>.
- (330) Wei, S.; Choudhury, S.; Xu, J.; Nath, P.; Tu, Z.; Archer, L. A. Highly Stable Sodium Batteries Enabled by Functional Ionic Polymer Membranes. *Adv. Mater.* **2017**, 29 (12), 1605512. <https://doi.org/10.1002/adma.201605512>.
- (331) Zhao, Y.; Goncharova, L. V.; Lushington, A.; Sun, Q.; Yadegari, H.; Wang, B.; Xiao, W.; Li, R.; Sun, X. Superior Stable and Long Life Sodium Metal Anodes Achieved by Atomic Layer Deposition. *Adv. Mater.* **2017**, 29 (18), 1606663. <https://doi.org/10.1002/adma.201606663>.
- (332) Wang, H.; Wang, C.; Matios, E.; Li, W. Critical Role of Ultrathin Graphene Films with Tunable Thickness in Enabling Highly Stable Sodium Metal Anodes. *Nano Lett.* **2017**, 17 (11), 6808–6815. <https://doi.org/10.1021/acs.nanolett.7b03071>.
- (333) Luo, W.; Lin, C.; Zhao, O.; Noked, M.; Zhang, Y.; Rubloff, G. W.; Hu, L. Ultrathin Surface Coating Enables the Stable Sodium Metal Anode. *Adv. Energy Mater.* **2017**, 7 (2), 1601526. <https://doi.org/10.1002/aenm.201601526>.
- (334) Brandt, K.; Stiles, J. A. R. Battery and Methods of Making the Battery. CA1190279A, 1985.
- (335) Hirai, T.; Yoshimatsu, I.; Yamaki, J. Influence of Electrolyte on Lithium Cycling Efficiency with Pressurized Electrode Stack. *J. Electrochem. Soc.* **1994**, 141 (3), 611–614. <https://doi.org/10.1149/1.2054778>.
- (336) Fang, C.; Wang, X.; Meng, Y. S. Key Issues Hindering a Practical Lithium-Metal Anode. *Trends Chem.* **2019**, 1 (2), 152–158. <https://doi.org/10.1016/j.trechm.2019.02.015>.
- (337) Fang, C.; Lu, B.; Pawar, G.; Zhang, M.; Cheng, D.; Chen, S.; Ceja, M.; Doux, J. M.; Musrock, H.; Cai, M.; Liaw, B.; Meng, Y. S. Pressure-Tailored Lithium Deposition and Dissolution in Lithium Metal Batteries. *Nat. Energy* **2021**, 6 (10), 987–994. <https://doi.org/10.1038/s41560-021-00917-3>.
- (338) Lu, B.; Bao, W.; Yao, W.; Doux, J.-M.; Fang, C.; Meng, Y. S. Editors' Choice—Methods—Pressure Control Apparatus for Lithium Metal Batteries. *J. Electrochem. Soc.* **2022**, 169 (7), 070537. <https://doi.org/10.1149/1945-7111/ac834c>.
- (339) Eshetu, G. G.; Elia, G. A.; Armand, M.; Forsyth, M.; Komaba, S.; Rojo, T.; Passerini, S. Electrolytes and Interphases in Sodium-Based Rechargeable Batteries: Recent Advances and Perspectives. *Adv. Energy Mater.* **2020**, 10 (20). <https://doi.org/10.1002/aenm.202000093>.
- (340) Doux, J. M.; Yang, Y.; Tan, D. H. S.; Nguyen, H.; Wu, E. A.; Wang, X.; Banerjee, A.; Meng, Y. S. Pressure Effects on Sulfide Electrolytes for All Solid-State Batteries. *J. Mater. Chem. A* **2020**, 8 (10), 5049–5055. <https://doi.org/10.1039/c9ta12889a>.
- (341) Cheng, D.; Lu, B.; Raghavendran, G.; Zhang, M.; Meng, Y. S. Leveraging Cryogenic

- Electron Microscopy for Advancing Battery Design. *Matter* **2022**, 5 (1), 26–42. <https://doi.org/10.1016/j.matt.2021.11.019>.
- (342) Chung, H.; Li, Y.; Zhang, M.; Grenier, A.; Mejia, C.; Cheng, D.; Sayahpour, B.; Song, C.; Shen, M. H.; Huang, R.; Wu, E. A.; Chapman, K. W.; Kim, S. J.; Meng, Y. S. Mitigating Anisotropic Changes in Classical Layered Oxide Materials by Controlled Twin Boundary Defects for Long Cycle Life Li-Ion Batteries. *Chem. Mater.* **2022**, 34 (16), 7302–7312. <https://doi.org/10.1021/acs.chemmater.2c01234>.
- (343) Ding, Z.; Tang, Y.; Sai, V.; Chakravadhanula, K.; Ma, Q.; Tietz, F.; Dai, Y.; Scherer, T.; Kübel, C. Exploring the Influence of Focused Ion Beam Processing and Scanning Electron Microscopy Imaging on Solid-State Electrolytes. *Microscopy* **2022**, 1–10.
- (344) Hong, Y. S.; Li, N.; Chen, H.; Wang, P.; Song, W. L.; Fang, D. In Operando Observation of Chemical and Mechanical Stability of Li and Na Dendrites under Quasi-Zero Electrochemical Field. *Energy Storage Mater.* **2018**, 11 (August 2017), 118–126. <https://doi.org/10.1016/j.ensm.2017.10.007>.
- (345) He, Y.; Ren, X.; Xu, Y.; Engelhard, M. H.; Li, X.; Xiao, J.; Liu, J.; Zhang, J. G.; Xu, W.; Wang, C. Origin of Lithium Whisker Formation and Growth under Stress. *Nat. Nanotechnol.* **2019**, 14 (11), 1042–1047. <https://doi.org/10.1038/s41565-019-0558-z>.
- (346) Jang, J.; Chen, Y. T.; Deysher, G.; Cheng, D.; Ham, S. Y.; Cronk, A.; Ridley, P.; Yang, H.; Sayahpour, B.; Han, B.; Li, W.; Yao, W.; Wu, E. A.; Doux, J. M.; Nguyen, L. H. B.; Oh, J. A. S.; Tan, D. H. S.; Meng, Y. S. Enabling a Co-Free, High-Voltage LiNi_{0.5}Mn_{1.5}O₄ Cathode in All-Solid-State Batteries with a Halide Electrolyte. *ACS Energy Lett.* **2022**, 7 (8), 2531–2539. <https://doi.org/10.1021/acsenergylett.2c01397>.
- (347) Cronk, A.; Chen, Y.; Deysher, G.; Ham, S.; Yang, H.; Ridley, P.; Sayahpour, B.; Nguyen, L. H. B.; Oh, J. A. S.; Jang, J.; Tan, D. H. S.; Meng, Y. S. Overcoming the Interfacial Challenges of LiFePO₄ in Inorganic All-Solid-State Batteries. *ACS Energy Lett.* **2023**, 8 (1), 827–835. <https://doi.org/10.1021/acsenergylett.2c02138>.
- (348) Chen, Y.-T.; Marple, M. A. T.; Tan, D. H. S.; Ham, S.-Y.; Sayahpour, B.; Li, W.-K.; Yang, H.; Lee, J. B.; Hah, H. J.; Wu, E. A.; Doux, J.-M.; Jang, J.; Ridley, P.; Cronk, A.; Deysher, G.; Chen, Z.; Meng, Y. S. Investigating Dry Room Compatibility of Sulfide Solid-State Electrolytes for Scalable Manufacturing. *J. Mater. Chem. A* **2022**, 10 (13), 7155–7164. <https://doi.org/10.1039/D1TA09846B>.
- (349) Deysher, G.; Chen, Y. T.; Sayahpour, B.; Lin, S. W. H.; Ham, S. Y.; Ridley, P.; Cronk, A.; Wu, E. A.; Tan, D. H. S.; Doux, J. M.; Oh, J. A. S.; Jang, J.; Nguyen, L. H. B.; Meng, Y. S. Evaluating Electrolyte-Anode Interface Stability in Sodium All-Solid-State Batteries. *ACS Appl. Mater. Interfaces* **2022**, 14 (42), 47706–47715. <https://doi.org/10.1021/acсами.2c12759>.